Unconventional superconductivity in quasi-2D materials with strong spin-orbit coupling

Raphaël Leriche

Thèse

Pour l'obtention du grade de

Docteur de Sorbonne Université

École doctorale Physique en Île de France - ED 564

Unconventional superconductivity in quasi-2D materials with strong spin-orbit coupling

Auteur :
Raphaël Leriche

Sous la direction de :
Dr. Tristan Cren
Dr. Christophe Brun

Composition du jury :

Pr. Christoph Renner	Rapporteur
Dr. Hermann Suderow	Rapporteur
Pr. Andrea Gauzzi	Examinateur
Dr. Marie-Aude Measson	Examinatrice
Dr. Nicolas Bergeal	Examinateur

Abstract

Unconventional superconductivity in quasi-2D materials with strong spin-orbit coupling

The realization of topological superconductors is one of the main current goals of condensed matter physics. It was indeed predicted that such systems should host Majorana fermions. These Majorana fermions possess both a non-Abelian statistics and, because of their topological origin, a certain robustness against local disorder, which makes them attractive for quantum computing applications. One approach likely to lead to topological superconductivity consists in considering superconducting systems with strong spin-orbit coupling and with broken inversion symmetry. It is in this framework that, during this thesis, I performed scanning tunneling microscopy and spectroscopy measurements on quasi-2D materials : $(LaSe)_{1,14}(NbSe_2)_2$ and Sr_2IrO_4.

I first studied the electronic properties of misfit compound LaNb2Se5, which is a parent of transition metal dichalcogenide 2H-$NbSe_2$. $(LaSe)_{1,14}(NbSe_2)_2$ is a heterostructure made out of alternations of $NbSe_2$ bilayers with trigonal prismatic geometry and LaSe bilayers with rocksalt structure. $(LaSe)_{1,14}(NbSe_2)_2$ is a potential candidate for topological superconductivity because of the presence of both a strong spin-orbit coupling and of broken inversion symmetry in $NbSe_2$ planes. Here, I present spectroscopic results showing that the electronic structure of $(LaSe)_{1,14}(NbSe_2)_2$ is very similar to the one of electron-doped monolayer $NbSe_2$ with a shift of the chemical potential of 0,3 eV, priorly never reached. I could also demonstrate the quasi-2D nature of $(LaSe)_{1,14}(NbSe_2)_2$ and more particularly the presence of a strong Ising spin-orbit coupling. Moreover, the observed weakness of superconductivity against non-magnetic disorder combined with quasiparticle interferences measurements allowed me to exhibit the unconventional nature of $(LaSe)_{1,14}(NbSe_2)_2$ superconducting order parameter. This study opens the possibility to use misfit heterostructures such as $(LaSe)_{1,14}(NbSe_2)_2$ to study the physics of transition metal dichalcogenides in the 2D limit, for which many theoretical studies predict topological superconductivity.

In this thesis, I also present a study on the effects of doping on the electronic properties of iridate compound Sr_2IrO_4. Sr_2IrO_4 is a spin-orbit induced Mott insulator. Because inversion symmetry is locally broken in Sr_2IrO_4, some theoretical predictions suggest that Sr_2IrO_4 should turn into a topological superconductor once doped. Here, I exhibit a nanometer-scale inhomogeneous doping-driven Mott insulator to pseudo-metallic phase transition. This work further justifies the importance of using a local probe such as scanning tunnelling microscopy in order to complete results on Mott physics obtained by integrative methods like angle-resolved photoemission spectroscopy.

Key words : Correlations (superconductivity, Mott insulator, charge density wave), 2D materials (transition metal dichalcogenides, iridate), scanning tunnelling microscopy and spectroscopy, spin-orbit coupling, topological superconductivity

Résumé

Supraconductivité non conventionnelle dans des matériaux quasi-2D à fort couplage spin-orbite

La réalisation de supraconducteurs topologiques constitue un des principaux enjeux actuels de la physique de la matière condensée. Il a en effet été prédit que ces systèmes devaient abriter des fermions de Majorana. Ces fermions de Majorana disposent à la fois d'une statistique non-abélienne et, du fait de leur origine topologique, d'une robustesse face au désordre local, ce qui les rend très attrayants pour des applications en informatique quantique. Une approche susceptible de conduire à de la supraconductivité topologique consiste à considérer des systèmes supraconducteurs à fort couplage spin-orbite et brisant la symétrie d'inversion. C'est dans cette optique que, dans le cadre de cette thèse, j'ai effectué des mesures de microscopie et spectroscopie par effet tunnel sur des matériaux quasi-bidimensionnels : $(LaSe)_{1,14}(NbSe_2)_2$ et Sr_2IrO_4.

J'ai tout d'abord étudié les propriétés électroniques du matériau incommensurable $(LaSe)_{1,14}(NbSe_2)_2$, proche parent du composé dichalcogénure de métaux de transition 2H-$NbSe_2$. $(LaSe)_{1,14}(NbSe_2)_2$ est une hétérostructure faite d'alternances de biplans $NbSe_2$ à géométrie prismatique trigonale et de biplans de LaSe avec une structure de sel de roche. Le fort couplage spin-orbite ainsi que la non-centrosymétrie présents dans les plans $NbSe_2$ font de $(LaSe)_{1,14}(NbSe_2)_2$ un potentiel candidat pour de la supraconductivité topologique. Dans cette thèse, je présente des résultats de spectroscopie montrant que la structure électronique de $(LaSe)_{1,14}(NbSe_2)_2$ est similaire à celle de la monocouche de $NbSe_2$ avec un dopage de type électron accompagné par un déplacement du potentiel chimique de 0,3 eV, jusqu'alors inégalé. J'ai également pu démontrer la nature quasi–bidimensionnelle de $(LaSe)_{1,14}(NbSe_2)_2$ et notamment la présence d'un fort couplage spin-orbite de type Ising. De plus, la faible robustesse de la supraconductivité vis à vis du désordre non magnétique couplée à des mesures d'interférences de quasiparticules m'a permis de mettre en avant le caractère non conventionnel du paramètre d'ordre supraconducteur dans $(LaSe)_{1,14}(NbSe_2)_2$. Cette étude permet d'envisager l'utilisation d'hétérostructures incommensurables telles que $(LaSe)_{1,14}(NbSe_2)_2$ pour explorer la physique des dichalcogénures de métaux de transition dans la limite bidimensionnelle, pour laquelle de nombreuses études théoriques ont prédit une supraconductivité topologique.

Dans cette thèse, je présente également une étude des effets du dopage sur les propriétés électroniques de l'oxyde d'iridium Sr_2IrO_4. Sr_2IrO_4 est un isolant de Mott non conventionnel puisqu'il doit cette propriété à la présence d'un fort couplage spin-orbite. Du fait d'une brisure locale de la symétrie d'inversion, certaines prédictions théoriques ont pu montrer que Sr_2IrO_4 devrait devenir un supraconducteur topologique une fois dopé. Ici, je montre qu'avec le dopage, Sr_2IrO_4 subit une transition de phase inhomogène à l'échelle nanométrique entre un état isolant de Mott et un état pseudo-métallique. Ce travail justifie la pertinence d'utiliser une sonde locale telle que le microscope à effet tunnel afin de venir compléter des résultats sur la physique de Mott obtenus par des méthodes intégratives comme la spectroscopie électronique résolue en angle.

Mots clés : Phase corrélées (supraconductivité, isolant de Mott, onde de densité de charge), matériaux 2D (dichalcogénure de métaux de transition, oxyde d'iridium), microscopie et spectroscopie à effet tunnel, couplage spin-orbite, supraconductivité topologique

Remerciements

Il y a beaucoup de gens que je souhaiterais remercier après ces trois années de thèse.

Tout d'abord, j'aimerais remercier les membres du jury pour avoir accepté de prendre de leur temps pour évaluer mon travail. Je remercie également Sorbonne Université qui a financé cette thèse, et l'EDPIF qui m'a, entre autres, permis de participer à un certain nombre de formations réellement enrichissantes.

Ensuite, j'aimerais bien évidemment remercier tous les membres de l'équipe de Spectroscopie de Nouveaux Etats Quantiques. Tout d'abord, je voudrais remercier Christophe pour m'avoir initié aux méthodes de l'ultravide, de la cryogénie et de la microscopie/spectroscopie à effet tunnel, et de l'avoir toujours fait avec beaucoup de pédagogie. Je remercie également François et Pascal qui ont su nous tirer d'affaire plus d'une fois face à des problèmes techniques, mais aussi pour leur bonne humeur toujours au rendez-vous. Je remercie aussi chaleureusement Alexandra avec qui j'ai passé de nombreuses heures dans les sombres sous-sols de Jussieu et avec qui, à force de persévérance, j'ai pu effectuer plusieurs des expériences présentées dans ce manuscrit. Je voudrais tout particulièrement remercier Tristan pour sa disponibilité et pour les nombreuses discussions que nous avons pu avoir ensemble et qui se sont toujours révélées très enrichissantes autant sur le plan scientifique que sur le plan humain. Je souhaiterais aussi remercier Matteo, Cesare et Marco pour tout le support théorique qu'ils ont fourni et la patience dont ils ont fait preuve durant toutes les discussions animées que nous avons pu avoir. Bien entendu, je remercie tous les autres membres de l'équipe, à savoir, Yves, Marie D., Marie H., Danilo et Mathis avec qui je n'ai peut-être pas collaboré scientifiquement mais qui ont sans le moindre doute contribué à la bonne ambiance de l'équipe.

De façon plus générale je remercie tous les membres du laboratoire avec qui j'ai pu avoir des interactions et en particulier tous les autres thésards, avec qui, même s'il m'est parfois arrivé de rester enfermé trop longtemps dans les sombres sous-sols de Jussieu, j'ai passé de bons moments. Merci aussi à Betty, Laetitia et Isabelle de la gestion financière qui ont toujours su se montrer compréhensives même lorsqu'il fallait organiser des missions à l'étranger dans un trop court délai.

Je remercie David, Richard et Florin du service des basses températures qui ont permis à mes cryostats de s'abreuver régulièrement de doux nectars cryogéniques. Merci également à David H. et Yanling de la plateforme de mesures physique à basses températures de l'Université ainsi qu'à David M. pour nous avoir aidé à caractériser nos échantillons par EDX.

Je voudrais remercier Peter, Tomas, Pavol et Ondrei de l'Institut de Physique des Basses Températures de Kosice en Slovaquie pour la collaboration scientifique que nous avons mise en place et pour l'excellent accueil qu'ils nous ont réservé les deux fois que nous leur avons rendu visite. Un grand merci à Laurent et Shunsuke de l'Institut Jean Rouxel de Nantes qui ont fourni un grand nombre des cristaux mesurés pendant cette thèse.

Parmi tous mes collaborateurs j'aimerais adresser un très grand remerciement à Imad, avec qui j'ai beaucoup appris mais aussi à Lise avec qui j'ai également passé un certain temps dans les sombres sous-sols de Jussieu à me débattre avec des pointes capricieuses et à redouter de fourbes vibrations.

Merci à ma famille, à mes amis et à Pooja pour leur soutien constant et pour avoir feint de

comprendre mes tentatives d'explications de ce qu'est un « supraconducteur topologique ».

Bien entendu cette liste n'est pas exhaustive et je souhaiterais remercier une dernière fois toute personne ayant contribué de quelque façon que ce soit, de près ou de loin au bon déroulement de cette thèse, qui m'a beaucoup apporté.

Contents

Introduction

Superconductivity was discovered more than a hundred years ago but still continues to be one of the most active areas of investigation in condensed matter physics. The past decades have indeed known the emergence of topological superconductivity, which generates increasing interest because of the potential applications it has in the field of quantum computing. The electron-hole nature of the low energy excitations of superconductors make them a natural and ideal platform to look for Majorana fermions, whose non-Abelian statistics and robustness to local disorder could be used in the implementation of some specific quantum algorithms. Such exotic states are predicted to appear at the edges of topological superconductors.

The first approach historically adopted to realize topological superconductivity consists in considering superconducting systems with strong spin orbit coupling, inversion symmetry breaking and time reversal symmetry breaking (magnetism). This approach was first followed in 2012 by the group of L. P. Kouwenhoven which exhibited zero-bias states at the ends of an InSb superconductor-semiconductor nano-wire devices [1]. In 2014, based on a similar approach, the group of A. Yazdani also observed zero-energy states at the ends of ferromagnetic Fe chains grown on superconducting bulk Pb crystal [2]. In those two studies, the zero-bias states were interpreted as Majorana bound states. This approach was also followed during the PhD theses of the two previous students of our group (but this time in 2D systems). In his thesis, G. Ménard considered the following system : a superconducting Pb monolayer grown on top of a Si(111) substrate with underlying magnetic CoSi islands. The idea was to tune the Pb monolayer into a topologically non-trivial regime right above the magnetic CoSi islands. Depending on the magnetic texture of the CoSi islands, G. Ménard observed states which were interpreted as chiral dispersive Majorana states and Majorana bound states, respectively [3, 4]. In the thesis of D. Longo, magnetic auto-organized manganese phthalocyanine molecules islands were grown on superconducting Pb trilayers [5]. Again, D. Longo observed what was interpreted as dispersive chiral Majorana states at the edges of the magnetic islands.

Another approach consists in inducing superconductivity by proximity into the topological surface state of a topological insulator. Here, breaking time reversal symmetry is not required to turn the system into a topologically non-trivial phase. However, applying an external magnetic field is necessary to point out the topologically non-trivial character of the material. On this basis, Majorana bound states were observed at the cores of vortices in both $Bi_2Te_3/NbSe_2$ heterostructures [6] and $FeTe_{0,55}Se_{0,45}$ [7].

In this thesis, we address another approach in which time reversal symmetry is preserved. Superconducting triplet correlations are one of the ingredients needed for the realization of topological superconductivity. Such unconventional triplet correlations can be induced in superconducting systems with strong spin-orbit coupling and in which the inversion symmetry is broken. Recent theoretical studies suggest that topologically non trivial triplet states (possibly p-wave or f-wave) could be realized in few layers transition metal dichalcogenide compounds which possess both strong spin-orbit coupling and inversion symmetry breaking [8]. In it in this framework that we carried out scanning tunnelling microscopy/spectroscopy experiments on superconducting misfit transition metal dichalcogenide $(LaSe)_{1,14}(NbSe_2)_2$, which also possesses the strong spin-orbit coupling and inversion symmetry breaking requirements [9]. The other

compound that was studied in this thesis is electron doped Sr_2IrO_4, which possesses a strong spin-orbit coupling reminiscent of a Rashba interaction. It was predicted that electron or hole doped Sr_2IrO_4 should enter a topological superconducting phase [10]. Here, superconductivity was not observed but we exhibit Mott physics signatures strongly correlated to the presence of intrinsic spin-orbit coupling in the material.

This thesis is organized in four chapters. The first chapter is a general introduction to the notion of topology in condensed matter physics systems, and more particularly in superconductors. The second chapter is dedicated to the description of the experimental method used during this thesis, namely scanning tunnelling microscopy/spectroscopy. Theoretical as well as technical aspects (such as data analysis, sample preparation or principle of the measurements) are presented. The third and fourth chapters present and discuss experimental results obtained in $(LaSe)_{1,14}(NbSe_2)_2$ and electron-doped Sr_2IrO_4, respectively.

Chapter 1 : In this introduction chapter, we develop the theoretical background necessary to address topological superconductivity. Firstly, we present the microscopic description of conventional superconductors through Bardeen-Cooper-Schrieffer theory and the Bogoliubov-de-Gennes approach. On this basis, we propose a generalized mathematical expression for the superconducting order parameter which naturally leads to the notion of unconventional superconductivity. Secondly, we explain the appearance of superconducting triplet correlations in systems with strong spin-orbit coupling and inversion symmetry breaking. Finally, we give a general introduction to the concept of topology in condensed matter physics and more particularly in the case of topological superconductors. The topical examples of the Kitaev chain and the 2D chiral p-wave superconductor are detailed to illustrate the notion of topological classes and topological invariants. Moreover, we show that those systems develop Majorana states at their edges. We discuss the non-Abelian statistics of such exotic states and their possible applications in quantum computing. At the end of the chapter, we present and comment the state-of-the-art potential experimental realizations of topological superconductivity to date.

Chapter 2 : In this chapter, we first introduce the theoretical background behind Scanning Tunnelling Microscopy and Scanning Tunnelling Spectroscopy (STM/STS). We show that this powerful experimental technique can be used as a local probe to both image the surfaces of materials and access their local density of states. We then present the principle of a spectroscopic grid experiment, often used during this thesis. More particularly, we explain the notion of quasiparticle interferences (QPIs) and how it is possible to take advantage of it *via* Fourier transform of STM/STS images to artificially reconstruct the band structures of materials. Furthermore, we give a short introduction to Ultra-High-Vacuum and very low temperatures experiments. Finally, we present the experimental set-ups on which most of the measurements were carried out during these three years. The advantages and limitations of the technique are discussed.

Chapter 3 : This chapter is dedicated to the study of superconducting transition metal dichalcogenide misfit compound $(LaSe)_{1,14}(NbSe_2)_2$. Firstly, we present STM/STS measurements performed in the normal phase. The incommensurate potential of misfit compound $(LaSe)_{1,14}(NbSe_2)_2$ acts as non-magnetic disorder and allows for the observation of QPIs. Our data are in very good agreement with Density Functional Theory calculations carried out by M. Calandra, C. Tresca and M. Campetella. Everything suggests that $(LaSe)_{1,14}(NbSe_2)_2$ behaves as electron-doped monolayer $NbSe_2$ with a shift of the chemical potential of approximatively $0,3$ eV, which is a level of doping which previous studies on few layers 2H-$NbSe_2$ could never attain. Moreover, our QPIs signal presents a splitting which can only be interpreted in the presence of a strong Ising spin-orbit coupling. Such kind of spin-orbit is predicted to induce unconventional superconducting triplet correlations. This is why we secondly present a similar

study of $(LaSe)_{1,14}(NbSe_2)_2$, but this time, in the superconducting phase. STM/STS measurements reveal a filling of the superconducting gap which we interpret as a consequence of the unconventional nature of the superconductivity, which is thus intrinsically weak against non-magnetic disorder. QPIs patterns obtained in the superconducting phase do not show any dispersion, which calls for a nodeless order parameter, possibly p-wave or f-wave. This work opens the possibility to use misfit heterostructures to further investigate quasi-2D physics in few layers 2H-$NbSe_2$.

Chapter 4 : In this chapter, we present a STM/STS study of electron-doped iridate compound $(Sr_{(1-x)}La_x)_2IrO_4$. The pristine compound Sr_2IrO_4 is a spin-orbit-induced Mott insulator and is predicted to turn into a topological superconductor once electron or hole doped. Here, we exhibit a Mott insulator to pseudo-metallic transition driven by La doping. Spectroscopic grid measurements revealed the inhomogeneous nature of this transition with the apparition of nanometer-size pseudo-metallic puddles on top of an insulating background. As the La doping increases, the puddles become more and more metallic but the background remains strongly insulating. We then confront our results with previous studies performed in similar systems. Moreover, we discuss the correlations between the position of La dopants and pseudo-metallic puddles and exhibit of a short-range orientational order in the puddles organization. Our study justifies the interest of using local probes such as STM in addition to integrative methods like Angle Resolved PhotoEmission Spectroscopy for which the interpretation of the results can be delicate. Our work is the first one which explores the full La doping range including pristine Sr_2IrO_4.

Chapter 1

Topological superconductivity

During the 19th century, physicists were racing for the liquefaction of gases, and *a fortiori*, contesting in accessing the lowest temperatures ever observed. In 1877, Louis Paul Cailletet and Raul Pictet independently liquified dioxygen for the first time, thus successfully reaching 90,2 K. In 1899, James Dewar was able to go as low as 20,18 K to liquify dihydrogen, which was previously thought as being a "permanent gas". In 1908, in Leiden, Netherlands, physicist Heike Kamerlingh Onnes was able to first liquify Helium at 4,2 K. This frantic race was motivated by an increasing need of looking at the properties of matter at very low temperatures. It is in this context that in 1911, Heike Kamerlingh Onnes got interested in measuring temperature dependence of the resistivity of mercury. By then, several theories were envisaged as to what should happen once getting closer to absolute zero. The experimental results were highly unexpected : a sharp drop in the resistivity was observed below 4,2 K. This experiment marked the discovery of superconductivity. Below a given critical temperature, superconductors, develop the ability of conducting electric currents without any dissipation. In addition to possess zero electric resistance, Walther Meissner and Robert Ochsenfeld discovered in 1933 that superconductors also have the property of expelling any magnetic field, thus making them perfect diamagnets. This second notable property is called the "Meissner effect" and is responsible for the magnetic levitation of superconductors. By 1933, superconductivity still remained not understood at all. It is only in 1935, that the brothers Fritz and Heinz London proposed an electrodynamical description of superconductivity, their famous equations being able to successfully explain the Meissner effect [11]. In 1950, Vitaly Lazarevich Ginzburg and Lev Landau imagined their empirical "Ginzburg-Landau" theory, still widely used today [12]. It is a second order phase transition theory in which the superconducting gap plays the role of the order parameter. This theory helped describing most of the macroscopic properties of superconductors, but did not provide any microscopic origin for the phenomenon. The first microscopic description of superconductivity was developed seven years later in 1957 by theoreticians John Bardeen, Leon Neil Cooper, and John Robert Schrieffer [13]. It is called the BCS theory, after the names of its inventors. It will be the topic of the following section.

1.1 BCS theory and the Bogoliubov approach

In 1956, Leon Cooper showed that if two electrons near the Fermi surface interact attractively, no matter how small the interaction, those two electrons will form a bound state, thus lowering the total energy of the system and leading to a "Fermi surface collapsing" [14]. This is exactly what happens in superconductors, where an attractive interaction bounds the electrons in pairs. This newly formed pair of electrons is called a "Cooper pair". In a conventional superconductor, the interaction between the electrons of these pairs is mediated by the phonons of the lattice they are moving in.

The BCS Hamiltonian.

The Hamiltonian describing the states of non-interacting electrons for a system of chemical potential μ is the following :

$$\hat{H}_0 = \sum_{k,\sigma} [\varepsilon_k c^\dagger_{k,\sigma} c_{k,\sigma} - \mu c^\dagger_{k,\sigma} c_{k,\sigma}] = \sum_{k,\sigma} \xi_k c^\dagger_{k,\sigma} c_{k,\sigma}, \tag{1.1}$$

where k is the momentum of an electron and σ its spin ($\uparrow\downarrow$). ε_k is the electrons dispersion relation and $\xi_k = \varepsilon_k - \mu$.

The most general Hamiltonian (which conserve total momentum and does not allow spin flip) describing the phonon-mediated interaction between the electrons is :

$$\hat{H}_{int} = \frac{1}{N} \sum_{k,k',q,\sigma,\sigma'} V(k,k',q) c^\dagger_{k+q,\sigma} c^\dagger_{k'-q,\sigma'} c_{k',\sigma'} c_{k,\sigma}, \tag{1.2}$$

In the original article by Bardeen, Cooper and Schrieffer (see [13]) it is suggested that the exchange interaction energetically favors interacting electrons with opposite spins such that :

$$\hat{H}_{int} = \frac{1}{N} \sum_{k,k',q} V(k,k',q) c^\dagger_{k+q,\uparrow} c^\dagger_{k'-q,\downarrow} c_{k',\downarrow} c_{k,\uparrow}, \tag{1.3}$$

A different and more satisfying justification of this simplification will be given shortly.

The arguments that are about to be presented follow the original description given by Bardeen, Cooper and Schrieffer [13]. Since we are using second quantization formalism, we can use a Foch space basis to describe the states. The interaction will tend to reduce the energy of the system if $\hat{H}_{int}$ connects a great number of Foch states *via* non-zero negative matrix elements. We can notice that the effect of the $V(k,k',q) c^\dagger_{k+q,\uparrow} c^\dagger_{k'-q,\downarrow} c_{k',\downarrow} c_{k,\uparrow}$ term is to destroy a $(k' \downarrow, k \uparrow)$ pair of states and create a pair of states $(k'-q \downarrow, k+q \uparrow)$ while conserving the total momentum $(k+k')$. Let us introduce the two Foch states :

$$\begin{cases} |\psi_1\rangle = c^\dagger_{k',\downarrow} c^\dagger_{k,\uparrow} |k \uparrow\!: 0, k' \downarrow\!: 0, (k+q) \uparrow\!: 1, (k'-q) \downarrow\!: 1, S\rangle\,, \\ |\psi_2\rangle = c^\dagger_{k+q,\uparrow} c^\dagger_{k'-q,\downarrow} |k \uparrow\!: 1, k' \downarrow\!: 1, (k+q) \uparrow\!: 0, (k'-q) \downarrow\!: 0, S\rangle\,, \end{cases} \tag{1.4}$$

where 0 means that the corresponding electronic state is unoccupied and 1 that it is occupied. S is a same collection of electronic states occupied in both $|\psi_1\rangle$ and $|\psi_2\rangle$.

The matrix elements between $|\psi_1\rangle$ and $|\psi_2\rangle$ Foch states are non-zero. The first conclusion is the following : $\hat{H}_{int}$ tends to stabilize the formation of $(k' \downarrow, k \uparrow)$ pairs of states. Those pairs of states are closely related to the previously mentioned Cooper pairs. Also, the number of non-zero matrix elements increases if all occupied pairs share the same total momentum $Q = (k+k')$. The second conclusion is that the most stable state is a superposition of paired states with same total momentum $Q = (k+k')$. Finally, the lowest energy configuration is the one where all the pairs have zero total momentum $Q = 0$ and *a fortiori*, their centers of mass have 0 kinetic energy.

As a summary, in a conventional superconductor, the electrons forming a Cooper pair have opposite momenta and spins. Because the interactive interaction is mediated by the phonons, only electrons of energy inferior to $\hbar\omega_D$ are likely to form Cooper pairs, where ω_D is the Debye frequency, which is the maximum vibration frequency in a crystal lattice.

Considering all these elements, one can add to $\hat{H}_0$ the following effective Hamiltonian in order to describe the interactions in a superconductor :

$$\begin{cases} \hat{H}_{int} = \frac{1}{N} \sum_{kk'} V_{kk'} c^\dagger_{k,\uparrow} c^\dagger_{-k,\downarrow} c_{-k',\downarrow} c_{k',\uparrow}, \\ V_{kk'} = \begin{cases} -V_0 \text{ if } |\xi_{k/k'}| \leq \hbar\omega_D \\ 0 \text{ else} \end{cases}, \end{cases} \tag{1.5}$$

$V_{kk'}$ is taken equal to a constant for energies lower than $\hbar\omega_D$ because the electrons of the pair are close to Fermi level, and thus $k \simeq k' \simeq k_F$, where k_F is the momentum of an electron at Fermi level. Written in this way, we see that this **constant** interaction is the Fourier transform of a contact interaction going as $V_0\delta(r-r')$, where r and r' are the positions of the two interacting electrons. Such an interaction can only occurs on a given site with the two electron sharing the same orbital and consequently having opposite spins to respect Pauli's exclusion principle.

The total Hamiltonian describing a conventional superconductor is $\hat{H}_{BCS} = \hat{H}_0 + \hat{H}_{int}$.

Bogoliubov mean field approach.

We will now present a mean field calculation first justified by Bogoliubov in 1958 (see [15, 16]), which allows to have a quadratic form for the Hamiltonian describing the interactions. Indeed, we have :

$$\begin{cases} c^\dagger_{k,\uparrow}c^\dagger_{-k,\downarrow} = \langle c^\dagger_{k,\uparrow}c^\dagger_{-k,\downarrow}\rangle + \underbrace{(c^\dagger_{k,\uparrow}c^\dagger_{-k,\downarrow} - \langle c^\dagger_{k,\uparrow}c^\dagger_{-k,\downarrow}\rangle)}_{\delta(c^\dagger_{k,\uparrow}c^\dagger_{-k,\downarrow})}, \\ c_{-k',\downarrow}c_{k',\uparrow} = \langle c_{-k',\downarrow}c_{k',\uparrow}\rangle + \underbrace{(c_{-k',\downarrow}c_{k',\uparrow} - \langle c_{-k',\downarrow}c_{k',\uparrow}\rangle)}_{\delta(c_{-k',\downarrow}c_{k',\uparrow})}, \end{cases} \tag{1.6}$$

where $\langle ... \rangle$ is the mean value taken over all the eigenstates of the perturbed system.

The mean field approximation consists in assuming that the action of the operator $\delta(c^\dagger_{k,\uparrow}c^\dagger_{-k,\downarrow})\delta(c_{-k',\downarrow}c_{k',\uparrow})$ on the eigenstates of the system is negligible. This approximation works well for systems with many Cooper pairs in a volume of size the typical size of a Cooper pair to the cube. Bogoliubov indeed showed that those terms were under extensive as their contribution grows more slowly that the total volume of the system. After calculation it gives :

$$\begin{cases} \hat{H}_{BCS} \simeq \hat{H}_{MF} = \sum_k [\xi_k(c^\dagger_{k,\uparrow}c_{k,\uparrow} + c^\dagger_{-k,\downarrow}c_{-k,\downarrow}) - \Delta_k c^\dagger_{k,\uparrow}c^\dagger_{-k,\downarrow} \\ \qquad\qquad -\Delta^*_k c_{-k,\downarrow}c_{k,\uparrow} + \Delta_k\langle c^\dagger_{k,\uparrow}c^\dagger_{-k,\downarrow}\rangle + \Delta^*_k\langle c_{-k,\downarrow}c_{k,\uparrow}\rangle], \\ \Delta_k = -\sum_{k'} V_{kk'}\langle c_{-k',\downarrow}c_{k',\uparrow}\rangle, \end{cases} \tag{1.7}$$

We will see in the following that this Hamiltonian can be diagonalized by applying a Bogoliubov transform :

$$\begin{cases} \gamma_{k,\uparrow} = u_k c_{k,\uparrow} - v_k c^\dagger_{-k,\downarrow}, \\ \gamma_{-k,\downarrow} = v_k c^\dagger_{k,\uparrow} + u_k c_{-k,\downarrow}, \end{cases} \tag{1.8}$$

By requiring that $|u_k|^2 + |v_k|^2 = 1$ one can check that $\begin{cases} \{\gamma_\alpha, \gamma_\beta\} = \{\gamma^\dagger_\alpha, \gamma^\dagger_\beta\} = 0 \\ \{\gamma_\alpha, \gamma^\dagger_\beta\} = \delta_{\alpha,\beta} \end{cases}$. This means that the operators γ_α are fermionic operators.

The inverse transformation is :

$$\begin{cases} c_{k,\uparrow} = u^*_k\gamma_{k,\uparrow} + v_k\gamma^\dagger_{-k,\downarrow}, \\ c^\dagger_{-k,\downarrow} = -v^*_k\gamma_{k,\uparrow} + u_k\gamma^\dagger_{-k,\downarrow}, \end{cases} \tag{1.9}$$

One can replace the c operators in equation 1.7 by their expression as a function of the γ operators (we no longer consider the constant term $\sum_k(\Delta_k\langle c^\dagger_{k,\uparrow}c^\dagger_{-k,\downarrow}\rangle + \Delta^*_k\langle c_{-k,\downarrow}c_{k,\uparrow}\rangle)$ in the mean field Hamiltonian). Besides, if one imposes that the terms in $\gamma^\dagger_{k,\uparrow}\gamma^\dagger_{-k,\downarrow}$ and in $\gamma_{-k,\downarrow}\gamma_{k,\uparrow}$ are zero (condition for the system to be diagonal in the γ basis), then one gets the following relation :

$$2\xi_k u_k v_k - \Delta^*_k(-v_k v_k) - \Delta_k(u_k u_k) = 0, \tag{1.10}$$

By multiplying 1.10 by $\frac{\Delta_k^*}{u_k^2}$, one finds a second degree polynomial equation for $x_k = \frac{\Delta_k^* v_k}{u_k}$ which solutions are: $x_k^{\pm} = -\xi_k \pm \underbrace{\sqrt{\xi_k^2 + |\Delta_k|^2}}_{E_k}$. At high energy, which means far from Fermi level ($\xi_k \to +\infty$), one must have $|v_k| \to 0$. Cooper pairs can, indeed, only be formed of electrons close to the Fermi level, hence, high energy excitations have to behave as electrons and thus $\gamma_{k,\uparrow} \xrightarrow[\xi_k \to +\infty]{} u_k c_{k,\uparrow} \iff |v_k| \to 0$. The correct solution of the polynomial equation then is x_k^-. Finally, by using the fact that $|u_k|^2 + |v_k|^2 = 1$, one finds :

$$\begin{cases} |v_k|^2 = \frac{1}{2}(1 - \frac{\xi_k}{E_k}), \\ |u_k|^2 = \frac{1}{2}(1 + \frac{\xi_k}{E_k}), \end{cases} \tag{1.11}$$

In the end, the mean field Hamiltonian is the following :

$$\hat{H}_{MF} = \sum_k E_k(\gamma_{k,\uparrow}^\dagger \gamma_{k,\uparrow} + \gamma_{-k,\downarrow}^\dagger \gamma_{-k,\downarrow}). \tag{1.12}$$

One can see after this derivation that $\hat{H}_{MF}$ is diagonal in the γ operators basis. The $\gamma^{(\dagger)}$ operators are quasiparticles annihilation (creation) operators. Those quasiparticules of energies $E_k = \pm\sqrt{\xi_k^2 + |\Delta_k|^2}$ are fermions and are sometimes called " bogoliubons". They are the low energy excitations of a superconductor.

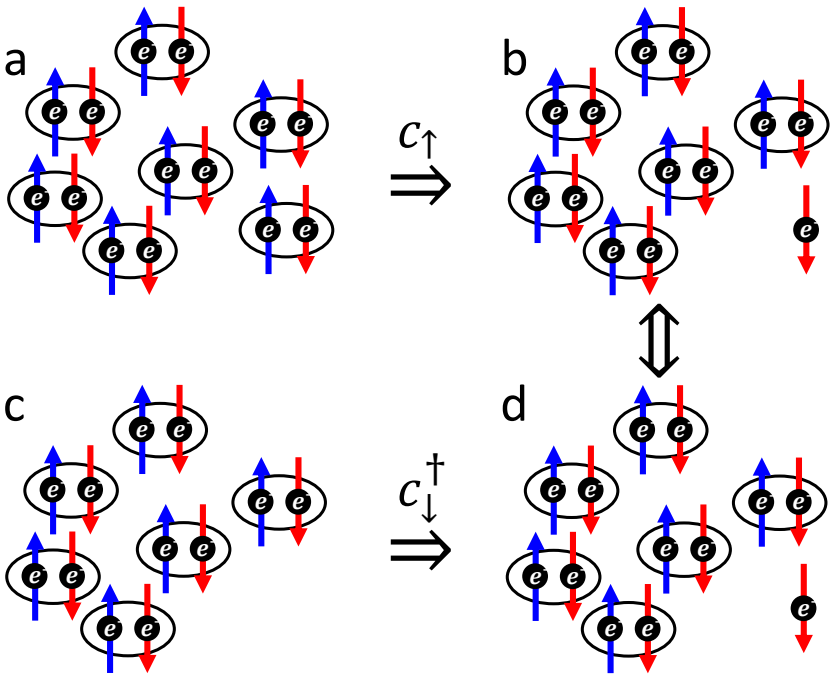

Figure 1.1: Illustration of the non-conservation of the total Cooper pairs number through low energy excitations of the system as combinations of creation and annihilation operators. **a**. System with 7 Cooper pairs. **b**. System **a** on which the annihilation of an electron of spin up was applied. **c**. System with 6 Cooper pairs. **d**. System **c** on which the creation of an electron of spin down was applied. The **b** and **d** configurations are equivalent.

By looking at equation 1.8, one can notice that the bogoliubons are combinations of annihilation and creation fermionic operators. This means that the low energy excitations of a

superconductor are a mixture of both electrons and holes. They consist in adding **and** taking off electrons, or saying differently, it is equivalent to either take or give an electron to the system. The only way to understand this is to admit that the total number of Cooper pairs is not conserved as illustrated in figure 1.1. Also, if we look at the expression of Δ_k in equation 1.7, we see that is it a combination of terms like $\langle cc \rangle$ which can only be non-zero if we are working in grand canonical ensemble for which the number of particles is not conserved.

In figure 1.1 **a**, the system has seven Cooper pairs and in figure 1.1 **c**, it has six Cooper pairs. In figure 1.1 **b**, the annihilation operator $c_\uparrow$ has been applied to the **a** configuration, and in figure 1.1 **d**, the creation operator $c_\downarrow^\dagger$ has been applied to the **c** configuration. The **b** and **d** configurations are equivalent to one another. The ground state $|\psi_{BCS}\rangle$ of the superconducting state necessarily is a linear combination of states with different Cooper pairs numbers.

The BCS ground state.

The BCS ansatz for the ground state of the superconducting system is the following :

$$|\psi_{BCS}\rangle = \prod_k (u_k + v_k c_{k,\uparrow}^\dagger c_{-k,\downarrow}^\dagger) |0\rangle , \tag{1.13}$$

Where $c_{k,\uparrow}^\dagger c_{-k,\downarrow}^\dagger$ is a pair state $(k_\uparrow, -k_\downarrow)$ creation operator and $|0\rangle$ is the fermionic vacuum.

One can notice that $|\psi_{BCS}\rangle$ acts like the vacuum for any bogoliubon annihilation, meaning that $\gamma_{k,\sigma} |\psi_{BCS}\rangle = 0$ (with $\sigma = \uparrow, \downarrow$). The justification of this ground state was given in 1958 by P. W. Anderson [17]. In his article, he defines the operator $B^\dagger = \sum_k \varphi_k c_{k,\uparrow}^\dagger c_{-k,\downarrow}^\dagger$, which can be interpreted as a Cooper pair creation operator. By being the composition of two fermions, the Cooper pairs are what we call composite bosons. This is the reason why Anderson suggests in his article that the ground state can be written in the same way as the coherent macroscopic ground state of a Bose-Einstein condensate :

$$\begin{aligned} |\phi_{BCS}\rangle &= \sum_{N=0}^{\infty} \frac{1}{N!} B^{\dagger N} |0\rangle = e^{B^\dagger} |0\rangle = \prod_k e^{\varphi_k c_{k,\uparrow}^\dagger c_{-k,\downarrow}^\dagger} |0\rangle \\ &= \prod_k (1 + \varphi_k (c_{k,\uparrow}^\dagger c_{-k,\downarrow}^\dagger) + \frac{1}{2} \varphi_k^2 (c_{k,\uparrow}^\dagger c_{-k,\downarrow}^\dagger)^2 + ...) |0\rangle , \end{aligned} \tag{1.14}$$

Because of the fermionic nature of the $c^\dagger$ operators, $(c_{k,\uparrow}^\dagger c_{-k,\downarrow}^\dagger)^n$ with $n > 1$ terms have zero contribution. Then :

$$|\phi_{BCS}\rangle = \prod_k (1 + \varphi_k c_{k,\uparrow}^\dagger c_{-k,\downarrow}^\dagger) |0\rangle , \tag{1.15}$$

By posing $\varphi_k = \dfrac{v_k}{u_k}$ and by normalizing $|\phi_{BCS}\rangle$, on finds back the expression of equation 1.13. This calculation was taken from ref. [18].

$\|v_k\|^2$ ($\|u_k\|^2$) is interpreted as the probability that the pair state $(k_\uparrow, -k_\downarrow)$ is occupied (unoccupied). Since superconductivity mixes electrons and holes up, the energy dispersion E_k can be understood in terms of band interaction between the electrons band of dispersion ξ_k and the hole band of dispersion $-\xi_k$ as it is represented in figure 1.2 **a**. This mixing between electrons and holes will be of the utmost importance in the framework of topological superconductivity (see section 1.4).

As it is shown in ref. [19], it is possible to choose u_k real and v_k complex with a $e^{i\varphi}$ phase equal to the phase of the superconducting order parameter, after what the BCS ground reads as :

$$|\psi_{BCS}\rangle = \prod_k (|u_k| + |v_k| e^{i\varphi} c^\dagger_{k,\uparrow} c^\dagger_{-k,\downarrow}) |0\rangle , \tag{1.16}$$

Written in this way, we see that the BCS ground state actually is a coherent state of Cooper pairs sharing the same phase and total momentum. The superconducting state is a condensate made out of these composite bosons and shares many similarities with Bose-Einstein condensate of regular bosons. Let us imagine that an electric field has been applied to the superconductor, thus giving a momentum to the centers of mass of the Cooper pairs and inducing the apparition of an electric current. In a normal metal, the finite resistivity comes from the scattering of carriers on any source of disorder, *i.e.*, on anything that breaks the periodicity of the crystal. By encountering disorder, a Cooper pair can potentially scatter from a state of total momentum Q to a state of total momentum $Q' \neq Q$, but, as it was said previously, in a superconductor, all the Cooper pairs must share the same total momentum Q. For scattering processes to be efficient and to lead to dissipation, one would thus have to imagine simultaneous scattering of all Cooper pairs, which is very unlikely. This argument, while not being detailed here, helps us explaining the zero-resistivity observed in superconductors. This property highly resembles the superfluidity seen in Bose-Einstein condensates. Moreover, superconduction permits to host very high intensity currents (called supercurrents) which can appear in response to strong magnetic fields, thus leading to perfect diamagnetism and Meissner effect. The two remarkable properties of superconductors can be understood within the BCS theory framework.

The BCS density of states.

The density of states of states $N(E_k)$ of the low energy excitations can be defined as $N(E_k)dE_k = N_0 d\xi_k$, where N_0 is the electronic density of states at Fermi level. If Δ_k is constant and equal to $-\Delta$, where Δ is called the gap (we will see in an instant why), then after calculation :

$$N(E_k) = N_0 \frac{|E_k|}{\sqrt{E_k^2 - |\Delta|^2}}, \tag{1.17}$$

This superconducting density of states is represented on figure 1.2 **b**. We see on the plot that there are no excitations of energies inferior in absolute value to Δ. This can be interpreted as the fact than one has to provide an energy 2Δ in order to break a Cooper pair and thus pass from a superconducting state to a normal one.

This microscopic BCS theory was very successful in describing s-wave superconductors, where the origin of the pairing of the electrons is the electron-phonon interaction, but in some materials, other interaction mechanisms can also lead to superconductivity. Such materials are called unconventional superconductors. Unconventional superconductivity will be the topic of the following section. The next section will be dedicated to the different possible symmetries for the superconducting order parameter and will not focus on the nature of the interactions leading to unconventional superconductivity.

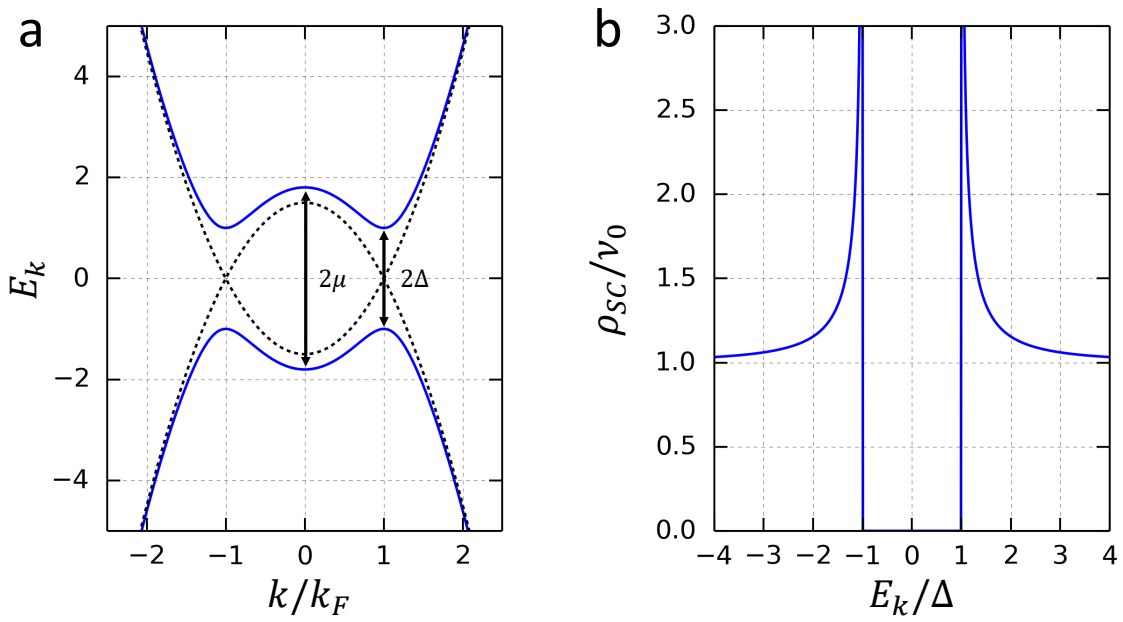

Figure 1.2: **a**. Dispersion a conventional superconductor. **b**. Density of states of the low-energy excitations of a conventional superconductor.

1.2 Unconventional superconductivity

A Cooper pair is a two-identical-particles fermionic state, thus, its wave function $\psi(k, -k, s_1, s_2)$ (where k and $-k$ are the momenta of the electrons and s_1 and s_2 are the spin of the electrons) must be antisymmetric under the exchange of the two electrons and one has: $\psi(k, -k, s_1, s_2) = -\psi(-k, k, s_2, s_1)$. In the previous section, we have seen that for conventional superconductor the expression of the gap function was $\Delta_{k,\downarrow,\uparrow} = -\sum_{k'} V_{k,k'} \langle c_{-k',\downarrow} c_{k',\uparrow} \rangle$. This notation is a bit different than the one of the previous section since it displays an explicit spin dependence. The reason behind this notation should become clear shortly. The idea is to compare $\Delta_{k,\downarrow,\uparrow}$ to $\Delta_{-k,\uparrow,\downarrow}$ to see if the gap function possesses the same antisymmetric property as the Cooper pair's wave function :

$$\Delta_{-k,\uparrow,\downarrow} = -\sum_{k'} V_{-k,k'} \langle c_{-k',\uparrow} c_{k',\downarrow} \rangle, \tag{1.18}$$

$$\Delta_{-k,\uparrow,\downarrow} = -\sum_{k'} V_{-k,-k'} \langle c_{k',\uparrow} c_{-k',\downarrow} \rangle, \tag{1.19}$$

Assuming a time reversal symmetric potential $V_{k,k'}$ and because of the anticommutation relation of fermionic operators, one finally has :

$$\Delta_{-k,\uparrow,\downarrow} = +\sum_{k'} V_{k,k'} \langle c_{-k',\downarrow} c_{k',\uparrow} \rangle = -\Delta_{k,\downarrow,\uparrow}, \tag{1.20}$$

Interestingly, for a conventional superconductor, the gap function, which is a function of k and of the spins of the electrons, is also antisymmetric under particle exchange. This can be generalized to all types of superconductors and it is why it is often said that the gap function can roughly be assimilated to the Cooper pair's wave function. Given this last statement, one understands that the gap function has both a spatial and a spin part. If one part is antisymmetric, the other is necessarily symmetric (to respect the antisymmetry of the total wave function).

In the case of a conventional superconductor, after recalling that $V_{kk'} = \{^{-V_0 \text{ if } |\xi_{k/k'}| \leq \hbar\omega_D}_{0 \text{ else}}$, one clearly sees that $\Delta_{k,\downarrow,\uparrow} = \Delta_{-k,\downarrow,\uparrow}$. This means that the spatial part of the gap function is even in k (symmetric) implying that the spin part is antisymmetric. It is then possible to write :

$$\Delta_{\alpha\beta}(k) = \Delta(k)\chi_{\alpha\beta}, \tag{1.21}$$

where $\Delta_{\alpha\beta}(k)$ is the gap function for any arbitrary type of superconductivity, $\Delta(k)$ is the spatial part of the gap function and $\chi_{\alpha\beta}$ (a 2×2 spinor matrix) is the spin part of the gap function. The α and β indices refer to the spin of the paired state. Starting from this expression one has the two following possibilities (respecting $\Delta_{\alpha\beta}(k) = -\Delta_{\beta\alpha}(-k)$) :

$$\begin{cases} \chi_{\alpha\beta} = -\chi_{\beta\alpha} \quad \text{and} \quad \Delta(k) = \Delta(-k), \\ \chi_{\alpha\beta} = \chi_{\beta\alpha} \quad \text{and} \quad \Delta(k) = -\Delta(-k), \end{cases} \tag{1.22}$$

The first case is referred to as spin-singlet pairing because the total spin of a Cooper pair S is equal to 0, while the second case is referred to as spin-triplet pairing because $S = 1$.

In all generality, the gap function can always be written as such :

$$\Delta_{\alpha\beta}(k) = [\Delta_0(k) + \overrightarrow{d}(k) \cdot \overrightarrow{\sigma}](i\sigma_2)_{\alpha\beta}, \tag{1.23}$$

where $\overrightarrow{\sigma} = (\sigma_1, \sigma_2, \sigma_3)$ and σ_1, σ_2 and σ_3 are the Pauli matrices. $(i\sigma_2)_{\alpha\beta}$ is in factor because σ_2 is the only antisymmetric Pauli matrix. Also, the product of any Pauli matrix with σ_2 is a symmetric matrix. This implies that $\Delta_0(k)$ is a even function of k since $\Delta_0(k)(i\sigma_2)_{\alpha\beta}$ has to by antisymmetric. On the contrary $\overrightarrow{d}(k)$ is necessarily odd in k. Hence, $\Delta_0(k)(i\sigma_2)_{\alpha\beta}$ and $(\overrightarrow{d}(k) \cdot \overrightarrow{\sigma})(i\sigma_2)_{\alpha\beta}$ encode the singlet and triplet parts of the superconducting order parameter, respectively.

In conventional superconductors, the Cooper pairs have a total angular momentum L equal to 0 which is why they are referred to as "s-wave". A Cooper pair with angular momentum $L = 1$ is triplet and the corresponding superconductivity is called "p-wave". If $L = 2$, the pairing is singlet, and the superconducting order parameter is d-wave. This kind of pairing is in particular encountered in cuprate-based high-T_c superconductors [20]. $L = 3$ represents a triplet f-wave pairing. More generally, an even angular momentum characterizes a singlet pairing, while an odd angular momentum characterizes a triplet pairing.

In 1961, P.W. Anderson showed that s-wave superconductors are very robust against non-magnetic disorder [21]. The Anderson's theorem tells that only interactions which break time reversal symmetry (like with magnetic impurities) are likely to induce in-gap states in an s-wave superconductor and consequently, potentially kill superconductivity. Things are very different in unconventional superconductors, where the symmetry of the Cooper pair wave function necessarily imposes sign changes in the superconducting order parameter, leading to the apparition of in-gap states, even in presence of non-magnetic disorder. This fragility to non-magnetic disorder is actually a signature of unconventional superconductivity and was especially observed in the framework of this thesis in the study of superconducting misfit compound $(LaSe)_{1,14}(NbSe_2)_2$ (see chapter 3).

Triplet superconductivity is one of the possible requirements to engineer topological superconductivity. For instance, the $p_x + ip_y$ 2D superconductor is the most famous example of p-wave pairing. It is characterized by $\Delta_0(k) = 0$ and $\overrightarrow{d}(k) = (k_x + ik_y, k_x + ik_y, 0)$ and is known to host Majorana bound states at the interface with superconductors of different topology. This will be addressed in great details in sections 1.4.2 and 1.4.3.

Historically, triplet superconductivity was observed for the first time in organic superconductors [22, 23]. Since then, triplet superconductivity was also discovered in other materials such as the heavy-fermions compounds [24, 25, 26]. In such compounds, it is thought that the superconducting state is due to spin fluctuations pairing mechanism rather than to phonon-mediated

attractive interaction like in conventional superconductors. This kind of exotic mechanism is not necessary to obtain triplet superconductivity. A mixed singlet-triplet superconducting order parameter can indeed be induced in materials with strong spin-orbit coupling and in which inversion symmetry is broken [27]. This will be the topic of the next section.

1.3 Inducing triplet superconductivity with spin-orbit coupling

1.3.1 Origin of spin-orbit coupling

The Dirac equation is a relativistic quantum wave equation formulated in 1928 by Paul Dirac. It was, at first, an attempt to incorporate special relativity to quantum theory. Schrödinger's equation is not invariant under Lorentz transformations since it presents second order derivative in space while having first order derivative in time. Space and time are thus not on equal footing as they should according to special relativity. The idea of Dirac was to find an equation which presented first order derivatives for both space and time coordinates. This last prerequisite necessarily implies a multi-components wave function. The Dirac equation reads as :

$$i\hbar\frac{\partial\left|\psi\right\rangle}{\partial t} = (mc^2\alpha_0 + c\overrightarrow{\alpha}\cdot\overrightarrow{p})\left|\psi\right\rangle, \tag{1.24}$$

where $|\psi\rangle$ is a four-components wave function, m is the mass of the particle, c is the velocity of light in vacuum, α_0 is 4×4 matrix, $\overrightarrow{\alpha} = (\alpha_1, \alpha_2, \alpha_3)$ with $\alpha_{1,2,3}$ 4×4 matrices and $\overrightarrow{p} = -i\hbar\overrightarrow{\nabla}$ is the impulsion operator. The different matrices have the following expressions :

$$\alpha_0 = \begin{pmatrix}\sigma_0 & 0\\ 0 & -\sigma_0\end{pmatrix} \quad \text{and} \quad \alpha_i = \begin{pmatrix}0 & \sigma_i\\ \sigma_i & 0\end{pmatrix}, \tag{1.25}$$

where σ_0 is the 2×2 identity matrix and $\sigma_{i=1,2,3}$ are the Pauli matrices.

This equation describes particles with half-integer spins such as the electron. It naturally takes into account the notion of spin, a physical quantity which was experimentally highlighted in the famous Stern and Gerlach experiment carried out a few years earlier in 1922, but also allowed to predict the existence of antiparticles. The stationary Dirac equation :

$$(mc^2\alpha_0 + c\overrightarrow{\alpha}\cdot\overrightarrow{p})\left|\psi\right\rangle = E\left|\psi\right\rangle, \tag{1.26}$$

If an external potential $V(\overrightarrow{r})$ is present, the equation becomes :

$$(mc^2\alpha_0 + c\overrightarrow{\alpha}\cdot\overrightarrow{p})\left|\psi\right\rangle = (E - V(\overrightarrow{r}))\left|\psi\right\rangle, \tag{1.27}$$

The wave function is decomposed into two subsets of components representing the electron and the positron (its antiparticle) respectively : $|\psi\rangle = (|\psi_e\rangle, |\psi_p\rangle)^T$ The two components of the electronic wave function $|\psi_e\rangle$ represent spin up and spin down states. In the following, we will forget about the positronic wave function $|\psi_p\rangle$ and focus on the differential equation in $|\psi_e\rangle$. In the non-relativistic limit, the relevant energy is ϵ and is defined by $E = mc^2 + \epsilon$. By supposing that $\epsilon \ll mc^2$ and also that $|V| \ll mc^2$, one can develop the equation to the first order in $\frac{\epsilon - V}{mc^2}$. The full calculation is performed in ref. [28] but in the end, we see the apparition of purely relativistic new terms in the expression of the full Hamiltonian, among which is the spin-orbit Hamiltonian (after applying minimal coupling $\overrightarrow{p} \to \overrightarrow{p} - e\overrightarrow{A}$ with $\overrightarrow{A}$ the vector potential) :

$$\begin{aligned}H = (\frac{1}{2m}(\overrightarrow{p} - e\overrightarrow{A})^2 + V + mc^2) - \frac{e\hbar}{2m}\overrightarrow{\sigma}\cdot\overrightarrow{B} - \frac{1}{8m^3c^2}(\overrightarrow{p} - e\overrightarrow{A})^4\\ + \frac{\hbar}{(2mc)^2}\overrightarrow{\sigma}\cdot(\overrightarrow{\nabla}V\times(\overrightarrow{p} - e\overrightarrow{A})) + \frac{\hbar^2 e}{8m^2c^2}\nabla^2 V,\end{aligned} \tag{1.28}$$

where the first term is the unrelativistic Hamiltonian, the second is the Zeeman term, the third represents the increasing inertia with increasing speed, the fourth one is the spin-orbit coupling Hamiltonian and the final one is the Darwin term.

If there is no magnetic field, the spin-orbit coupling Hamiltonian is :

$$H_{SOC} = \frac{\hbar}{(2mc)^2} \overrightarrow{\sigma} \cdot (\overrightarrow{\nabla} V \times \overrightarrow{p}), \tag{1.29}$$

with $\overrightarrow{\sigma} = (\sigma_1, \sigma_2, \sigma_3)$. As suggested by its name, the spin-orbit interaction couples the motion of a charged particle to its spin. In order to understand the physical origin of this coupling, let us imagine an electron moving at a velocity $\overrightarrow{v}$ in a crystal ionic lattice generating an electric field $\overrightarrow{E}$. From the point of view of the electron, it is the lattice which is moving, and a special relativity calculation would show that in the reference frame of the electron, the electron feels an effective magnetic field $\overrightarrow{B}_{eff} = -\frac{\overrightarrow{v}}{c} \times \overrightarrow{E}$. The spin $\overrightarrow{S} = \frac{\hbar}{2}\overrightarrow{\sigma}$ of the electron couples to this magnetic field effectively changing its energy by $-\gamma \overrightarrow{S} \cdot \overrightarrow{B}$ where γ is the gyromagnetic ratio of the electron. The gradient of potential $\overrightarrow{\nabla} V$ is proportional to the electric field $\overrightarrow{E}$ such that $(\overrightarrow{\nabla} V \times \overrightarrow{p}) \propto \overrightarrow{B}_{eff}$. In the end, $H_{SOC} \propto \overrightarrow{S} \cdot \overrightarrow{B}_{eff}$, which illustrates qualitatively this phenomenon.

In the work presented in this thesis, mainly three types of spin-orbit couplings were encountered. The first one is the Rashba spin-orbit coupling, which typically appears at the surface of materials where the inversion symmetry is broken. It will be the subject of subsection 1.3.2. The second one is the Ising coupling, present in non-centrosymmetric materials such as in $(LaSe)_{1,14}(NbSe_2)_2$, and which will be detailed in subsection 1.3.3. Rashba and Ising spin-orbit couplings are likely to induce superconducting spin triplet correlations. The spin-orbit coupling present in iridate compound Sr_2IrO_4 is a more conventional type of "atomic" spin-orbit coupling [29].

1.3.2 Rashba spin-orbit coupling

By definition, inversion symmetry is broken at the surface of a crystal because the surface is the interface between two different semi-infinite spaces (the crystal on one side and the vacuum on the other). This can easily be seen by thinking of the electrostatic potential gradient present at surfaces which prevents electrons to leak into the vacuum (work function). Because of symmetry considerations, this implies that the superficial electric field's direction will always have a component perpendicular to the surface. Moreover, if we consider that the electrons only move parallelly to the surface in a 2D fashion with momentum $\overrightarrow{p} = \hbar \overrightarrow{k} = \hbar(k_x, k_y)$, then the expression of the spin-orbit coupling Hamiltonian becomes :

$$H_{Rashba} = \alpha(k_x \sigma_y - k_y \sigma_x), \tag{1.30}$$

With α the strength of the Rashba spin-orbit coupling interaction. It is easy to check that H_{Rashba} does not commute with any component of the spin $\overrightarrow{S}$, which means that neither S_x, S_y or S_z are conserved. If we consider a 2D electron gas in the presence of Rashba spin-orbit coupling, the eigenenergies of the system are :

$$E_{\pm}(\overrightarrow{k}) = \frac{\hbar^2 \overrightarrow{k}^2}{2m} \pm \alpha \| \overrightarrow{k} \|, \tag{1.31}$$

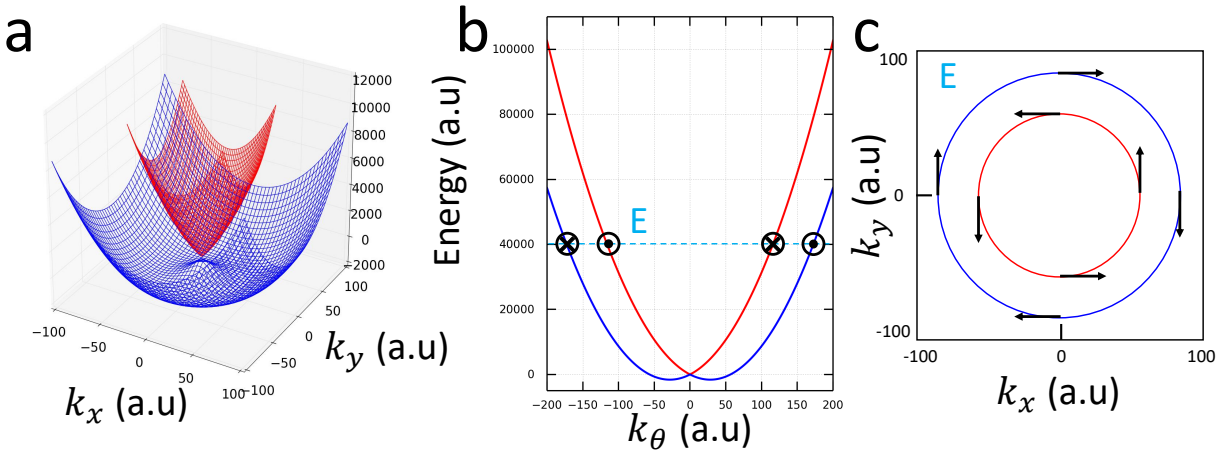

Figure 1.3: **a**. 3D representation of the Rashba spin orbit coupling effect on a parabolic dispersion. **b**. Cut of the same dispersion. **c**. Energy contour of the dispersion of **b** at energy E. The black arrows represent the fact that the spin tends to lock in the direction perpendicular to the momentum. The red and blue bands have opposite chiralities.

The dispersion is represented in figure 1.3 **a** in which $E_-(\overrightarrow{k})$ is blue and $E_+(\overrightarrow{k})$ is red. A cut along an arbitrary direction θ of the $\overrightarrow{k}$ vector is displayed in figure 1.3 **b**. Besides, an isoenergy surface at energy E is shown is figure 1.3 **c**. Within $E_+(\overrightarrow{k})$, the spin is not conserved, but the projection of the spin on the direction perpendicular to the momentum of the electron is conserved. Rashba spin-orbit coupling ensure that the spin of an electron remains perpendicular to its momentum. The same can be said for $E_-(\overrightarrow{k})$, and the $+$ and $-$ set of states have opposite chiralities as suggested by the black arrows of figure 1.3 **c**.

If $|\overrightarrow{k}\uparrow\rangle$ and $|\overrightarrow{k}\downarrow\rangle$ were the eigenvectors of the system without spin orbit coupling, then it is possible to show that the eigenvectors of the total system are :

$$|\overrightarrow{k}\pm\rangle = \frac{|\overrightarrow{k}\uparrow\rangle \pm ie^{i\theta}|\overrightarrow{k}\downarrow\rangle}{\sqrt{2}}, \tag{1.32}$$

Again, it is clear that the eigenstates of the system are a mixture of states with up and down spins. Since the spin is no longer a good quantum number and the inversion symmetry is broken, a two-particles wave function will automatically be a superposition of singlet **and** triplet states. Because the gap function can be assimilated to the Cooper pair's wave function, s-wave conventional superconductors will undoubtedly develop superconducting spin triplet correlations. This last point has been theoretically described in 1989 by V. M. Edel'shtein [30] and in 2001 by Lev P. Gor'kov and Emmanuel I. Rashba [31]. However, even if triplet correlations can be induced in this way, the ratio between the triplet and singlet parts of the order parameter highly depends on the studied system. Such spin-orbit coupling can induce unconventional superconductivity but not inevitably a topological regime.

1.3.3 Ising spin-orbit coupling

Ising spin-orbit coupling is a type of spin-orbit which is observed in 2D systems which possess out of plane mirror symmetry and break in-plane mirror symmetry. On the overall, inversion symmetry is also broken. By taking into consideration what has already been discussed in the previous section, triplet correlations will also necessarily appear in superconducting materials with strong spin-orbit coupling and such geometries. The reference example is monolayer $NbSe_2$, which structure is for instance presented in ref. [32] and exposed in greater details in section

3.1. Monolayer $NbSe_2$ basically consists in an hexagonal lattice of Nb atoms in which each Nb is at the center of a Se prism. This structure possesses the same symmetry as the cell of figure 1.4 **a**, where the blue sphere is a Nb atom and the yellow spheres are Se atoms.

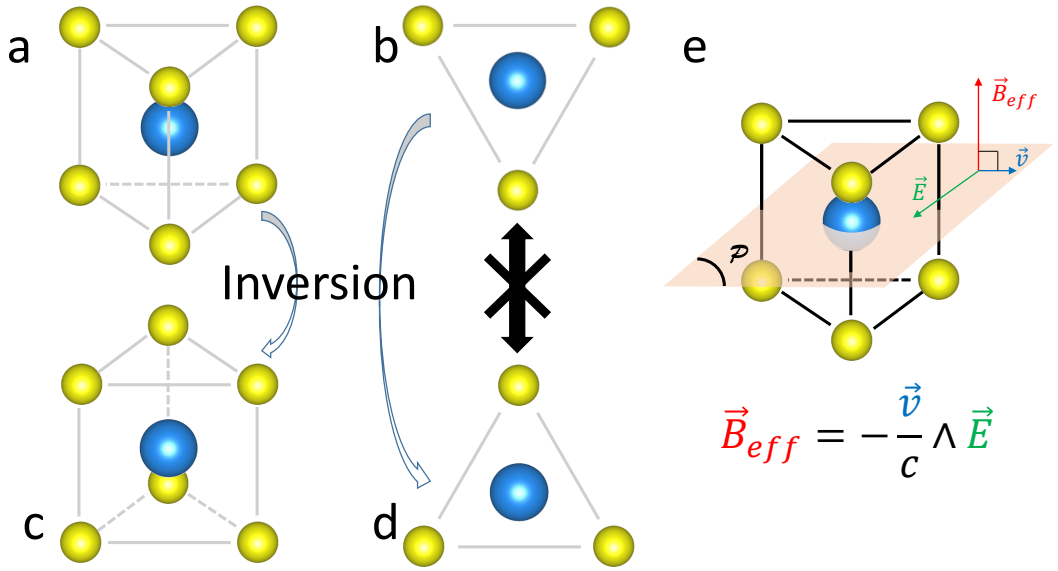

Figure 1.4: Effect of the geometry of the lattice on the nature of the spin-orbit coupling in monolayer $NbSe_2$. **a**. Prism which center is a Nb atom (blue) and apexes are Se (yellow) atoms. It has the geometry of the trigonal prismatic lattice of monolayer $NbSe_2$. **b**. Top view of **a**. **c**. Inversion symmetric of **a**. **d**. Top view of **c**. **e**. The P plane is a symmetric plane for the whole structure. This imposes that the spin-orbit coupling magnetic field effectively felt by the electron is oriented along the out-of-plane direction.

A top view of this cell is represented in figure 1.4 **b**. In figure 1.4 **e**, one can notice that the structure is unchanged under the P plane mirror operation. Figure 1.4 **c** and **d** are the inversion transforms of **a** and **b**. It is clear that **b** and **d** are not superimposable.

In $NbSe_2$, the physics is borne by the $4d$ electrons of Nb, which allows for two things : strong and intrinsic spin-orbit coupling **and** 2D motion of the electrons in the hexagonal lattice of Nb atoms. The velocity $\overrightarrow{v}$ of an electron as well as the electric field of the lattice (because of symmetry arguments) are both bound to belong to the P plane of figure 1.4 **e**. An electron will thus effectively feel a magnetic field $\overrightarrow{B}_{eff}$ which will be oriented in the out-of-plane direction. This effective magnetic field can be intense, such that it tends to lock the spins of the electrons in the out-of-plane direction. For a superconducting compound, this leads to substantially high in-plane upper magnetic critical fields [33, 34, 35, 36], above the Clogston-Chandrasekhar limit (also called Pauli paramagnetic limit). This will be further developed in section 3.4.

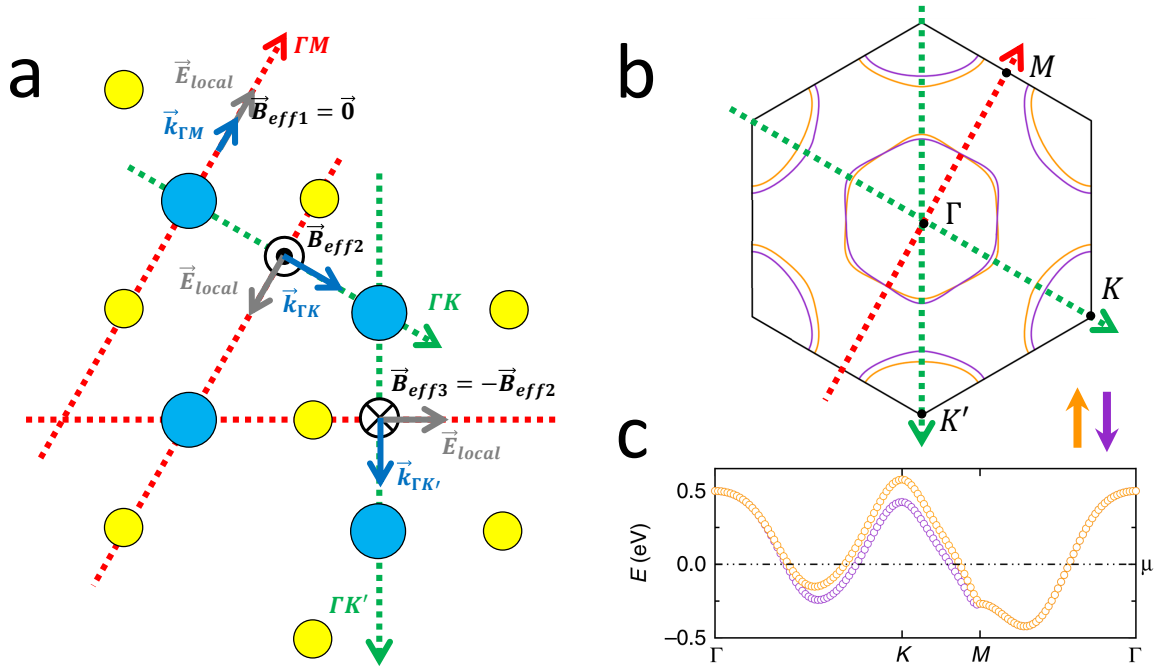

Figure 1.5: **a**. Illustration of the effective Ising magnetic field felt by the electrons in monolayer $NbSe_2$ with a top view of the trigonal prismatic lattice of monolayer $NbSe_2$ in which the blue spheres are Nb atoms and the yellow ones are Se atoms. **b**. Fermi surface of monolayer $NbSe_2$. **c**. Band structure of monolayer $NbSe_2$. The Ising splitting between spin up and spin down bands can be seen in both **b** and **c**, and is particularly pronounced around K/K' points.

A microscopic semi-classical origin of this Ising spin-orbit coupling is illustrated in figure 1.5. In this figure, both real and reciprocal spaces (**a** and **b** respectively) are correctly oriented with respect to each other such that the ΓM, ΓK and $\Gamma K'$ directions were also superimposed in real space in 1.5 **a**.

In figure 1.5 **b** and **c**, the orange and purple curves respectively represent spin up and spin down bands. The Ising spin-orbit coupling induces a splitting of spin up and spin down bands around both Γ and K/K' points. This splitting is alernated as one turns of $\frac{\pi}{3}$ around Γ, thus explaining the chosen "Ising" terminology. Moreover, no splitting is observed in the ΓM directions.

We will now explain figure 1.5 **a** in great detail. We can notice that the planes parallel to the ΓM directions, perpendicular to the monolayer and which contain Nb atoms are symmetry planes for the structure. This means that the local electric field $\vec{E}_{local}$ evaluated at any point of such a plane belongs to this plane. If we consider an electron of momentum $\vec{k}_{\Gamma M}$ belonging to such a plane, the effective spin-orbit magnetic field $\vec{B}_{eff1} \propto -\vec{k}_{\Gamma M} \times \vec{E}_{local}$ is equal to $\vec{0}$, thus explaining why no splitting is expected in the ΓM directions. On the contrary, the planes parallel to the ΓK or $\Gamma K'$ directions, perpendicular to the monolayer and which contain Nb atoms are not symmetry planes for the structure, and the local electric field $\vec{E}_{local}$ evaluated at any point of such a plane does certainly not belong to this plane. If we consider an electron of momentum $\vec{k}_{\Gamma K}$ belonging to such a plane, but also to a "ΓM" plane, the local electric field will belong to the "ΓM" plane and in the end, the effective spin-orbit magnetic field $\vec{B}_{eff2} \propto -\vec{k}_{\Gamma K} \times \vec{E}_{local}$ will be oriented out of the surface. An electron of momentum $\vec{k}_{\Gamma K'}$ (with $\|\vec{k}_{\Gamma K'}\| = \|\vec{k}_{\Gamma K}\|$) belonging to both "$\Gamma K'$" and "$\Gamma M$" planes, will have an effective spin-orbit magnetic field $\vec{B}_{eff3} \propto -\vec{k}_{\Gamma K'} \times \vec{E}_{local}$ equal to $-\vec{B}_{eff2}$, thus explaining the three-fold

alternation of spin splitting in the band structure.

One last remark we can make, is that the magnitude of the splitting rises up as $\| \overrightarrow{k} \|$ becomes bigger, or, saying differently, as we go away from Γ. This explains why the splitting is more pronounced for the K/K' pockets than for the Γ pocket (see figure figure 1.5**c**). If we electron-dope the system (as it was effectively done in chapter 3), given the hole character of the bands around K/K' and Γ, the Ising spin splitting will increase around K/K' and decrease around Γ.

1.4 Topological superconductors

1.4.1 Introduction to topology in condensed matter systems

Topology is the branch of mathematics which studies the properties of space which are preserved under continuous deformations. For example, a mug and a torus, while being completely different objects, share a common topology. One can indeed deform continuously one to obtain the other never applying neither "cutting" or "glueing" of any sorts. This is illustrated in figure 1.6 **a**.

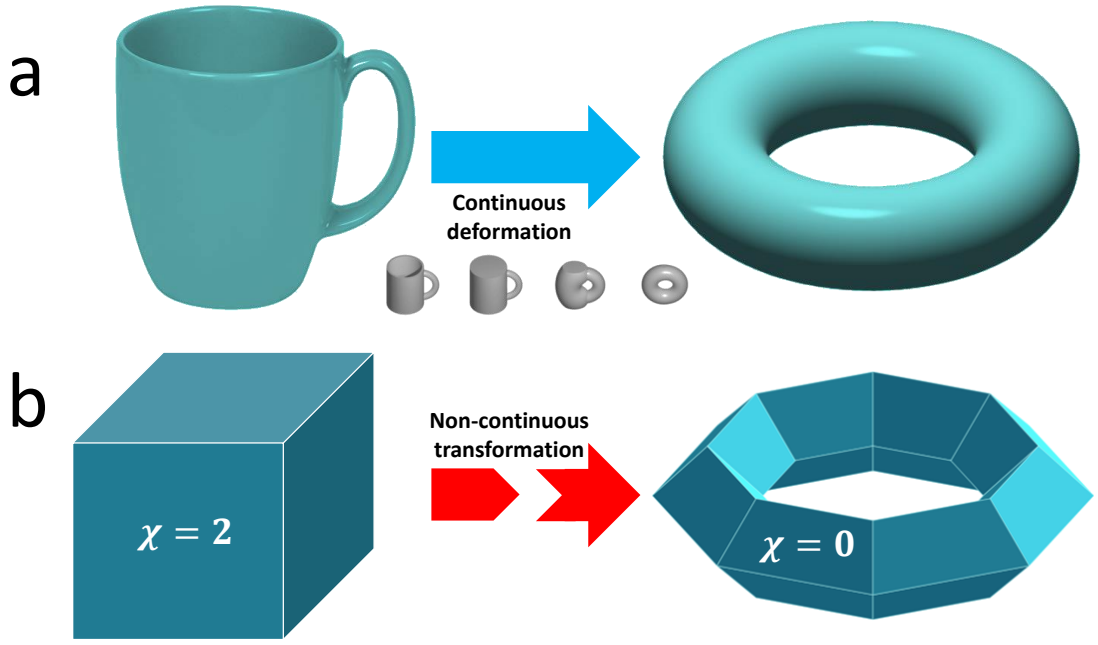

Figure 1.6: **a**. Continuous deformation of a mug into a torus. **b**. Illustration of the concept of topological invariant in polyhedra through the Euler characteristics.

One also understands that it is impossible to continuously change a sphere into a torus. A hole would have to be done into the sphere at some point, and "making a hole" cannot be described mathematically by any continuous transformation. Similarly, a torus cannot be turned continuously into a two-hole torus. It would seem that the number of holes is a quantity fit to discriminate all 3D volumes into separate topology classes. We say that the number of holes is a topological invariant, or so to say, a mathematical quantity shared by all the objects within a given topology class.

To further explore the notion of topological invariant, we will now focus on polyhedra. Again, we intuitively see that a cube can be deformed into a tetrahedron or into an octahedron, but it seems very unlikely to be continuously turned into the holed polyhedron displayed in figure 1.6 **b**. Even though we instinctively understand that the topological invariant will be linked to the total number of holes, it is necessary to properly define it mathematically. For

polyhedra, the topological invariant of interest is called the Euler characteristic and has the following expression: $\chi = V + F - E$. V is the number of vertices (apexes) of the polyhedron, F its number of faces and E its number of edges. For any polyhedron with no hole, one has $\chi = 2$. For the holed polyhedron of figure 1.6, χ takes a different value and is equal to 0. Any one-hole polyhedron will always have $\chi = 0$.

The Berry phase.

We now are a bit more familiar with the concepts of topology and topological invariants. In this section, we will see how these notions apply in the framework of quantum physics. The topological nature of a quantum system is related to the constraints imposed by the system's geometry on the phase of wave functions. This statement will become clear after the short calculation we are about to present. Let $H(\overrightarrow{R})$ be the Hamiltonian of a quantum system fully described by the set of parameters $\overrightarrow{R}$. We call $|n(\overrightarrow{R})\rangle$ and E_n the eigenstates and eigenenergies of the system respectively, which explicitly depend on $\overrightarrow{R}$. One has :

$$H(\overrightarrow{R})\,|n(\overrightarrow{R})\rangle = E_n(\overrightarrow{R})\,|n(\overrightarrow{R})\rangle\,,$$

In the following, we will consider that the system was initially in $|n(\overrightarrow{R}_{initial})\rangle$ state. If the set of parameters $\overrightarrow{R}$ varies slowly enough with time, then, the adiabatic theorem tells us that at each instant t the system is in an eigenstate of the-time dependent Hamiltonian $H(\overrightarrow{R}(t))$ and one has the relation :

$$H(\overrightarrow{R}(t))\,|n(\overrightarrow{R}(t))\rangle = E_n(\overrightarrow{R}(t))\,|n(\overrightarrow{R}(t))\rangle\,, \tag{1.33}$$

In addition to this, there always is a degree of freedom on the phase of the wave function such that the state $|\psi(t)\rangle$ of the system at time t can be written in a more general way like : $|\psi(t)\rangle = e^{-i\theta(t)}\,|n(\overrightarrow{R}(t))\rangle$. It is important to emphasize that the phase θ also explicitly depends on time. Its expression can be derived using Schrödinger equation :

$$H(\overrightarrow{R}(t))\,|\psi(t)\rangle = i\hbar\frac{d}{dt}\,|\psi(t)\rangle\,, \tag{1.34}$$

This gives us a differential equation in $\theta(t)$:

$$E_n(\overrightarrow{R}(t)) - i\hbar\,\langle n(\overrightarrow{R}(t))|\,\frac{d}{dt}\,|n(\overrightarrow{R}(t))\rangle = \hbar\frac{d\theta}{dt}, \tag{1.35}$$

Which can be integrated and finally :

$$\theta(t) = \overbrace{\frac{1}{\hbar}\int_0^t dt' E_n(\overrightarrow{R}(t'))}^{\text{dynamical phase}} \overbrace{-i\int_0^t dt'\,\langle n(\overrightarrow{R}(t'))|\,\frac{d}{dt'}\,|n(\overrightarrow{R}(t'))\rangle}^{-\gamma_n \;=\; \text{geometrical phase}}, \tag{1.36}$$

$$\gamma_n = i\int_{\mathcal{C}} d\overrightarrow{R}\cdot\langle n(\overrightarrow{R})|\,\nabla_{\overrightarrow{R}}\,|n(\overrightarrow{R})\rangle\,, \tag{1.37}$$

In addition to the well-known dynamical phase, the wave function of the system acquires another phase related to the adiabatic transport in $\overrightarrow{R}$ parameters space. γ_n is a geometrical phase and is often called the Berry phase. Given this expression of γ_n, it is possible to define the Berry connection : $\overrightarrow{A} = i\,\langle n(\overrightarrow{R})|\,\nabla_{\overrightarrow{R}}\,|n(\overrightarrow{R})\rangle$. The Berry phase is thus the circulation of the Berry connection over a given path $\mathcal{C}$.

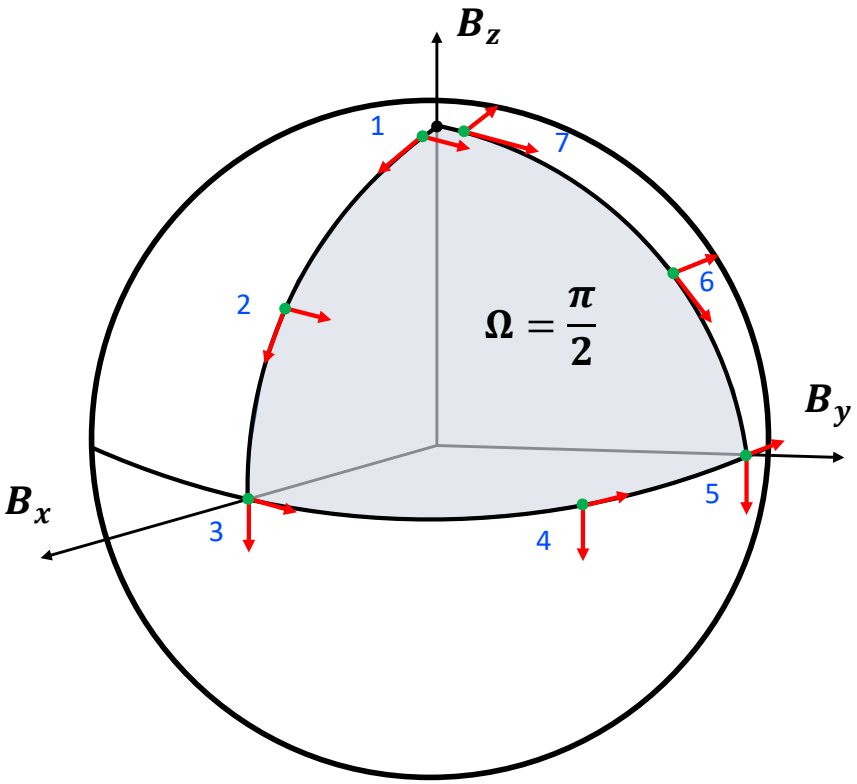

Figure 1.7: Illustration of the notion of geometrical phase with the example of a spin rotating thanks to an adiabatically varying orientation of the magnetic field.

In order to see a situation is which a quantum system acquires a geometrical phase we will now present the example of a spin under a magnetic field $\overrightarrow{B}$, example which is very well detailed in ref. [37]. Here, the set of parameters is $\overrightarrow{R} = \overrightarrow{B}$. One of the conditions for this Berry phase to show up is adiabatic transport in parameters space. We will consider that the initial state is an eigenstate of the system and that the magnetic field's orientation slowly varies in time while keeping its magnitude constant. We choose it to follow the closed curve in $\overrightarrow{B}$ space represented in figure 1.7. The full calculation is performed in ref. [37] but the idea can easily be understood with the help of the cartoon of figure 1.7. When a spin is in presence of a magnetic field, it precesses with a given pulsation ω around the direction of the magnetic field. After a time Δt has passed, the wave function of the particle possessing the spin will have acquired a dynamical phase $\omega\Delta t$. The angular position of the spin is spotted with the help of the system of axes represented in red in figure 1.7. One can notice on the drawing that as the path is travelled in $\overrightarrow{B}$ space, the red axes' orientation changes and ends up being rotated of $\frac{\pi}{2}$ in final step 7 compared to initial step 1. This means that in addition to the dynamical phase, the system also acquires a dynamical phase γ_n equal to $\frac{\pi}{2}$. This $\frac{\pi}{2}$ phase reflects the solid angle Ω defined by the travelled closed path. This later results is actually valid for spin 1 particles. But for all spin, the acquired geometrical phase can always be related to the enclosed solid angle. For example, for spin 1/2, the geometrical phase is equal to $\Omega/2$. If $\Omega = 2\pi$, meaning a full rotation in parameters space, one recovers the fact that a spin 1/2 particle acquires a π phase when submitted to a 2π rotation.

Majorana fermions.

In the two following sections, we will present two topical examples of topological superconductivity. The first one is the 1D p-wave superconductor also called the Kitaev chain. The second is the 2D p-wave superconductor. In this later case, the topological nature of the system will be related to the Berry phase. For the Kitaev chain, where one can easily check that the Berry phase is zero, the topological nature of the system rather lies in unavoidable obstruction in the paving of the wave functions' phase across the first Brillouin zone.

The questions that arises now are the following : are there any experimental signatures of the topological nature of a quantum system ? ; could we imagine applications of topology in condensed matter physics ? In order to answer those questions, we will ask another one. What happens at the interface between a superconductor 1 and a superconductor 2 with different topologies ? This is a legitimate question since the interface neither possesses the topology of 1 or 2. We will see in the examples that it is never possible to continuously tune the properties of 1 to obtain the topology of 2 without closing the superconducting gap. This closing of the gap can be assimilated to the "cutting" and "glueing" operations mentioned at the beginning of this chapter. What we will see is that in-gap states are supposed to appear at the interface between the two superconductors, these states often being Majorana fermions.

A Majorana fermion is a fermion (half integer spin) which is its own antiparticle. Majorana fermions were described theoretically in 1937 by physicist Ettore Majorana in the framework of particle physics. They differ from regular Dirac fermions (such as the electron). No elementary particle has yet been identified as a Majorana fermion to date, but neutrinos are possible candidates. It is rather in condensed matter physics that Majorana fermions are likely to be oberved as quasiparticle excitations.

Since a Majorana fermion is its own antiparticle, its electrical charge necessarily is 0. As it was shown in section 1.1, the low energy quasiparticle excitations of a superconductor are fermions and are part electron and part hole, or saying differently, part a particle and part its antiparticle. Superconductors are thus the natural playground to look for Majorana quasiparticles.

A Majorana fermion respects the relation $\gamma^\dagger = \gamma$, where $\gamma^\dagger$ and γ are the creation and annihilation operators of a Majorana fermion respectively. It also verifies the anticommutation relation : $\{\gamma_a^\dagger, \gamma_b^\dagger\} = \{\gamma_a^\dagger, \gamma_b\} = \{\gamma_a, \gamma_b^\dagger\} = \{\gamma_a, \gamma_b\} = 2\delta_{a,b}$, also meaning that $\gamma^2 = 1$.

Remark : The relation $\gamma^\dagger = \gamma$ is actually valid for spinless Majorana bound states. In the case of a $\frac{1}{2}$ spinful Majorana fermion labelled with momentum k one actually has $\gamma_{k,\uparrow}^\dagger = \gamma_{-k,\downarrow}$.

Majorana fermions virtually appears in condensed matter (more presisely in the physics of electrons in solids) systems because they mathematically are a superposition of fermionic states $c^\dagger$ and c. One can always write $\gamma = c^\dagger + c$. On the contrary, a Dirac fermion and more particularly an electron can also be decomposed as a superposition of two distinct Majorana fermions which we will label A and B in the following. Hence :

$$\begin{cases} \gamma^A = c + c^\dagger \\ \gamma^B = i(c - c^\dagger) \\ c^\dagger = \dfrac{(\gamma^A + i\gamma^B)}{2} \\ c = \dfrac{(\gamma^A - i\gamma^B)}{2} \end{cases} , \tag{1.38}$$

Majorana fermions, unlike bosons or Dirac fermions neither respect Bose-Einstein nor Fermi-Dirac statistics. If we consider a N-particle state of identical bosons, if one swaps the positions of two arbitrary bosons, the wave function of the system remains unchanged. If one again permutes two arbitrary bosons, the wave function is still unchanged. For Dirac fermions, the first

permutation of two arbitrary identical fermions multiplies by -1 the wave function, and the second permutation again multiplies the function by -1 such that in the overall, the wave function of the system is unchanged. As a summary, the order in which the two arbitrary permutations are performed does not matter for both bosons and Dirac fermions. If the permutations are called σ_1 and σ_2, the actions of $\sigma_1\sigma_2$ and $\sigma_2\sigma_1$ on the total N-particle state are the same. We say that Bose-Einstein and Fermi-Dirac statistics are Abelian statistics.

Majorana fermions obey a non-Abelian statistics (see refs.[38, 39]). This could be used in yet to be coming quantum computers. A 2N-Majorana particle system can be written as a superposition of 2^N-Dirac particle Foch states. Carrying out permutations on a 2N-Majorana particle system allows to encode information in such a superposition. The so called "braiding" operations are needed to carry out some specific quantum computing algorithms [40]. In addition to this, Majorana fermions are very robust against disorder and consequently against decoherence, which is of the utmost importance in quantum computing to guarantee an appropriate calculation progress before the "reading" procedure which reduces the wave packet. This robustness comes from the topological origin of Majorana in-gap states : we say that they are topologically protected [41, 42]. The existence of the Majorana states is dictated by the topology of the system, which is a global property. Such topological edge states are thus insensitive to perturbations such as local disorder. The search for Majorana fermions has been an active field of condensed matter physics for the past decade. Recently, Majorana particle have been claimed to be observed (this will further be discussed in the following sections), but the non-Abelian statistics was never addressed experimentally, which means that a lot of progress still needs to be done, for it is the only way to prove without any ambiguity the Majorana nature of such exotic states of matter.

1.4.2 The Kitaev chain

The topological superconductivity model presented in this section comes from the pioneering theoretical article of A. Yu Kitaev [43]. In this article, Kitaev showed that Majorana bound states with non-Abelian statistics could appear at the ends of a one-dimensional spinless p-wave superconductor.

Theoretical model.

Let us consider a superconducting one-dimensional atomic chain with one **spinless** electron per site. This spinless fermionic system can be viewed as a system in which all the electrons have been spin-polarized into a given exclusive spin state (either up or down). Applying a strong enough external magnetic field is a way of realizing such a configuration. In this 1D chain, adjacent sites are separated by a distance a. We choose a p-wave triplet superconducting pairing (respecting $\Delta(-k) = -\Delta(k)$). The Bogoliubov-de-Gennes Hamiltonian of the system is the following:

$$H_{BdG} = \frac{1}{2}\sum_k \psi_k^\dagger \overbrace{\begin{pmatrix} \varepsilon(k)-\mu & 2i\Delta\sin(ka) \\ -2i\Delta\sin(ka) & -(\varepsilon(k)-\mu) \end{pmatrix}}^{\mathcal{H}(k)} \psi_k, \tag{1.39}$$

where $\psi_k^\dagger = (c_k^\dagger, c_{-k})$, with $c_k^\dagger$ and c_k the creation and annihilation operators of spinless electron of momentum k, respectively, $\varepsilon(k)$ is the free electron dispersion, μ is the chemical potential and Δ is the superconducting gap amplitude. $\mathcal{H}(k)$ is the Bloch Hamiltonian. This Hamiltonian is different from the total Hamiltonian but it is the one which encodes the topological properties of the system. $\mathcal{H}(k)$ can be written as such :

$$\mathcal{H}(k) = (\varepsilon(k)-\mu)\tau_z + 2\Delta\sin(ka)\tau_y = \overrightarrow{d}(k)\cdot\overrightarrow{\tau}, \tag{1.40}$$

Where $\overrightarrow{\tau} = (\tau_x, \tau_y, \tau_z)$, and $\tau_{x,y,z}$ are the Pauli matrices on the particle-hole basis. By considering only a positive first neighbour hopping parameter t, the $\overrightarrow{d}(k)$ vector has the expression :

$$\overrightarrow{d}(k) = \begin{cases} d_x = 0 \\ d_y = 2\Delta \sin(ka) \\ d_z = -2t\cos(ka) - \mu \end{cases}, \tag{1.41}$$

Diagonalizing $\mathcal{H}(k)$ leads to the eigenenergies: $E_\pm(k) = \pm\sqrt{d_x^2 + d_y^2 + d_z^2} = \pm\sqrt{4\Delta^2\sin^2(ka) + (-2t\cos(ka) - \mu)^2}$ and to the corresponding eigenstates $|\pm\rangle_k$. In order to give the expression of $|\pm >_k$, we will first introduce the normalized version of $\overrightarrow{d}(k)$:

$$\hat{d}(k) = \frac{\overrightarrow{d}(k)}{\parallel \overrightarrow{d}(k) \parallel} = \frac{1}{\sqrt{d_z^2 + d_y^2}}(0, d_y, d_z) = (0, \hat{d}_y, \hat{d}_z), \tag{1.42}$$

This later vector lives on a diameter of the Bloch sphere and since $\hat{d}_z^2 + \hat{d}_y^2 = 1$, one can write $\hat{d}_z = \cos(\theta_k)$ and $\hat{d}_y = \sin(\theta_k)$ with θ_k the angle between $\hat{d}(k)$ and the z direction. One can easily check that the normalized eigenstates of the system are $|+\rangle_k = \begin{pmatrix} \cos(\frac{\theta_k}{2}) \\ i\sin(\frac{\theta_k}{2}) \end{pmatrix}$ and $|-\rangle_k = \begin{pmatrix} \sin(\frac{\theta_k}{2}) \\ -i\cos(\frac{\theta_k}{2}) \end{pmatrix}$.

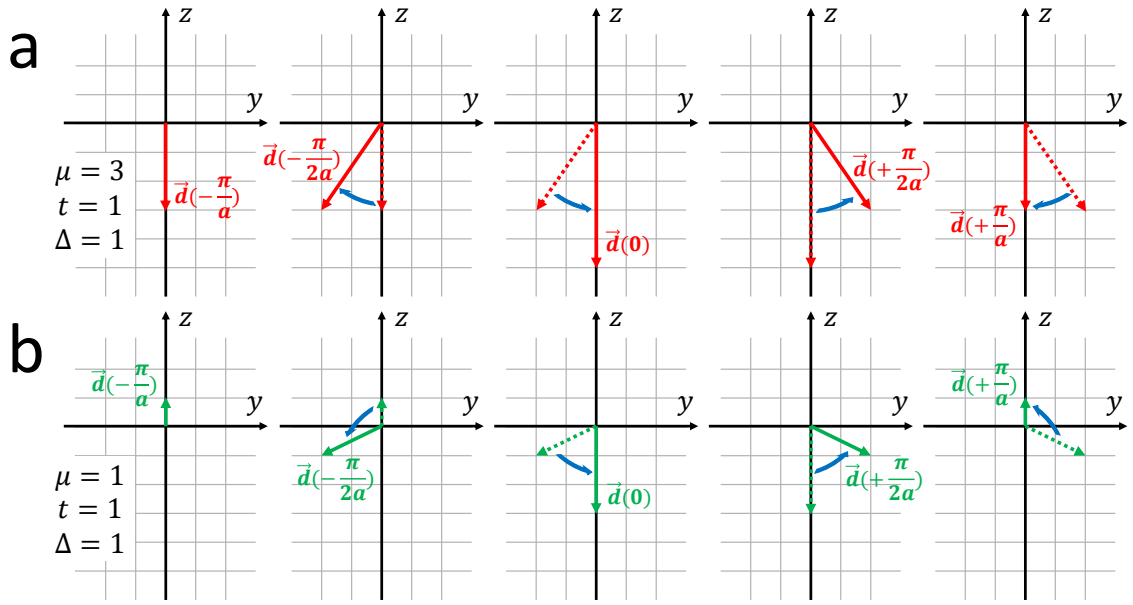

Figure 1.8: **a**. Trivial regime : $\overrightarrow{d}(k)$ does not wind around the origin. **b**. Topological regime : $\overrightarrow{d}(k)$ winds once around the origin.

We see that $E_\pm(k)$ (and also $\overrightarrow{d}(k)$) becomes equal to zero, and thus that the gap closes at $k = 0$ for $\mu = -2t$ and at $k = \pm\pi$ for $\mu = +2t$. We will show in the following that those gap closings separate regions in parameters space with different topologies. Depending on the value

of μ, the system is either in a trivial or in a topological regime. We will see that for $-2t < \mu < 2t$, the system is topologically non-trivial and for $\mu > 2t$ ($\mu < -2t$) it is topologically trivial.

The topological characteristic of the system depends on the number of rotation $\overrightarrow{d}(k)$ performs around the origin while k travels across the whole first Brillouin zone $[-\frac{\pi}{a}, +\frac{\pi}{a}]$. In figure 1.8 **a**, is represented $\overrightarrow{d}(k)$ for k going from $-\frac{\pi}{a}$ to $+\frac{\pi}{a}$ in a case where $\mu > 2t$. In figure 1.8 **b**, is represented $\overrightarrow{d}(k)$ for k going from $-\frac{\pi}{a}$ to $+\frac{\pi}{a}$ in a case where $-2t < \mu < 2t$.

For $\mu > 2t$ (the case $\mu < -2t$ is analogous), one can clearly see that as k goes through the first Brillouin zone, $\overrightarrow{d}(k)$ does not perform any rotation around the origin while for $-2t < \mu < 2t$, $\overrightarrow{d}(k)$ makes **one** turn around the origin. Saying differently, in the trivial phase, as k varies continuously from $-\frac{\pi}{a}$ to $+\frac{\pi}{a}$, θ_k varies continuously from 0 to 0. In the topological phase, as k varies continuously from $-\frac{\pi}{a}$ to $+\frac{\pi}{a}$, θ_k varies continuously from 0 to 2π. The suited topological invariant can be defined by $\nu = \frac{1}{2\pi}\int_{1BZ} d\theta_k$. For $\mu > 2t$, $\nu = 0$ and for $-2t < \mu < 2t$, $\nu = +1$.

As a summary, we have seen that depending on the region in parameters space, the system enters either a topological or a trivial phase. The different topologies can be understood in terms of winding number ν of $\overrightarrow{d}(k)$ vector around the origin. This winding number is an integer. It is not possible to tune the system from a topological phase to another without closing the superconducting gap. At the set of parameter for which the gap closes, ν is no longer properly defined. For example, here the gap closes at $\mu = 2t$. When $\mu = 2t$, $\overrightarrow{d}(\frac{\pi}{a}) = \overrightarrow{0}$, such that for this specific point, θ_k is ill-defined. By extension, the topological invariant ν is also ill-defined right at the topological phase transition.

So far, the topological nature of the system was addressed using abstract mathematical quantities but it is possible to get more physical insight by looking at what actually happens to the quasiparticle wave functions. We have seen that in the topological regime, one could continuously vary θ_k from 0 to 2π by going from one end of the Brillouin zone to the other. It also means that $|+>_k$ can continuously pave the first Brillouin zone from $k = -\frac{\pi}{a}$ to $k = +\frac{\pi}{a}$. However, one can notice that $|+\rangle_{k=-\frac{\pi}{a}} = \begin{pmatrix}1\\0\end{pmatrix} = -|+\rangle_{k=+\frac{\pi}{a}}$. The wave function at $k = +\frac{\pi}{a}$ is equal to the wave function at $k = -\frac{\pi}{a}$ but necessarily up to a $e^{i\pi}$ phase. It is not possible to make both ends of the first Brillouin zone correspond without any discontinuity. We speak of topological obstruction. Such an obstruction can be prevented in the topologically trivial phase. In this example, the topological nature of the system is related to the existence of an obstruction in the paving of the wave functions over the whole Brillouin zone.

In what follows, we will see what happens in the case of a finite-length chain of spinless 1D p-wave superconductor. The wire is isolated and thus surrounded by vacuum. Vacuum is topologically equivalent to a trivial superconductor (by considering an infinite superconducting gap). If the wire is in a topological regime, we can legitimately wonder what happens at the interface between both wire and vacuum for that interface neither possesses the topology of one or the other. More generally speaking, it is interesting to look at the interface between materials of different topology. In this particular example, we will show that Majorana bound states appear at opposite ends of the 1D chain.

If the chain has N sites, the Bogoliubov de Gennes Hamiltonian can be written in real space as follows :

$$H_{BdG} = \sum_{i=1}^{N-1} (tc_{i+1}^{\dagger}c_i + \Delta c_i^{\dagger}c_{i+1}^{\dagger} + h.c.) - \mu \sum_{i=1}^{N} c_i^{\dagger}c_i, \tag{1.43}$$

where $c_i^\dagger$ and c_i are the creation and annihilation operators of a spinless electron at site i. One can check that $\Delta c_i^\dagger c_{i+1}^\dagger = -\Delta c_{i+1}^\dagger c_i^\dagger$ and hence that $\Delta(k) = -\Delta(-k)$, or so to say, that we are dealing with a triplet order parameter. Following the mathematical procedure described in section 1.4.1, each Dirac fermions can be decomposed as two Majorana fermions :

$$\begin{cases} c_i^\dagger = \dfrac{(\gamma_i^A + i\gamma_i^B)}{2} \\ c_i = \dfrac{(\gamma_i^A - i\gamma_i^B)}{2} \\ \gamma_i^A = c_i + c_i^\dagger \\ \gamma_i^B = i(c_i - c_i^\dagger) \end{cases}, \tag{1.44}$$

After what, the Hamiltonian can be rewritten as :

$$H_{BdG} = -i \sum_{i=1}^{N-1} (\omega_+ \gamma_{i+1}^A \gamma_i^B - \omega_- \gamma_{i+1}^B \gamma_i^A) + i\frac{\mu}{2} \sum_{i=1}^{N} (\gamma_i^A \gamma_i^B + i), \tag{1.45}$$

with $\omega_+ = \dfrac{t+\Delta}{2}$ and $\omega_- = \dfrac{t-\Delta}{2}$.

If we take $t = \Delta = 0$ and $\mu > 0$, then $\mu > 2t$ and the system is in the trivial regime. In this case the Hamiltonian reads as :

$$H_{BdG} = i\frac{\mu}{2} \sum_{i=1}^{N} (\gamma_i^A \gamma_i^B + i) = -\mu \sum_{i=1}^{N} c_i^\dagger c_i, \tag{1.46}$$

We clearly see that the system is diagonal in the $c_i^\dagger$ basis with i going from 1 to N. Hence, the system has N eigenstates localized at sites i and of energy $-\mu$. This situation is summarized in the top sketch of figure 1.9.

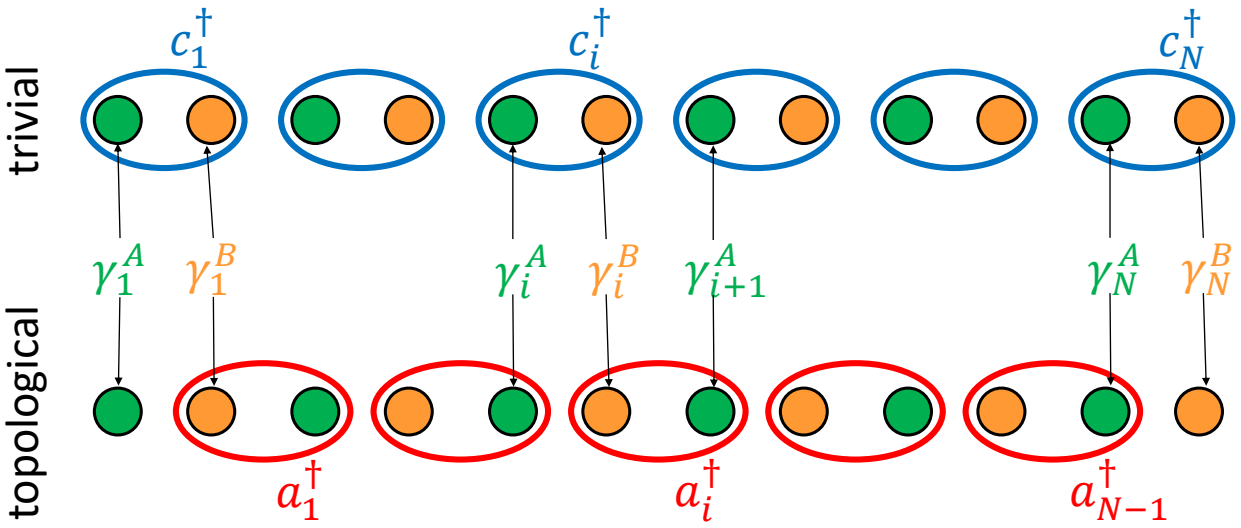

Figure 1.9: Top sketch : Trivial regime. Bottom sketch : Topological regime : different recombination of Dirac fermions leading to the appearance of Majorana bound states at the ends of the chain.

However, if we take $t = \Delta \neq 0$ and $\mu = 0$, then $-2t < \mu < 2t$ and the system is in a topological regime. The Hamiltonian of the system is thus :

$$H_{BdG} = -i\Delta \sum_{i=1}^{N-1} \gamma_{i+1}^{A} \gamma_{i}^{B}, \tag{1.47}$$

We recall that two combined Majorana fermions form a Dirac fermion. The Majorana operators displayed in equation 1.47 were obtained by writing each Dirac fermion localized at sites i as such a combination. Nevertheless, it is also possible to recombine two Majorana fermions coming from adjacent sites, thus giving rise to new Dirac fermions $a_i^\dagger$:

$$\begin{cases} a_i^\dagger = \dfrac{(\gamma_i^B + i\gamma_{i+1}^A)}{2} \\ a_i = \dfrac{(\gamma_i^B - i\gamma_{i+1}^A)}{2} \\ \gamma_i^B = a_i + a_i^\dagger \\ \gamma_{i+1}^A = i(a_i - a_i^\dagger) \end{cases}, \tag{1.48}$$

Following this procedure, the Hamiltonian now has the following expression :

$$H_{BdG} = -2\Delta \sum_{i=1}^{N-1} a_i^\dagger a_i, \tag{1.49}$$

The Hamiltonian is diagonal in the new $a_i^\dagger$ basis, but contrary to the trivial case, this writing of the Hamiltonian, although correct, only highlight $N-1$ eigenstates of energies -2Δ. This is problematic because the total number of eigenstates must not change from trivial to topological regime : one eigenstate is missing. The only Majorana fermions which were not taken into account in the recombining are γ_1^A and γ_N^B, or saying differently, the two Majorana fermions lying at the two ends of the wire. Those two Majorana fermions can recombine into $a^\dagger = \dfrac{(\gamma_N^B + i\gamma_1^A)}{2}$ Dirac fermions, after what one can simply add a $a^\dagger a$ term at the Hamiltonian :

$$H_{BdG} = 0a^\dagger a - 2\Delta \sum_{i=1}^{N-1} a_i^\dagger a_i, \tag{1.50}$$

We now have $N-1$ states at energy -2Δ and one state at 0 energy: the total number of eigenstates is recovered. The two Majorana end states are combinations of 0 energies electron and hole states, they consequently also lie at 0 energy. If the wire is long enough, the two Majorana states won't recombine efficiently and will be localized at each end of the chain. In view of this last calculation, one can also notice that Majorana states necessarily come by pair. An isolated Majorana fermion cannot be observed in condensed matter systems. This later situation is represented in the bottom sketch of figure 1.9.

The example that was discussed in this section is a toy model for topological superconductivity in one-dimensional systems and is not realistic since spinless electrons do no exist. However, if one finds a way to spin-polarize the electrons condensating into the superconducting state, the required triplet order parameter might be obtained as well as 1D topological superconductivity. Several experimental realizations of the topical Kitaev chain have been proposed since 2012.

Zero bias states in superconductor-semiconductor nano-wire devices.

The first approach adopted by V. Mourik *et al.* consisted in considering superconductor-semiconductor nano-wire devices [1]. In their study, they performed transport measurements on a InSb wire electrically contacted to a s-wave superconductor. The presence of a magnetic field in the direction of the wire provoked a Zeeman splitting strong enough to have **one** band crossing at Fermi level. Moreover, superconductivity was induced in the wire by proximity

to the superconducting electrode. The strong Rashba spin-orbit splitting, due to the absence of inversion symmetry, gave a triplet part to the superconducting order parameter. Finally, by mean of gating, the authors claim to have finely tuned the wire into a topological regime reminiscent of the Kitaev chain and observed 0-bias states which they identified as Majorana fermions. Their data is represented in figure 1.10.

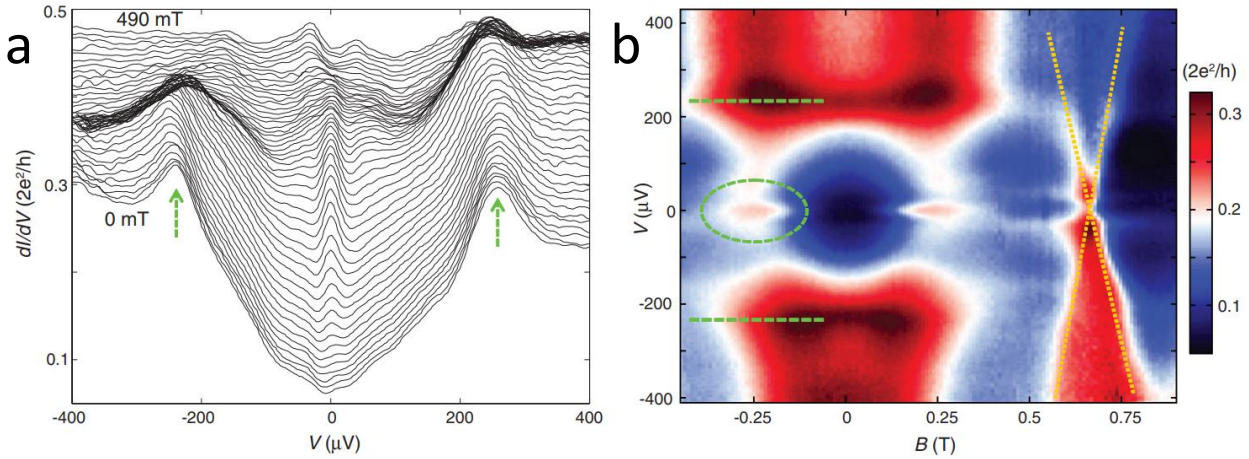

Figure 1.10: **a** dI/dV spectra *vs* magnetic field with (from 0 to 490 mT). **b** Color scale plot of dI/dV *vs* magnetic field and bias voltage. Figure taken from ref. [1].

This interpretation is controversial since V. Mourik *et al.* did not observe any hard superconducting gap. As it can be seen in figure 1.10 **a**, the superconducting gap is filled by many states and the zero bias state is far from being isolated.

A similar study was carried by A. Das *et al.* this time using semiconducting InAs nano-wires in proximity to superconducting Al [44]. The general idea behind this work is the same than in ref. [1]. In this article, they observe a 0-bias state which however splits with increasing magnetic field (see figure 1.11). This is in contradiction with the expected robustness of Majorana state against magnetic field.

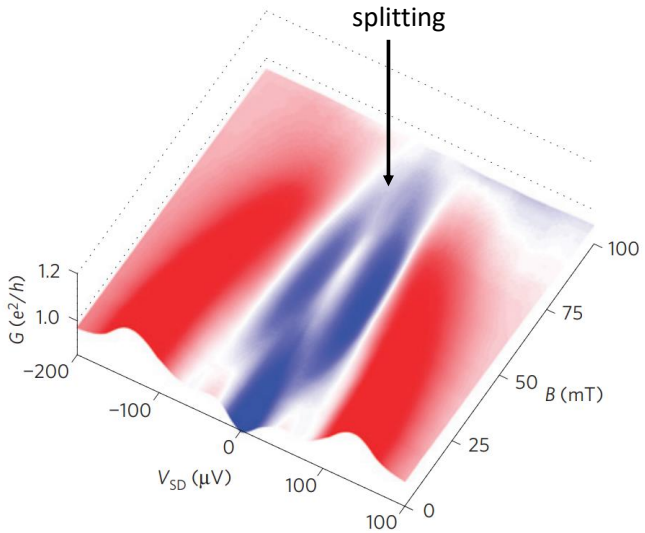

Figure 1.11: Color plot of the measured conductance as a function of bias voltage and magnetic field. Figure taken from ref. [44].

In refs. [45] and [46], the group of C. M. Marcus also studied InAs nano-wires in proximity to superconducting Al. In ref. [45], they observed a exponential suppression of the magnetic field-induced energy-splitting with increasing wire length. Moreover, in ref. [46], they could even realize wires where the 0-bias states would remain at 0 energy with magnetic fields high enough to ensure the closing of the superconducting gap (see figure 1.12).

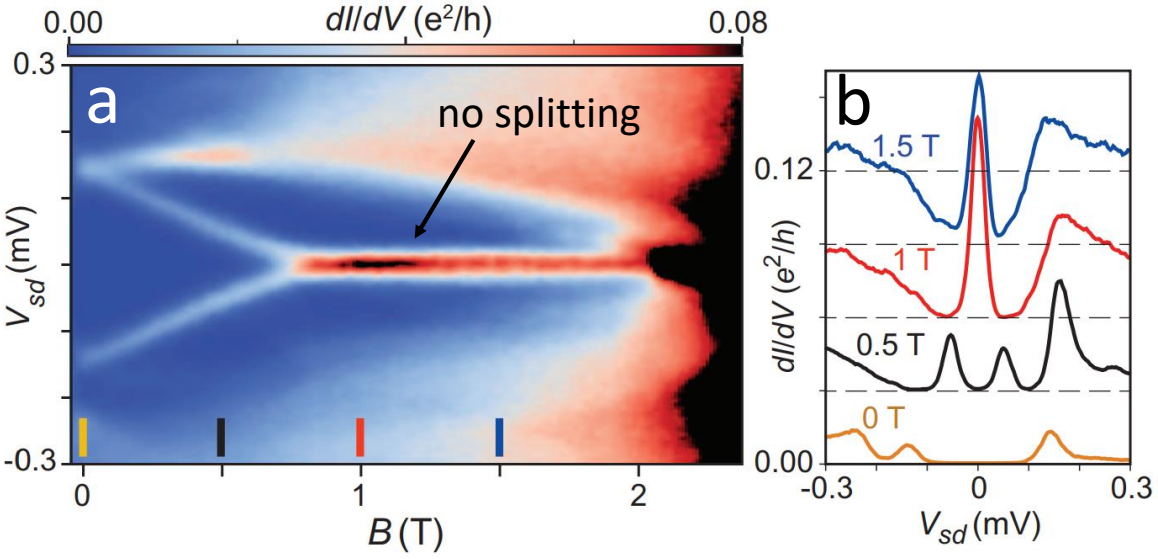

Figure 1.12: **a**. Color plot of differential conductance as a function of bias voltage and magnetic field. **b**. Differential conductance spectra as a function of bias voltage and at magnetic fields going from 0 T to 1,5 T. Figure taken from ref. [46].

It would seem that the conceptual difficulties encountered in these systems can be explained in terms of recombination of Majorana end states due to small wire length. However, recent theoretical studies tend to show that the zero-bias states could rather be interpreted as non-topological Andreev bound states [47], or even, that the chosen geometry would mean a significant shift of the chemical potential, turning the system in a topologically trivial regime[48, 49]. The semiconducting nano-wire approach, nevertheless, remains promising. Recently, S. Vaitekenas *et al.* pursued in this direction, using new geometry, this time considering InAs nano-wires with a **full-shell** of superconducting Al [50]. This study seems to be the most successful since the data is in perfect agreement with theoretical calculations. Nevertheless, the full-shell geometry of the system does not permit the use of gating, on which are based most of the reasonable Majorana fermions braiding procedures.

Exploiting superconducting proximity effect in semiconducting systems presenting strong spin-orbit coupling was the first of several attempts towards topological superconductivity. Yet, from these studies, one can extract the essential ingredients : superconductivity, Zeeman splitting and finally, spin-orbit coupling (to induce a p-wave component in the superconducting order parameter).

Zero bias states at the ends of magnetic chains.

From 2011 to 2013, many theoretical papers proposed an alternate way of realizing Majorana fermions using chains of magnetic atoms on top of a superconductor[51, 52, 53, 54, 55]. The main message of these articles is the fact that a superconducting spiral chain of magnetic moments is mathematically equivalent to a superconductor in presence of magnetic field and spin-orbit coupling, and thus, is likely to exhibit Majorana bound states at its ends. It is

also mathematically equivalent to a ferromagnetic chain with superconductivity and spin-orbit coupling.

The pioneering work which followed this approach is the one of S. Nadj-Perge *et al.* in 2014 [2]. In this STM/STS study, ferromagnetic chains of Fe were grown on top of a superconducting bulk Pb crystal in the (110) direction. Zero energy states were observed at the ends of the wires, which were interpreted as Majorana bound states. The Majorana end states are expected to be particle-hole symmetric as well as spin-polarized. These features were claimed to be observed in 2017, when the results were reproduced by the same group with better energy resolution [56] and using spin-polarized STM/STS [57]. In 2015, M. Ruby *et al.* [58] carried out a STM/STS study on the same system as S. Nadj-Perge *et.al.*. Apparently, the Majorana end states interpretation would imply a topological gap too small ($\leq 60\ \mu eV$) to be observed at the temperature at which the experiments of ref. [2] were performed (namely 1,4 K). Hence, the existence of topological superconductivity in Fe/Pb(110) is not consensual in the community. M. Ruby *et al.* also carried out STM/STS studies on a similar system were the Fe atoms were replaced by magnetic Co atoms. In this work, zero-bias modes were delocalized along the chain suggesting a non topological origin. Finally, in 2018, H. Kim *et al.* built, by atomic manipulation, spin spiral Fe magnetic chains on top of a superconducting Re(0001) substrate [59]. In this work, the existence of Majorana bound states is under debate due to missing well-defined zero bias peaks[1]. Nevertheless, this last study opens an alternative and promising new platform to engineer topological superconductivity.

The following section will be dedicated to two-dimensional superconductivity through the topical 2D p-wave superconductor.

1.4.3 The 2D p-wave superconductor

Let us consider a square superconducting two-dimensional lattice with one **spinless** electron per site and of lattice parameter a. In this example, the electron are again considered to be spinless, like in section 1.4.2. The hamiltonian describing the system is :

$$H_{BdG} = \frac{1}{2}\sum_{\overrightarrow{k}} \psi^{\dagger}_{\overrightarrow{k}} \overbrace{\begin{pmatrix} \varepsilon(\overrightarrow{k}) - \mu & 2i\Delta(\sin(k_x a) + i\sin(k_y a)) \\ -2i\Delta(\sin(k_x a) - i\sin(k_y a)) & -(\varepsilon(\overrightarrow{k}) - \mu) \end{pmatrix}}^{\mathcal{H}(\overrightarrow{k})} \psi_{\overrightarrow{k}}, \qquad (1.51)$$

where $\psi^{\dagger}_{\overrightarrow{k}} = (c^{\dagger}_{\overrightarrow{k}} \quad c_{-\overrightarrow{k}})$, with $c^{\dagger}_{\overrightarrow{k}}$ and $c_{\overrightarrow{k}}$ the creation and annihilation operators respectively, of spinless electron of momentum $\overrightarrow{k} = (k_x, k_y)$, $\varepsilon(\overrightarrow{k})$ is the electron dispersion, μ is the chemical potential and Δ is the superconducting gap amplitude. $\mathcal{H}(\overrightarrow{k})$ is the Bloch Hamiltonian and can be written as such :

$$\mathcal{H}(\overrightarrow{k}) = -2\Delta\sin(k_y a)\tau_x - 2\Delta\sin(k_x a)\tau_y + (\varepsilon(\overrightarrow{k}) - \mu)\tau_z = \overrightarrow{d}(\overrightarrow{k}) \cdot \overrightarrow{\tau}, \qquad (1.52)$$

where $\overrightarrow{\tau} = (\tau_x \quad \tau_y \quad \tau_z)$, and $\tau_{x,y,z}$ are the Pauli matrices on the particle-hole basis. By considering only a positive first neighbour hopping parameter t, the $\overrightarrow{d}(k)$ vector has the expression :

$$\overrightarrow{d}(k) = \begin{cases} d_x = -2\Delta\sin(k_y a) \\ d_y = -2\Delta\sin(k_x a) \\ d_z = -2t(\cos(k_x a) + \cos(k_y a)) - \mu \end{cases}, \qquad (1.53)$$

Similarly to the 1D case, the eigenenergies of the system are function of the components of $\overrightarrow{d}(k)$. One has :

[1] The observed peaks also develop along the whole chain, which is not is favor of Majorana bound states.

$$E_{\pm}(\overrightarrow{k}) = \pm\sqrt{d_x^2 + d_y^2 + d_z^2}, \tag{1.54}$$

$E_{\pm}(\overrightarrow{k})$ is equal to zero for four values of (k_x, k_y, μ) which are : $(0, 0, -4t)$, $(0, \pi, 0)$, $(\pi, 0, 0)$ and $(\pi, \pi, 4t)$. Three topological phases corresponding to $|\mu| > 4t$, $-4t < \mu < 0$ and $0 < \mu < 4t$ appear, since it is impossible to continuously tune the chemical potential to go from one of these phases to an other without closing the superconducting gap. We will now see what is the nature of the topological invariant distinguishing all three cases.

As it was done in 1D, we will introduce the quantity $\widehat{d}(\overrightarrow{k})$:

$$\widehat{d}(\overrightarrow{k}) = \frac{\overrightarrow{d}(\overrightarrow{k})}{\parallel \overrightarrow{d}(\overrightarrow{k}) \parallel} = \frac{1}{\sqrt{d_x^2 + d_y^2 + d_z^2}}(d_x \quad d_y \quad d_z) = (\hat{d}_x \quad \hat{d}_y \quad \hat{d}_z), \tag{1.55}$$

$\widehat{d}(\overrightarrow{k})$ is normalized to one and lives on the Bloch sphere. Let us first consider the $\mu > 4t$ topological case. We can notice that $\hat{d}_z$ always is strictly inferior to zero which means that only one hemisphere of the Bloch sphere is explored. On the contrary, in the $0 < \mu < 4t$ topological case, $\hat{d}_z$ explores the whole Bloch sphere. This can easily be checked by taking an example. For instance, if $\Delta = t$ and $\mu = 2t$, then, for $(k_x, k_y) = (-\frac{\pi}{a}, -\frac{\pi}{a})$, $\widehat{d} = (0 \quad 0 \quad 1)$ points to the "north" pole while for $(k_x, k_y) = (0, 0)$, $\widehat{d} = (0 \quad 0 \quad -1)$ points to the "south" pole. The topological invariant can be defined as the degree of wrapping of the $\widehat{d}(\overrightarrow{k})$ vector around the Bloch sphere when $\overrightarrow{k}$ explores the first Brillouin zone [37]. The associated topological invariant is called the first Chern number. In the $4t < \mu$ case, the Chern number is zero while in the $0 < \mu < 4t$ phase, $\widehat{d}(\overrightarrow{k})$ wraps one time the Bloch sphere. Formally, this Chern number can be related to the Berry phase introduced in section 1.4.1. In topological physics, there is a property called the "bulk-edge correspondence". This property says that there is a matching between the number of edge states and the value of the topological invariant defined for the bulk material. In this example, the Chern number can take any integer value, which means that topological phases presenting any number of edge states can potentially arise.

We will prove the existence of in-gap edge states at the interface between two p-wave superconductors in different topological regimes. We have seen previously that the superconducting gap was closing at $(k_x, k_y, \mu) = (0, 0, -4t)$. We will thus consider an interface between a $\mu < -4t$ and a $-4t < \mu < 0$ phases with a spatial dependence of the chemical potential along the x direction. The system is taken translationally invariant in the y direction. We propose :

$$\mu(x) = \begin{cases} -\mu_1 & \text{if} \quad x < 0, \\ -\mu_2 & \text{if} \quad x > 0, \end{cases} \tag{1.56}$$

with $-\mu_1 < -4t$ and $-4t < -\mu_2 < 0$. In addition, since the topological transition occurs at $(k_x, k_y) = (0, 0)$, we can develop $\mathcal{H}(\overrightarrow{k})$ to first order in (k_x, k_y) around $(0, 0)$ and :

$$\mathcal{H}(\overrightarrow{k}) = \begin{pmatrix} -4t - \mu(x) & 2a\Delta(\frac{\partial}{\partial x} - k_y)) \\ 2a\Delta(-\frac{\partial}{\partial x} - k_y)) & -(-4t - \mu(x)) \end{pmatrix}, \tag{1.57}$$

Since the system is invariant under translation in the y direction, k_y is a good quantum number and will label any eigenstates of $\mathcal{H}(\overrightarrow{k})$. Also, if we call $|\psi_{k_y}(x, y)\rangle$ such an eigenstate, it can generically be written like $|\psi_{k_y}(x, y)\rangle = e^{ik_y y} |\phi(x)\rangle$, where $|\phi(x)\rangle$ is a spinor which depends on x. One can verify that $|\phi(x)\rangle = \frac{1}{\sqrt{2}} e^{\frac{1}{2a\Delta}\int_0^x dx'(4t+\mu(x'))}(1, 1)^T$ and that the corresponding eigenenergies are $E(k_y) = -2a\Delta k_y$, which can be arbitrarily close to zero. We see that a band of states fill the superconducting gap. It is shown in ref. [37] that these Dirac fermionic states can

also be decomposed in pairs of Majorana states just as in the Kitaev chain. However, contrary to the one-dimensional case, those Majorana fermions are not zero energy bound states but rather what we call "dispersive Majorana states".

Spinless superconductivity is unrealistic. In order to reproduce the physics that was just presented, sometimes referred to as chiral p-wave superconductivity, one possibility is to have a combination of both Rashba spin orbit-coupling and Zeeman effect [60], just as in the 1D case. The chiral p-wave superconductor has first been claimed to be observed in 2017 by G. Ménard *et al.* [3]. In this STM/STS work, they grew a superconducting Pb monolayer on top of a Si(111) substrate. Strong Rashba spin-orbit coupling is present at the surface and induced triplet correlations in the superconducting order parameter. Moreover, CoSi magnetic islands likely to provide Zeeman splitting were embedded under the Pb monolayer. The idea is that Zeeman splitting is such that the area of the Pb monolayer which is right above the CoSi islands enters a topologically non trivial regime. At the boundary between this topological "island" and the remaining of the Pb monolayer, they saw dispersive states, which were interpreted as chiral edge states. In 2018, A. Palacio-Morales *et al.* performed a STM/STS study on a magnet-superconductor hybrid consisting of Fe islands on top of a Re(0001)-O(2×1) surface, and also observed such dispersive edge states suggesting the formation of a topologically non-trivial phase [61].

Although having a topological origin, such chiral edge states cannot be used for the braiding operations that were previously mentioned but could hypothetically lead to quantum computation applications [62]. It does not mean that Majorana bound states cannot be obtained in 2D systems. In refs. [63, 37], it is shown that Majorana bound states are expected in the vortex core of a p-wave superconductor. From 2015 to 2018, several experimental realizations of such states were reported. The first kind was obtained by G. Ménard *et al.* in Pb/Co/Si(111) [4]. It would seem that some of the topological domains that were already presented in ref. [3] present a symmetry-authorized spin-orbit vortex configuration. Two zero-energy bound states were observed at the center of the domain (the core of the spin-orbit vortex) and at its edge, respectively. In the other realizations, a magnetic field was applied, thus inducing the apparition of regular magnetic vortices in the system. The second type of experimental evidence of Majorana bound states at the cores of vortices was attained in $Bi_2Te_3/NbSe_2$ heterostructures [6] exploiting the fact that it is possible to generate p-wave correlations at the surface of a topological insulator in proximity to a conventional superconductor as shown theoretically in ref. [64]. Finally, it was shown that Fe-based superconductors can enter a topologically non-trivial regime through doping [65, 66]. On this basis, STM/STS studies performed on $FeTe_{0,55}Se_{0,45}$ [7] and on $(Li_{0,84}Fe_{0,16})$OHFeSe [67] highlighted the presence of zero-bias states in the cores of vortices, also in agreement with a Majorana bound state interpretation. We once again stress that none of the zero-bias bound states observations listed in the two last sections, although very promising, can be taken as indisputable evidence of Majorana bound states features since the non-Abelian statistics as yet not been addressed.

Chapter 2

Scanning Tunnelling Microscopy/Spectroscopy

Scanning Tunnelling Microscopy (STM) is a technique which can be used to probe the electronic properties of surfaces of materials. STM was invented in 1982 by Gerd Binnig and Heinrich Rohrer [68] and takes advantage of the well-known quantum tunnelling effect. This invention eventually lead both Rohrer and Binnig to win the Nobel Prize in Physics in 1986. In this chapter, we will briefly present the principle of STM as well as what are the different measurements it allows to perform. The great majority of results which are presented in this thesis were obtained using this experimental technique.

First, in section 2.1, we will introduce the procedure to image the surfaces of materials using STM. Second, in section 2.2, we will explain what is Scanning Tunnelling Spectroscopy (STS) technique and how it gives access to the local density of states (LDOS) of samples, making it a very powerful tool. Finally, in section 2.3, we will show how Fourier transform STM and more specifically Quasiparticle Interferences (QPIs) can be used to artificially rebuilt the band structures of materials.

2.1 Topographic constant current mode

Let us consider an electron of energy E submitted to an unidimensional rectangular potential barrier of height W and of width d such as represented in figure 2.1. The time-independent Schrödinger equation between the edges of the rectangular barrier is the following :

$$-\frac{\hbar^2}{2m_e}\frac{d^2}{dx^2}\Psi(x) + (W-E)\Psi(x) = 0. \tag{2.1}$$

The solution of this equation is trivial and in the end :

$$\Psi(x) \propto e^{-\frac{\sqrt{2m_e(W-E)}x}{\hbar}} = e^{-\kappa(E)x}. \tag{2.2}$$

Thus, $|\Psi(d)|^2 \propto e^{-\frac{2\sqrt{2m_e(W-E)}d}{\hbar}}$. One can see that $|\Psi(d)|^2$, the probability that the electron is transmitted through the barrier, decreases exponentially with d. The electrons at the surface of a given material have thus a small probability of leaking into the vacuum. In this case, W is called the work function, which is of the order of 4 eV in metals (see any work function table of common metals).

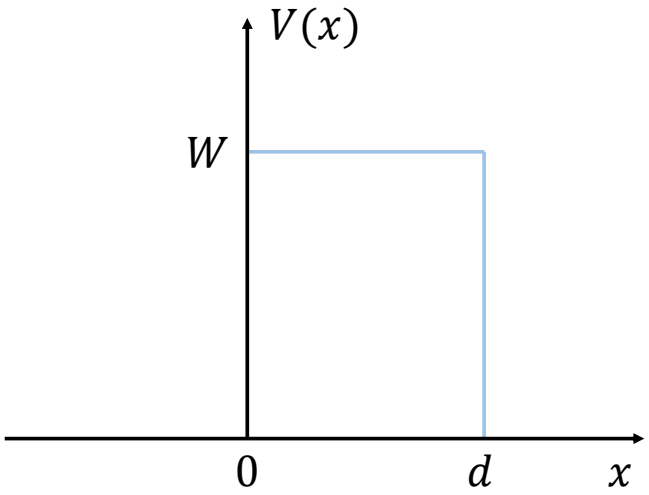

Figure 2.1: Unidimensional rectangular potential barrier of height W and of width d.

If a conducting tip is now brought very close to that very surface (typically at 5 to 10 Å from it), and if a bias voltage V is applied between the tip and the surface, electrons have a non-zero probability to hop from the tip to the surface or inversely, depending on the sign of V, thus giving rise to a tunnelling current. The tunnelling current and the applied bias voltage are independent parameters. A given set of those parameters however defines a specific tunnelling regime and fixes the tip-sample distance. This technique is highly surface-sensitive since if the tip-sample distance increases of 1 Å, the tunnelling current is divided by a factor 10. Only electrons within few Å from the tip will contribute to the total tunnelling current.

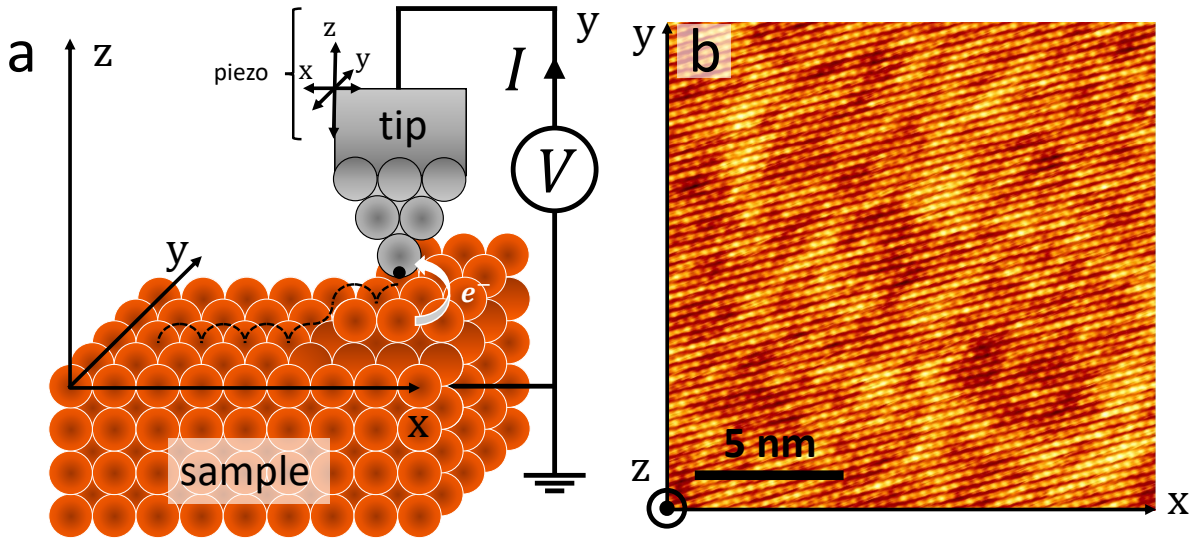

Figure 2.2: **a**. Schematic drawing of the principle of STM. **b**. Topographic image of the surface of $(LaSe)_{1,14}(NbSe_2)_2$ obtained with STM.

All the topographic imaging performed in this thesis was obtained using constant current mode scanning. This mode works as follows : the tip is moved laterally across the surface while maintaining a constant tunnelling current thanks to a feedback loop which adjusts the height of the tip. Those changes in the vertical position of the tip are recorded as a function of lateral coordinates thus allowing the construction a topographic image of the studied sample.

Piezoeletric compounds are used so as to obtain the short three-dimensional displacements of the tip which are needed in order to realize atomically resolved topography[1]. By fixing the tip at the top of a piezoelectric tube, and by applying the correct bias voltages between several sides of this tube, it is possible to bend it, contract it or expand it at will (see figure 2.2).

2.2 Probing the local density of states of samples *via* STS

While STM is a very powerful technique to access the crystal structure of surfaces, one must always keep in mind that topographic data also contains electronic spectroscopic features of the material. In this section, we will show how tunnel effect can be exploited to access to LDOS of a material.

2.2.1 Expression of the tunneling current

In this part, we will derive the expression of the tunnelling current between two conducting materials when a voltage difference is applied between them.

Let us consider two conducting materials labelled 1 and 2. The Hamiltonian of the system can be decomposed as follows :

$$\begin{cases} \hat{H} = \hat{H}_1 + \hat{H}_2 + \hat{H}_T, \\ \hat{H}_T = \sum_{kk',\sigma}(T_{kk'}c^\dagger_{1k,\sigma}c_{2k',\sigma} + T^*_{kk'}c^\dagger_{2k',\sigma}c_{1k,\sigma}) = \underbrace{\sum_{kk',\sigma} T_{kk'}c^\dagger_{1k,\sigma}c_{2k',\sigma}}_{T(t)} + \underbrace{\sum_{kk',\sigma} T^*_{kk'}c^\dagger_{2k',\sigma}c_{1k,\sigma}}_{T^\dagger(t)}, \end{cases} \tag{2.3}$$

where $\hat{H}_1$ and $\hat{H}_2$ are the Hamiltonians describing respectively systems 1 and 2, $\hat{H}_T$ describes the tunnelling between the two conducting materials, and $T_{kk'}$ is the hopping amplitude between an electronic state of momentum k in one material and an electronic state of momentum k' in the other material.

A Voltage difference $V = V_1 - V_2$ is applied between the two systems, so that the chemical potentials of systems 1 and 2 (respectively μ_1 and μ_2) are different. Moreover, we have :

$$\begin{cases} \mu_1 = \mu + eV_1 \\ \mu_2 = \mu + eV_2 \end{cases}, \tag{2.4}$$

The electric current going from 1 to 2 can be defined by : $\hat{I} = -e\langle\hat{I}_p\rangle$ where $\hat{I}_p = -\dfrac{d\hat{N}_1}{dt}$ with $\hat{N}_1 = \sum_{k,\sigma} c^\dagger_{1k,\sigma}c_{1k,\sigma}$, the number operator of the first system. $\langle ...\rangle$ is the mean value taken on the perturbed system. Similarly, the number operator of the second system is $\hat{N}_2 = \sum_{k,\sigma} c^\dagger_{2k,\sigma}c_{2k,\sigma}$.

A calculation where system 2 is supposed to be a metal (and thus having a constant density of states around Fermi level) is done in Annex.1 and eventually leads to the following equation for the measured differential conductance :

$$\frac{d\hat{I}}{dV} = e^2 2\pi|T|^2 n_0 \int_{-\infty}^{+\infty} d\omega n_1(\omega)\frac{dn_F}{d\omega}(\omega + eV), \tag{2.5}$$

where n_0 is the density of states at Fermi level of system 2, $n_1(\omega)$ the density of states at energy ω of system 1 and n_F the Fermi-Dirac function.

At zero temperature, $\dfrac{dn_F}{d\omega}(\omega + eV) = \delta(\omega + eV)$, so it gives :

[1] A piezoelectric material is a material which can be electrically polarized when it is subject to mechanical stress and reciprocally can be deformed if a bias voltage is applied at its edges.

$$\frac{d\hat{I}}{dV} = e^2 2\pi |T|^2 n_0 n_1(-eV). \tag{2.6}$$

The tunnelling conductance $\frac{d\hat{I}}{dV}$ is proportional to $n_1(-eV)$, the density of states of system 1 at energy $-eV$. Experimentally, one can access the density of states of a sample by measuring this conductance using STS (see 2.2.2 for details). At finite temperature, the tunnelling conductance is proportional to the convolution of the density of states of the studied material with the derivative of the Fermi-Dirac function. This leads to an enlargement in energy of $3,5k_BT$ of the states at temperature T. At 300 mK, this enlargement in energy is about ~ 90 μeV. The effect of thermal broadening on the measured conductance is illustrated in figure 2.3.

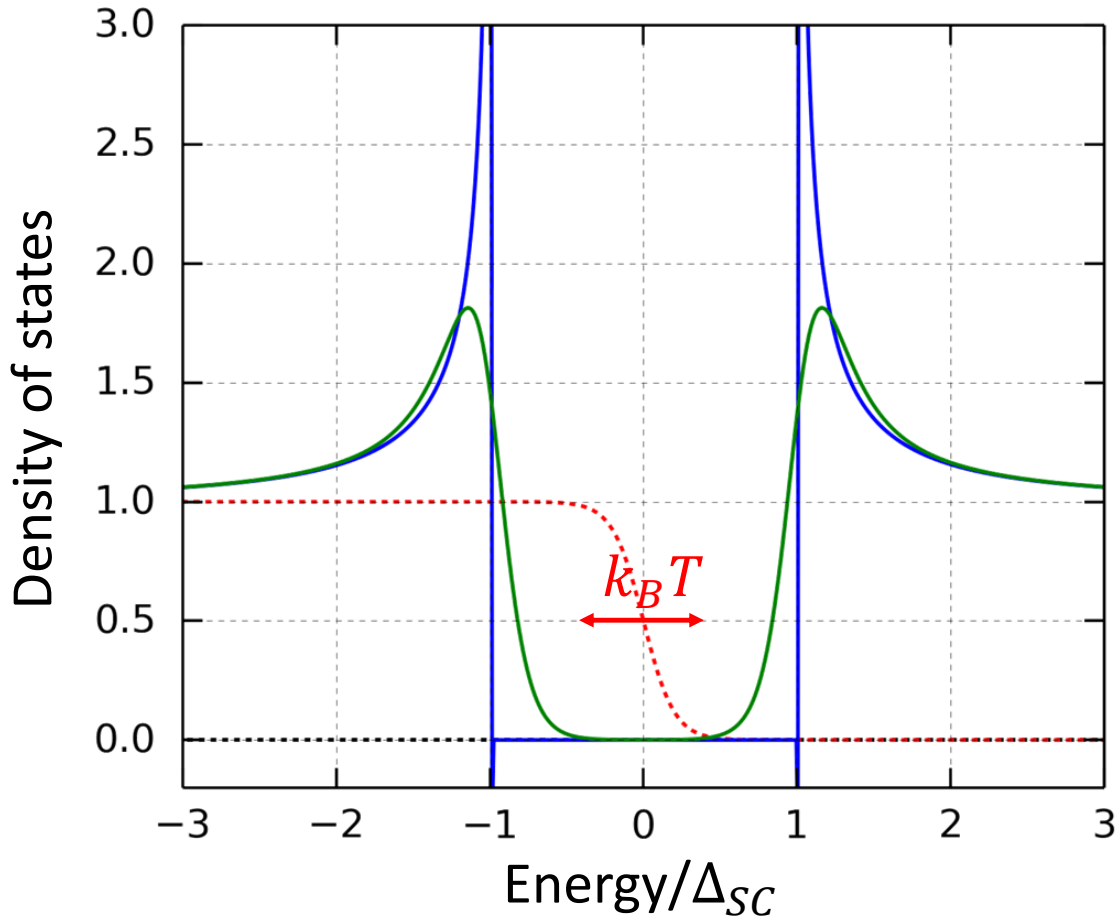

Figure 2.3: The blue line is the theoretical BCS density of states at zero temperature (see section 1.1). The dotted red line is the Fermi Dirac distribution obtained at temperature T. The green line is the measured superconducting dI/dV spectrum obtained at temperature T with a normal tip.

2.2.2 Tunneling Spectroscopy

A Scanning Tunnelling Spectroscopy (STS) experiment is similar to a STM one, both method being based on quantum tunnelling effect and permitting to study surfaces. In STS, the tip is brought very close to the sample surface. Here again, a bias voltage V is applied between tip

and sample, thus inducing a tunnelling current. Because of formula 2.6, if one uses a metallic tip whose density of states is known and constant in the voltage range of the measurement, then, by varying the value of V while measuring the tunnelling current (and deriving numerically the conductance as a function of V) it is possible to probe the local density of states at a specific point (x, y) of the studied sample. The local density of states at energy E is defined as :

$$n(E, x, y) = \sum_n |\psi_n(E_n, x, y)|^2 \delta(E - E_n), \tag{2.7}$$

where the ψ_n are the eigenfunctions of the system associated to eigenvalues E_n.

A summary of the principle of the measurement is represented on figure 2.4. In case where the sample is a superconductor (see figure 2.4 **b**), electrons can hop from tip to sample only when an electronic state is available. Therefore, by scanning the surface, it is possible to obtain a map of the local density of states of a region of the sample, and this, for several values of $-eV$ or equivalently of E.

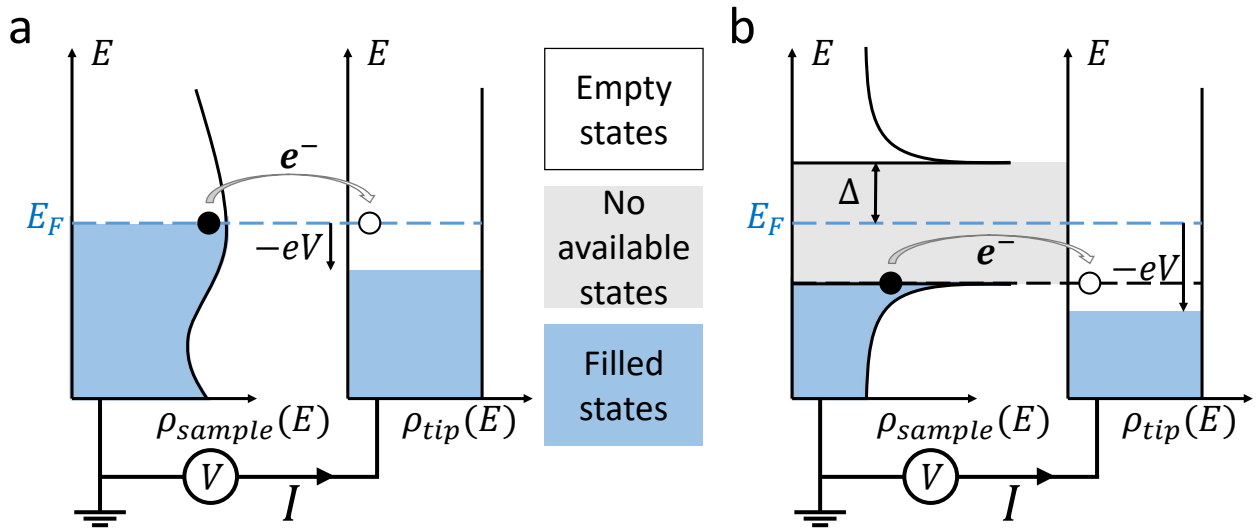

Figure 2.4: **a**. Principle of STS illustrated by tunnelling processes in a metal. **b**. Principle of STS illustrated by tunnelling processes in a superconductor.

Remark: STM and STS are very often done simultaneously. By doing so, the topography of the studied surface and the spatial dependence of electronic states visible on spectroscopy can be correlated.

Tunnelling selectivity.

As it was already mentioned in section 2.1, the wave functions of the electrons at the surface of a material decay exponentially into the vacuum. Moreover, in a periodic crystal, the electrons can be described by Bloch wave functions labelled by crystalline momentum $\overrightarrow{k}$. The periodicity along the direction perpendicular to the surface is broken, such that at the surface, one can only label the wave functions of the electrons with the component of the momentum parallel to the surface $\overrightarrow{k}_{\parallel}$. In ref. [69], J. Tersoff and D. R. Hamann give the expression of such wave functions :

$$\psi_{\overrightarrow{k}_{\parallel},E} = \sum_{\overrightarrow{G}} c_{\overrightarrow{k}_{\parallel},\overrightarrow{G}} e^{i(\overrightarrow{k}_{\parallel}+\overrightarrow{G})\cdot\overrightarrow{r}} \exp\left(-\alpha_{\overrightarrow{k}_{\parallel}+\overrightarrow{G}} z\right), \tag{2.8}$$

where $\alpha_{\overrightarrow{k}_{\parallel}+\overrightarrow{G}} = \sqrt{|\overrightarrow{k}_{\parallel}|^2 + \kappa(E)^2}$, $\overrightarrow{G}$ is a vector of the reciprocal lattice, z is the distance to the surface, $\overrightarrow{r}$ is the in-plane position and $c_{\overrightarrow{k}_{\parallel},\overrightarrow{G}}$ are the components of the Fourier series development of $\psi_{\overrightarrow{k}_{\parallel},E}$.

If the system is in a tip-parallel-to-the-z-direction geometry, one sees from the expression of $\alpha_{\overrightarrow{k}_{\parallel}+\overrightarrow{G}}$ that the wave functions with small $\overrightarrow{k}_{\parallel}$ (momenta close to Γ) decay over longer distances into the vacuum than the wave functions with bigger $\overrightarrow{k}_{\parallel}$ (momenta far from Γ). This last observation means that, in this geometry, the electrons close to Γ in reciprocal space are the ones which mostly contribute to the total tunnelling current. Scanning tunnelling spectroscopy experiments are then intrinsically more sensitive to electronic states with smaller wave vectors $\overrightarrow{k}_{\parallel}$. We speak of tunnelling selectivity.

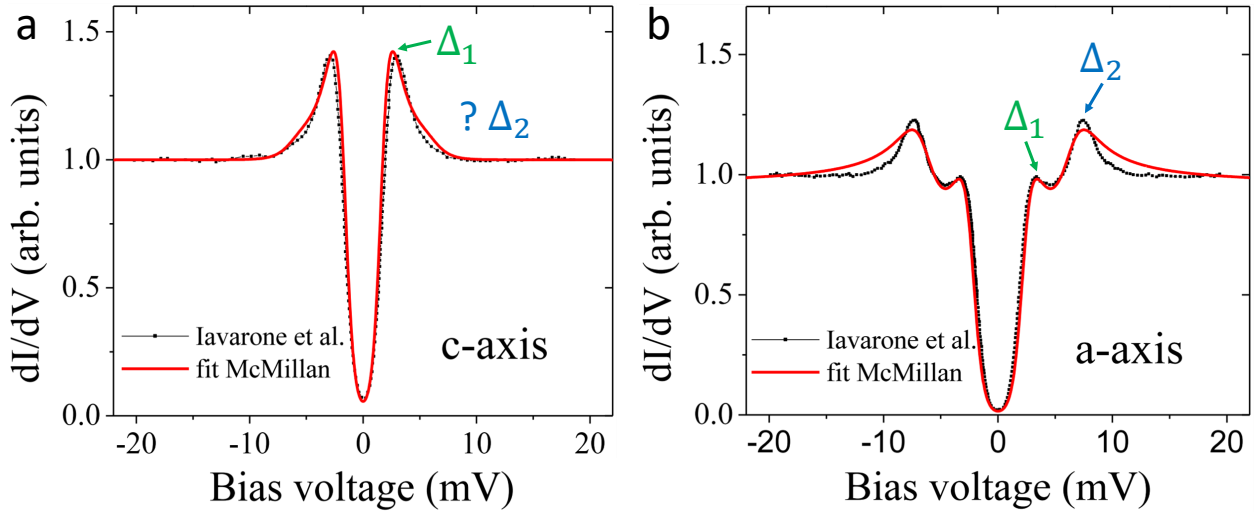

Figure 2.5: **a**. dI/dV spectrum taken on MgB_2 with the tip aligned along the c-axis. **b**. dI/dV spectrum taken on MgB_2 with the tip aligned along the a-axis. Figure taken from [70].

A famous example of such tunnelling selectivity effects is the one of two-band superconductivity in MgB_2. In 2002, M. Iavarone *et al.* observed different dI/dV spectra depending on the orientation of MgB_2 crystals with respect to their tip [71]. When the tip is aligned with the c-axis of MgB_2, they see dI/dV spectra exhibiting one superconducting gap Δ_1 (see figure 2.5 **a**). However, when the geometry is different and the tip is oriented along the a-axis of MgB_2, the Δ_1 is still seen but together with an additional Δ_2 superconducting gap (see figure 2.5 **b**). The calculations confirmed that this effect was actually due the faster decay of the electronic states associated to Δ_2 with respect to the ones responsible for Δ_1 [70].

2.2.3 Data treatment

In experiments, $I(V)$ curves are measured. In order to access the local density of states, one has to numerically compute the derivative of I with respect to V. However, as illustrated by the red $I(V)$ spectrum in figure 2.6 **a**, experimental data will always present a certain degree of noise. As a consequence, the derivative dI/dV of a raw spectrum will necessarily diverge at many bias voltages. Such divergences are not physical since only related to the level of noise present during the acquisition of the data. Hence, a "smoothing" procedure has to be applied beforehand. During this thesis we applied the following data treatment to all $I(V)$ individual spectra : first, the data is convoluted with a normalized Gaussian of width $3,5k_BT$ (our energy

resolution is limited by thermal broadening), second, a Savitzky-Golay filter is also applied [72]. Single raw and filtered $I(V)$ spectra are represented in figure 2.6 **a**. After filtering the data, it is finally possible to obtain the derivative of the experimental single $I(V)$ spectrum (see figure 2.6 **b**). We see that this spectrum still remains noisy and particularly on the "wings" (which is normal because the noise is proportional to the current). The more time spent for each point during the data acquisition and the finer the energy sampling, the more efficient will be the filtering procedure. Depending on the information one wants to highlight, it might or nor be important to have nice individual spectra. On the one hand, if one is interested in getting a dI/dV spectrum within a given energy range and representative of a given sample, one can simply average a collection of individual dI/dV spectra taken in the same conditions. On the other hand, if one wants to access the local density of states maps at several energies (in a way explained in 2.2.4), then, it is crucial to make sure information can easily be extracted from all individual spectra.

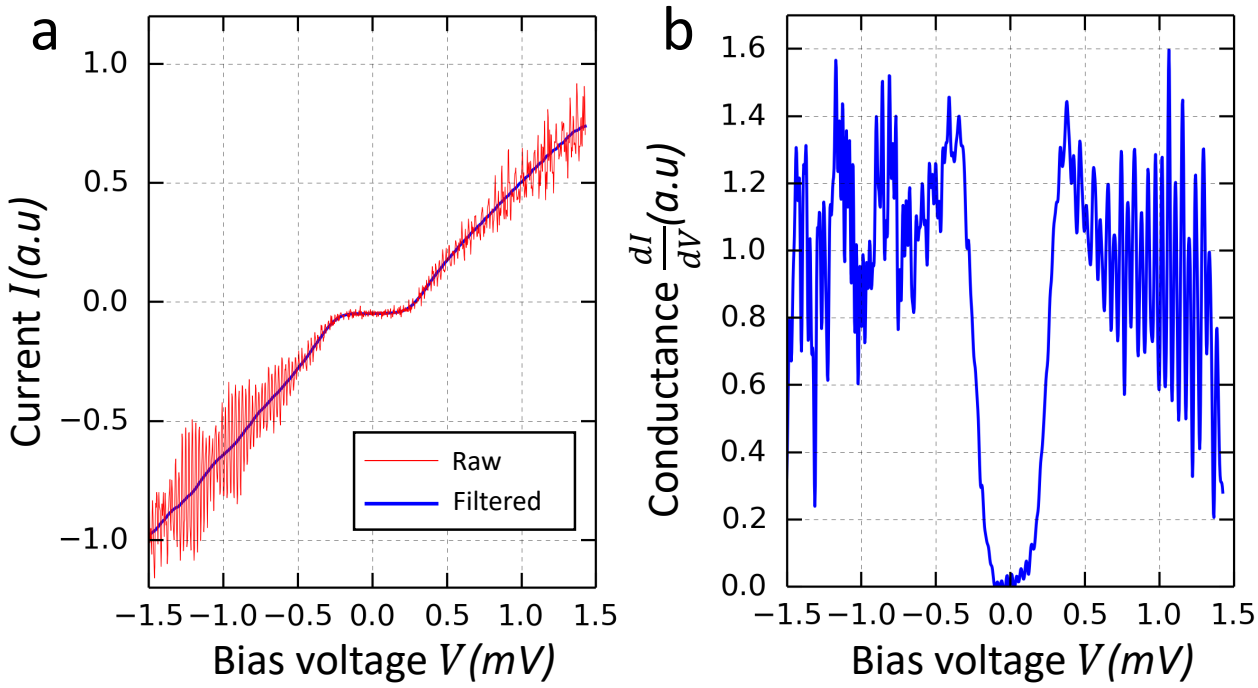

Figure 2.6: **a**. The red $I(V)$ spectrum is an individual spectrum taken on a superconducting monolayer of Pb/(Si(111). In blue is the same $I(V)$ spectrum after performing of gaussian and Savitzky-Golay filtering. **b**. This dI/dV spectrum was obtained by numerically derivating the filtered $I(V)$ spectrum of **a**.

2.2.4 Spectroscopic grid experiments

In this subsection, we expose the principle of spectroscopic grid experiments which we have used to obtain most of the results presented in this thesis. We will base our explanation on the schematic representation of figure 2.7. In figure 2.7 **a** is represented an area of a sample illustrated by a topography map. A predefined square grid with $N \times N$ nodes is superimposed (blue crosses) on top of this topography map. The general idea is to take $I(V)$ spectra [2] with common bias voltage range $[V_{start}, V_{end}]$ and sampling at the positions of all the nodes of this

[2] One chooses a given set point corresponding to a couple of current and bias voltage $(I_{setpoint}, V_{setpoint})$, thus fixing a given tip-sample distance. Before sweeping the voltage and taking the $I(V)$ curve, one opens the feedback loop, meaning that the spectrum is acquired at constant height.

grid. In the end, after performing a similar data treatment as in subsection 2.2.3, one has a collection of $N \times N$ dI/dV spectra which contain the spatial dependence of the density of states of the sample and this for all energies within $[V_{start}, V_{end}]$. If V_j is an arbitrary bias voltage belonging to $[V_{start}, V_{end}]$, one can indeed build up a local density of states map at energy eV_j by defining $N \times N$ matrices which all components are the values of all dI/dV spectra evaluated for $V = V_j$.

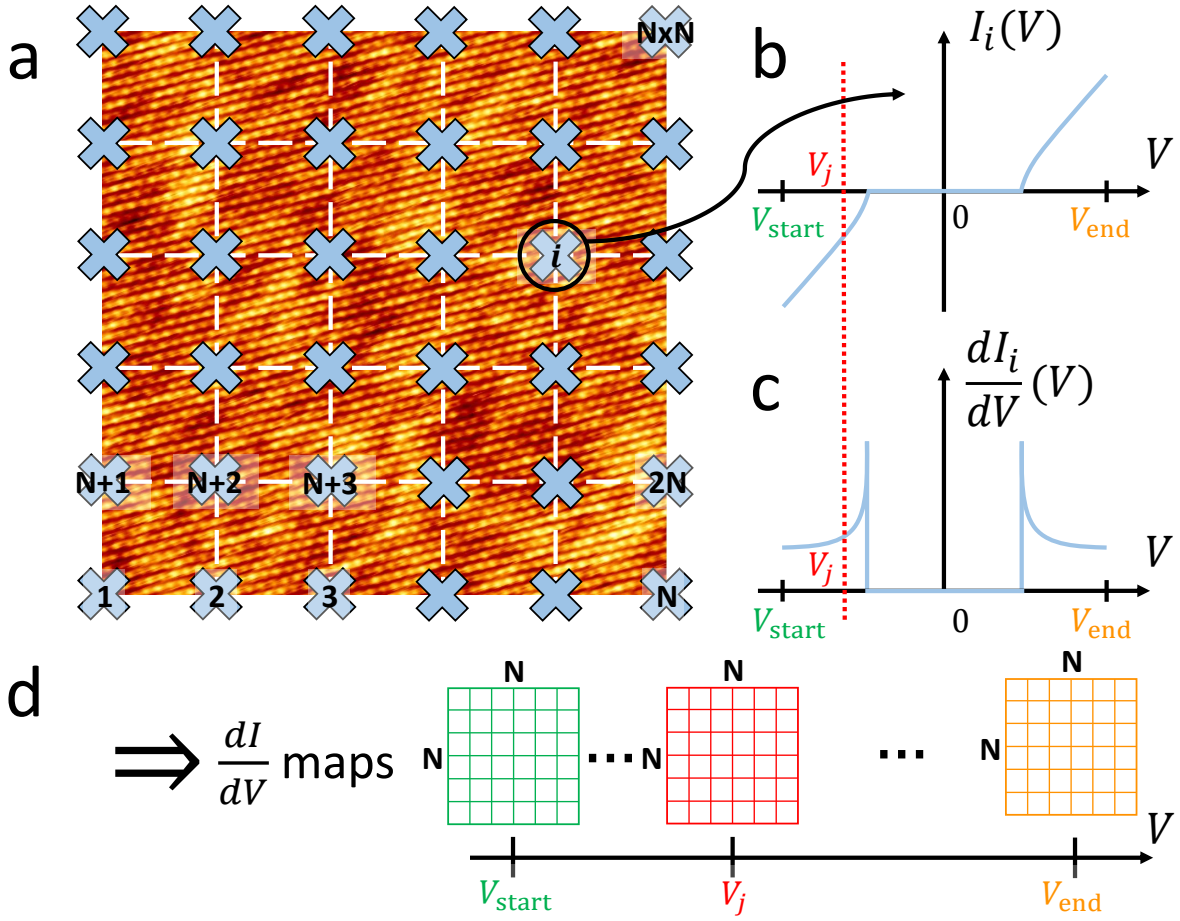

Figure 2.7: **a**. Grid of STS data. $I(V)$ spectra are taken at the nodes of a predefined spatial square grid. **b**. Typical $I(V)$ individual spectrum taken at the i node position in the $[V_{start}, V_{end}]$ bias voltage range. **c**. Derivative of the $I(V)$ spectrum of **b**. **d**. Construction of density of states maps for all the energies belonging to $[V_{start}, V_{end}]$.

2.3 Quasiparticle interferences and Fourier transform STM

In this section, we will see how those spectroscopic grids can be used to access quasiparticle interferences patterns.

In a crystal, the electrons evolve in the periodic potential of the ionic lattice. Bloch's theorem tells us that the eigenstates of the systems are labelled by crystal momentum $\mathbf{k}$ and are similar to plane waves however modulated by a complex function $u_{\mathbf{k}}(\mathbf{r})$ with the periodicity of the lattice. Those eigenstates are called Bloch wave functions and have the following expression: $\psi_{\mathbf{k}}(\mathbf{r}) = e^{i\mathbf{k}\cdot\mathbf{r}} u_{\mathbf{k}}(\mathbf{r})$. Any source of disorder (defects, steps, dislocations...) breaks the translational symmetry of the periodic crystal such that $\mathbf{k}$ is no longer conserved and $\psi_{\mathbf{k}}$ is no longer an

eigenstate. A given electron with incoming momentum $\mathbf{k_i}$ and in $\psi_{\mathbf{k_i}}$ state will be likely to scatter once encountering a defect. If only elastic scattering is considered, this electron might scatter in a final state with momentum $\mathbf{k_f}$ and $\psi_{\mathbf{k_f}}$ state. Since both incoming and final states have the same energy, they can interfere, and the electron is in the superposition of both : $\psi_{\mathbf{tot}} = \psi_{\mathbf{k_i}} + \psi_{\mathbf{k_f}}$. In the following, we will derive the expression of the local density of states or so to say $\mid \psi_{\mathbf{tot}} \mid^2$. We recall that the local density of states is the physical quantity probed in STS :

$$\psi_{\mathbf{tot}} = e^{i\mathbf{k_i}\cdot\mathbf{r}} u_{\mathbf{k_i}}(\mathbf{r}) + e^{i\mathbf{k_f}\cdot\mathbf{r}} u_{\mathbf{k_f}}(\mathbf{r}), \tag{2.9}$$

$$\mid \psi_{\mathbf{tot}} \mid^2 = (e^{i\mathbf{k_i}\cdot\mathbf{r}} u_{\mathbf{k_i}}(\mathbf{r}) + e^{i\mathbf{k_f}\cdot\mathbf{r}} u_{\mathbf{k_f}}(\mathbf{r}))(e^{-i\mathbf{k_i}\cdot\mathbf{r}} u^*_{\mathbf{k_i}}(\mathbf{r}) + e^{-i\mathbf{k_f}\cdot\mathbf{r}} u^*_{\mathbf{k_f}}(\mathbf{r})), \tag{2.10}$$

and we define $\mathbf{q} = \mathbf{k_f} - \mathbf{k_i}$

$$\mid \psi_{\mathbf{tot}} \mid^2 = \mid u_{\mathbf{k_i}}(\mathbf{r}) \mid^2 + \mid u_{\mathbf{k_f}}(\mathbf{r}) \mid^2 + 2\Re(e^{i\mathbf{q}\cdot\mathbf{r}} u^*_{\mathbf{k_i}}(\mathbf{r}) u_{\mathbf{k_f}}(\mathbf{r})), \tag{2.11}$$

In QPIs measurements, one plots the square modulus of the Fourier transform of the local density of states map, one thus has to calculate $FT(\mid \psi_{\mathbf{tot}} \mid^2)(\mathbf{K})$ where FT designs the Fourier transform. We will now look at the first term $FT(\mid u_{\mathbf{k_i}} \mid^2)(\mathbf{K})$. We have $u_{\mathbf{k_i}}(\mathbf{r}) = \sum_{\mathbf{G}} c_{\mathbf{k_i}+\mathbf{G}} e^{i\mathbf{G}\cdot\mathbf{r}}$. In this last relation, the sum is on the reciprocal lattice $\mathbf{G}$ vectors. Moreover :

$$FT(\mid u_{\mathbf{k_i}} \mid^2)(\mathbf{K}) = (FT(u_{\mathbf{k_i}}) * FT(u^*_{\mathbf{k_i}}))(\mathbf{K}), \tag{2.12}$$

Given the fact that the Fourier transform of a product is the convolution product of the Fourier transforms (convolution product is designed by $*$). Because Fourier transform is a linear operation and also that the Fourier transform of $e^{i\mathbf{G}\cdot\mathbf{r}}$ is $\delta(\mathbf{K} - \mathbf{G})$, we have $FT(u_{\mathbf{k_i}})(\mathbf{K}) = \sum_{\mathbf{G}} c_{\mathbf{k_i}+\mathbf{G}} \delta(\mathbf{K} - \mathbf{G})$. In the end, computing $FT(\mid \psi_{\mathbf{tot}} \mid^2)(\mathbf{K})$ is just about computing convolution products between $\delta(\mathbf{K} - \mathbf{G})$ and $\delta(\mathbf{K} + \mathbf{G}')$ Dirac functions.

$$\int \delta(\mathbf{K}' - \mathbf{K} - \mathbf{G})\delta(\mathbf{K} + \mathbf{G}')d\mathbf{K} = \delta(\mathbf{K}' - (\mathbf{G} - \mathbf{G}')), \tag{2.13}$$

The $FT(\mid u_{\mathbf{k_i}} \mid^2)(\mathbf{K})$ term then only gives signal for $\mathbf{K}'$ equal to any reciprocal lattice vector or saying differently at the Bragg peaks positions. The $FT(\mid u_{\mathbf{k_f}} \mid^2)(\mathbf{K})$ term is similar and also gives signal at Bragg peaks positions. This results is not really surprising since similar terms arise when there are no defects and thus no QPIs. If one indeed looks at the Fourier transform of a local density of states map of a perfect surface, only signal at the Bragg peaks position are possible. Nevertheless, the $TF(2\Re(e^{i\mathbf{q}\cdot\mathbf{r}} u^*_{\mathbf{k_i}} u_{\mathbf{k_f}})(\mathbf{K})$ term is only present through interferences. We have :

$$\begin{aligned} 2\Re(e^{i\mathbf{q}\cdot\mathbf{r}} u^*_{\mathbf{k_i}}(\mathbf{r}) u_{\mathbf{k_f}}(\mathbf{r})) = 2\Re((&\cos(\mathbf{q}\cdot\mathbf{r}) + i\sin(\mathbf{q}\cdot\mathbf{r})(\Re(u_{\mathbf{k_i}}(\mathbf{r})) \\ &-i\Im(u_{\mathbf{k_i}}(\mathbf{r})))(\Re(u_{\mathbf{k_f}}(\mathbf{r})) + i\Im(u_{\mathbf{k_f}}(\mathbf{r}))), \end{aligned} \tag{2.14}$$

$$\begin{aligned} 2\Re(e^{i\mathbf{q}\cdot\mathbf{r}} u^*_{\mathbf{k_i}}(\mathbf{r}) u_{\mathbf{k_f}}(\mathbf{r})) = &2[\cos(\mathbf{q}\cdot\mathbf{r})\Re(u_{\mathbf{k_i}}(\mathbf{r}))\Re(u_{\mathbf{k_f}}(\mathbf{r})) + \cos(\mathbf{q}\cdot\mathbf{r})\Im(u_{\mathbf{k_i}}(\mathbf{r}))\Im(u_{\mathbf{k_f}}(\mathbf{r})) \\ &- \sin(\mathbf{q}\cdot\mathbf{r})\Re(u_{\mathbf{k_i}}(\mathbf{r}))\Im(u_{\mathbf{k_f}}(\mathbf{r})) + \sin(\mathbf{q}\cdot\mathbf{r})\Im(u_{\mathbf{k_i}}(\mathbf{r}))\Re(u_{\mathbf{k_f}}(\mathbf{r}))], \end{aligned} \tag{2.15}$$

It is now time to compute the Fourier transform of the expression that was just derived. The computation of only $TF(2\cos(\mathbf{q}\cdot\mathbf{r})\Re(u_{\mathbf{k_i}})\Re(u_{\mathbf{k_f}}))(\mathbf{K}'')$ is similar to the computation of all other three terms left, that is why we will only be focusing on this one. Since the Fourier transform of $2\cos(\mathbf{q}\cdot\mathbf{r})$ is $\delta(\mathbf{K} - \mathbf{q}) + \delta(\mathbf{K} + \mathbf{q})$. We have :

$$TF(2\cos(\mathbf{q}\cdot\mathbf{r})\Re(u_{\mathbf{k_i}})\Re(u_{\mathbf{k_f}}))(\mathbf{K}'') = ((\delta(\mathbf{K}' - \mathbf{q}) + \delta(\mathbf{K}' + \mathbf{q})) * TF(\Re(u_{\mathbf{k_i}})\Re(u_{\mathbf{k_f}})))(\mathbf{K}''), \tag{2.16}$$

Also, $\Re(u_{\mathbf{k_i}}(\mathbf{r})) = \sum_{\mathbf{G}} a^i_{\mathbf{G}} \cos(\mathbf{G}\cdot\mathbf{r})$ and $\Re(u_{\mathbf{k_f}}(\mathbf{r})) = \sum_{\mathbf{G}} a^f_{\mathbf{G}} \cos(\mathbf{G}\cdot\mathbf{r})$, because both $\Re(u_{\mathbf{k_i}})(\mathbf{r})$ and $\Re(u_{\mathbf{k_f}})(\mathbf{r})$ are real periodic functions of $\mathbf{r}$ and can be expanded in Fourier series. Consequently, $TF(\Re(u_{\mathbf{k_i}}))(\mathbf{K}) = \sum_{\mathbf{G}} a^i_{\mathbf{G}}(\delta(\mathbf{K}-\mathbf{G}) + \delta(\mathbf{K}+\mathbf{G}))$ and $TF(\Re(u_{\mathbf{k_f}}))(\mathbf{K}) = \sum_{\mathbf{G}} a^f_{\mathbf{G}}(\delta(\mathbf{K}-\mathbf{G}) + \delta(\mathbf{K}+\mathbf{G}))$. We use again the properties of Fourier transform : $TF(\Re(u_{\mathbf{k_i}})\Re(u_{\mathbf{k_f}})))(\mathbf{K}') = (TF(\Re(u_{\mathbf{k_i}})) * TF(\Re(u_{\mathbf{k_f}})))(\mathbf{K}')$ and it is again about computing convolution products between $\delta(\mathbf{K}' \pm \mathbf{G})$ and $\delta(\mathbf{K}' \pm \mathbf{G}')$. The Fourier transform of $\Re(u_{\mathbf{k_i}})\Re(u_{\mathbf{k_f}}))$ is a sum of Dirac functions $\delta(\mathbf{K}' - \mathbf{G}))$ centered on reciprocal lattice vectors $\mathbf{G}$. Lastly, everything results in calculating convolution products between $\delta(\mathbf{K}' - \mathbf{q})$ and $\delta(\mathbf{K}' - \mathbf{G}')$:

$$\int \delta(\mathbf{K}'' - \mathbf{K}' - \mathbf{q})\delta(\mathbf{K}' - \mathbf{G}')d\mathbf{K}' = \delta(\mathbf{K}' - (\mathbf{q} + \mathbf{G}')), \tag{2.17}$$

The final conclusion is that QPIs give signal at scattering wave vector $\mathbf{q}$ position up to a reciprocal lattice vector $\mathbf{G}'$. The incoming and final states interfere giving rise to standing waves patterns of wave vector $\mathbf{q}$.

According to Fermi's golden rule, and as explained in ref. [73], the amplitude of scattering between states at $(E_i, \mathbf{k_i})$ and $(E_f, \mathbf{k_f})$ is :

$$\omega(i \to f) \propto \frac{2\pi}{\hbar} \mid V(\mathbf{q}) \mid^2 n_i(E_i, \mathbf{k_i}) n_f(E_f, \mathbf{k_f}), \tag{2.18}$$

where $V(\mathbf{q})$ is Fourier transform of scattering potential at scattering wave-vector $\mathbf{q} = \mathbf{k_f} - \mathbf{k_i}$ and $n(E, \mathbf{k})$ is the density of states at energy E and wave-vector $\mathbf{k}$. E_i is considered equal to E_f since we only consider elastic scattering. This expression tells us that the higher the number of incoming and final states and consequently the flatter (the lower the group velocity) the bands between which scattering occurs, the higher the transition probability. Moreover, if two initial and final collections of states are linked by a same scattering wave-vector $\mathbf{q}$, the probability of observing standing-wave at this very vector $\mathbf{q}$ becomes larger too. By gathering all the information that were exposed up to know, we can conclude that QPIs patterns at a given energy E can be obtained by doing a sort of autoconvolution of the energy contour at E, taking into account the spectral weight distribution across this energy contour. We speak of joint density of states (JDOS).

The expected QPIs patterns for simple energy contours are discussed in figure 2.8. In all of the examples, we consider systems with hexagonal Brillouin zones. The reason behind this is that the experimental QPIs results of this thesis were obtained on $NbSe_2$ layers, which have an hexagonal lattice. Figure 2.8 **a** represents a circular energy contour of radius r and centered on Γ. The scattering wave-vector $\mathbf{q}$ (of norm $2r$) displayed on the image possesses good nesting properties because the two circular portions of energy contour it links are tangent to one another. The same can be said of all wave-vectors with arbitrary directions but same norm as $\mathbf{q}$. The expected QPIs pattern is represented in figure 2.8 **a** and is a circle centered on Γ and of radius $2r = \parallel \mathbf{q} \parallel$, *i.e.* twice as big as the one of the corresponding energy contour. In figure 2.8 **c** is represented an hexagonal-shaped energy contour. $\mathbf{q_1}$ scattering wave-vector links two straight and vertical portions of the energy contour which means that a collection of incoming states can scatter into a collection of many final states with the same scattering wave-vector $\mathbf{q_1}$. Hence, it is very likely that QPIs patterns will have a strong contribution at $\mathbf{q_1}$ position in reciprocal space. By symmetry, the same can be said about $\mathbf{q_2}$ and $\mathbf{q_3}$ vectors. The QPIs pattern displayed in figure 2.8 **d** is thus made out of six spots at $\parallel \mathbf{q_1} \parallel$ distance from Γ and lying along ΓM directions.

The most famous example of the observation of QPIs signal is the case of Cu(111) surface [74]. A parabolic free-electron-like band is present at the surface of Cu(111) (see figure 2.8 **e**). The Fermi surface is consequently similar to the one of figure 2.8 **a**. In this STM study, Crommie *et al.* observed ripples around structural defects due to the interference of quasi-electrons' wave functions (standing-waves). Figure 2.8 **f**) illustrates how the selectivity of the

scattering channels can be influenced by the geometry of the defect. Here, the considered defect is a step. Let us call x the direction parallel to the step. The lattice remains periodic along x, such that k_x is a good quantum number. The consequence of this last remark is that only scattering wave vectors conserving k_x will contribute to the overall QPIs signal.

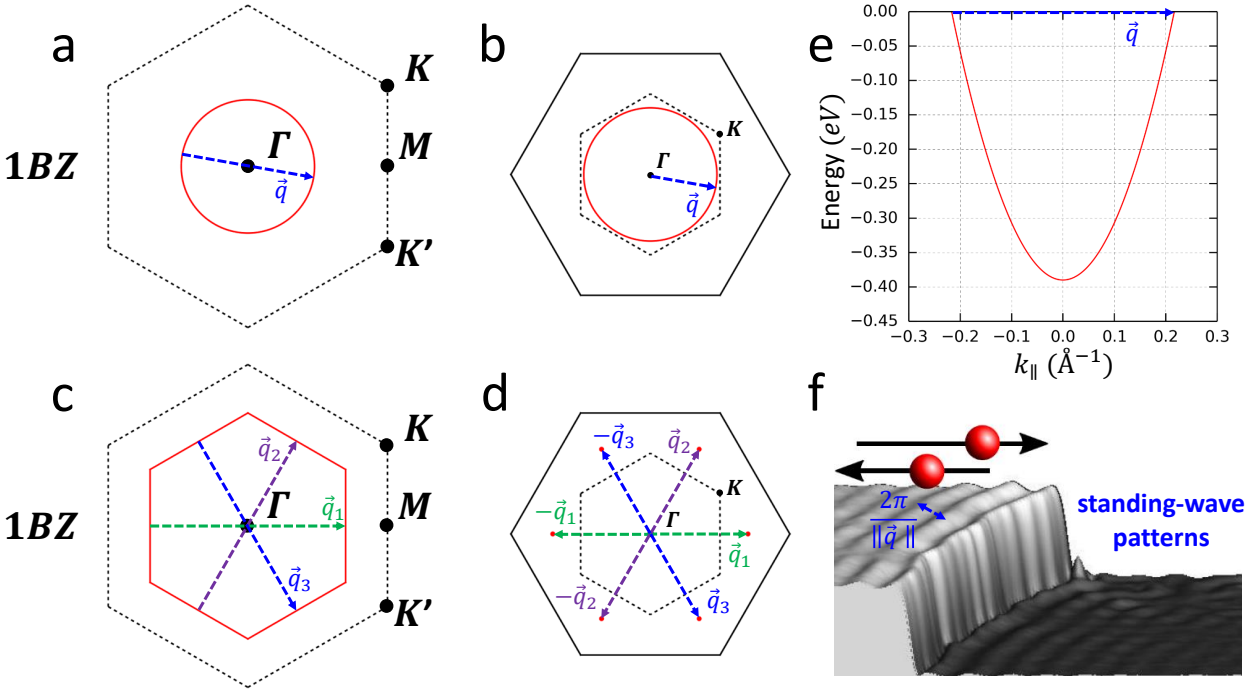

Figure 2.8: **a**. The red line is a circular energy contour of diameter q and centered on Γ. **b**. The red line represents the expected QPIs pattern for the circular energy contour of **a**. The result is a circle centered on Γ and of radius q. **c**. The red line is a hexagonal energy contour. q_1, q_2 and q_3 are good nesting vectors. **d**. The red points lie at q_1, q_2 and q_3 positions ans represent the expected QPIs patterns for the hexagonal energy contour of **c**. **e** Energy dispersion of the surface state of Cu(111) [74]. This famous example is an illustration of what happens in **a** and **b**. **f**. Standing-wave patterns with periodicity $2\pi/q$ visible along a step in Cu(111) [74].

Scattering channels depend on the symmetry of the defect and also on its spin texture. For example, an incoming electron of spin up might interact with a magnetic impurity and scatter into a spin down state. If spin is conserved, the incoming and scattered states cannot interfere because the spin part of the respective incoming and scattered wave functions are orthogonal and thus, scattering occurs but not QPIs. Nevertheless, if the defect couples the spin of the incoming electron to its momentum (we speak of spin-orbit impurity), spin might no longer be a a good quantum number and new channels open regarding QPIs patterns [75]. Materials with strong intrinsic spin-orbit coupling should in principle also open QPIs channels with opposite spins but it is not necessarily observed. The Rashba spin-orbit split surface state of Au(111) is indeed not seen in QPIs measurements or at least not directly. In ref. [76], P. Leicht *et al.* grew epitaxial graphene flakes on Au(111). In this article, the Rashba band splitting was indirectly exhibited thanks to graphene to gold QPIs scattering channels and not through gold to gold QPIs scattering channels.

All the concepts developed in this section will be necessary to interpret the results presented in chapter 3. In this case, the disorder potential is *a priori* non-magnetic and not spin-orbit-like.

2.4 Experimental set-ups

In this section, we will present the two experimental set-ups on which all the scanning tunnelling microscopy/spectroscopy measurements discussed in this manuscript were performed. First, we will present the M3 microscope on which of the results of chapter 3 were obtained. Second, we will present the Low Temperature Omicron STM, on which some of the results of chapter 3 and all the experimental data of chapter 4 were acquired.

2.4.1 M3 STM

UHV equipment.

Figures 2.9 **a** and **b** represent a photograph and a schematic top view of the M3 STM system, respectively. This set-up is an home-made apparatus allowing to perform scanning tunnelling microscopy/spectroscopy measurements under ultra-high vacuum (UHV), down to 300 mK and under strong magnetic fields (up to 7 T). This equipment is composed of two ultra-high vacuum chambers : a preparation chamber, in which samples can be prepared *in situ*, and the STM chamber, where one can change samples or/and tips. Ii is also in the STM chamber that the samples are cleaved. In both chambers, the pressure is around 10^{-11} mbar. An ionic pump as well as titanium sublimators maintain this very low pressure in each chamber[3]

An extra chamber, called the load lock, is attached to the system in order to introduce the samples in UHV. This load lock is linked to a primary pump (which allows at first the load lock to reach a pressure of 10^{-2} mbar) and to a turbo pump which eventually leads to a load lock pressure of $\simeq 2.10^{-8}$ mbar. A magnetic manipulator allows to transfer the samples from the load lock to the preparation chamber on condition that the load lock pressure is low enough. It is indeed important not to pollute the preparation chamber nor to break the vacuum.

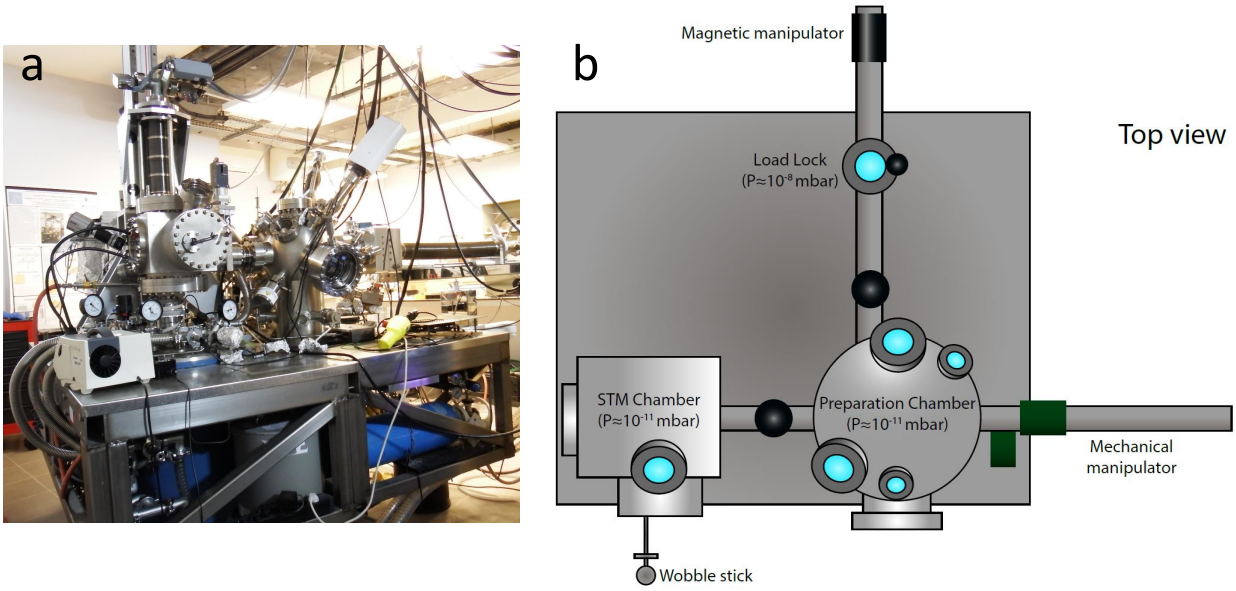

Figure 2.9: **a** Photograph of the M3 setup. **b** Schematic top view of the M3 setup.

Remark: The STM chamber is never put in direct contact with the load lock. This additional security measure ensures the cleanliness of the environment in which the measurements

[3]Such pressures can be reached after performing a bake out procedure which consist in heating the chambers at 150°C for two to four days to degas the internal surfaces.

are carried out.

The preparation chamber contains, among other things, a quartz crystal microbalance (QCM) and an evaporator which allowed me to deposit lead on $(LaSe)_{1,14}(NbSe_2)_2$. The QCM is used to calibrate the deposition rate per unit of surface.

The mechanical manipulator allows to move the samples from preparation chamber to STM chamber and inversely. The STM chamber contains a carousel in which one can store several tips and samples. Those tips/samples can be manipulated with the help of a wobble stick in order to be put in or out of the microscope.

The approach of the tip to the surface is done with the help of a camera filming the reflection on a mirror (located in the chamber) of the tip-sample ensemble. It is crucial to approach the tip as close as possible from the surface so as to gain time on the fine approach, which is done *via* automatic piezoelectric displacements[4]. In practice, due to optical lenses and geometrical angle, the tip-sample distance cannot be better controlled than about 20 micrometers.

Moreover, in STM/STS experiment, so as to have atomic resolution, one needs to be properly isolated from external mechanical vibrations. The whole experimental set-up is, hence, mounted on three compressed-air-alimented vibration dampers, which ensure a good isolation from external mechanical noises.

Low temperature circuit.

In measurement position, the microscope is taken down to the cryostat through a guide rod. The cryostat is the part of the setup in which the microscope will be brought down to very low temperatures. A 60 L hollow cylinder filled with liquid ^{4}He at $4,2$ K is separated by an Internal Vacuum Can (IVC) at $\simeq 10^{-8}$ mbar from an internal pot filled with ^{3}He[5]. This later pot is itself in thermal contact with the very bottom of the microscope (this part is called the ^{3}He tail). A sorption pump made out of activated carbon is connected through a capillary to the ^{3}He pot. Right next to it, a pot drains liquid ^{4}He from the ^{4}He bath, again, through a capillary. By pumping on this pot filled with liquid ^{4}He, it is possible to effectively decrease its temperature down to 1 K. This is why this pot is called the 1K-pot.

Cooling procedure.

In this short subsection we will explain the condensation process which allows to cool the system down to 300mK. At the beginning of the cooling process, all the ^{3}He is cryosorbed on the walls of the charcoal sorption pump. A resistor attached to the sorption pump is heated up to 50 K. This leads to the releasing of all the ^{3}He gas into the ^{3}He pot. Because the ^{3}He is now gaseous and occupies all the ^{3}He pot space, it is likely to do heat transfer with the 1K-pot whose temperature can be taken down to $\sim 1,5$ K. The 1K-pot is driving the ^{3}He pot temperature descent, and when the sorption pump reaches 39 K, the activated carbon starts to pump ^{3}He again. This cryopumping of ^{3}He has the effect of decreasing the pressure in the ^{3}He pot, and thus, the temperature. Below a given pressure and temperature, the ^{3}He liquefies and falls down to the ^{3}He tail. At the end of the condensation, the liquid ^{3}He present in the ^{3}He tail reaches a temperature of $0,3$ K. This condensation can last between 36 and 40 hours. All the different elements involved in the condensation can be seen in the schematic cut of figure 2.10 **b**. The time dependence of both the temperature of the 1K-pot and the temperature of the ^{3}He tail obtained

[4]The fine approach procedure consists in alernating the elongation of the z piezoelectric tube (in order to fine a tunnelling current) and coarse piezoelectric displacements. Of course the coarse displacements must be smaller than the full z piezoelectric tube's extension to avoid any tip crashes. With decreasing temperature, the length of the displacements shortens and, *a fortiori*, the whole procedure duration increases.

[5]At first, the IVC is filled with gazeous ^{4}He which allows for the STM to thermalize with the $4,2$ K cryostat. Then, the IVC is pumped in order to isolate the STM from the cryostat and to go down to lower temperatures by mean of ^{3}He condensation.

during an actual condensation are represented in figure 2.10 **a**. This plot is representative of a typical condensation procedure. During the first 25 minutes of the condensation, the 1K-pot drives the temperature descent of the ^{3}He tail. Then, when the sorption pump reaches 39 K and that both 1K-pot and ^{3}He tail are around $1,6$ K, ^{3}He is starting to condense until it reaches a temperature of 300 mK. The peaks one can see on the 1K-pot curve between 50 minutes and 65 minutes are due to the fact that at the corresponding moments, the 1K-pot dried out, and thus, had to be refilled.

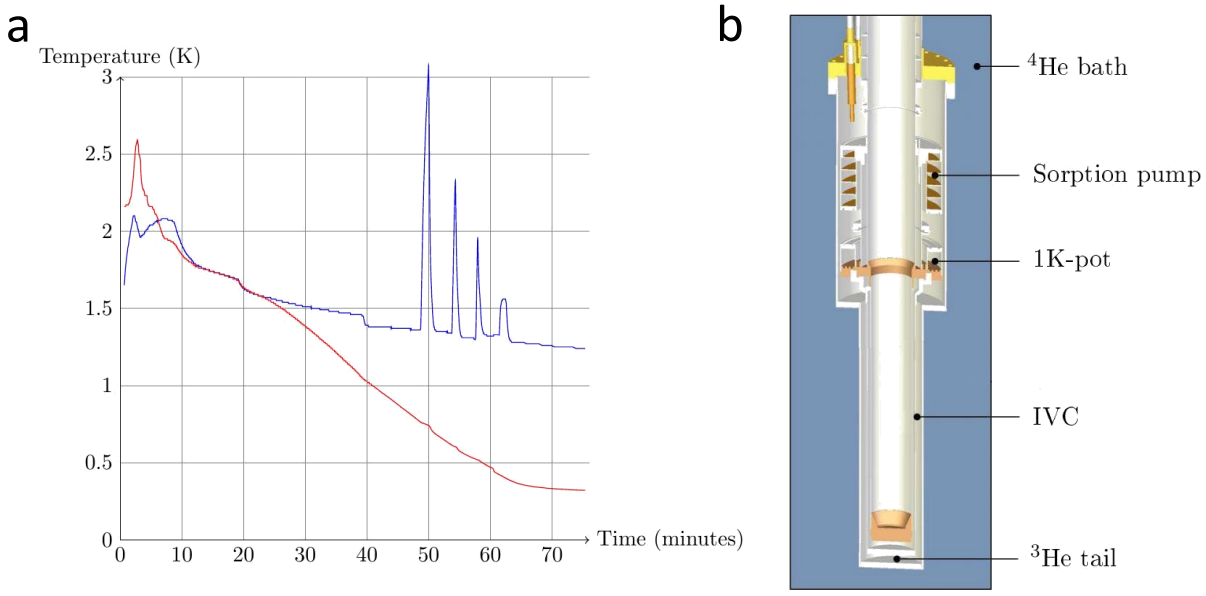

Figure 2.10: **a**. Standard temperature versus time plot of a condensation. The blue curve represents the temperature of the 1K-pot whereas the red one represents the temperature of the ^{3}He tail. **b**. Schematic cut of the cryogenics of M3 STM.

Remark: The temperature of the 1K-pot can be changed by playing on the flow of liquid ^{4}He going through the capillary. Indeed, it it easier to pump on a smaller quantity of liquid ^{4}He, and thus possible to reach smaller temperatures by imposing a relatively low flow of liquid ^{4}He. Moreover, it is important to refill the 1K-pot for a minute at the end of a condensation and then reduce the liquid ^{4}He flow to its minimum value in order to make sure that the 1K-pot will not dry out during the 36 hours the condensation is supposed to last.

2.4.2 LT Omicron STM

Many of the measurements presented in this thesis were performed on a different set-up : namely the LT (for low temperature) Omicron STM. Thanks to our collaboration with Imad Arfaoui, working at MONARIS, a chemistry laboratory of our university, I could access this other equipment. This experimental set-up allows for ultra-high vacuum scanning tunnelling spectroscopy experiments and is composed out of the same parts as M3, namely a load lock, a preparation chamber and a STM chamber. During my thesis, the preparation chamber was not equipped yet, meaning that studies could be carried out only on crystals grown outside the chamber. This LT STM however possesses a cryostat, thus allowing to perform STM/STS measurements at room temperature, 77 K (liquid nitrogen temperature) and $4,2$ K (liquid helium temperature). The system also possesses an outer volume which can be filled with liquid nitrogen and plays the role of sheath, thus allowing to increase the time separating two consecutive cryostat fillings of either liquid nitrogen or liquid helium. The autonomy of the

system is approximatively of 30 hours working at 77 K and 18 hours working at $4,2$ K (or twice as less as the duration of the condensation in M3 STM). A Foucault current damping system allows to isolate efficiently the LT STM from vibrations. As it will be shown in the next subsection, this set-up has the advantage of permitting a relatively easy tip treatment procedure, absolutely crucial to perform quasiparticle interferences experiments.

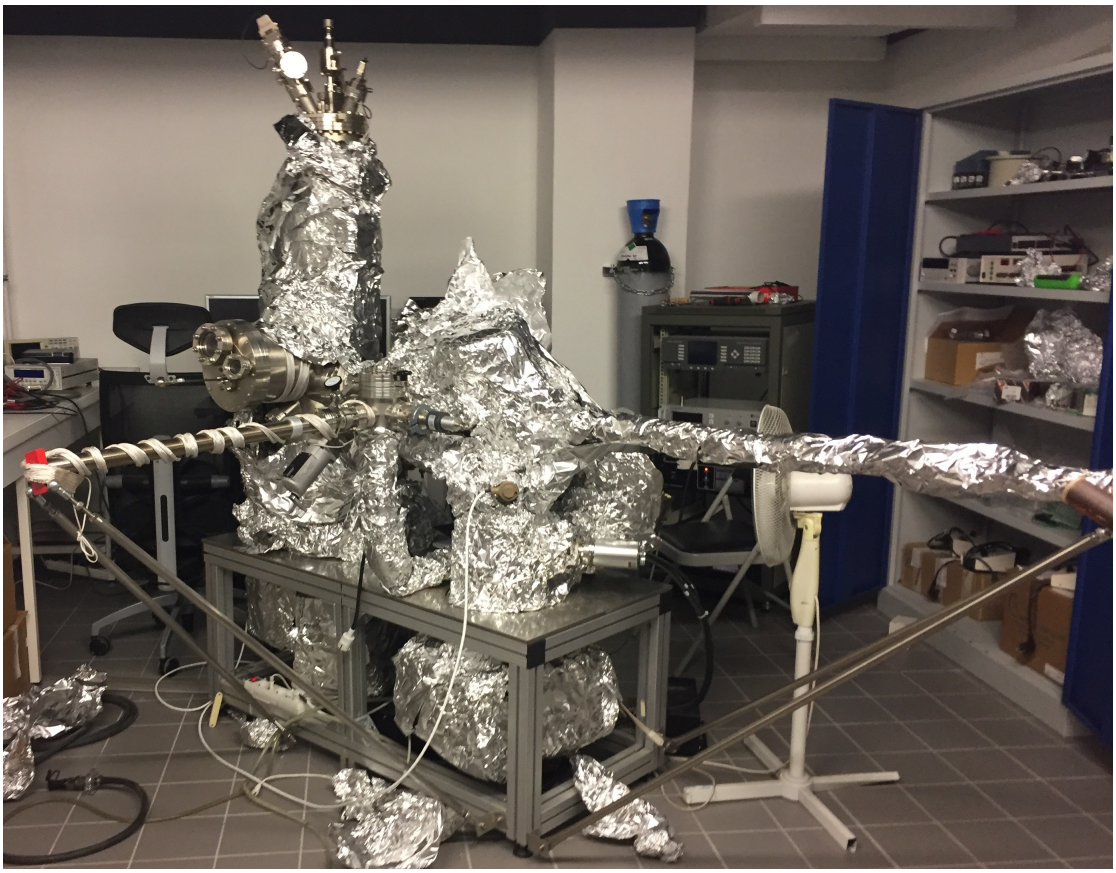

Figure 2.11: Photograph of the LT Omicron STM setup.

2.4.3 Preparation of the samples

Cleaving the samples.

In this subsection, we explain how both the samples and the tips we worked with were prepared. During this thesis, we observed crystals which where grown outside the set-up, either at the Institut des Matériaux Jean Rouxel in Nantes for the $(LaSe)_{1,14}(NbSe_2)_2$ crystals, or in Laboratoire de Physique des Solides, Orsay for the $(Sr_{(1-x)}La_x)_2IrO_4$ crystals. Most of the time, they did not need any additional *in situ* preparation other that cleaving to ensure that the observed surfaces were not contaminated in any way. In figure 2.12 **a** is shown a sample holder on which was glued a crystal. A cleaver is also glued on top of this crystal. Both sample and cleaver were glued using EPOTEK EE129-4, an epoxy which dries at ambient temperature to prevent heating up potentially fragile crystals.

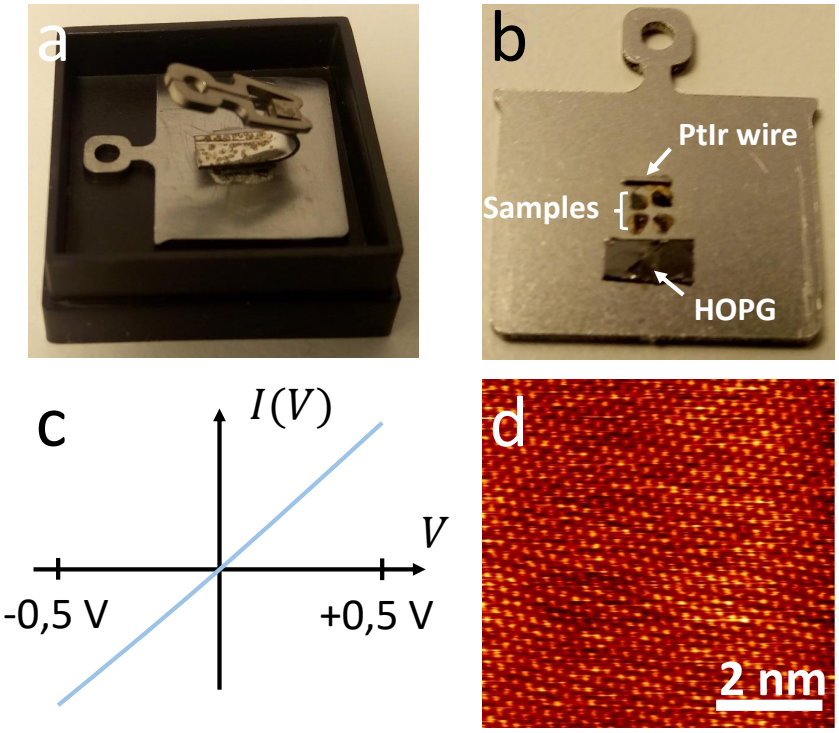

Figure 2.12: **a**. Cleaver glued on top of a $(LaSe)_{1,14}(NbSe_2)_2$ crystal. The cleaver can be handled with a wobble-stick and thus can be taken out of the set-up. The cleaving occurs *in situ* and ensure cleanliness of the surface of the sample. **b**. Typical sample holder organization for the experiments that were carried out on LT Omicron STM. **c**. When the measured $I(V)$ spectra are linear over a big enough bias voltage range, it means that the tip is featureless and good for spectroscopy measurements. If the tip does not present such behavior, it is crashed into the Pt/Ir wire (see **b**). **d**. One checks that the tip presents nice atomic resolution on HOPG sample.

The tips that were used in this thesis were made out of Pt80%Ir20% wire and simply cut with scissors to make their termination sharp enough. Pt80%Ir20% are indeed known to be suited to both topography and spectroscopy measurements. In figure 2.12 **b** is shown the typical organization of a sample holder for experiments performed on LT Omicron STM. A Pt/Ir wire and a graphite (HOPG) samples are glued next to the samples of interest. Glueing all those elements together on the same sample holder makes the treatment of the tip much easier. The Pt80%Ir20% tip is crashed onto the Pt/Ir wire and $I(V)$ spectroscopy is performed. When the spectra have the linear shape represented in figure 2.12 **c**, it means that both tip and wire are metallic and we conclude that the tip is featureless, which is necessary to ensure that the dI/dV spectra are proportional to the local density of states. In addition to being good in spectroscopy, the tip must also be able to image surfaces with atomic resolution. In order to verify the last point, one finally performs imaging on HOPG. This procedure was applied prior to all the following measurements : the whole study of doped iridate compound $(Sr_{(1-x)}La_x)_2IrO_4$, and the quasiparticle interferences observed in the normal phase of $(LaSe)_{1,14}(NbSe_2)_2$.

Pb deposition.

As is will be shown in 3.6, in a series of experiments, we deposited Pb on top of $(LaSe)_{1,14}(NbSe_2)_2$ in order to see the effect of non-magnetic impurities on superconductivity. In order to avoid pollution, the standard procedure consists in first degassing the Pb source

without any sample present in the preparation chamber (the power is fixed at 2/3 of the power used during evaporation). This preliminary step allows the potential oxidation of the sources to be eliminated and guarantees a cleaner final deposition. We deposited Pb *via* evaporation. The principle of evaporation is the following : a current flows into a filament in vicinity to a crucible filled with a clean Pb source. A voltage difference applied between the filament and the crucible accelerates the electrons emitted by the filament. Such electrons then collide the crucible and heat it sufficiently for Pb to evaporate (Pb starts to evaporate at $327,5°C$). Since the crucible is oriented towards the sample, Pb atoms are deposited on top of the $(LaSe)_{1,14}(NbSe_2)_2$ surface. In the experiment presented at the end of subsection 3.6.5, $0,47$ monolayer of Pb was deposited on the superficial $NbSe_2$ layer[6] of by applying a bias voltage of 800 V between the crucible and the filament and flowing a $1,78$ A current in the filament, resulting in a $0,66$ nA measured flux current[7].

[6]Pb and $NbSe_2$ have approximatively the same lattice constants such that in one monolayer of $NbSe_2$ there is the same number of Nb atoms than in a Pb monolayer.

[7]This current corresponds to the number of ionized Pb emitted per unit of time. This value can be converted into a Pb depositing rate by performing a calibration with the quartz crystal microbalance.

Chapter 3

Quasi-2D physics in a misfit heterostructure

In this chapter, we present a STM/STS study of misfit transition metal dichalcogenide (TMD) compound $(LaSe)_{1,14}(NbSe_2)_2$. This material is a parent compound of TMD 2H-$NbSe_2$ and shares many physical properties with it. $(LaSe)_{1,14}(NbSe_2)_2$ indeed is an heterostructure made out of a stacking of trigonal prismatic **$NbSe_2$ bilayers** and rock-salt LaSe layers. Also, just as in bulk 2H-$NbSe_2$, the $NbSe_2$ layers are van der Waals bonded. Similarly to 2H-$NbSe_2$, at low enough temperature, $(LaSe)_{1,14}(NbSe_2)_2$ enters a regime where both a lattice charge modulation and superconductivity coexist. Although being a bulk material, $(LaSe)_{1,14}(NbSe_2)_2$ presents 2D features, such as a strong Ising spin-orbit coupling, just as in few layers $NbSe_2$.

In addition to all those shared properties with 2H-$NbSe_2$, $(LaSe)_{1,14}(NbSe_2)_2$ is an incommensurate material. The only symmetry operation which leaves the whole structure unchanged is the identity, making $(LaSe)_{1,14}(NbSe_2)_2$ even more delicate to address. Before presenting our experimental results, it is necessary to understand the physics at play in these systems. The first section of this chapter is thus dedicated to the physics of 2H-$NbSe_2$, which has been known and intensively studied for decades, while $(LaSe)_{1,14}(NbSe_2)_2$ was hardly studied at all since the 1990's. In the second section, the crystal structure of $(LaSe)_{1,14}(NbSe_2)_2$ will be presented in great details and compared to STM topographic data. In the third part of this chapter, we present STS measurements performed in the normal phase of $(LaSe)_{1,14}(NbSe_2)_2$. We discuss and compare our data to DFT calculations results. The fourth section focuses on theoretical predictions of unconventional/topological superconductivity in parent monolayer TMD compounds. Finally, we discuss experimental data obtained in the superconducting phase of $(LaSe)_{1,14}(NbSe_2)_2$.

3.1 Tuning the electronic properties of $2H - NbSe_2$

2H-$NbSe_2$ is a transition metal dichalcogenide (TMD) known for housing several interesting electronic features. As is will be shown in this section, it is possible to tune the electronic properties of 2H-$NbSe_2$ by changing a certain number of its intrinsic parameters such as : the strain, the degree of disorder, the number of $NbSe_2$ layers (or dimensionality) and the doping level. We will see that $(LaSe)_{1,14}(NbSe_2)_2$ behaves in many aspects as 2H-$NbSe_2$ for which those parameters were modified. It is why this chapter is dedicated to the physics of 2H-$NbSe_2$ submitted to such perturbations.

The structure of 2H-$NbSe_2$ is represented in figure 3.1. It consists in an alternation of $NbSe_2$ bilayers with trigonal prismatic structure and separated by van der Waals gaps. The unit cell (a, b, c) is superimposed on the structure.

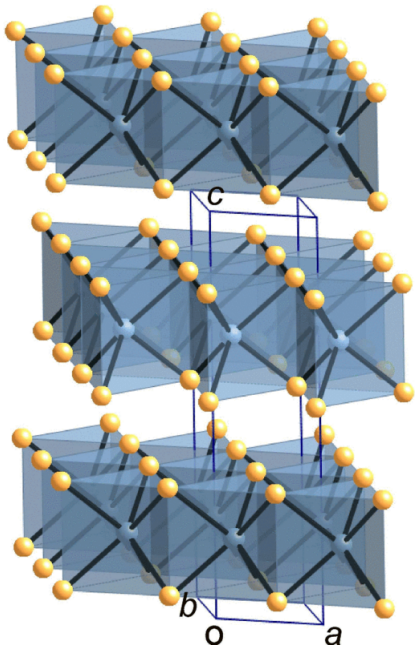

Figure 3.1: Bulk 2H-$NbSe_2$ consists in a stacking of $NbSe_2$ bilayers ($c = 12,55$ Å). Each $NbSe_2$ layer has a trigonal prismatic structure. The Nb atoms (blue spheres) sit at the nodes of a hexagonal lattice of lattice parameters $a = b = 3,44$ Å. Each Nb atom lies at the center of a prism which six apexes are Se atoms (yellow spheres). Figure adapted from ref. [77].

3.1.1 Charge density wave order

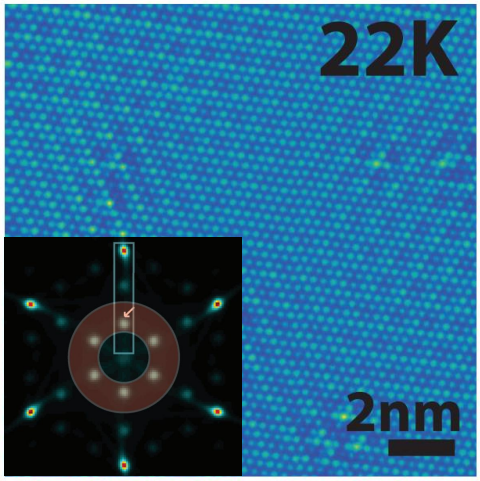

Figure 3.2: STM image of the 3×3 CDW in 2H-$NbSe_2$. The CDW reciprocal wave vectors can be seen in the Fourier transform of this image (taken from ref [78]).

The first noticeable phenomenon encountered in 2H-$NbSe_2$ is its charge density wave (CDW) order [78]. A CDW is a periodic reorganization of charge in a crystal. It appears below a critical temperature, T_{CDW}. The period of this additional charge modulation is greater that the period of the lattice in the unperturbed phase (above T_{CDW}). Historically, the existence of CDWs was predicted Peierls in atomic chains. In the Peierls model, thanks to the nesting properties of the Fermi surface of a half-filled 1D lattice with only first neighbour hopping, one indeed expects an electronic kinetic energy gain in atoms dimerization, and thus, the appearance of

a charge surmodulation with a new periodicity, twice as long as the one of the unperturbed lattice. However, it was shown that this simple picture cannot explain the presence of CDW orders in materials when the dimension of the system is 2 or 3, and most of CDWs can rather be understood in terms of strong coupling between the electrons and the lattice known as electron-phonon coupling [78, 79, 80].

Bulk 2H-$NbSe_2$ exhibits a 3×3 CDW below $T_{CDW} = 33,5K$. A STM topography map of the surface of 2H-$NbSe_2$ displaying this 3×3 charge modulation is shown in figure 3.2. The modulation occurs in all three directions of the hexagonal lattice of $NbSe_2$. We thus speak of 3Q charge order. This can also be seen in reciprocal space (the Fourier transform of the topography map is shown in the inset of figure 3.2) where 6 spots are located at one third of the distance of the 6 Bragg peaks (actually the spots do not lie exactly at one third of the Bragg meaning that the charge modulation is incommensurate). If the modulation was only occurring along one direction, we would be speaking of 1Q charge modulation.

3.1.2 Superconducting order

The second remarkable electronic phenomenon observed in 2H-$NbSe_2$ is superconductivity below $T_{SC} = 7,2K$ [77]. The origin of superconductivity has already been discussed in chapter 1. In the case of a conventional superconductor such as 2H-$NbSe_2$, electron-phonon coupling is also responsible for the formation of Cooper pairs. However, multigap superconductivity was observed in 2H-$NbSe_2$ leading to deviations from a pure single-gap BCS description [77, 35, 81]. In figure 3.3, one can see two distinct spectroscopic signatures (Δ_1 and Δ_2) giving rise to an overall non-BCS-like dI/dV spectrum.

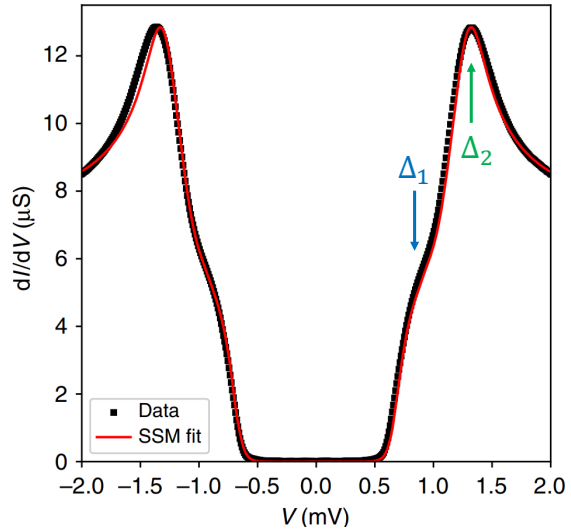

Figure 3.3: dI/dV spectrum taken on bulk 2H-$NbSe_2$ and displaying two-gap superconductivity (taken from ref [35]).

Such spectroscopic features in the measured differential conductance spectra were first interpreted in terms of a continuous gap distribution [82]. In the STM/STS study of ref. [77], the authors rather speak of two-gap superconductivity, one gap developing around the K Nb pockets of the Fermi surface of 2H-$NbSe_2$ because of strong electron-phonon coupling and the other developing around the Γ Nb pockets by mean of quasiparticle inter-band scattering. To add even more complexity, I. Guillamon *et al.* exhibited in a series of STM/STS measurements atomic-scale modulations of the superconducting gap of 2H-$NbSe_2$, suggesting an anisotropic nature of the gap in reciprocal space [81].

Interestingly, similar tunnelling selectivity effects as the ones observed in MgB_2 (see sub-

section 2.2.2) occur in 2H-$NbSe_2$ [77]. In figure 3.4, one sees that depending on the tip-sample tunneling geometry, the orbital selectivity changes and favors either the observation of the small gap or of the large gap. It is important to keep this last point in mind since, in section 3.6, we will interpret some of our results obtained in parent compound $(LaSe)_{1,14}(NbSe_2)_2$ in terms of tunnelling selectivity.

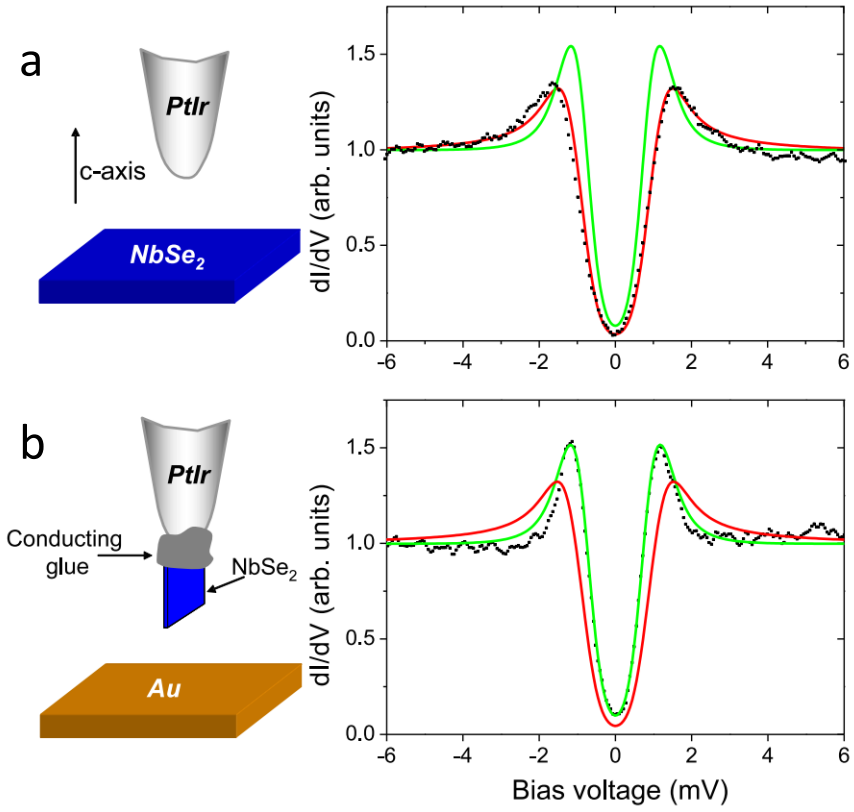

Figure 3.4: This figure illustrates the effect of tunnelling selectivity on the measured differential conductance spectra. **a**. In black is represented an experimental dI/dV spectrum taken on bulk 2H-$NbSe_2$ with tunnelling oriented along the c-axis of 2H-$NbSe_2$. **b**. In black is represented an experimental dI/dV spectrum taken on bulk 2H-$NbSe_2$ with tunnelling oriented along the a(b)-axis of 2H-$NbSe_2$. Depending on the tunnelling configuration, one clearly sees that one gap is observed when the other is not. In green (red) is the theoretical expectation for 100% tunnelling small (big) gap (taken from ref [77]).

Remark: The coexistence of both phonon-mediated superconductivity and CDW in 2H-$NbSe_2$ raises the question of the interplay between the two orders. This problematic is at the center of many of the studies presented in this section.

The origin and nature of both CDW and superconductivity can be addressed by tuning several $NbSe_2$ intrinsic parameters. In what follow, we will briefly expose those parameters and the consequences their modifications can have on the electronic properties of $NbSe_2$.

3.1.3 Effects of strain

Lattice compression or dilation is likely to change the electronic properties of 2H-$NbSe_2$. In ref. [83], Shang Gao *et al.* pasted a crystal of bulk 2H-$NbSe_2$ on top of a silica plate. Due to the

different thermal expansion coefficients of 2H-$NbSe_2$ and silica respectively, cooling down the system from room temperature to 4 K generated strain in the attached 2H-$NbSe_2$ sample. STM measurements were then performed under those conditions of low temperature and substantial strain going up to 2,5% in some areas. The main result of this study is the observation of a strain-induced phase transition between 3Q CDW of periodicity $3a$ and a mix of 1Q CDW of periodicity $4a$ and 3Q CDW of periodicity $2a$. Since strain acts on the lattice, it is not surprising that phonon-mediated electronic feature such as CDW is modified. Figure 3.5 illustrates the strain-induced phase transition between different types of CDWs in 2H-$NbSe_2$. Superconductivity is however unaddressed in this paper.

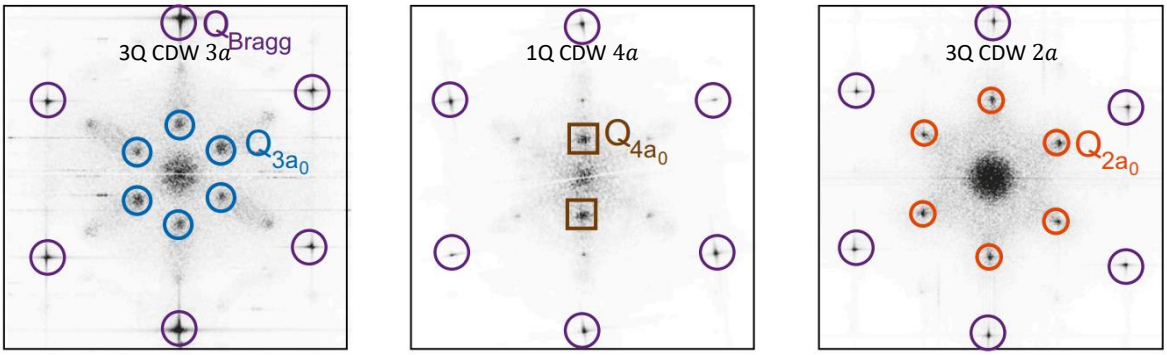

Figure 3.5: Fourier transform of topography maps taken in areas with different strain values. Depending on the strain, the structure either goes a $3Q3a$, a $1Q4a$ or a $3Q2a$ CDW phase (from ref. [83]).

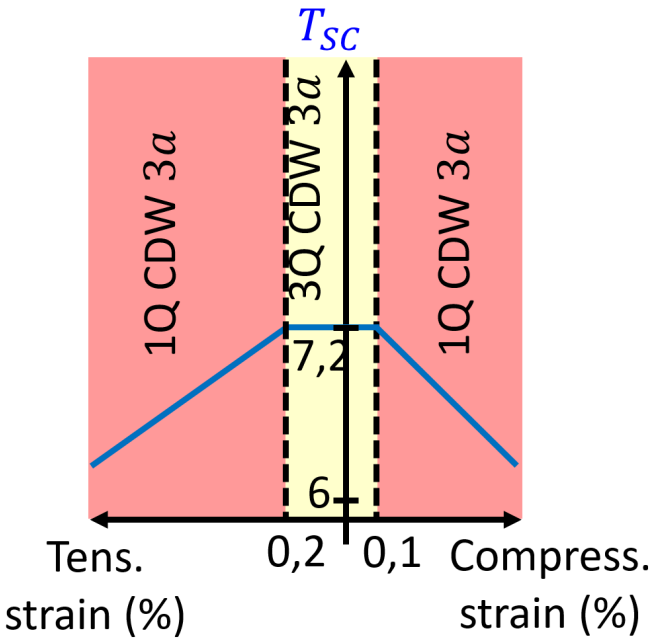

Figure 3.6: Modification of normal to superconducting transition induced by controlled tensile and compressive strain. In blue is represented the superconducting critical temperature as a function of strain. The black dotted lines separate different CDW phases (from ref. [84]).

In ref. [84], tensile as well as compressive strain (0% to 0,7%) was generated on bulk 2H-

$NbSe_2$ in a controlled way with the help of a pair of stacks of shear piezoelectric actuators (their measurements are summarized in figure 3.6). Transport measurements showed that up to a certain critical strain value (0,1% for compressive strain, 0,2% for tensile strain), the superconducting critical temperature is unmodified, suggesting peaceful cohabitation between CDW and superconductivity. Nevertheless, when one exceeds the critical strain value, superconductivity weakens with increasing strain. Theoretical calculations show that this sudden change coincides with a phase transition between a 3Q CDW phase at low strain to a 1Q CDW phase for higher strain. The CDW periodicity yet remains equal to $3a$. Depending of the nature of the CDW, superconductivity and CDW might or not be in competition.

3.1.4 Effects of disorder

Disorder can also have an impact on the electronic properties of 2H-$NbSe_2$. In ref. [85], Cho, K. *et al.* artificially introduced disorder in bulk 2H-$NbSe_2$ samples through electron radiation. Their conclusion is somehow similar to the one of ref. [84] for no correlations between superconductivity and CDW order are observed under an estimated critical disorder ($1C/cm^2$ of residual resistivity), while above this critical value, both superconductivity and charge modulation weaken jointly (see figure 3.7).

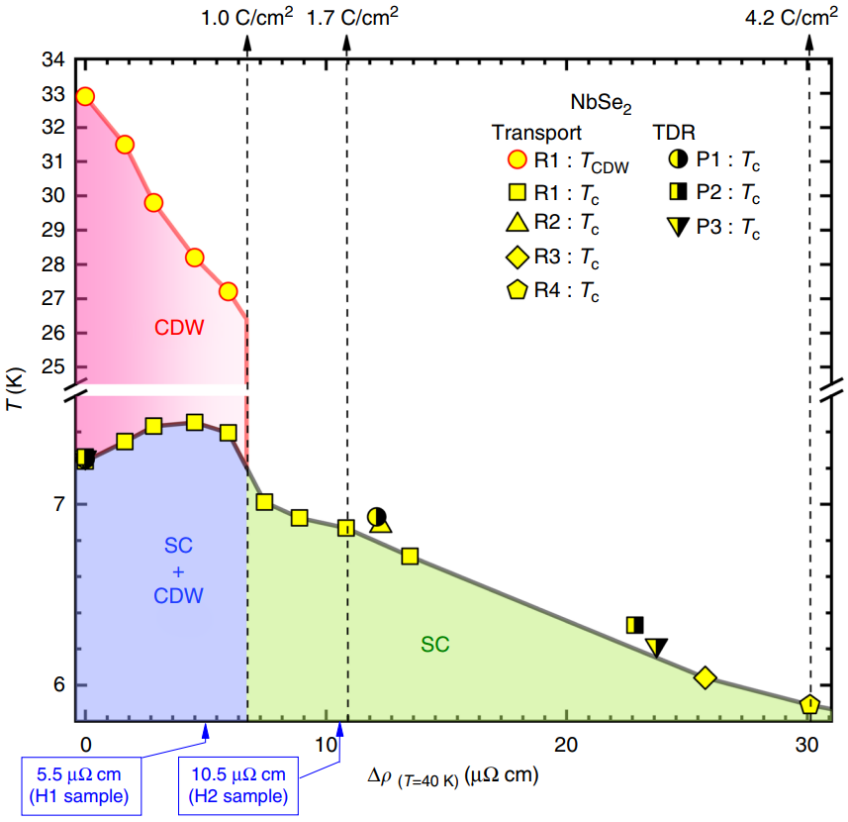

Figure 3.7: Temperature *vs* residual resistivity (disorder) phase diagram of electron-radiated disordered 2H-$NbSe_2$ (from ref. [85]).

3.1.5 Effects of doping

Doping is yet another parameter likely to modify the physical properties of 2H-$NbSe_2$. In ref. [86], electron-donating atoms of Cu were intercalated in between neighbouring $NbSe_2$ layers. In this work, Huixia Luo *et al.* observed a decrease of superconducting critical temperature

of Cu_xNbSe_2 with increasing level of Cu doping x through transport measurements (see figure 3.8 **a**). Electron diffraction experiments also clearly support a joint weakening of CDW order because of reduced sharpness of 3×3 peaks meaning reduced in-plane coherence length for the charge modulations.

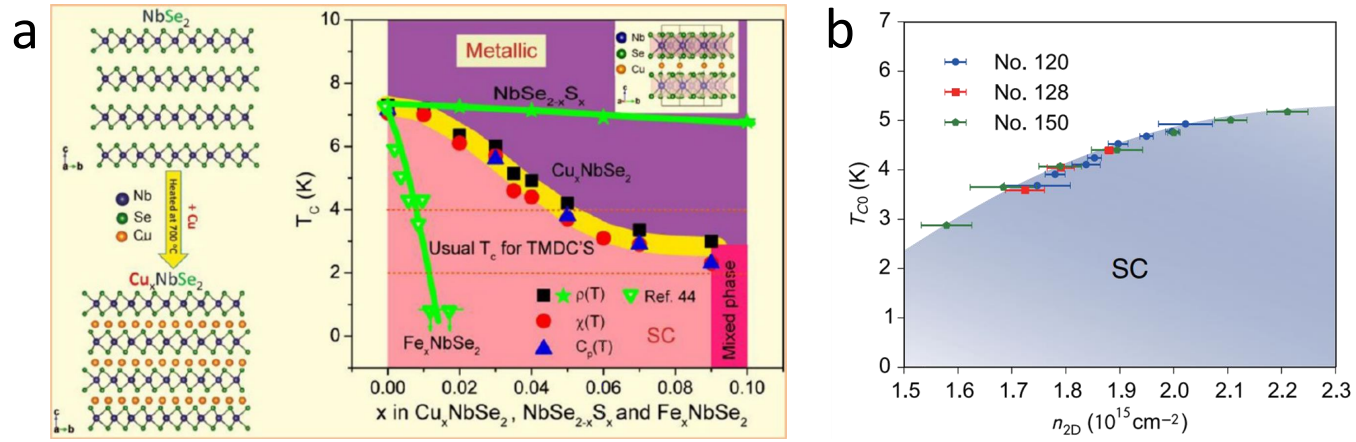

Figure 3.8: **a**. Critical superconducting temperature vs doping level in Cu_xNbSe_2 (from ref. [86]). T_C goes down with increasing electron doping. **b**. Critical superconducting temperature *vs* carrier density (doping level) in bilayer 2H-$NbSe_2$ (from ref. [87]). T_{C0} goes up with increasing electron doping.

One can also achieve doping by ionic liquid gating. This was done in ref. [87], where bilayer $NbSe_2$ was electron and hole doped by electrostatic gating. In this study, they have been able to reversibly tune the carrier density of 6.10^{14} electrons per cm^2 namely 30% of the intrinsic density of bilayer 2H-$NbSe_2$, achieving to shift the Fermi level of approximatively $+0,07$ eV. Once again, the conclusion seems to call for a joint enhancement of superconductivity and CDW since by tuning the Fermi level position from hole-doped to electron-doped regime, superconducting critical temperatures go from $2,8$ K to $5,1$ K, and the characteristic drop around T_{CDW} in Hall coefficient *vs* temperature curves vanishes (see figure 3.8 **b**).

3.1.6 Reducing the number of $NbSe_2$ layers

Doping is not the only parameter that was changed in ref. [87]. The studied sample was indeed bilayer $NbSe_2$ and not bulk 2H-$NbSe_2$. Modifying the dimensionality of the sample, *i.e.* the number of $NbSe_2$ layers is also another fruitful approach. For example, by varying $NbSe_2$ samples thicknesses from bulk to single layer limit, a competition between electron-phonon-driven CDW and superconducting orders was exhibited in ref. [88]. Reducing the number of layers induced a decrease of T_{SC} and an increase of T_{CDW} up to 145 K in monolayer $NbSe_2$, or so to say way, higher than the $33,5$ K of the bulk (see figure 3.9).

Moreover, approaching the 2D limit also implies breaking inversion symmetry and consequently the appearance of a strong Ising spin-orbit coupling. This exotic spin-orbit coupling gives rise to spin-momentum locking in the out of plane direction and also to unconventional Ising superconducting pairing [33, 34, 35] but this problematic was already mentioned in section 1.3.3 and will be explored in more details in section 3.4.

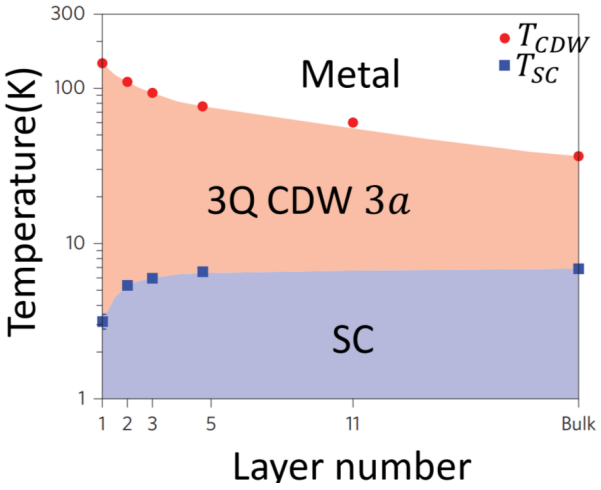

Figure 3.9: Competition between superconducting and CDW orders exhibited across 2H-$NbSe_2$ samples with thickness going from single layer to bulk (from ref. [88]).

One can wonder whether the multigap physics present in bulk $NbSe_2$ (which was mentioned previously in this chapter) remains with decreasing number of layer. In their article, T. Dvir *et al.* measured dI/dV spectra of few-layer superconducting $NbSe_2$ samples using van der Waals tunnel junctions [35]. They observe multigap superconductivity down to their thinner samples (namely 3 layers $NbSe_2$). Moreover, they observe a robustness of the large superconducting gap to strong in-plane magnetic fields, which is in favor of Ising spin-orbit coupling physics (see sections 1.3.3 and 3.4), while the small gap is killed. This last example illustrates how superconducting order parameters of different natures can coexist in few layer TMDs.

Interestingly, and as it will be shown in the following sections, $(LaSe)_{1,14}(NbSe_2)_2$ can in first approximation be seen as reduced-dimensionality electron-doped 2H-$NbSe_2$ with disorder and strain, possibly making it an ideal platform for studying the electronic properties of quasi-2D transition metal dichalcogenides.

3.2 Structure of misfit compound $(LaSe)_{1,14}(NbSe_2)_2$

$(LaSe)_{1,14}(NbSe_2)_2$ is a misfit layered compound consisting in alternation of TMD 2H-$NbSe_2$ bilayers with trigonal prismatic structure and of rock-salt LaSe bilayers. This material was almost not studied at all since the 90's and its structure is known from X-rays experiments carried out in 1993 [89]. Unlike in bulk 2H-$NbSe_2$ the lattice of $NbSe_2$ layers is not exactly hexagonal but rather rectangular centered as it is slightly compressed along the $\mathbf{a_2}$ direction. The angle represented in figure 3.10 **d** is $\theta = 59,6°$. The lattice vectors of the primitive cell of $NbSe_2$ layers are $\mathbf{a_1}$ ($\| \mathbf{a_1} \| = a_1 = 3,457$ Å) and $\mathbf{a_2}$ ($\| \mathbf{a_2} \| = a_2 = 3,437$ Å), respectively. The LaSe bilayers possess a square lattice of lattice vectors $\mathbf{b_1}$ and $\mathbf{b_2}$ ($\| \mathbf{b_1} \| = \| \mathbf{b_2} \|$). In what follows, it will be more convenient to adopt a centered cell of lattice vectors $\mathbf{b_1}$ ($\| \mathbf{b_1} \| = b_1 =$ 6 Å) and $\mathbf{a_2}$ for the $NbSe_2$ layers. Given this last remark, since both $NbSe_2$ and LaSe layers share the same $\mathbf{b_1}$ lattice vector, the material is commensurate in the $\mathbf{b_1}$ direction. Nevertheless, the ratio between the norms of $\mathbf{a_2}$ and $\mathbf{b_2}$ vectors, which share a common direction, is an irrational number ($\| \mathbf{b_2} \| / \| \mathbf{a_2} \| = 1,751\ldots$) making $(LaSe)_{1,14}(NbSe_2)_2$ incommensurate in the $\mathbf{a_2}$ direction. However, $\| \mathbf{b_2} \| / \| \mathbf{a_2} \| \simeq 7/4$ such that $(LaSe)_{1,14}(NbSe_2)_2$ is « almost » periodic in the $\mathbf{a_2}$ direction with an approximate commensurate lattice vector $\mathbf{m}$ ($\| \mathbf{m} \| = 7 \| \mathbf{a_2} \| \simeq 4 \| \mathbf{b_2} \|$). The lattice parameter in the out-plane-direction is $\mathbf{c}$ ($\| \mathbf{c} \| = c = 36,5$ Å). The crystal

structure seen from different angles in represented in figure 3.10.

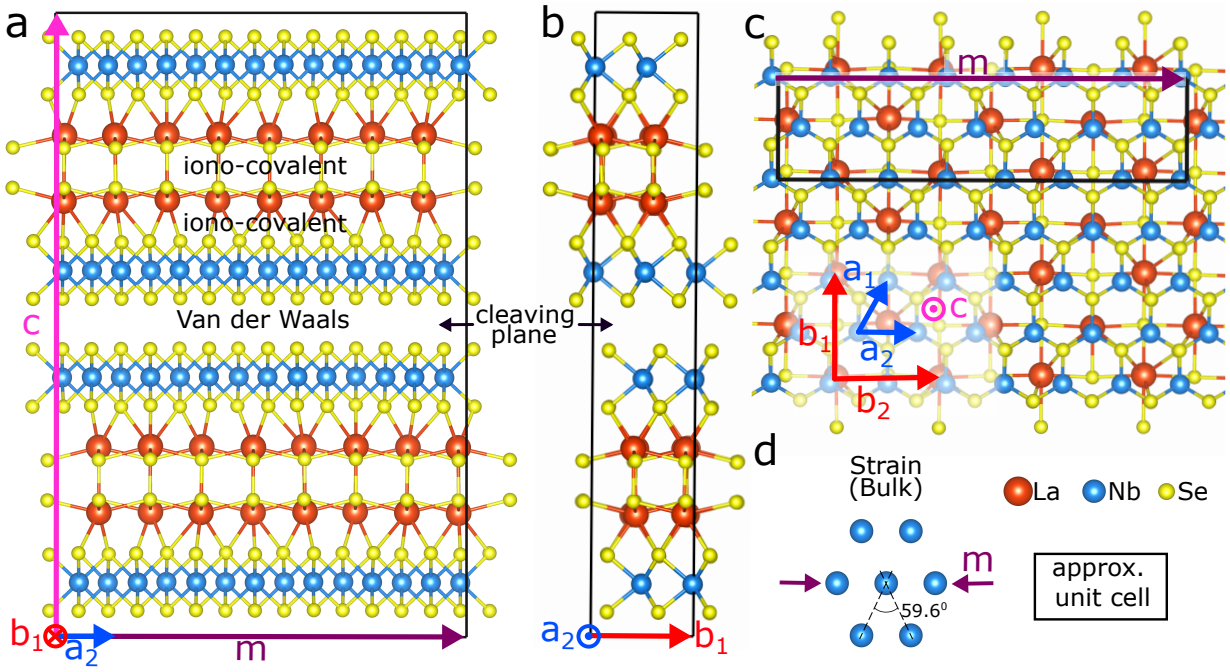

Figure 3.10: Crystal structure of $(LaSe)_{1,14}(NbSe_2)_2$ seen from different perspectives. **a**. Side view. **b**. Side view orthogonal to **a**. **c**. Top view. The Nb atoms are represented by blue balls, the Se atoms are represented by yellow balls and the La atoms are represented by red balls. The black rectangle represents the approximate unit cell considered in DFT calculations since the material is not exactly commensurate. **d**. Cartoon illustrating the compression along the misfit axis for the $NbSe_2$ lattice.

One can write all the lattice vectors on $(\mathbf{i}, \mathbf{j})$ orthonormal basis :

$$\begin{cases} \mathbf{a_1} = a_1(cos(\theta/2)\mathbf{i} + sin(\theta/2)\mathbf{j}), \\ \mathbf{a_2} = a_2\mathbf{j}, \\ \mathbf{b_1} = b_1\mathbf{i}, \\ \mathbf{b_2} = b_2\mathbf{j}, \\ \mathbf{m} = 7\mathbf{a_2} = 4\mathbf{b_2}, \end{cases} \tag{3.1}$$

Such that in reciprocal space after a short calculation :

$$\begin{cases} \mathbf{a_1^*} = \dfrac{2\pi}{a_1 cos(\theta/2)}\mathbf{i}, \\ \mathbf{a_2^*} = \dfrac{2\pi}{a_2 cos(\theta/2)}(-sin(\theta/2)\mathbf{i} + cos(\theta/2)\mathbf{j}), \\ \mathbf{b_1^*} = \dfrac{2\pi}{b_1}\mathbf{i}, \\ \mathbf{b_2^*} = \dfrac{2\pi}{b_2}\mathbf{j}, \\ \mathbf{m}^* = \dfrac{2\pi}{7a_2}\mathbf{j} = \dfrac{2\pi}{4b_2}\mathbf{j}, \end{cases} \tag{3.2}$$

To fully explain the spectroscopic results that will be presented in section 3.4, theoreticians from our group (Matteo Calandra, Marco Campetella and Cesare Tresca) carried out first principles Density Functional Theory (DFT) calculations using Quantum expresso *ab initio* software. In order to perform such calculations, one has to consider a periodic system. Since $(LaSe)_{1,14}(NbSe_2)$ is incommensurate, it is by definition not periodic along the misfit direction

m. Nevertheless, the approximate commensurate lattice vector **m** is good enough to consider the system periodic and of unit cell $(\mathbf{m}, \mathbf{b_1}, \mathbf{c})$. This unit cell is represented by a black rectangle on figure 3.10. Here, we will only present the DFT calculations results regarding the crystal structure of $(LaSe)_{1,14}(NbSe_2)_2$. The obtained band structure will be commented and compared to experimental data in section 3.4. In this framework, it is possible to numerically obtain the full structure of $(LaSe)_{1,14}(NbSe_2)_2$ and in particular to exhibit the nature of the bonding between different layers. After relaxation, significant deviations from perfect rock-salt structure appear within the LaSe layers (see figure 3.11).

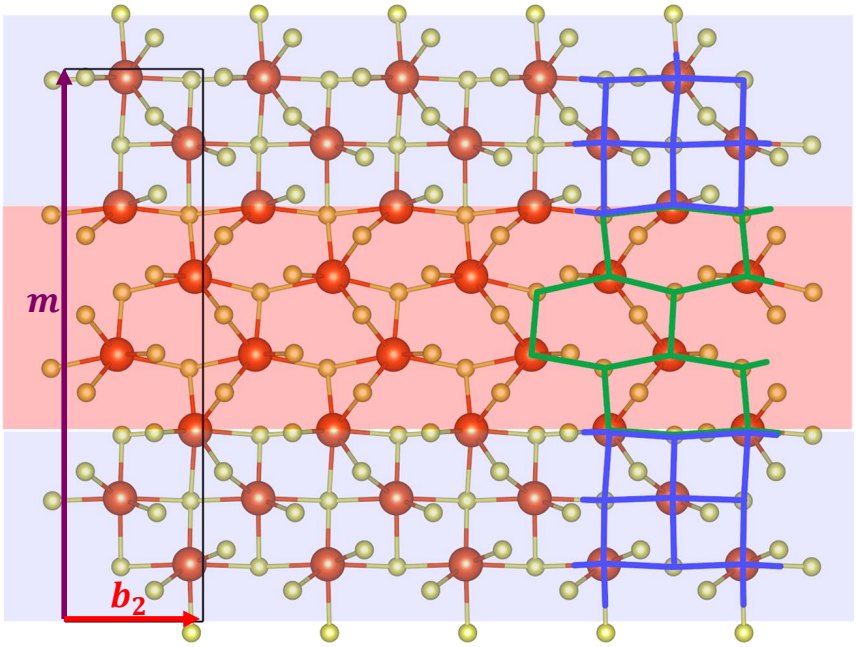

Figure 3.11: Focus on one LaSe layer (top view afer removal of Nb atoms). Deviations from perfect rocksalt structure can be seen. Some La atoms tend to gather (blue grids) while others tend to move part from each other (green grid).

DFT calculations show that a significant but incomplete charge transfer occurs between LaSe and $NbSe_2$ layers, effectively doping the $NbSe_2$ layers, shifting the Fermi level to higher energies. Each Nb atom indeed receives $1,14/2$ electrons from the closer LaSe layer. The La atoms thus make a iono-covalent bonding with the closest Se atoms of the neighbouring $NbSe_2$ layer. Finally, similarly to bulk 2H-$NbSe_2$, the adjacent $NbSe_2$ layers are separated by a van der Waals gap. This later bond being the weakest in the whole structure, the samples cleave on a monolayer $NbSe_2$ terminated surface.

3.2.1 Incommensurability probed by STM

Now that we have a good idea of the structure of $(LaSe)_{1,14}(NbSe_2)_2$ thanks to X-Rays data, it is important to check that we indeed recover those structural features on STM topographic map. All the observed crystals were grown by Laurent Cario and Shunsuke Sasaki using iodine vapor transport technique in Institut des Matériaux Jean Rouxel (IMN) in Nantes. Their compositions were determined via EDX measurements and are in good agreement with expected stoichiometric ratios. The samples were cleaved at room temperature in ultra-high vacuum under a pressure of approximatively 8.10^{-11}mbar or low 10^{-11}mbar (depending on if the experiment was done on the LT Omicron STM or on M3 homemade microscope) directly before being loaded into the STM head.

Before actually looking at topographic data let us first present what can be expected beforehand. In figure 3.12 **a**. is represented a simulated hexagonal lattice reflecting the hexagonal lattice of Se at the surface. The modulus square of its Fourier transform is displayed right beneath in figure 3.12 **d**. Without any surprise the reciprocal lattice is also an hexagonal lattice but turned of 30°. In figure 3.12 **b**. is shown a simulated potential of periodicity $\| \mathbf{m} \| = 7 \| \mathbf{a_2} \|$ oriented in $\mathbf{a_2}$ direction meant to represent the incommensurate potential felt by the superficial $NbSe_2$ layer because of its interaction with the underlying LaSe layer. The corresponding modulus square Fourier transform can be seen in figure 3.12 **e**. For realism, the periodic potential was considered to possess several harmonics (namely second, third and sixth harmonics). The visible peaks in reciprocal space are aligned in the misfit direction and are located at $\mathbf{m}^*$, $2\mathbf{m}^*$, $3\mathbf{m}^*$ and $6\mathbf{m}^*$ wave vectors. Figure 3.12 **c**. represents the hexagonal lattice of **a** multiplied by the "incommensurate potential" of **b**. The corresponding Fourier transform in **f** presents both collections of peaks of **d**. and **e**. but also other peaks developing along the misfit direction starting from the Bragg peaks of hexagonal lattice. Those peaks are replica (or satellites) which lie at linear combinations of q-vectors typical of both signals. This typically appears once two periodic signals are modulated by one another. We will see that this simple cartoon actually describes rather faithfully the observations.

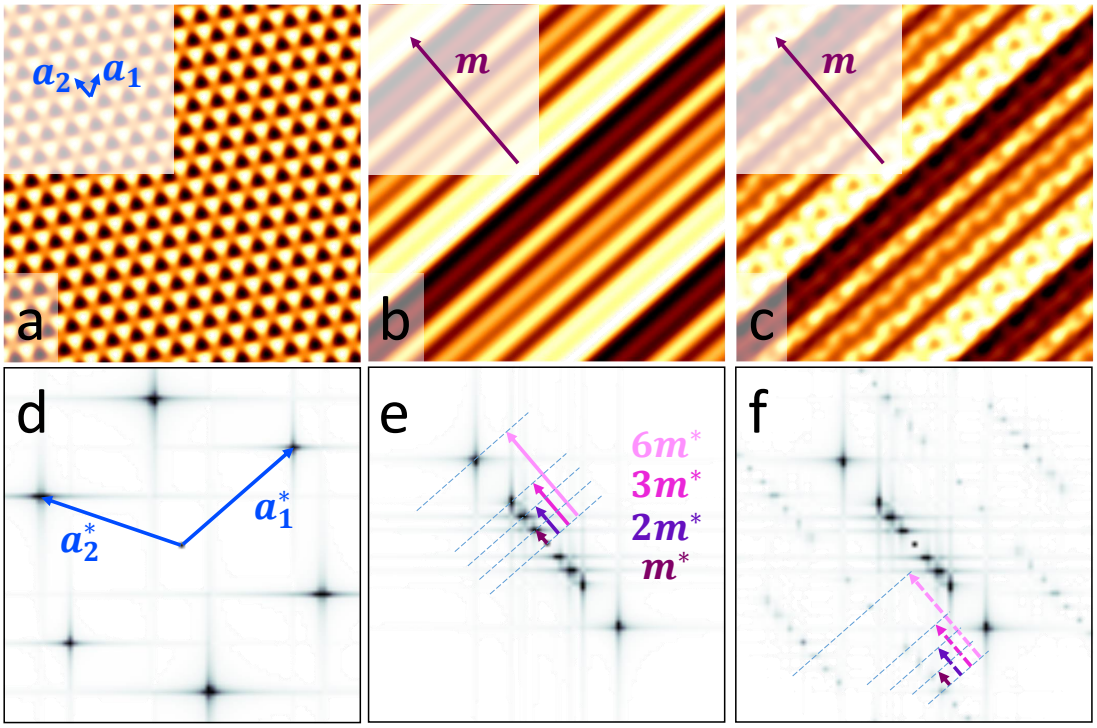

Figure 3.12: Simulated triangular lattice (**a**.), incommensurate potential with additional second, third and sixth harmonics (**b**.), and triangular lattice modulated by incommensurate potential ((**c**.). **d**., **e**. and **f**. Modulus square of the Fourier transforms of **a**., **b**. and **c**. respectively. Relevant lattice vectors and reciprocal lattice vectors are represented on all images.

A typical STM topography map of $(LaSe)_{1,14}(NbSe_2)_2$ surface is represented in figure 3.13 **a**. For simplicity, in the following, the rectangular centered lattice of $NbSe_2$ will be referred to as hexagonal. Since the surface is $NbSe_2$ terminated[1], the probed atoms are Se. The Se hexagonal lattice is clearly visible but one can also notice the presence of multiple additional

[1]It was already said that the samples cleave in between two adjacent van der Waals bonded $NbSe_2$ layers.

spatial modulations across the surface which are due to the interaction with the underlying LaSe layer. In order to properly characterize the origin of those modulations, the modulus of the Fourier transform of a similar but larger scale topographic image taken on the same area with same scanning angle is represented in figure 3.13 **b**. The Bragg peaks of the reciprocal lattice of $NbSe_2$ are highlighted by full dark-blue circles. The sharp peak circled in burgundy corresponds to the reciprocal approximate commensurate vector $\mathbf{m}^*$. It also gives the misfit direction represented by a burgundy arrow. The second, third and sixth harmonics of the approximate periodic misfit potential are highlighted by full purple, dark-pink and light-pink circles respectively. Other harmonics (fourth, fifth, seventh...) are never seen thus explaining the chosen signal construction in figure 3.12. The satellites replica starting from $NbSe_2$ Bragg peaks of both third and sixth harmonics are also observed and accented by dotted dark-pink and light-pink circles respectively. Our interpretation is that the structure factors of the material are such that the replica of $\mathbf{m}^*$ and $2\mathbf{m}^*$ can't be seen.

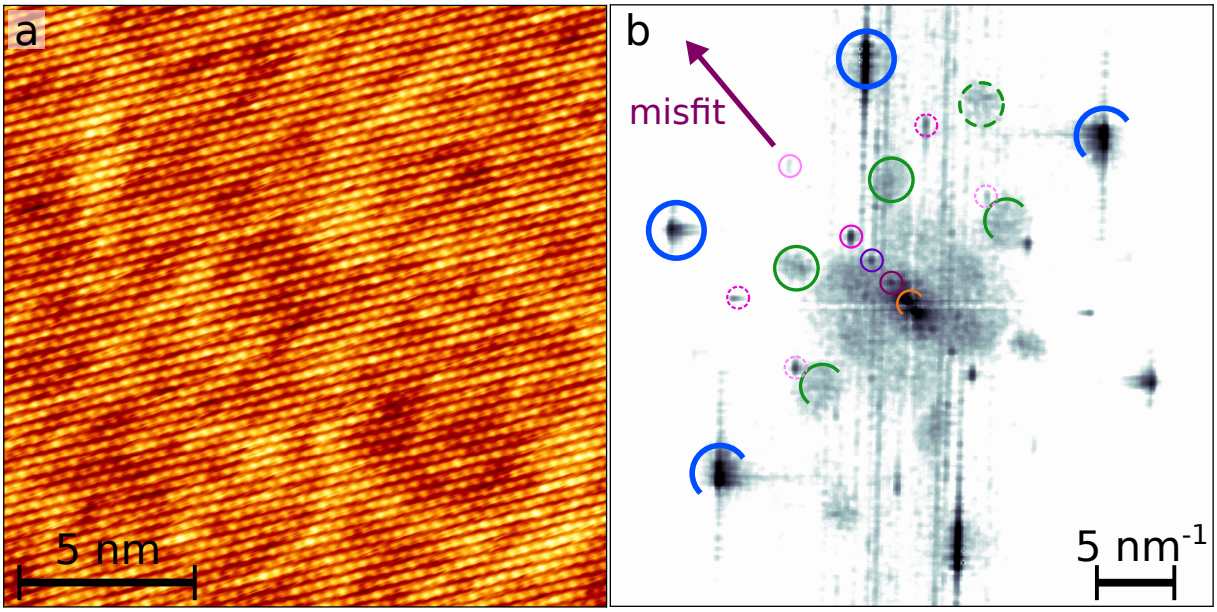

Figure 3.13: **a**. Topographic STM image of $(LaSe)_{1,14}(NbSe_2)_2$ surface. **b**. Modulus square of the Fourier transform of a larger scale topographic image. The full blue circles highlight the Bragg peaks of the hexagonal lattice of $NbSe_2$. The full burgundy circle (and purple, dark pink and light pink full circles) highlight the reciprocal lattice vector (and its second, third and and sixth harmonics, respectively). The full green circles highlight the 2×2 charge modulation. The orange half circle highlight higher order approximate incommensurate vectors. The dotted circles are replica of the peaks that were just mentioned.

Moreover, large and intense spots encircled in orange very close to Γ and aligned in the misfit axis suggest long-range modulations in the incommensurate direction. Such long-range modulations can be seen (highlighted by yellow oscillations) on figure 3.14 which represents the autocorrelation map of the same STM map that gave the Fourier transform of figure 3.13. These modulations render higher order approximate commensurate vectors. 7/4 is a fairly good incommensurate ratio but other ratios such as 30/17, 33/19, 37/21, 40/23 or 44/25 have a less than one percent difference with the proper ratio$\| \mathbf{b_2} \| / \| \mathbf{a_2} \| = 1,751$. The distance separating two adjacent long-range maxima is indeed of the order of $30a_2$. The approximate commensurate lattice parameter m is also visible on the autocorrelation map since dark lines (stressed by burgundy dotted lines) separated of $7a_2$ alternate the misfit direction.

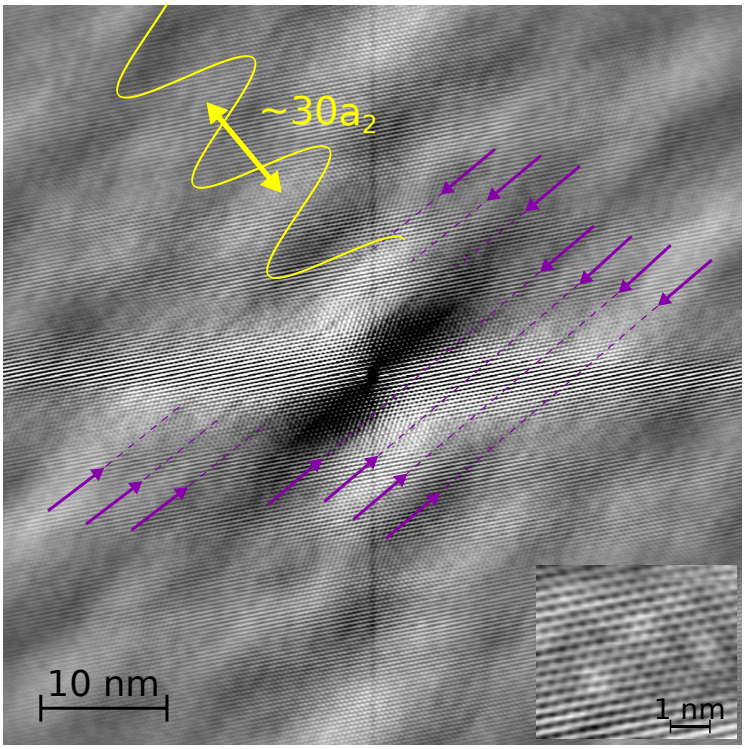

Figure 3.14: Autocorrelation map of a topographic STM image displaying long-range modulations interpreted as higher-order approximate commensurate ratios.

The signals presented so far can directly be deducted from the theoretical crystal structure supporting than we indeed are observing the right material. In addition to those, one can also observe other contributions. Let us now reconsider the Fourier transform image of figure 3.13 **b**. First, diffuse peaks (highlighted by green circles) lie at half the Bragg of the $NbSe_2$ hexagonal lattice. They express the presence a 2×2 charge modulation in the system. This charge order will be fully discussed further. Second, the halo surrounding Γ and quasi-reaching half the Bragg peaks can be interpreted as integrated QPIs spectroscopic signal but this will be the topic of the following section.

3.3 $(LaSe)_{1,14}(NbSe_2)_2$ as electron-doped single-layer $NbSe_2$

In this section, we will show by mean of quasiparticle interferences measurements compared to theoretical DFT calculations that $(LaSe)_{1,14}(NbSe_2)_2$ behaves as an electron-doped monolayer $NbSe_2$. We will also investigate the origin of the 2×2 charge modulation.

3.3.1 Scattering potentials in quasiparticle interferences

Quasi particle interferences are observed whenever there are scattering centers (see section 2.3). For example, in ref. [90], very clean samples of bulk 2H-$NbSe_2$ were studied via STM and such signal was never observed. On the contrary, in ref. [91], C. J. Arguello and collaborators intentionally introduced S impurities (S is isovalent to Se, thus no additional charge carriers are brought to the system), and could consequently performs very nice QPIs measurements. The STM image of figure 3.13 **a** does not present any visible defects such as vacancies, steps or dislocations. Such clean surfaces are representative of all the samples that were measured. Yet, as it was already mentioned, QPIs spectroscopic signal were even observed in topographic mode. QPIs are thus due to another kind of scattering potential. Everything suggests that incommensurability plays the role of disorder potential. Disorder and incommensurability are

indeed compatible as shown by the theoretical study of ref. [92] where incommensurability leads to localization but also in ref. [93] where specific heat measurements done in many incommensurate compounds revealed disordered glass-like behaviour.

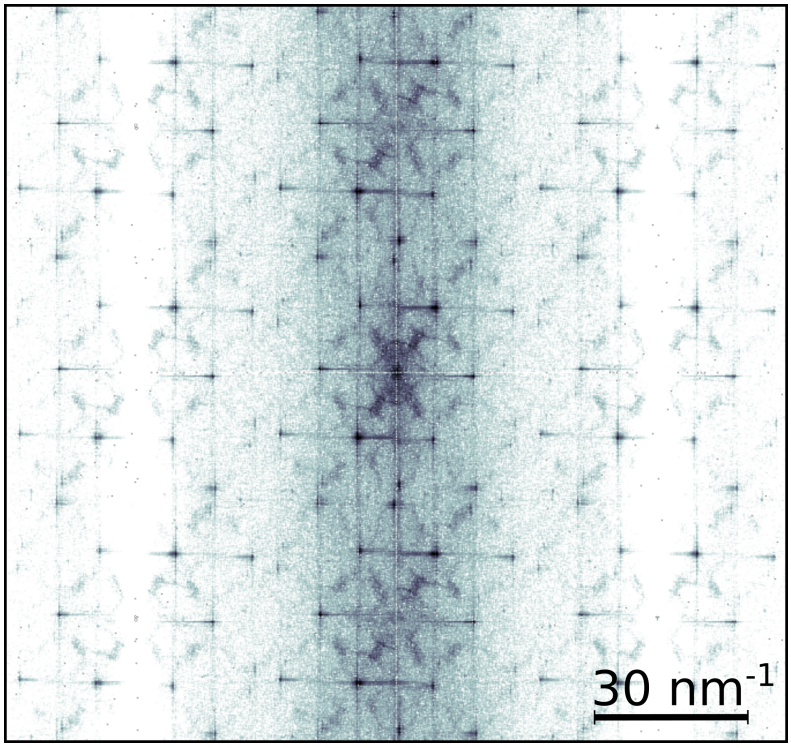

Figure 3.15: Modulus square of the Fourier transform of a topographic STM image performed at -20meV. In first approximation, it can be interpreted as a dI/dV map at Fermi energy.

Figure 3.15 represents the Fourier transform modulus of a topography map (where the misfit axis is vertical) taken at -20mV bias voltage. In figure 3.15, only electrons between 0meV and -20meV contributed to the total tunnelling current, or in other words, electrons reasonably close to Fermi level to consider it to be the Fourier transform modulus of a LDOS map at Fermi level. This will be supported later on since the band dispersion over [0meV,-20meV] is negligible. Given this last argument, the fact that the QPIs signal mostly develops along the misfit direction further supports the incommensurable disorder potential hypothesis. Apart from this observation, it is also possible to see many fine QPIs structures, but before interpreting them, we will first present the spectroscopic DFT results.

Remark : In the case of 3.13 **b**, electrons of energies varying from 0 meV to −200 meV contributed to the total tunnelling current, meaning that the spectroscopic halo around Γ is actually a mix between the QPIs patterns for all energies ranging from 0 meV to −200 meV.

3.3.2 Energy dispersion from DFT calculations

In order to numerically access the band structure of $(LaSe)_{1,14}(NbSe_2)_2$, the DFT calculations were performed on the last slab of $(LaSe)_{1,14}(NbSe_2)_2$ as shown in figure 3.16 **d**. The reason behind this is that such a slab is van der Walls interacting with similar slabs and is consequently almost electronically independent[2] The spectroscopic data are hence very likely to match faithfully the *ab initio* results. Moreover, given the great number of atoms present in the $(\mathbf{m}, \mathbf{b_1}, \mathbf{c})$

[2]The theoreticians verified beforehand that the band structure of the bulk was very similar to the one of the slab.

unit cell, dividing it by two can significantly reduce the full calculation time, but, the calculation still represents a quite heavy operation.

The band structure of $(LaSe)_{1,14}(NbSe_2)_2$ is represented in the approximate commensurate Brillouin zone on figure 3.16 **a** in which the red dots represent the La character of the bands[3]. The approximate commensurate Brillouin zone corresponding to the $(\mathbf{m}, \mathbf{b_1}, \mathbf{c})$ unit cell is represented and compared to the hexagonal Brillouin zone of $NbSe_2$ in figure 3.16 **c**. As it was said previously, a significant charge transfer occurs in $(LaSe)_{1,14}(NbSe_2)_2$, LaSe layers giving electrons to their neighbouring $NbSe_2$ layers. We will see in what follows that the band structure of $(LaSe)_{1,14}(NbSe_2)_2$ is actually similar to the one of monolayer $NbSe_2$ but rigidly shifted towards lower energies. The existing iono-covalent bonding between LaSe and $NbSe_2$ layers tends to decouple even more each $NbSe_2$ layers within a 2H-$NbSe_2$ bilayer. This suggests that the electronic structure of the material could actually be closer to the one electron-doped monolayer $NbSe_2$ than to the one electron-doped bilayer 2H-$NbSe_2$.

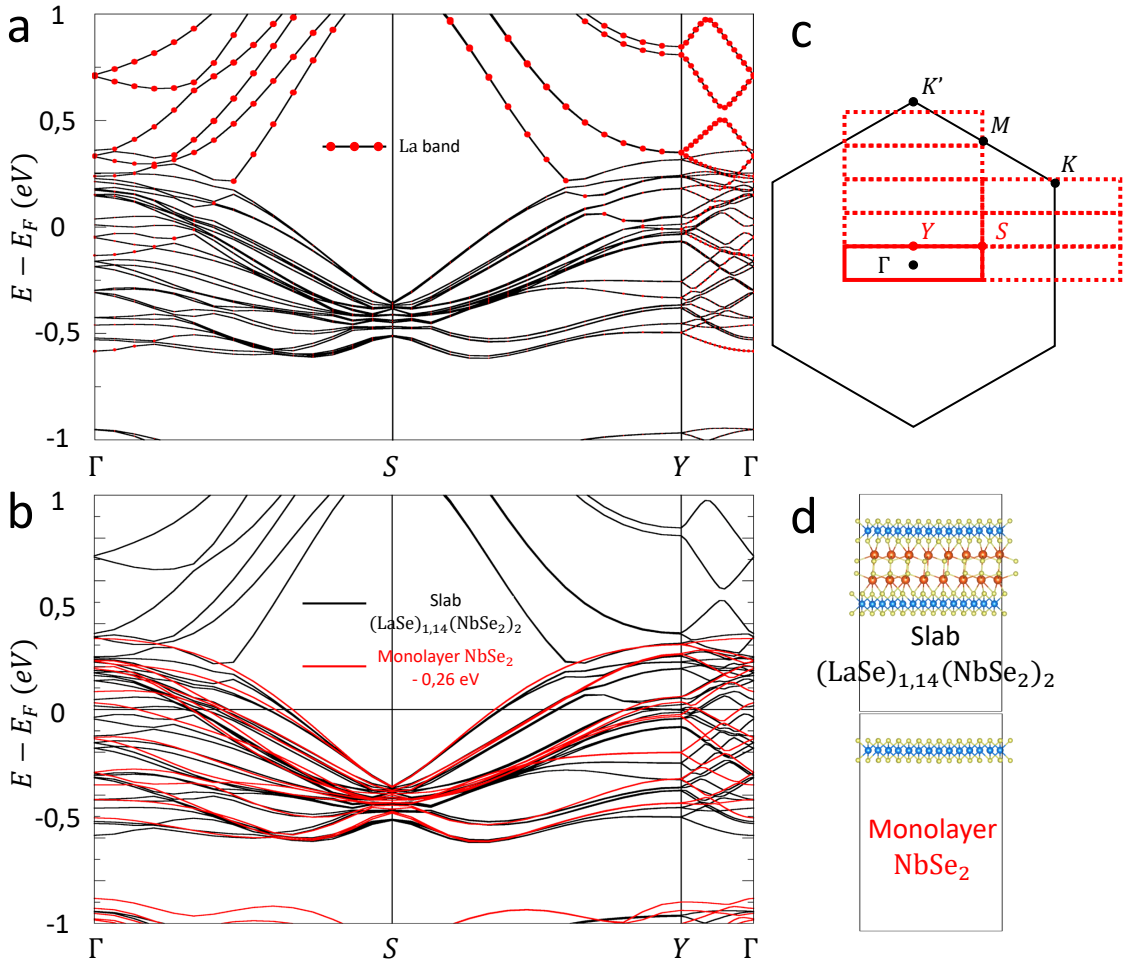

Figure 3.16: **a**. Band structure of $(LaSe)_{1,14}(NbSe_2)_2$. The bands with a pronounced La character are higlighted with red dots. **b**. Comparison between the band structures of $(LaSe)_{1,14}(NbSe_2)_2$ and of $0,3$ eV e-doped monolayer $NbSe_2$. **c**. Superimposition of the Brillouin zones of $(LaSe)_{1,14}(NbSe_2)_2$ (red) and of $NbSe_2$ (black). **d**. Unit cells on which were performed the DFT calculations presented in **b**.

[3]It is possible to develop the band structure of $(LaSe)_{1,14}(NbSe_2)_2$ in the hexagonal Brillouin zone of $NbSe_2$ by a process called unfolding. The obtained unfolded band structure is represented in 3.17 **a** and resembles the one of $NbSe_2$ but this will be presented in greater details shortly.

DFT calculations were also carried out for monolayer $NbSe_2$. The monolayer was compressed along one direction to match perfectly the compression seen in $NbSe_2$ layers of $(LaSe)_{1,14}(NbSe_2)$. The band structure of this constrained $NbSe_2$ monolayer shifted of $0,26$ eV towards negative energies was superimposed on the band structure of the $(LaSe)_{1,14}(NbSe_2)_2$ slab. One can first observe a very good agreement between the two band structures meaning that the rigid energy shift scenario is actually quite convincing. Nevertheless, some bands marked with red spots in figure 3.16 **a** cannot be seen in the case of monolayer $NbSe_2$. As is was already said, DFT calculations shows that those are La bands. Interestingly, one of these bands barely crosses Fermi level meaning that the LaSe are not completely insulating. This is a consequence of the iono-covalent bonding between LaSe and $NbSe_2$ layers, the charge transfer being incomplete. A partial conclusion to this *ab initio* study is that $(LaSe)_{1,14}(NbSe_2)_2$ behaves as monolayer $NbSe_2$ with a chemical potential shifted of $\simeq 0{,}26$ eV apart from a small La contribution. This theoretical result now has to be confronted to STS experimental data.

3.3.3 Comparison between the DFT calculations and the quasiparticle interferences

In figure 3.10, one can notice that the QPIs signal seems to reflect the periodicity of the hexagonal Brillouin zone of $NbSe_2$ rather than the one of the reduced Brillouin zone of $(LaSe)_{1,14}(NbSe_2)_2$. This might be due to matrix elements involved in scattering processes. This also means that in order to theoretically reproduce the QPIs data, the band structure of $(LaSe)_{1,14}(NbSe_2)_2$ should rather be expanded in $NbSe_2$ Brillouin zone.

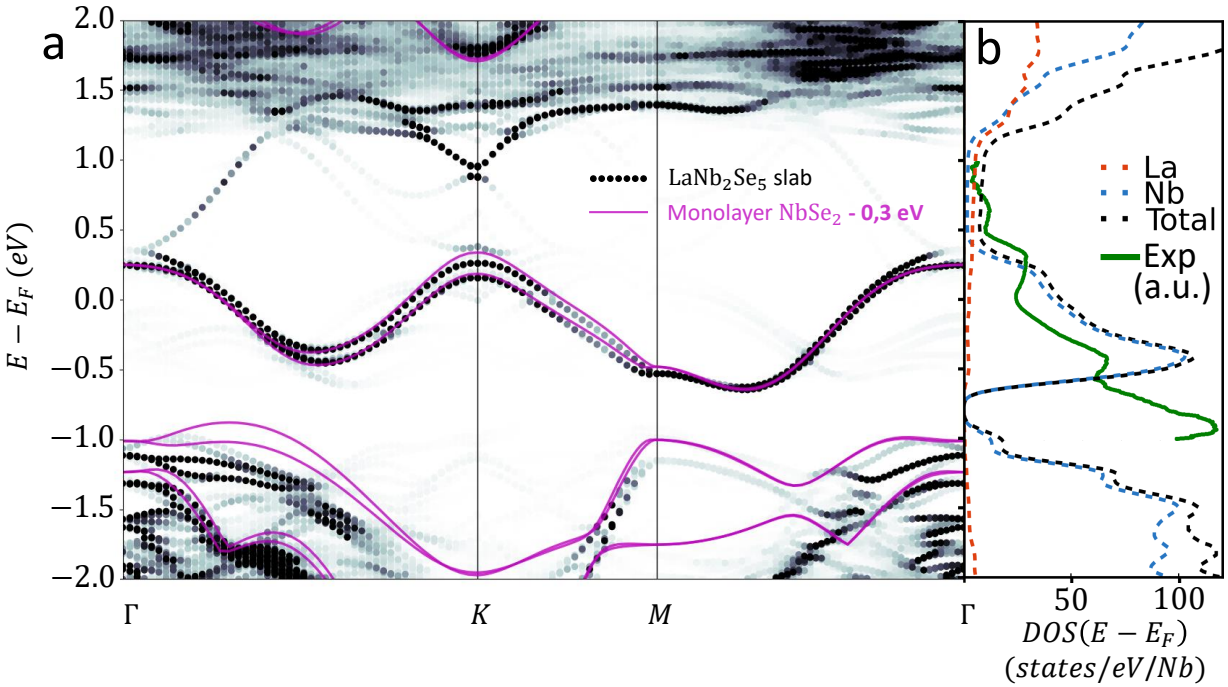

Figure 3.17: **a**. Comparison between the band structure of $(LaSe)_{1,14}(NbSe_2)_2$ and the one of $0,3$ eV e-doped $NbSe_2$ in the unfolded Brillouin zone. The dot color scale follows the spectral weight of the band. The darkest the higher the weight. **b**. Comparison between the expected La, Nb and total density of states and the one obtained experimentally.

This expansion in $NbSe_2$ Brillouin zone was done through a procedure called unfolding. The unfolded band structure of $(LaSe)_{1,14}(NbSe_2)_2$ is represented on figure 3.17 **a**. The band structure of monolayer $NbSe_2$ shifted of 0,3 eV is superimposed. From now, we will refer to it

as e-doped $NbSe_2$. The matching between the two band structures is even more accentuated in the unfolded Brillouin zone representation. On figure 3.17 **a**, the darker the dot, the higher the spectral weight of the band.

In figure 3.17 **a**, we see that at the energy range in which one should see the La bands, namely between $0,4$ eV and 1 eV (see figure 3.16 **a**), the bands are made of light grey dots, meaning small spectral weight contribution. This is confirmed in 3.17 **b** in which we can see that the La contribution (red dashed line) to the total density of states around Fermi level is negligible with respect to the Nb contribution (blue dashed line), which further comforts our hypothesis of $(LaSe)_{1,14}(NbSe_2)_2$ behaving as electron doped monolayer $NbSe_2$.

Since a strong Ising spin-orbit coupling is present in monolayer $NbSe_2$, it is very important to emphasize that a good correspondence between the two band structures also implies the presence of such a spin-orbit coupling in $(LaSe)_{1,14}(NbSe_2)_2$. The splitting due to this spin-orbit coupling is indeed visible, particularly in the unfolded representation of the band structure of $(LaSe)_{1,14}(NbSe_2)_2$ (see the splitting around K in figure 3.17 **a**). Contrary to bulk 2H-$NbSe_2$ in which no such effect was observed, theoretical calculations show here that $(LaSe)_{1,14}(NbSe_2)_2$, although being a bulk material, actually possesses a quasi-2D physics. This will be of the utmost importance when we will present the results obtained in the superconducting phase of $(LaSe)_{1,14}(NbSe_2)_2$ in 3.6.

A ± 1 V dI/dV spectrum was acquired and is superimposed on top of the density of states of $(LaSe)_{1,14}(NbSe_2)_2$ for comparison (green full line in figure 3.17 **b**). All the visible peaks can be related to positions in energy at which the group velocities of the bands are zero and thus at which a lot of spectral weight is expected in the density of states. For positive energies, there is a whole energy span for which there are almost no states. One thus expects the conductance to be close to zero within this range which is also supported by a strong depletion visible in the experiment. Also, around $-0,8$ eV, we see a gap in the expected density of states. In the experimental data, a small depletion of density of states seems to reflect this feature. The gap is however not seen, and we attribute this to the fact that, as the bias voltage increases, one starts to probe the bulk material rather that the surface. The density of states observed experimentally is in an overall good agreement with the DFT one, enforcing the validity of our first principles calculations.

The following paragraphs are dedicated to the comparison between the theoretical QPIs patterns and the experimental ones. In order to do so, we will base our discussion on figure 3.18[4]. In figure 3.18 **a**, is represented the Fermi surface of e-doped $NbSe_2$ with two nearly superimposed spin-polarized pockets around Γ and two split spin-polarized pockets around K/K' (due to Ising spin-orbit coupling). In figure 3.18 **b** is plotted the expected QPIs patterns (spin-selective joint DOS) at 0-energy for e-doped $NbSe_2$. The tiny black dots are located at Bragg peaks positions. Figure 3.18 **d** depicts the Fourier transform modulus of dI/dV map at 0 energy[5]. In the following, we will see if it is possible to interpret our STS data in terms of QPIs generated by nesting properties of the Fermi surface of e-doped $NbSe_2$. Calculating the expected QPIs patterns for $(LaSe)_{1,14}(NbSe_2)_2$ would be too costly numerically speaking.

Remark : According to what was said in section 2.3 dedicated to the theoretical description of QPIs, only scattering channels which conserve the spin are to be considered. The wave functions of an incoming electron and a scattered electron with opposite spin are, indeed, orthogonal and thus, cannot interfere and lead to standing-wave patterns. The QPIs expected patterns are thus given by the calculation of the **spin-selective** joint DOS.

A few scattering wave vectors which connect efficiently (good nesting) different parts of the

[4]For all panels of figure 3.18, the misfit direction is along the vertical axis.

[5]400×400 $I(V)$ spectra were acquired in a 30nm×30nm area, following the grid spectroscopy procedure described in figure 2.7 of section 2.2.4.

Fermi surface were drawn on figure 3.18 **a**. Q1 links the hole pocket around Γ to itself. It gives the big red circle in figure 3.18 **b**. Other circles with same radius can be observed around all six Bragg peaks. Their corresponding wave vectors link the pocket around Γ in 1BZ to the one in 2BZ. Due to Ising spin-orbit coupling present in monolayer $NbSe_2$ (in which inversion symmetry is broken), a spin up/spin down band splitting occurs around K/K' point. This splitting also exists around Γ (not along ΓM though) but is negligible. Q2 is a scattering wave vector linking the hole pocket around Γ and the K/K' inner pocket. It gives rise in QPIs patterns to arcs which are displayed in green in figure 3.18 **b**. Again, scattering processes between 1BZ and 2BZ also lead to similar arcs. One is highlighted in green at the bottom of figure 3.18 **b**. Q3 is a scattering wave vector linking the hole pocket around Γ and the K/K' outer pocket. It gives rise in QPIs patterns to arcs which are displayed in blue in figure 3.18 **b**.

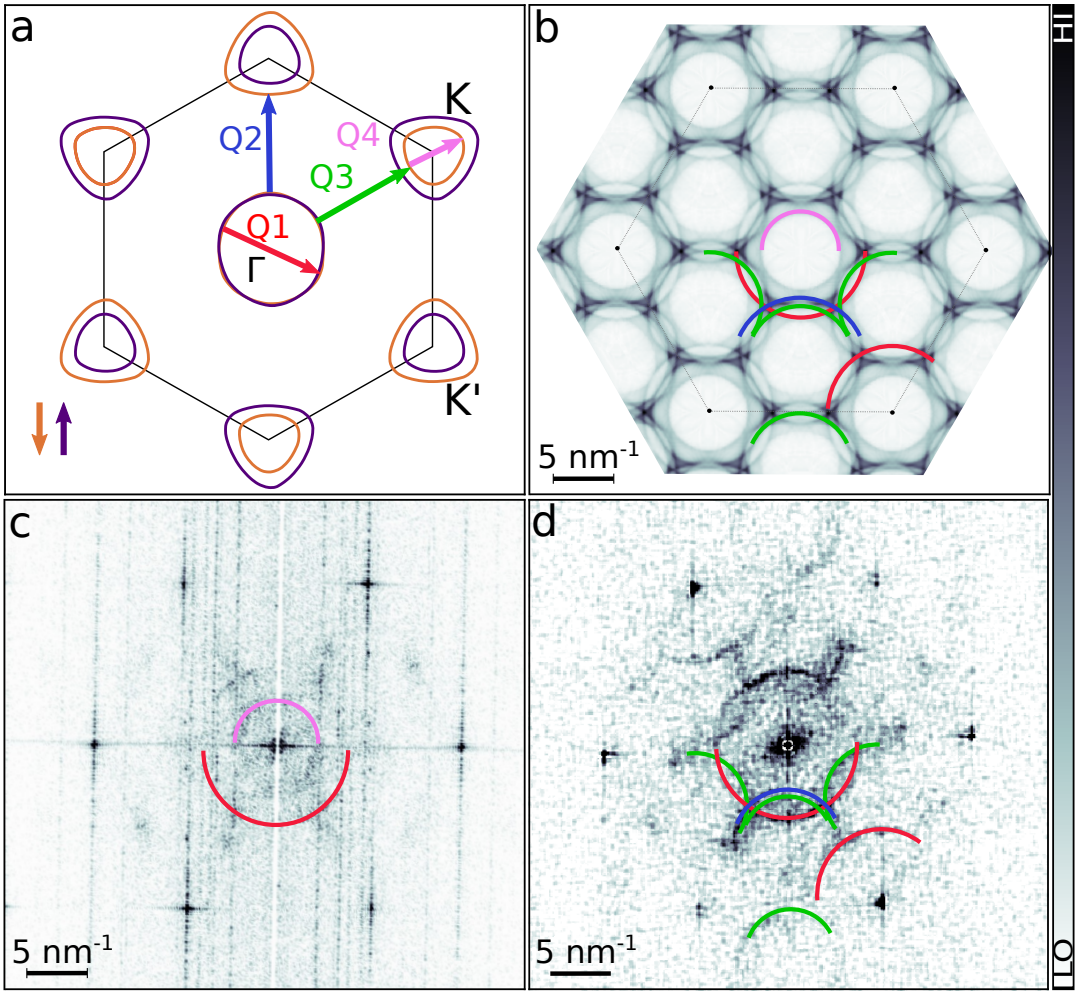

Figure 3.18: **a**. Fermi surface of e-doped monolayer $NbSe_2$. **b**. Spin-selective joint DOS of the Fermi surface of e-doped monolayer $NbSe_2$ reflecting expected QPIs patterns. **c**. Modulus square Fourier transform of a STM image taken at $-0,25$ meV bias voltage. **d**. Modulus square Fourier transform of a STS dI/dV map at 0 energy.

All the expected QPIs patterns that were presented so far can be seen in 3.18 **d** and at the right positions in reciprocal space. The only spectroscopic signal that cannot be simply interpreted with the Joint DOS of e-doped $NbSe_2$ Fermi surface is the intense halo around Γ. A study which is not detailed here but that was done by the theoreticians of our group showed that this signal cannot be explained by QPIs for the La band crossing Fermi level. In figure 3.16 **c**, it is possible to see that the S and Y points of the approximate commensurate Brillouin

zone, which are close to Γ, are repeated many times throughout the image. Several reduced Brillouin zones are indeed contained within the hexagonal first Brillouin zone, meaning that strong signal can potentially be sent to Γ thanks to the incommensurability. This is only an hypothesis but it could also explain the unexpectedly large widths of the Bragg peaks.

The spin-splitting due to strong Ising spin-orbit coupling predicted theoretically is also present. In figure 3.18 **d**, this last statement is highlighted by the splitting between the two arc in the misfit direction (with blue and green arcs as guide for the eye). In our knowledge, it is the first time that this Ising spin-orbit coupling splitting is seen *via* STS, regardless of the compound.

Q4 is a scattering wave vector linking the inner pockets around K/K' points. It conduced to the presence of a circle around Γ highlighted by a pink arc in figure 3.18 **b**. Figure 3.18 **c** is the modulus square of the Fourier transform of a topographic STM image taken at -25 meV. Figure **??c** also clearly displays the Q1 contribution, but also the Q4 contribution with the smaller radius signal around Γ, which further comforts the rigidly shifted monolayer $NbSe_2$'s band structure scenario.

Partial conclusion : In this study, we demonstrated that due to charge transfer occurring between La and Nb atoms, the system behaves as electron-doped monolayer $NbSe_2$ (rigid band structure shift) with a $5,8 \cdot 10^{14}$ electron per cm^2 increase in carrier density (60% of intrinsic density) and chemical potential shift of +0,3 eV. In figure 3.19, is represented the band structure of monolayer $NbSe_2$. On top of this band structure is superimposed a grey band delimiting the accessible doping range achieved in ref. [87] by mean of ionic gating. The value of electron-doping reached in this study was the best achieved in similar systems so far, but it is more that four times lower than ours (see orange line in figure 3.19). Our study opens the possibility to use misfit exotic TMD heterostructures to thoroughly tune doping to unprecedented values and thus considerably modify the electronic properties of quasi-2D $NbSe_2$.

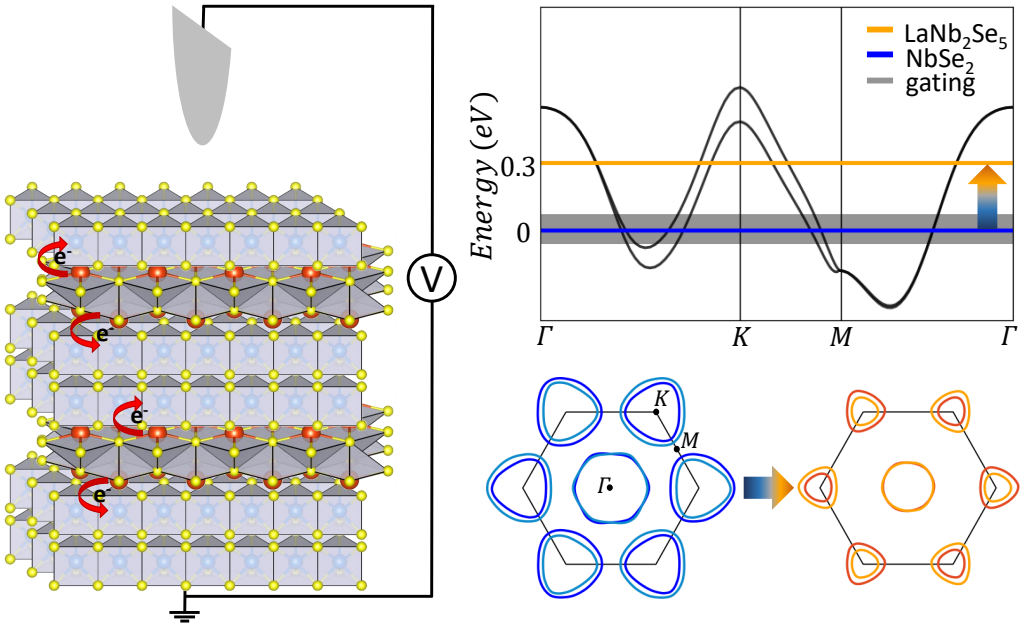

Figure 3.19: $(LaSe)_{1,14}(NbSe_2)_2$ acts as a electron-doping device for $NbSe_2$. The Fermi level position is shifted of 0,3 eV. The Fermi surfaces of monolayer $NbSe_2$ and e-doped $NbSe_2$ are represented next to each other, hence illustrating the possible electronic changes provoked by strong electron doping.

3.3.4 2×2 charge modulation order

Here, we will focus on the 2×2 CDW in $(LaSe)_{1,14}(NbSe_2)_2$ that was previously mentioned in the text. First, we will look at the temperature dependence of this charge order and second, we will see if it can be predicted through electron-phonon dispersion DFT calculations performed on electron-doped monolayer $NbSe_2$.

For now, we only stressed the 2×2 CDW signature in reciprocal space, but it can also be seen in real space. Figure 3.20 is a topographic map taken at $4,2$ K. On this image, we can see that, locally, one every two atoms appears brighter. White circle were superimposed on the image as a guide for the eye. In figure 3.21 **a** is represented a STM image acquired at 25 meV and 2 K. One every two atomic columns appears darker, and this, in two directions as suggested by the guide-for-the-eye white lines. The Fourier transform modulus on this image is displayed in figure 3.21 **b**, where the four CDW spots are clearly visible. On the right, are plotted modulus Fourier transforms of STM images taken at 77 K, 100 K and 300 K, respectively. Only a part of the full images is represented to emphasize on the temperature evolution of CDW spots only. At 77 K and 100 K the CDW spots can still be seen. Nevertheless, at room temperature the CDW is no longer present. By performing STM imaging while increasing slowly the temperature, the CDW survives up to 105 K, temperature which we evaluated as being the CDW critical temperature. This critical temperature is above the 3×3 CDW critical temperature observed in monolayer $NbSe_2$ in ref.[94] (between 25 K and 45 K), but beneath the 3×3 CDW critical temperature of ref. [88] (around 145 K).

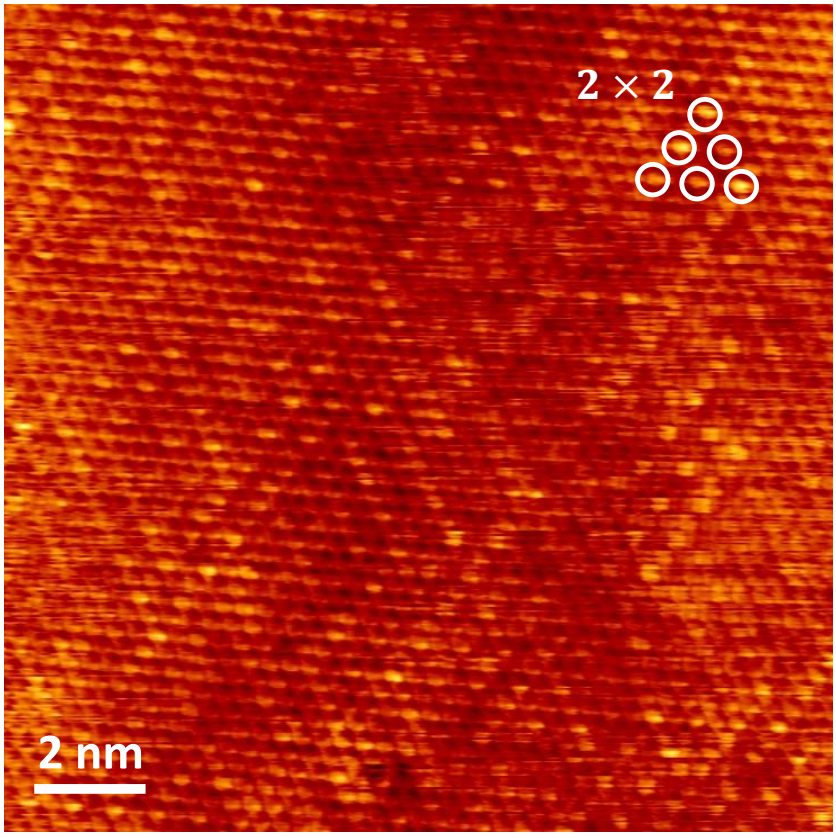

Figure 3.20: Topography map of $(LaSe)_{1,14}(NbSe_2)_2$ taken at $4,2$ K displaying a 2×2 CDW order in real space. Locally, every other atom appears brighter. The white circles are a guide for the eye.

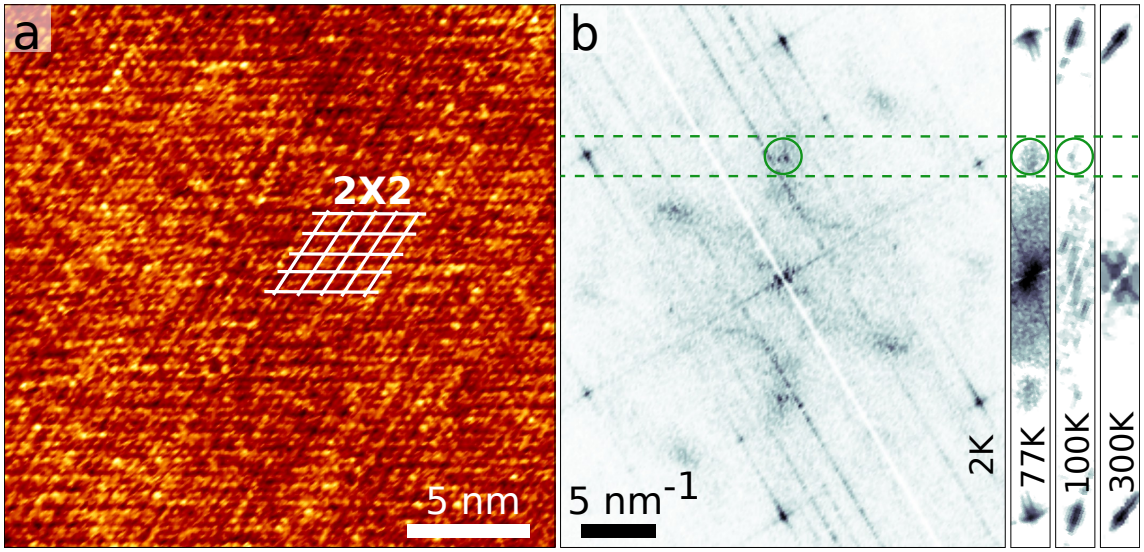

Figure 3.21: **a**. Topography image of $(LaSe)_{1,14}(NbSe_2)_2$ displaying a 2×2 CDW in real space. **b**. Fourier transforms of topography maps taken at 2 K, 77 K, 100 K and 300 K, respectively. The transition between CDW and normal phase occurs around 100 K.

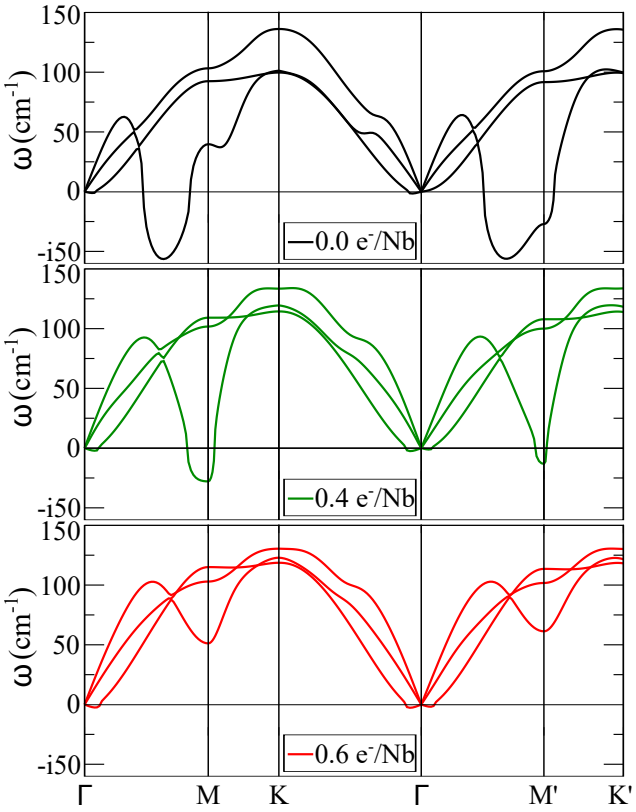

Figure 3.22: Phonon dispersions for e-doped monolayer $NbSe_2$ with no doping (black curves), 0,4 e^-/Nb doping (green curves) and 0,6 e^-/Nb doping (red curves). The correct amount of strain necessary to reproduce the one of $(LaSe)_{1,14}(NbSe_2)_2$ was taken into account in the DFT calculations.

It is interesting to see whether the 2×2 CDW naturally appears in e-doped monolayer $NbSe_2$. The $NbSe_2$ monolayer considered in this study has two particularities. The first one is the compression along the misfit direction. The theoreticians from our group observed a

tendency to switch from a 3×3 CDW to a 2×2 CDW with increasing compression but this was for distortions far much substantial than the one $(LaSe)_{1,14}(NbSe_2)_2$ is dealing with. Strain is, hence, not likely to be responsible for the 2×2 CDW order in our compound. The second particularity is electron-doping.

In figure 3.22 are represented phonon dispersions for 0 charge transfer, 0,4 electrons per Nb atom charge transfer and 0,6 electrons per Nb atom charge transfer[6]. For 0 charge transfer, the well-known phonon softening (imaginary frequency) mode lying at about $2/3[\Gamma M]$ and responsible for the 3×3 CDW order (see [95]) is quite visible. For 0,4 e^-/Nb doping the phonon softening mode move from $2/3[\Gamma M]$ to $[\Gamma M]$, or so to say, a 2×2 CDW naturally appears with increasing electron doping. In our experiment, given our QPIs results, our doping level should be around 0,6 e^-/Nb charge transfer. Unfortunately, the phonon softening does not survive up to our experimental doping value. It seems like the calculations do not show any phonon softening for the doping (or the evaluated charge transfer) expected for our compound.

Partial conclusion : This study can mean two things : either our model is wrong or incomplete, or the 2×2 CDW has another origin differing from regular electron-phonon coupling. Our e-doped monolayer $NbSe_2$ model might not be correct regarding the 2×2 CDW. It is probably wrong to neglect the iono-covalent interaction between $NbSe_2$ and LaSe layers, interaction which probably induces modifications in the phonon spectrum and thus shift the doping levels at which the 2×2 CDW survives. At least this simple model grabs the tendency of the system to switch from 3×3 to 2×2 charge modulations with electron-doping. However, it is important to note that numerical simulations of STM topography maps of our compound (not shown here but performed by M. Calandra, C. Tresca and M. Campetella) do not show such 2×2 modulations. Another possible interpretation would be that the presence of La vacancies (invisible to our probe because lying beneath the $NbSe_2$ top layer) tend to locally change the chemical potential (the local electron doping is lower) and thus locally tune the system into a 2×2 charge modulation phase. This last hypothesis could also explain the "blurry" nature of our 2×2 CDW.

3.4 $(LaSe)_{1,14}(NbSe_2)_2$: an Ising superconductor

As we have seen in the first chapter (see section 1.1), when a BCS superconductor is submitted to an external magnetic field, counter currents will start to flow contributing to globally expel this field. We speak of orbital effects, since it is the motion of Cooper pairs which is at the origin of the suppression of the magnetic field. Let us now consider a superconducting plane in presence of a magnetic field taken parallel to this plane. Because of the two-dimensional nature of the system, the motion of the electrons is limited in the direction perpendicular to the superconducting plane and the orbital effects are thus considerably limited. This does not mean that a 2D superconductor can support any arbitrarily strong magnetic field. In a conventional superconductor, the electrons forming a Cooper pair have opposite spins. When submitted to a magnetic field, the interaction of one of the spins of the Cooper pair with the magnetic field is energetically unfavorable, potentially leading to Cooper pair breaking[7]. Let us call H_c the value of the magnetic field for which the interaction with the magnetic field overcomes the pairing energy. Above H_c, superconductivity is killed and one has : $H_c = 1,85 T_{SC}$ (where H_c is expressed in tesla and T_{SC} in kelvin) [19]. This is called the Pauli paramagnetic limit.

In few layers $NbSe_2$, in-plane upper critical fields are several times bigger than the Pauli paramagnetic limit [33, 34, 35]. This is due to the competition between the external in-plane

[6]This value corresponds to the charge transfer effectively occurring in our compound.

[7]Such pair breaking occurs because of the Zeeman splitting between the states with opposite spins of the electrons of the Cooper pair. It becomes efficient when $g\mu_B H$ (with g the Landé factor), the energy difference between the two states, becomes of the order of 2Δ (with Δ the superconducting gap).

magnetic field and the strong Ising spin-orbit coupling which tends to lock the spins of the electrons in the out-of-plane direction[8]. Very high in-plane upper critical fields are one of the signatures of Ising superconductivity.

As shown in ref. [89], $(LaSe)_{1,14}(NbSe_2)_2$ is superconducting under $5,3$ K (see figure 3.23 **a**). It was shown one year later that $(LaSe)_{1,14}(NbSe_2)_2$ possesses a substantial in-plane upper critical field (more than 25 T by extrapolating the resitivity vs magnetic field curve of figure 3.23 **c**, while $H_{c,Pauli} \simeq 10$ T) implying the presence of a strong Ising spin-orbit coupling [9]. This is further corroborated by the DFT calculations presented in the previous section.

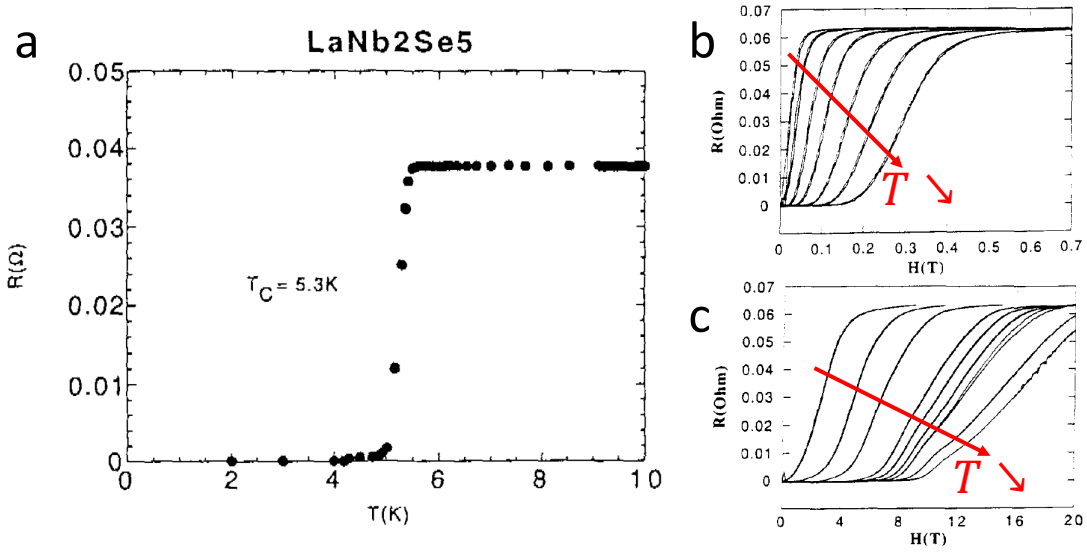

Figure 3.23: **a**. Resistivity *vs* temperature in $(LaSe)_{1,14}(NbSe_2)_2$ showing superconducting behaviour under $5,3$ K (from [89]). **b**. Resistivity *vs* perpendicular magnetic field in $(LaSe)_{1,14}(NbSe_2)_2$ (from [9]). **c**. Resistivity *vs* parallel magnetic field dependence of $(LaSe)_{1,14}(NbSe_2)_2$ (from [9]). The different plots obtained in **b** and **c** were taken at temperatures going from $4,2$ K to 2 K.

3.5 Topological superconductivity in monolayer $NbSe_2$

In this section, we will show that some theoretical studies predict the existence of unconventional superconductivity and possibly topological superconductivity in monolayer transition metal dichalcogenides. The conclusion of section 3.3 was that $(LaSe)_{1,14}(NbSe_2)_2$ was behaving up to some extent as an electron-doped monolayer $NbSe_2$. Because of this, we think that $(LaSe)_{1,14}(NbSe_2)_2$ could possibly host unconventional superconductivity.

In ref. [97], it was shown that dichalcogenides monolayer $NbSe_2$ and TaS_2 should enter a nodal superconducting topological regime when submitted to in-plane magnetic fields higher than the Pauli paramagnetic limit field but smaller than the critical field H_{c2}. This nodal topological phase is a consequence of the strong Ising spin-orbit coupling present in these materials. As it was already detailed in section 1.3.3, the locking of the electrons' spins in the out of plane direction does not occur along ΓM lines. The in-plane magnetic field first shifts the positions in reciprocal space of spin up and spin down bands along the ΓM lines in a way illustrated in figure 3.24 **a**. Second, since the applied in-plane magnetic field is higher that the Pauli limit field, superconductivity is killed along those lines, and the gap closes at the green and yellow dots (referred to as "nodal points") positions of figure 3.24 **a**, leading to nocal superconductivity.

[8] In order to suppress superconductivity, the Zeeman effect of an external magnetic field has to be stronger than the effective spin-orbit field, which can be huge (around 100 T in MoS_2 [36, 96]).

Wen-Yu He *et al.* then demonstrated that Majorana flat bands should link each couple of nodal points, as represented in figure 3.24 **b**. The topological nodal feature can further be understood by noticing that those Majorana zero-bias states only develop along specific edges oriented in ΓM directions (k_y direction in figure 3.24).

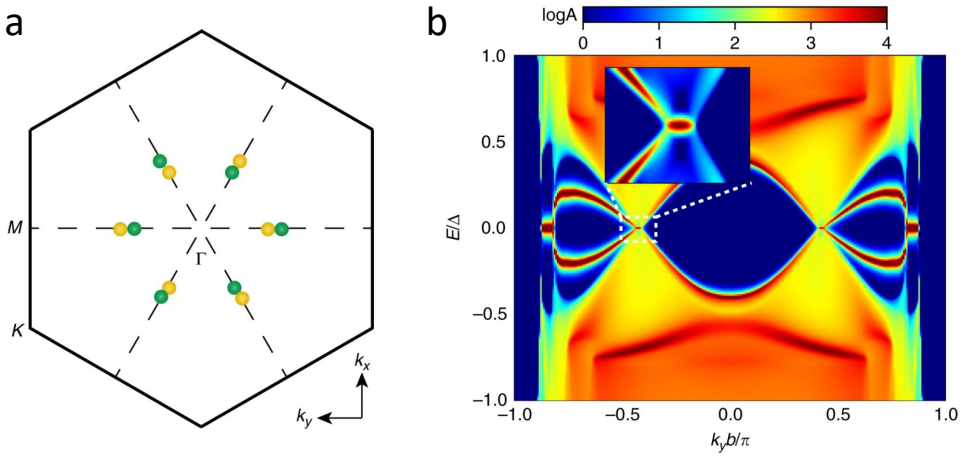

Figure 3.24: **a**. The in-plane magnetic field induces a shift in the Fermi surface between the spin up and spin down band along the ΓM lines. **b**. Majorana zero modes developing between couples of nodal points (taken from [97]).

In ref. [8], D. Shaffer *et al.* assumed the most general symmetry-authorized Hamiltonian describing pairing interactions in monolayer $NbSe_2$ (see figure 3.25). Similarly to ref. [97], they considered Ising spin-orbit coupling but they additionally investigated the effect of Rashba spin-orbit coupling, which is also likely not to be negligible in monolayer $NbSe_2$ (which has to be grown on a substrate) as well as in $(LaSe)_{1,14}(NbSe_2)_2$. Interestingly, the first noticeable effect of Rashba spin-orbit coupling is to lift the degeneracy between spin up and spin down bands along the ΓM direction. The nodal topological phase of ref. [97] however remains reachable by applying in-plane magnetic field in the $\Gamma K/\Gamma K'$ directions. The Fermi surface then looks like the one represented in figure 3.25.

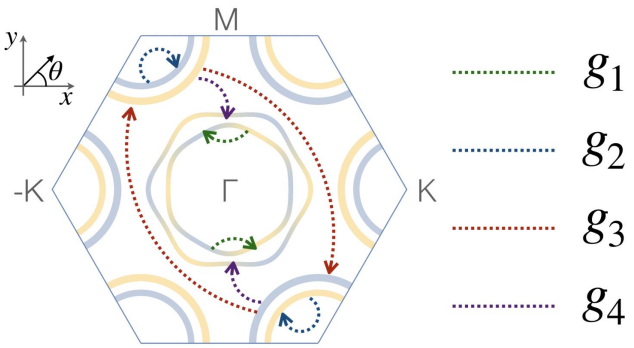

Figure 3.25: Fermi surface of monolayer $NbSe_2$ in presence of Rashba SOC. The different pairing interactions are represented by dotted arrows with diffrent colors. (taken from [8])

Their interaction Hamiltonian had the following form :

$$H_{int} = \frac{g_1}{2} d^\dagger_{\Gamma s} d^\dagger_{\Gamma s'} d_{\Gamma s} d_{\Gamma s'} + \frac{g_2}{2} d^\dagger_{Ks} d^\dagger_{-Ks'} d_{Ks} d_{-Ks'} + \frac{g_3}{2} d^\dagger_{Ks} d^\dagger_{-Ks'} d_{-Ks} d_{Ks'} + \frac{g_4}{2} d^\dagger_{\pm Ks} d^\dagger_{\mp Ks'} d_{\Gamma s'} d_{\Gamma s} + h.c., \tag{3.3}$$

For simplicity the momentum indices were suppressed. Here, s, s' are spin indices and $d^\dagger_{Xs}$ (d_{Xs}) is the creation (annihilation) fermionic operator of an electron of spin s in the X band. The different interactions are schematically represented in figure 3.25. It would seem that a superconducting instability becomes possible provided that either g_3 or g_4 inter-pocket interactions overcome intra-pocket interactions g_1 or g_2. The article then exposes the topological phase diagrams of monolayer $NbSe_2$ as a function of the Rashba spin-orbit coupling and the in-plane magnetic field oriented along the ΓK direction depending on which interaction between g_3 or g_4 is dominant.

Their conclusions are summarized in the phase diagrams shown in figure 3.26.

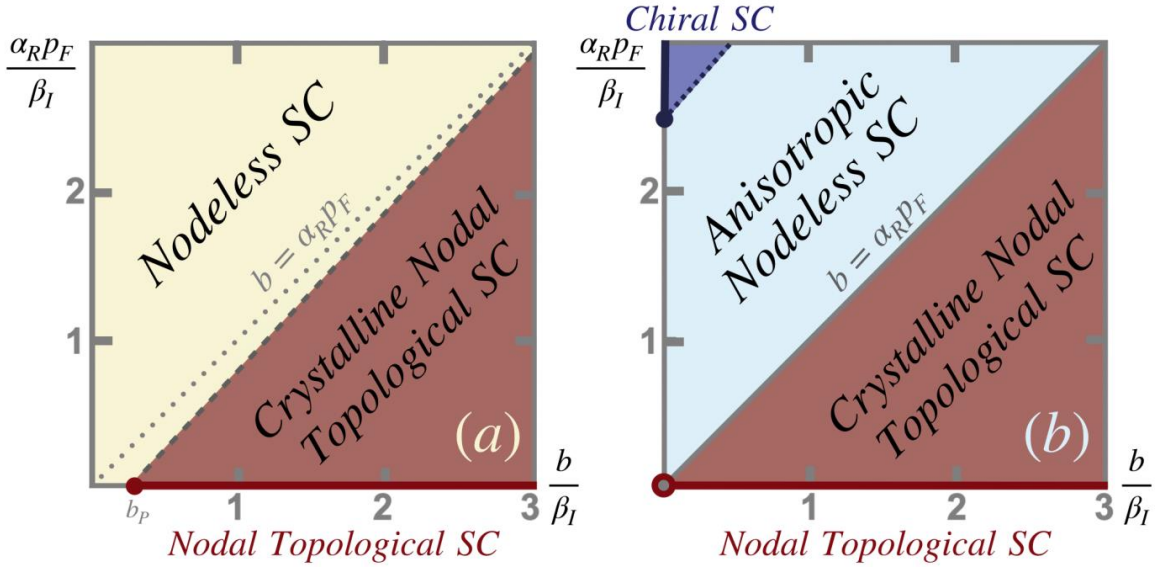

Figure 3.26: On the left is displayed the topological phase diagram of monolayer $NbSe_2$ as a function of Rashba SOC and ΓK oriented magnetic field when the g_4 interaction is dominant. On the right is displayed the topological phase diagram of monolayer $NbSe_2$ as a function of Rashba SOC and ΓK oriented magnetic field when the g_3 interaction is dominant. (taken from [8])

When g_4 is dominant, at zero magnetic field and any value of Rashba spin-orbit coupling, the system is in a s-wave topologically trivial superconducting phase. Nevertheless, by increasing the value of the ΓK oriented magnetic field, the system can enter a nodal topological regime similar to the one of ref. [97].

For now, we only focused on cases where in-plane magnetic fields are needed to turn 2D-like transition metal dichalcogenides into nodal topological phases. This approach was thus not feasible in our case since the experiments at 350 mK presented in the next section were performed on the M3 set-up presented in section 2.4, on which only **out-of plane** magnetic field up to 7 T can be applied.

The case in which the g_3 interaction dominates is very interesting because it allows for topological phases to emerge without any magnetic field. At zero magnetic field and Rashba spin-orbit coupling, the system naturally is in a f-wave triplet phase. Although being topologically trivial, the associated superconducting state is nonetheless unconventional. It is also

important to emphasize on the fact that two gaps are expected, one around Γ and one around K/K'. The K/K' gap is found to be momentum independent[9] while the Γ gap goes as $\cos(3\theta)$ (θ is the angle made by the momentum vector and is defined in figure 3.25), and therefore closes for θ equal to any odd multiple of $\frac{\pi}{6}$. The nodal feature of the Γ gap can be removed by including small s-wave correlations authorized by the symmetry which prevent it from going to zero.

When the value of the Rashba spin-orbit coupling becomes high enough, the system enters a $p \pm ip$ topologically non-trivial triplet superconducting state exhibiting gapless chiral edge modes reminiscent of the physics presented in section 1.4.3.

In ref. [98], Y. Hsu *et al.* also predicted the possible existence of topological phases in monolayer transition metal dichalcogenides. The study mainly focuses on compounds such as hole-doped monolayer MoS_2 [99] which do not present the hole bands around Γ, but most of the results can also be applied in the case of monolayer $NbSe_2$ since most of the arguments are symmetry-based and are *a fortiori* also valid for monolayer $NbSe_2$.

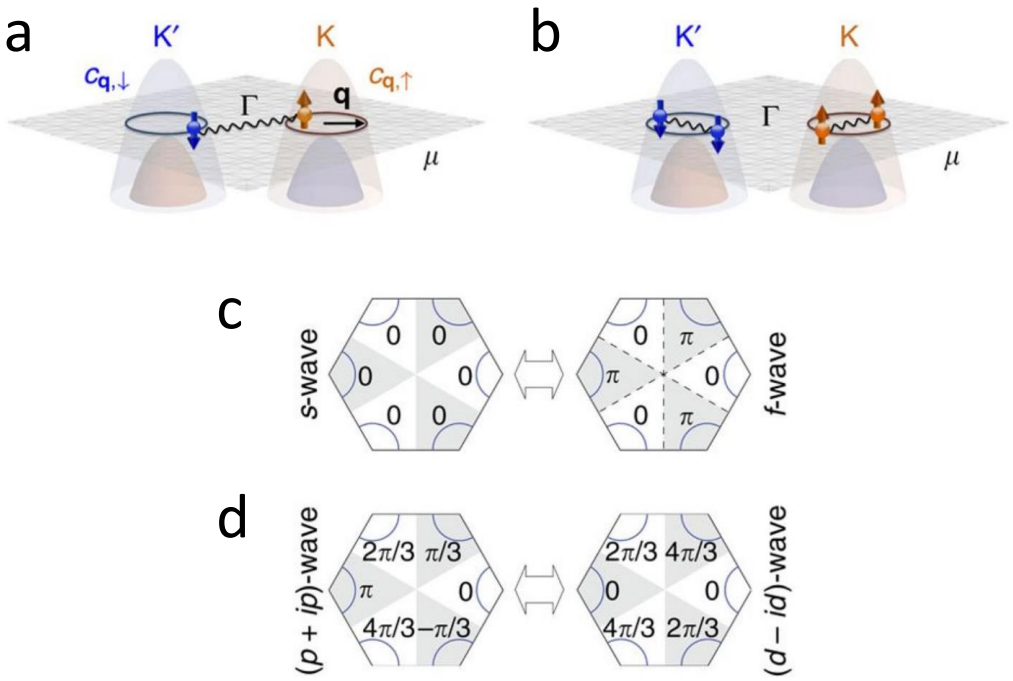

Figure 3.27: **a**. Inter-pocket pairing between K and K' hole-like pockets. **b**. Intra-pocket pairing within a K (K') pocket. **c**. and **d**. The absence of inversion symmetry allows for mixing between even and odd parity order parameters. The C_{3v} symmetry of the material authorizes s-wave to mix with f-wave and $(p \pm ip)$ to mix with $(d \mp id)$ (taken from [98]).

So far, the considered pairing interactions were only in favor of Cooper pairs with zero total momenta. One of the originalities of ref. [98] is the consideration of intra-pocket pairing within a K (K') pocket. Such a pairing is sketched in figure 3.27 **b**. The two electrons of the Cooper pair are at opposite locations in reciprocal space with respect to K (K') but not with respect to Γ leading to non-zero center of mass momenta for the Cooper pairs. Such kind of pairing is called Fulde–Ferrell–Larkin–Ovchinnikov (FFLO) and provokes spatial modulations either of the superconducting phase or of the superconducting gap amplitude across the sample [100]. In the case of monolayer $NbSe_2$, given the Ising splitting around K/K' points, it also favors

[9] More precisely, its magnitude is momentum independent but the gap changes sign as going from a K point to a K' point.

superconducting triplet correlations. However, it is important to understand that this intra-pocket pairing becomes less and less probable as the trigonal warping of the K pocket becomes more and more pronounced (illustrated in figure 3.28)

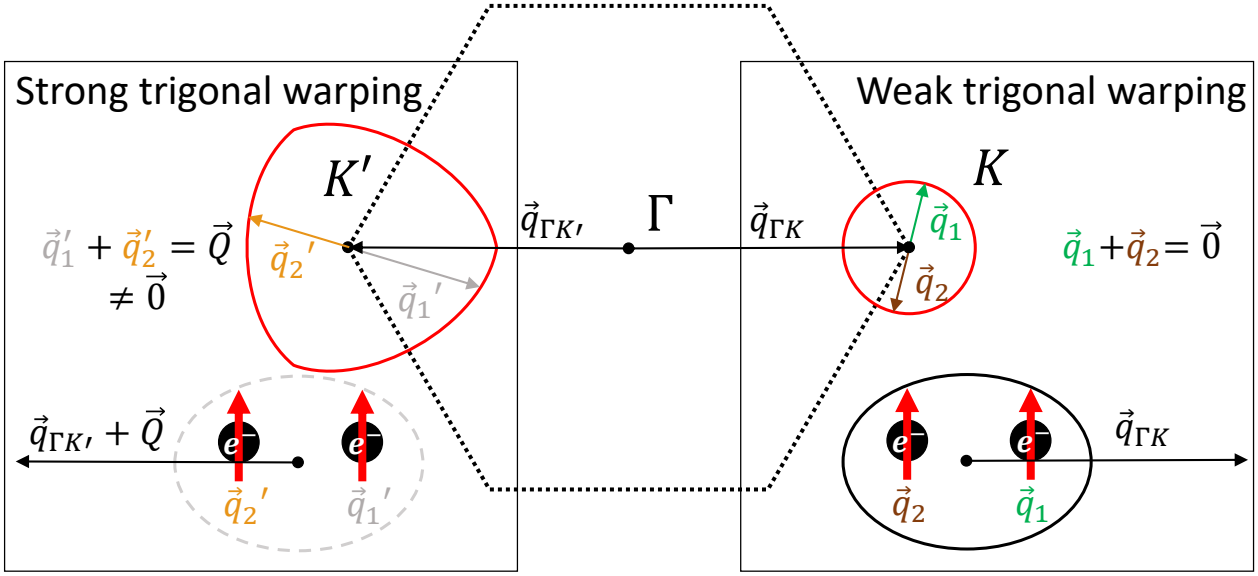

Figure 3.28: Illustration of the fact that a strong trigonal warping is less favorable for FFLO pairing than a nearly circular pocket around K/K'. On the left, because of strong trigonal warping, the Cooper pair is formed by two electrons which do not have opposite momenta q_1' and q_2' with respect to K'. The pairing is thus considerably reduced (illustrated by the light grey dotted ellipse). On the contrary, on the right, no trigonal warping is present and the two electrons have opposite momenta q_1 and q_2 with respect to K. The pairing is, hence, much more favorable (illustrated by the full black ellipse) than is the trigonal warped case. In both cases, the Cooper pairs have non-zero center-of-mass momenta (FFLO pairing) as represented by the $q_{\Gamma K'} + Q$ and $q_{\Gamma K}$ vectors, respectively.

On the left of figure 3.28, is represented a pocket with a strong trigonal warping. In this case, the electrons of the Cooper pair do not have opposite momenta with respect to K'. This situation is thus less favorable than the weak trigonal warping case represented on the right for which the electrons of the Cooper pair do not have opposite momenta with respect to K. In both cases, the Cooper pair has a total momentum different from zero.

We recall that as monolayer $NbSe_2$ is electron-doped, the trigonal warping is less pronounced around K/K' points at Fermi level. This means that $(LaSe)_{1,14}(NbSe_2)_2$ is potentially a good platform for FFLO superconducting pairing.

3.6 $(LaSe)_{1,14}(NbSe_2)_2$ in the superconducting phase

3.6.1 Measurement of the superconducting critical temperature

Before performing STS measurements on our samples, it was mandatory to priorly check whether they indeed were superconducting. In order to do so, we performed magnetometry experiments using a SQUID device in the Mesures Physique à très Basses Températures (MPBT) platform at Sorbonne university. The samples were 0-field cooled down to $1,8$ K after what they were submitted to a perpendicular magnetic field of 10 Oe. The value of the magnetic field was chosen so that the diamagnetic response of the system was maximized. The experiments were carried out on two samples of the same batch referred to as batch#2-sample3 and batch#2-sample5,

respectively. The obtained magnetic moment *vs* temperature curves are represented in figure 3.29 **a**.

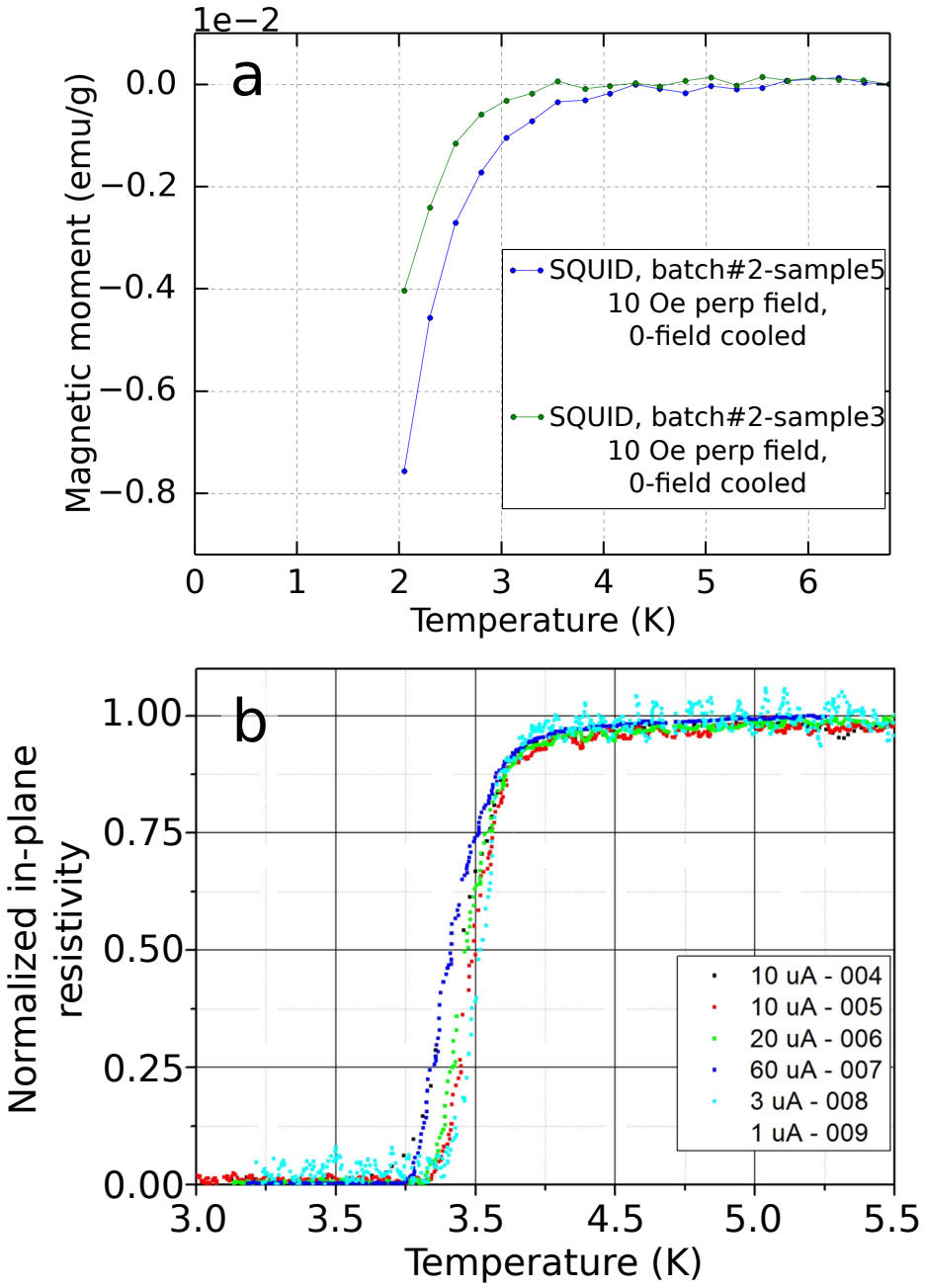

Figure 3.29: **a**. Magnetic moment *vs* temperature dependence for two $(LaSe)_{1,14}(NbSe_2)_2$ samples. The samples were 0-field cooled down and submitted to an external magnetic field of 10 Oe. **b**. Resistivity *vs* temperature transport measurements carried out by our collaborators in Slovakia.

Batch#2-sample3 exhibited a superconducting critical temperature approximatively equal to $3,6$ K whereas the batch#2-sample5 (which is the one on which the QPIs measurements presented in section 3.3 were done) exhibited a slightly higher superconducting critical temperature approximatively equal to 4 K. Complementary transport measurements were also carried out by our collaborators of the Center of Low Temperature Physics of Kosice and revealed a superconducting critical temperature of $\sim 4,3$ K for samples of the same batch as ours. Surprisingly, our combined results present critical temperatures inferior to $T_{SC} = 5,3$ K evaluated

in $(LaSe)_{1,14}(NbSe_2)_2$ during the 1990's [89]. A re-investigation of the old data showed that such a T_{SC} could be found in one specific part of an old sample, the remaining of the sample rather exhibiting superconducting critical temperatures comparable to ours, pointing out that the superconducting critical temperature is extremely sensitive to disorder and growth conditions. The magnetometry and transport measurements combined with the observed Ising superconductivity reported by the old data comforts the bulk superconducting nature of our $(LaSe)_{1,14}(NbSe_2)_2$ samples.

3.6.2 Measured differential conductance in the superconducting phase

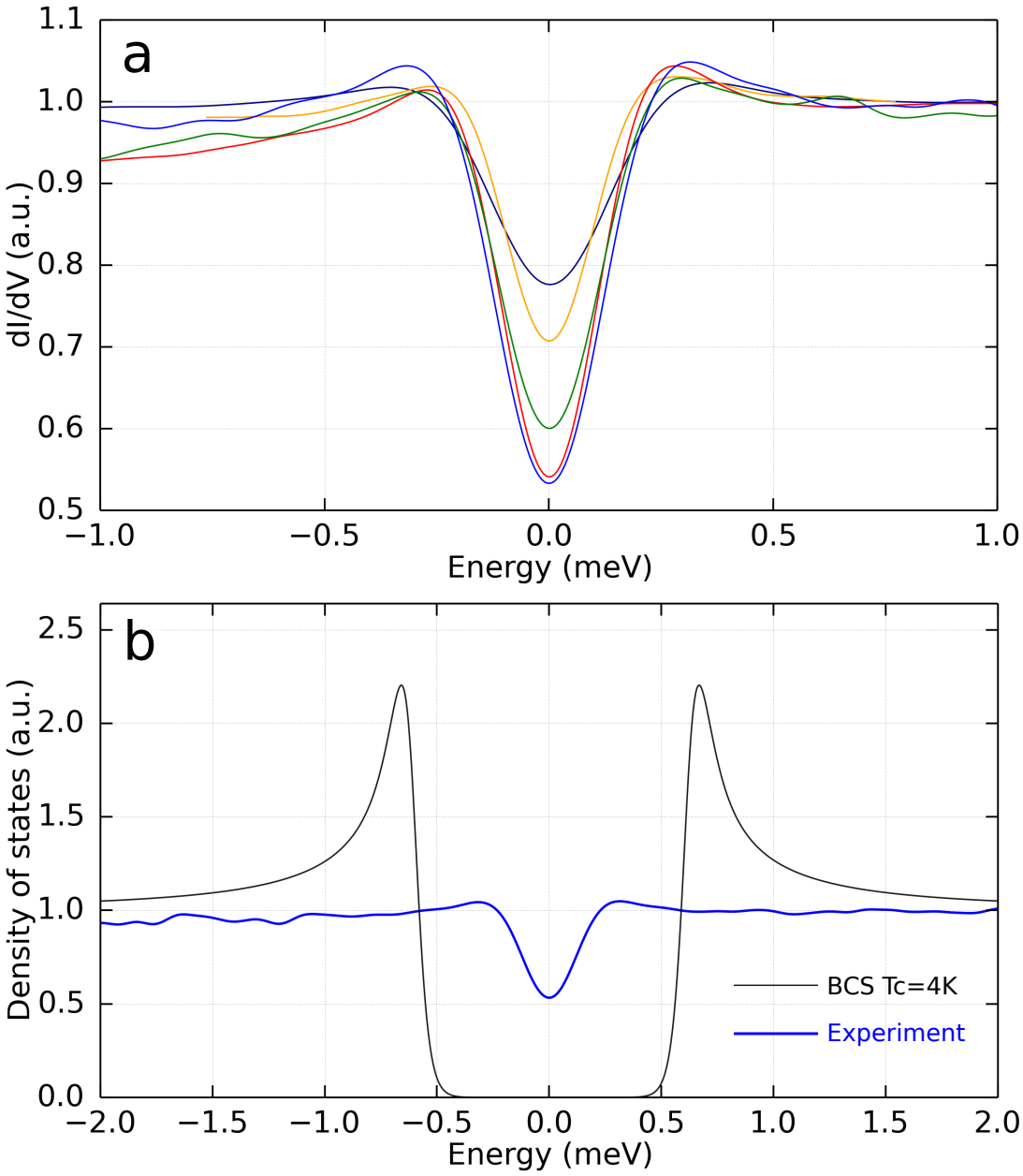

Figure 3.30: **a**. Collection od dI/dV spectra taken on several areas of two different samples. **b**. Comparison between a typical experimental dI/dV spectrum (blue) and the expected dI/dV spectrum in the case of a BCS superconductor presenting a superconducting critical temperatures equal to 4 K.

After this preliminary verification, the samples were prepared in the same way as shown in section 2.4.3 and were cooled down to 350 mK using ^{3}He condensation process (see section 2.4). In figure 3.30 **a** is represented a collection of averaged dI/dV spectra taken at many places of two samples of two different growth batches. The value of the superconducting gap does not change significantly with both location and sample but we do observe different filling of the gap depending on the approaching area. In-gap states fill the superconducting gap up to more than 50%. It is not rare to see gap filling comprised between 70% and 80%. We emphasize on the fact that such spectra were observed in all explored areas of two different samples (among which one clearly exhibited superconductivity in SQUID) of two different batches. On figure 3.30 **b** is represented (blue line) a typical dI/dV spectrum obtained at the surface of $(LaSe)_{1,14}(NbSe_2)_2$ at 350 mK, and thus, well under the superconducting critical temperature. The expected dI/dV spectra at 350 mK in the case of conventional superconductors of critical temperature equal to 4 K (black) is superimposed on figure 3.30 **b**. This T_{SC} was chosen to match the one measured in SQUID. First, the measured gap is equal to $\Delta_{SC} = 0,28$ meV. This value is more than twice as small as the BCS expectation for our samples (0,6 meV for $T_{SC} = 4$ K). Second, at zero bias, the conductance does not fall to zero and a hard gap is never seen. One can notice that the experimental dI/dV spectrum differs greatly from the one of a conventional BCS superconductor.

3.6.3 Exclusion of a proximity effect between the bulk and the surface

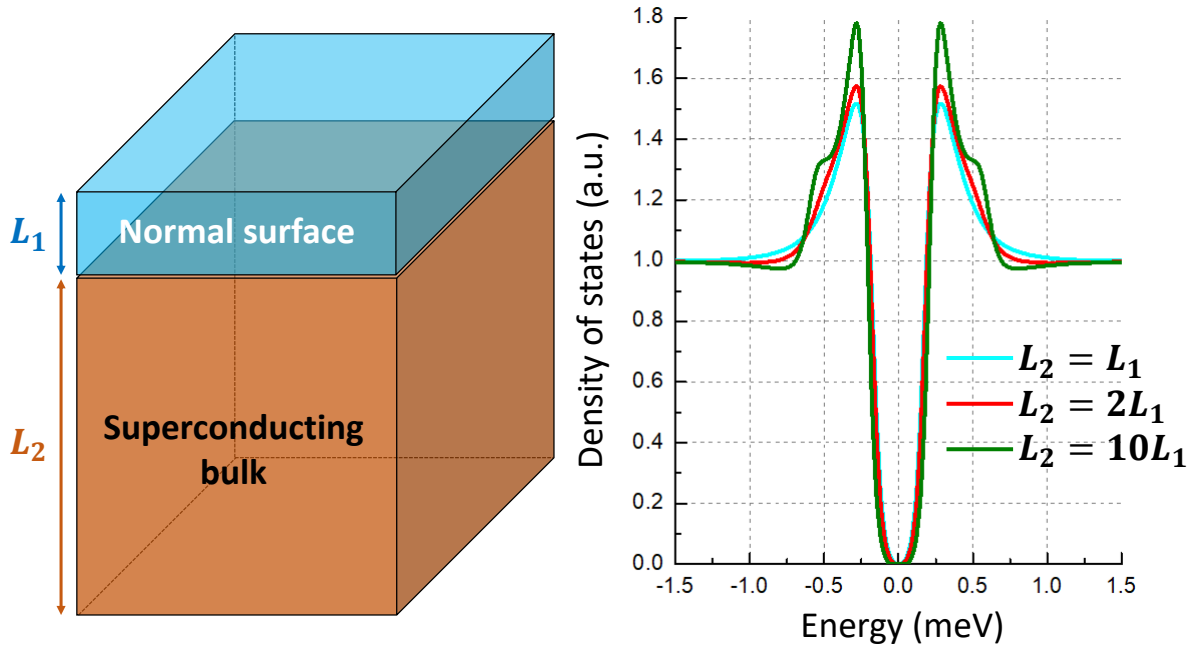

Figure 3.31: Proximity effect between a normal surface and a superconducting layer with of superconducting gap equal to 0,6 meV. The proximity gap is imposed to be equal to 0,28 meV. Changing the thickness of the superconducting layer does not change much the proximity spectrum. This model does not explain our experimental features meaning that proximity effect is not at the origin of our observed gap.

One could first think that such behaviour is the result of a superconducting proximity effect between the bulk of the sample (demonstrated to be superconducting *via* SQUID and transport measurements) and the surface, should it act as a normal metal. Proximity effect can indeed change both the gap value and its shape and would be a natural explanation of what we observe.

This last hypothesis was removed by numerically considering a system with the following geometry : a superficial normal layer, of width L_1, on top of a superconducting layer with varying thickness L_2 (this is schematically illustrated in figure 3.31). By using Usadel formalism and by imposing a bulk gap of $0,6$ meV[10] and a proximity gap of $0,28$ meV (our measured gap at the surface), we looked at the expected density of states at 350 mK for geometries in which $L_2 = L_1$, $L_2 = 2L_1$ and $L_2 = 10L_1$, respectively. The results are displayed in figure 3.31. The main conclusion of this short study is the fact that no matter the considered superconducting layer thickness, the experimental filled-V-shaped gap is not reproduced. This means that we must look for our measured gap's origin somewhere else.

3.6.4 Other signatures of superconductivity

Figure 3.32 presents other experimental results further attesting the superconducting nature of the samples. Figure 3.32 **a** represents the evolution of the dI/dV spectra with temperature from 350 mK to $2,2$ K clearly highlighting the disappearance of superconductivity with temperature.

The appearance of vortices in the presence of an external magnetic field is another signature of superconductivity which can be probed by performing grid spectroscopy. However, we never succeeded in observing vortices. Our guess is that the vortices are not easily pinned and are thus constantly moving, making their observation impossible. This absence of pinning of the vortices is probably due to the quasi-2D nature of $(LaSe)_{1,14}(NbSe_2)_2$. Here, the $NbSe_2$ planes of $(LaSe)_{1,14}(NbSe_2)_2$ are more decoupled than they are in bulk 2H-$NbSe_2$ in which the vortices tend to align from one $NbSe_2$ plane to the next consequently stabilizing their position/pinning [101]. It does not mean that it is impossible to find signatures of vortices in the material. Figure 3.32 **b** represents the bottom of the gap as a function of increasing perpendicular magnetic field H. In order to obtain the curve we used the "lazy fisherman" technique [102]. It basically consists in continuously taking $I(V)$ spectra at a given position while the magnetic field increases. This method is called the "lazy fisherman" method because, sometimes, a moving vortex can flow under the tip's position and be "caught" just as a fish can be caught by a fishing rod fixed to the shore. It is in this way that we interpret the sudden filling of the gap observed in figure 3.32 **b** around 70 mT which is probably the signature of a moving vortex that was passing by.

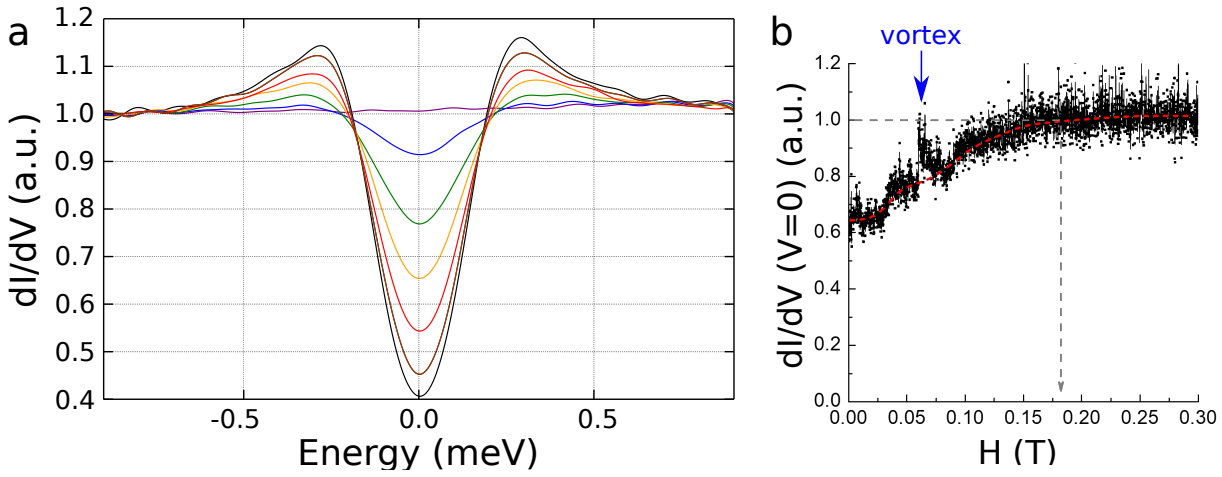

Figure 3.32: **a**. Evolution of dI/dV spectra with temperatures going from 350 mK to $2,2$ K. **b**. Bottom of the gap as a function of perpendicular applied magnetic field.

[10] Again supposing a superconducting critical temperature of 4 K.

3.6.5 QPIs in the superconducting phase

In order to further investigate the potential unconventional nature of the order parameter, we performed quasiparticle interferences measurements but this time in the superconducting phase. The experiments, which are presented here, were carried out on two different samples of different batches and with different Pt/Ir tips. The QPIs obtained at $0,2$ meV for the first and the second samples are represented in figure 3.33 **c** and **d**, and their corresponding mean dI/dV spectra in figure 3.33 **e** and **f**, respectively. The chosen energy ($0,2$ meV) is inferior to the gap magnitude and yet, we can still attribute the observed QPIs patterns to scattering processes already encountered in the normal phase. The circle around Γ and of radius Q_1, where Q_1 is the scattering wave-vector linking states of the Γ pocket to itself, is still visible, and this, in both experiments. The Q_4 scattering process linking inner K pockets to themselves is also observed but only for the first experiment, probably because the two tips did not favor the exact same tunnelling channels.

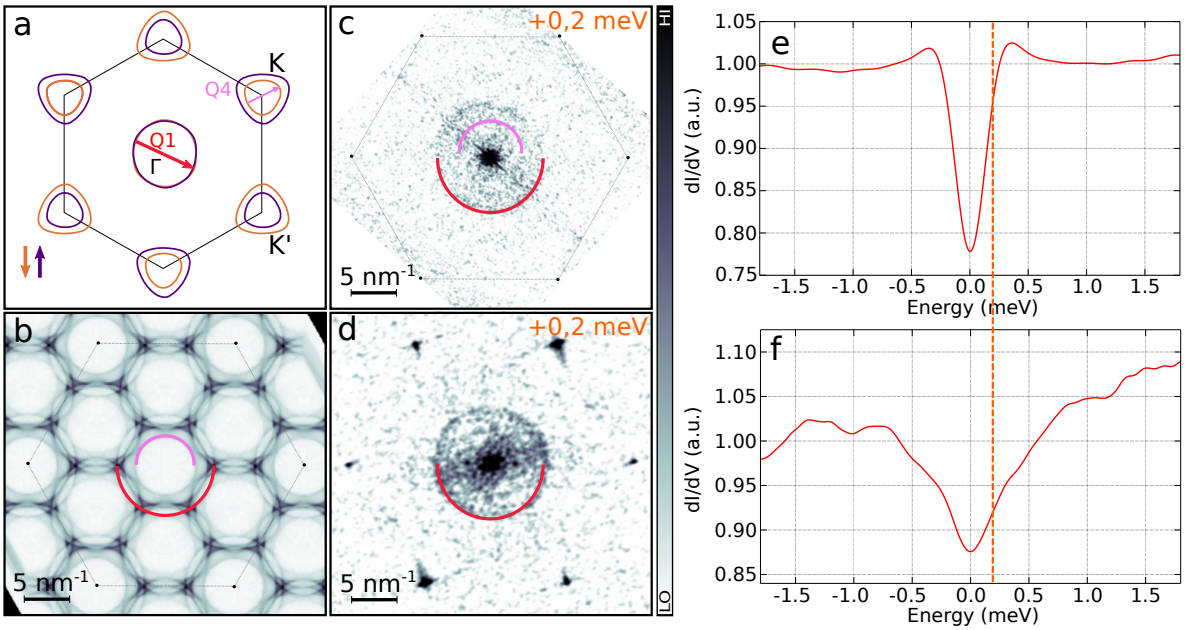

Figure 3.33: **a**. Fermi surface of electron-doped monolayer $NbSe_2$. Scattering processes between Γ pocket to Γ pocket are labelled by Q_1 wave vector. Scattering processes linking inner K/K' pocket to itself are labelled by Q_4 wave vector. **b**. Expected QPIs patterns at Fermi energy for electron-doped monolayer $NbSe_2$. **c**. QPIs obtained at $0,2$ meV for the first sample. **d**. QPIs obtained at $0,2$ meV for the second sample. **e**. Averaged dI/dV spectrum of the first sample. **f**. Averaged dI/dV spectrum of the second sample.

One can notice that the averaged dI/dV spectrum of the second sample (figure 3.33 **f**) has a different shape than the one of the first sample and the ones of figure 3.31 **b**. We recall that the differential conductance dI/dV can be assimilated to the local density of states of the sample only if the density of states of the tip in constant. It is important to prove that the measured dI/dV spectra of the second sample (typically the one of figure 3.33 **f**), reflect the superconducting nature of the system and not something else.

Before performing spectroscopy in the second sample, other measurements were done using the same tip and in particular, the one from which the spectra displayed in figure 3.34 **a** were extracted. This other measurement was also taken at 350 mK. At the beginning of this other spectroscopic grid, the spectra had the shape of the red dI/dV curve characteristic of the filled superconducting gaps observed many times. By the end of the map, the tip might have

interacted with the surface and changed to give the blue dI/dV curve of figure 3.34 **a**.

This change can simply be illustrated with the help of figure 3.34 **b** in which the dotted red curve represents the density of states of the superconducting sample and the dotted green curve represents an hypothetical density of state for the tip. Here, the tip presents a small depletion of density of states around Fermi level. By convoluting the density of states of the sample and this hypothetical tip's density of states one obtains (at 350 mK) the blue curve, which reproduces rather satisfyingly the experimental data. One can clearly see elbows at the gap positions in energy in both numerical calculation and experiment. The shape of the density of states within $[-\Delta_{SC}, +\Delta_{SC}]$ is almost not changed meaning that in this energy range our data can really be seen as a collection of local density of state maps. Moreover, this additional tip background is not likely to either add or kill any information because it does not depend on space contrary to QPIs patterns. Deconvoluting the experimental data by the supposed density of states of the tip (which was not done here) however remains the best and cleanest way of treating the data. One last argument in favor of the validity of the second experiment's results is the fact that spectroscopy performed in the first sample (for which the tip had no apparent background) leads to the same conclusions. Exploiting the second sample measurement has two purposes : first it confirms the reproducibility of the results and second it is more spatially resolved than the first experiment, leading to also better resolved QPIs patterns.

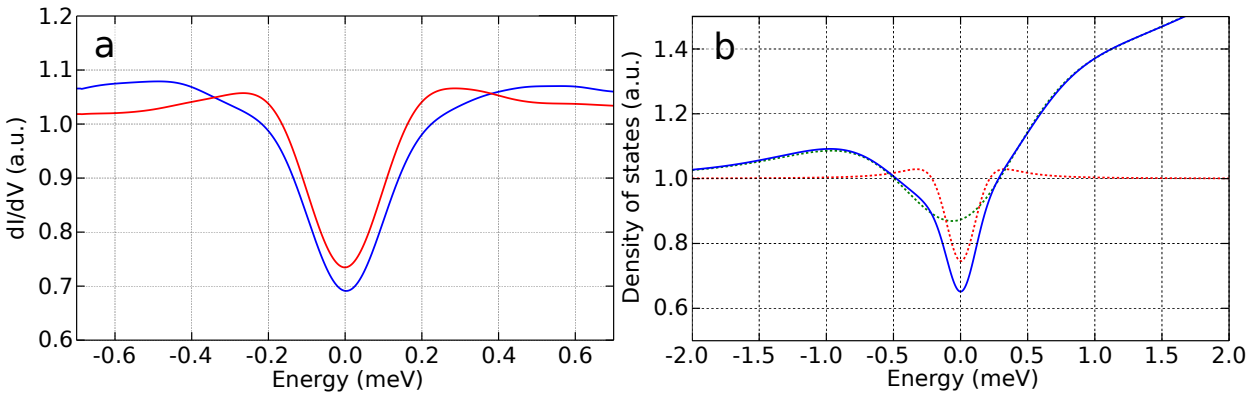

Figure 3.34: **a**. Spectroscopic grid experiment performed with the same tip as in the second sample. We see that during data acquisition, the typical dI/dV spectra changed from red to blue curve. **b**. Interpretation of the shape of the dI/dV spectra in the second sample. The measured signal (blue) is related to the convolution between the density of states of the sample (red) and a depleted tip's density of states (green).

We mentioned in the previous paragraph that the results on first and second samples are consistent with one another. We will now present those results.

In figure 3.35 **c**, **d** and **f** are represented the Fourier transforms of the local density of states maps obtained at $-0,25$ meV, 0 meV and $+0,25$ meV, respectively. What is striking is the great similarity between the three QPIs patterns. This observation can be extended for any energies within $[-\Delta_{SC}, +\Delta_{SC}]$. The only recognizable QPIs feature is the one resulting from Γ to Γ scattering (see figure 3.33).

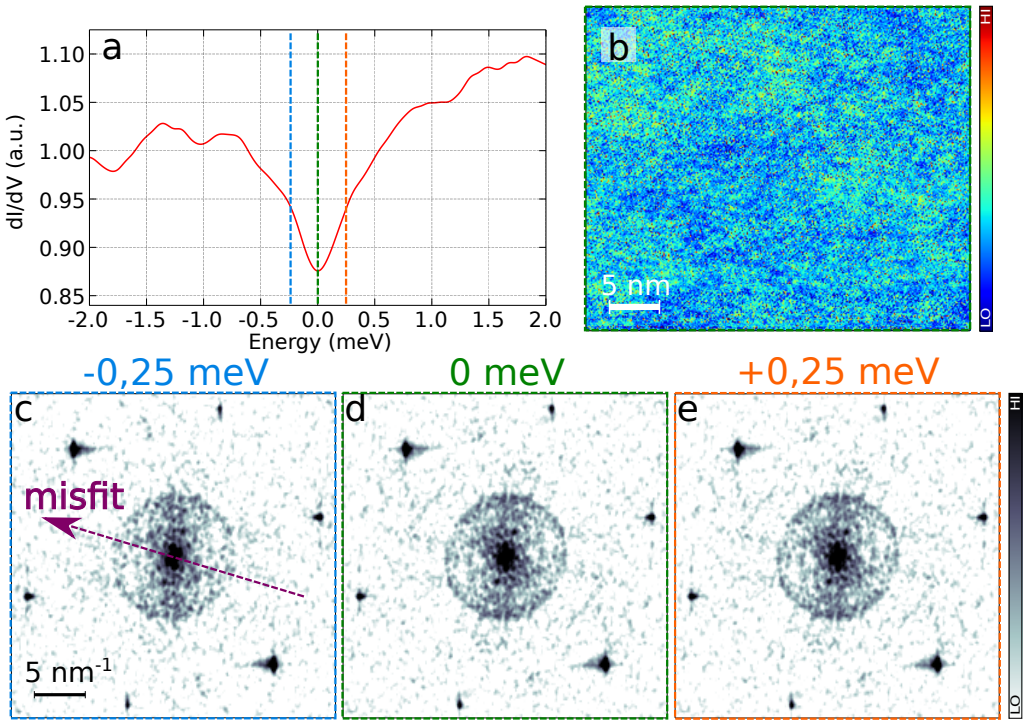

Figure 3.35: **a**. Averaged dI/dV spectrum of the second experiment. **b**. Fermi level dI/dV map. **c**. Fourier transform of the dI/dV map at $-0,25$ meV. **d** Fourier transform of the dI/dV map at Fermi level. **e** Fourier transform of the dI/dV map at $+0,25$ meV.

Two main observations can be extracted from this QPIs study in the superconducting phase. Firstly, the QPIs patterns are not different from the ones observed in the normal phase. Secondly, the QPIs patterns are non-dispersive as they do not depend on the considered energy.

In ref. [103], Brian B. Zhou *et al.* performed Fourier transform STM on superconducting heavy fermion compound $CeCoIn_5$. They exhibited the d-wave nature of the superconducting order parameter by observing **dispersive QPIs patterns** at the energy scales of superconductivity. Such a dispersion is actually expected whenever the order parameter presents nodes, as it was the case there. If one is dealing with a nodal superconductor with gap magnitude Δ_{nodal}, then, partly hole and partly electron low energy excitations appear at energies inferior in absolute value to Δ_{nodal}. Scattering between those states, which are dispersive, can eventually lead to QPIs in presence of disorder.

We think that the absence of dispersion in our QPIs calls for a nodeless order parameter. The states filling the superconducting gap should then be seen as a superposition of many Shiba-like states[11]. Those Shiba states being a mixture of electrons and holes are then likely to scatter on the misfit potential thus leading to QPIs patterns reflecting the normal phase energy contours rather than the symmetry of the order parameter. In ref. [105], Gerbold C. Menard *et al.* deposited Co magnetic impurities on a conventional superconducting monolayer of Pb, leading to the apparition of in-gap Shiba-states. Around those magnetic impurities, QPIs patterns mirroring the Fermi surface of the Pb monolayer in the normal phase were observed. This last example shows that the QPIs obtained in the superconducting phase can sometimes reflect the Fermi surface in the **normal phase**.

This does not mean that no information can be extracted through QPIs performed on a nodeless superconductor. In our case, the sensitivity to non-magnetic disorder definitely implies

[11] Yu-Shiba-Rusinov states are electron-hole excitations which appear when one introduces magnetic impurities in a superconductor (see ref. [104]). In STS, they manifest as pairs of in-gap states with opposite energies. Similar states can appear in unconventional superconductors in presence of **non-magnetic** impurities.

unconventional superconductivity. Also, if the system is in a topologically non-trivial phase, one should see topological edge states at the interface with a region with different topology.

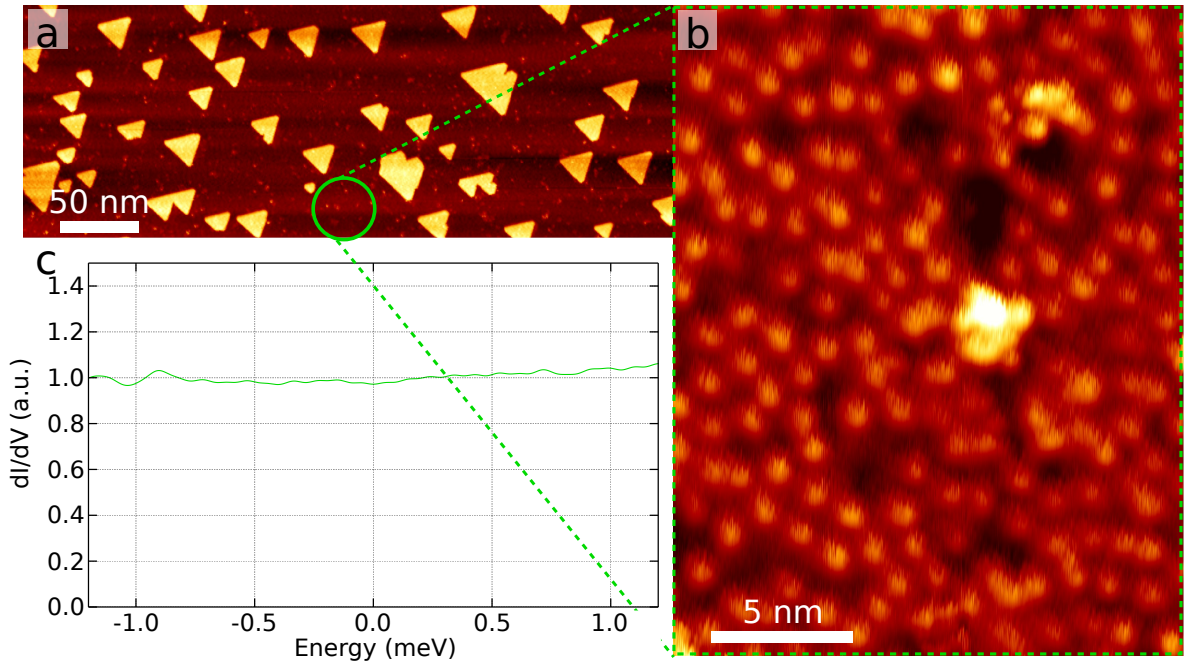

Figure 3.36: **a**. Trilayer Pb islands grown on top of $(LaSe)_{1,14}(NbSe_2)_2$. **b**. Zoomed topography map taken far from the islands. The visible balls are Pb atoms. After counting, there is a 5% coverage. **c**. Averaged dI/dV spectra obtained in an area similar to **b**.

Atomic steps naturally define an interface between the material and the vacuum. If the system is already topological (recalling that vacuum is equivalent to a topologically trivial medium) then one should observe edge states along such steps. Unfortunately, after countless tries we never were able to find any steps small enough not to damage our tip during scanning regulation. We thus opted for another solution : depositing enough Pb to grow conventional superconducting Pb islands which could potentially define better interfaces with $(LaSe)_{1,14}(NbSe_2)_2$[12].

After our first Pb deposition, we grew triangular-shaped trilayer Pb islands of typically 30 nm lateral extension in a way explained in subsection 2.4.3 (see figure 3.36 **a**). The obtained Pb islands were however too small to develop superconductivity [106]. Away from the islands, in areas like the one encircled in green on figure 3.36 **a**, one can observe Pb atoms distributed randomly across the surface (see figure 3.36 **b**). After counting, we evaluated a 5% Pb coverage in such areas, meaning that there is 1 Pb atom for every 20 Nb atoms of the superficial $NbSe_2$ monolayer.

On figure 3.36 **c**, is represented the averaged dI/dV spectrum in an area similar to the one of figure 3.36 **b**. This spectrum is completely flat and does not present any of the features encountered in previous experiments. This means that a 5% coverage of non magnetic Pb impurities is enough to kill superconductivity which is, according to us, a clear signature of the unconventional nature of superconductivity in $(LaSe)_{1,14}(NbSe_2)_2$. Nevertheless, one needs to be cautious, for this experiment was only performed once on few areas of one same sample (which nonetheless exhibited clear superconducting signatures before Pb evaporation). Moreover, some areas of the samples presented significant filling of the gap up to more than 90%. It is not impossible that our tip landed in such areas. To further study the effect of non-magnetic disorder on superconductivity we are planning on performing spectroscopy measurements on

[12]One way of seeing the unconventional nature of the superconducting order parameter (gap sign changes) is to use well-controlled defects.

samples on which disorder was introduced by electron irradiation.

3.6.6 Interpretation of the small value of the superconducting gap in terms of tunnelling selectivity

For now, we mostly commented on the filling of the superconducting gap but not much on its small value $\Delta_{SC} = 0,28$ meV. We recall that if $(LaSe)_{1,14}(NbSe_2)_2$ was a BCS superconductor, its superconducting gap should be approximatively equal to $0,6$ meV. The potential unconventional nature of the superconductivity in $(LaSe)_{1,14}(NbSe_2)_2$ is not sufficient to fully understand this difference. In the following, we propose an interpretation able to explain the smallness of the measured gap Δ_{SC}.

With all this in mind, we can now give a possible interpretation for the observed superconducting gap of $0,28$ meV in $(LaSe)_{1,14}(NbSe_2)_2$. Thanks to the theoretical predictions of ref. [8], one can expect to have two unconventional order parameters : one developing around Γ and the other one around K/K'. Since the electrons of the K/K' pockets possess higher momenta $\overrightarrow{k}_{\parallel}$ compared to the ones of the Γ pocket, it is possible that our tip-sample tunnelling geometry was mostly sensitive to the Γ gap and only to a limited degree to the K/K' gap (see subsection 2.2.2). The fact that such tunnelling selectivity was also observed in parent compound 2H-$NbSe_2$ further supports our hypothesis [107]. Nevertheless, this assertion needs to be proven experimentally. One way of verifying this hypothesis would be to carry out spectroscopy measurements with a different tip-sample geometry. For example, one can imagine to approach a Au surface with a $(LaSe)_{1,14}(NbSe_2)_2$ sample glued to a tip holder in a configuration such that the $NbSe_2$ layers are perpendicular to the Au surface. In this configuration the tunnelling selectivity might greatly differ and it could in principle be possible to look for previously "invisible" spectroscopic signatures. We are currently planning on performing this experiment.

3.7 Example of another misfit compound

This short subsection is meant to illustrate the fact that it is possible to exploit other, but similar, heterostructures to study the physics of few layers TMDs. Here, we consider the example of $(LaSe)_{1,14}(NbSe_2)$. This compound in another misfit superconducting compound of the family of $(LaSe)_{1,14}(NbSe_2)_2$. Both materials are very similar. $(LaSe)_{1,14}(NbSe_2)$ consists in alternation of LaSe bilayers and of $NbSe_2$ **monolayers**. The two kind of layers are also commensurate in one direction and incommensurate in the perpendicular one with an approximate commensurate ratio also of $7/4$ (just as $(LaSe)_{1,14}(NbSe_2)_2$). In the end, the main structural difference between the two compounds is the number of $NbSe_2$ layers sandwiched between LaSe bilayers.

Since in $(LaSe)_{1,14}(NbSe_2)$, only one monolayer of $NbSe_2$ is sandwiched between LaSe bilayers, $NbSe_2$ is potentially twice as electron doped as $(LaSe)_{1,14}(NbSe_2)_2$. Taking into account the tendency of $(LaSe)_{1,14}(NbSe_2)_2$ to behave as e-doped monolayer $NbSe_2$, one can easily imagine than $(LaSe)_{1,14}(NbSe_2)$ will behave as monolayer $NbSe_2$ but with a different doping value. When cleaving $(LaSe)_{1,14}(NbSe_2)$, the top cleaved surface is either a LaSe terminated surface or a $NbSe_2$ terminated surface with a $1/2$ probability. This is due to the fact that no adjacent layers are van der Walls bonded.

In figure 3.37 **a**, is displayed a STM image (taken at 2 mV) of $(LaSe)_{1,14}(NbSe_2)$ surface. The modulus of the Fourier transform of the STM map of figure 3.37 **a** is represented in figure 3.37 **b**. Those images were obtained by collaborators of the Center of Low Temperature Physics of Kosice, Slovakia. The topography image presents $NbSe_2$ terminated surface. A 2×2 charge modulation, just as the one observed at the surface of $(LaSe)_{1,14}(NbSe_2)_2$, can be seen. This later one is also seen in the Fourier transform, lying at half the Bragg peaks. What is striking in this Fourier transform image is the similarities it shares with its $(LaSe)_{1,14}(NbSe_2)_2$ homologous. The incommensurability peaks and replica are all present as well as the "Q1"

generated QPIs circle around Γ sitting at the exact same position in reciprocal space as the one seen in $(LaSe)_{1,14}(NbSe_2)_2$. This might seem a bit unsettling given the arguments on the doping that were just exposed, but one has to remember that this $NbSe_2$ terminated surface does not behave as the bulk. For bulk $(LaSe)_{1,14}(NbSe_2)$, a monolayer $NbSe_2$ receives electrons from its two adjacent LaSe layers. For the surface, **only one** LaSe layer is likely to give electrons to the superficial $NbSe_2$ layer. The surface of $(LaSe)_{1,14}(NbSe_2)$ thus behaves as the bulk of $(LaSe)_{1,14}(NbSe_2)_2$. Luckily for us, the surface of $(LaSe)_{1,14}(NbSe_2)_2$ shares the same doping level as bulk $(LaSe)_{1,14}(NbSe_2)_2$. The critical superconducting temperatures and, *a fortiori*, the superconducting properties of $(LaSe)_{1,14}(NbSe_2)$ and $(LaSe)_{1,14}(NbSe_2)_2$ differ[13]. Studying $(LaSe)_{1,14}(NbSe_2)$'s surface potentially means studying monolayer $NbSe_2$ in the same doping regime as in $(LaSe)_{1,14}(NbSe_2)_2$ but with different superconducting properties.

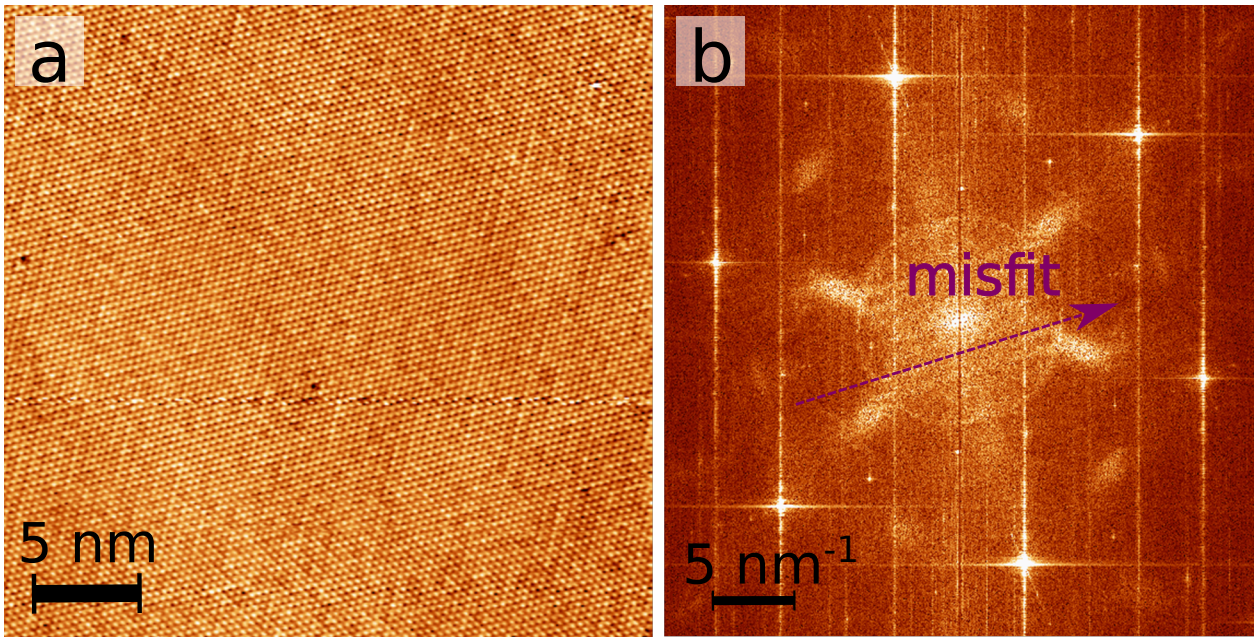

Figure 3.37: **a**. Topography STM image of parent misfit compound $(LaSe)_{1,14}(NbSe_2)$. **b**. Modulus of the Fourier transform of **a**.

3.8 Conclusion

In this chapter, we have seen (by mean of QPIs experiments) that the band structure of $(LaSe)_{1,14}(NbSe_2)_2$ is very similar to the one of monolayer $NbSe_2$, but rigidly shifted of approximatively $0,3$ eV towards lower energies. In particular, the comparison between our STS measurements and DFT calculations showed the presence of a strong Ising spin-orbit coupling in $(LaSe)_{1,14}(NbSe_2)_2$. Our work opens the possibility of using bulk misfit heterostructures (such as $(LaSe)_{1,14}(NbSe_2)_2$) to investigate the physics of few layers transition metal dichalcogenides at electron-doping levels never achieved in the literature. More specifically, one can imagine to either change the rock-salt layer (by replacing LaSe with PbSe for example) or the number of $NbSe_2$ layers to effectively change the doping, and consequently, the electronic properties of the misfit heterostructure.

In our doping regime, we observed different electronic features than in monolayer $NbSe_2$. First, we highlighted the presence of a 2×2 charge modulation in place of the 3×3 CDW observed in both bulk and monolayer $NbSe_2$. DFT calculations exhibited the tendency of

[13] In ref. [9], it is shown that the superconducting critical temperature of $(LaSe)_{1,14}(NbSe_2)$ is equal to $2,2$ K. We recall that $(LaSe)_{1,14}(NbSe_2)_2$ has a superconducting critical temperature somewhere between 4 K and $5,3$ K.

monolayer $NbSe_2$ to undergo a electron-doping-driven phase transition from a 3×3 charge order to a 2×2 charge order. Nevertheless, such a transition should occur at lower electron doping realizations than ours, which either means that the 2×2 charge modulation has a different origin (possibly correlations which were not taken into account in the calculations) or that the charge transfer (and *a fortiori* the doping) locally varies because of invisible-to-our-probe La vacancies, thus allowing the system to, locally, enter a 2×2 charge order. Second, we observed signatures of nodeless unconventional superconductivity, in qualitative agreement with theoretical works which predict triplet superconducting order parameters (p-wave or f-wave) and a possible route towards topological superconductivity. In order to confirm the unconventional nature of the order parameter we plan on performing several additional experiments such as specific heat measurements, quasiparticle interferences measurements after introduction of defects in a controlled way by mean of Ar sputtering or electron irradiation and finally, performing spectroscopy in another tip-sample configuration to exhibit eventual tunnelling selectivity effects.

Chapter 4

Inhomogeneous insulating to pseudo-metallic transition in a doped Mott insulator

The Iridate compound Sr_2IrO_4 was originally studied because it shares a common structure with the cuprate La_2CuO_4. This material was thus likely to provide new physical insight as to the intriguing nature of the pseudo-gap phase and the origin of superconductivity in high-T_c superconductors [108, 109]. However, as a spin-orbit induced Mott insulator, Sr_2IrO_4 also presents a different yet equally interesting kind of physics. Moreover, recent theoretical works suggest that doping should turn the material into a topological superconductor.

In this chapter, we present a STM/STS study performed on electron-doped Sr_2IrO_4. We first show that, as the doping increases, the system undergoes an inhomogeneous phase transition from a Mott insulating phase to a pseudo-metallic one. Second, we also exhibit the appearance of orientational order in the organization of the pseudo-metallic areas. Finally, we present spectroscopy performed on pure Sr_2IrO_4. This study is the only one, in our knowledge, which combines measurements in both pristine and doped compound. As for the question of topological superconductivity, further studies are yet to be done.

The first section presents one of our motivations, namely the theoretical prediction of topological superconductivity in doped Sr_2IrO_4. The second section consists in a short introduction to Mott physics. The third section explains the spin-orbit origin of the Mott insulating behaviour of Sr_2IrO_4. Sections 4, 5 and 6 are dedicated to the presentation and discussion of the STM/STS results obtained during the thesis.

4.1 Predictions of topological superconductivity in doped Sr_2IrO_4

The crystal structure of Sr_2IrO_4 is represented in figure 4.1 and is close to being a perfect perovskite layered structure. The material is made out of alternations of IrO_2 layers and SrO bilayers. All Ir atoms lie at the centers of oxygen octahedra. An IrO_2 plane of a perfect perovskite structure is represented in figure 4.2 **a**. Nevertheless, the structure of Sr_2IrO_4 is slightly deviated from a perfect perovskite structure and rather looks like the one of figure 4.2 **b**. In the actual compound, the oxygen octahedra are rotated of $\theta \simeq 12°$, resulting in an expanded unit cell [110].

One of the consequence of this tilting is that all the O atoms within an IrO_2 plane are no longer inversion centers for the structure, as they were in the perfect perovskite scenario. This implies that the electron hopping between two neighbouring Ir atoms becomes spin-dependent, thus making the hopping Hamiltonian very similar to a Rashba spin-orbit coupling Hamiltonian. If Sr_2IrO_4 can be made superconducting, then, according to what has already been said in

section 1.3, the superconducting order parameter necessarily mixes both spin-singlet and spin-triplet contributions. It was predicted that Sr_2IrO_4 could be turned into a superconductor by mean of electron or hole doping [108, 111]. In 2015, Y. J. Yan *et al.* performed a STM/STS study in which they deposited potassium on top of Sr_2IrO_4, consequently electron-doping it, and observed what was interpreted as a superconducting V-shaped low-energy gap [112]. In 2017, it was shown that hole-doped Sr_2IrO_4 should theoretically enter a topological regime [10].

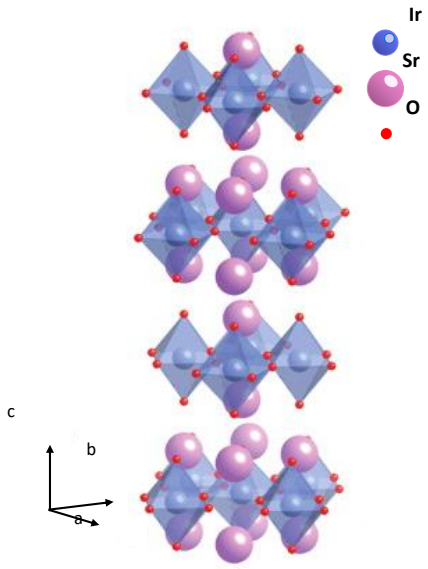

Figure 4.1: Crystal structure of Sr_2IrO_4.

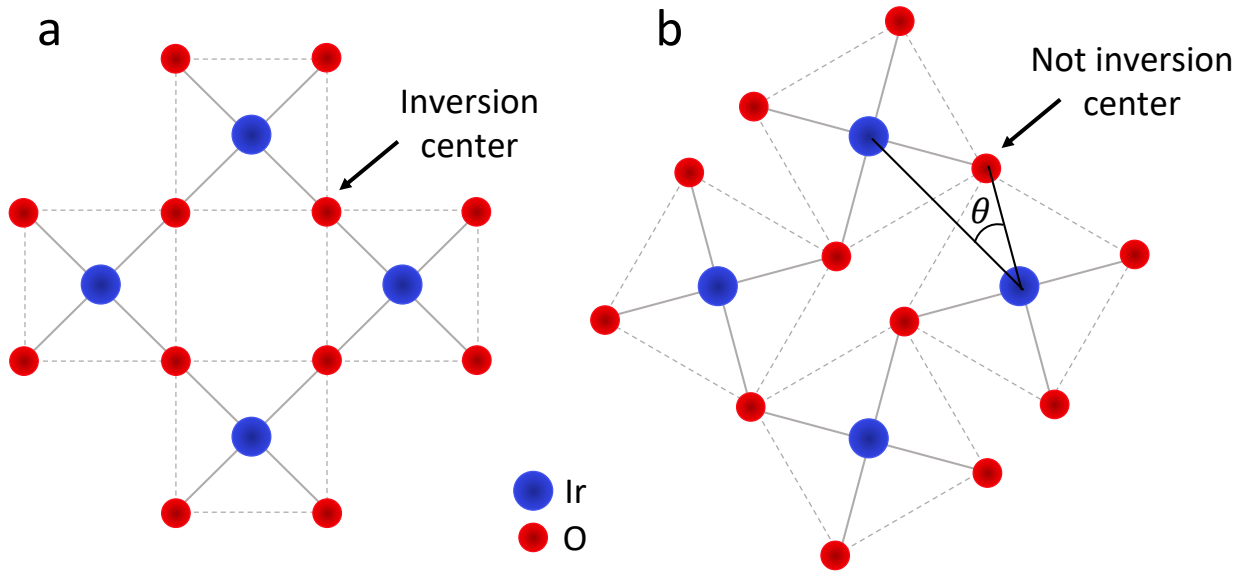

Figure 4.2: **a**. Top view of an IrO_2 plane if the structure was perfectly perovskite-like. **b**. Top view of an IrO_2 plane of Sr_2IrO_4. Contrary to **a**, the oxygen atoms are no longer inversion centers.

4.2 Mott insulators

Band theory was developed in the 1930s and describes the states of electrons in solid materials. In the same way that there are a collection of accessible electronic levels in an individual atom, which can be either empty or occupied, band theory predicts that not all energies are available for the electrons in a solid but only energies within given ranges. When atoms are brought together in a periodic fashion in order to form a solid, the atomic orbitals will overlap and give rise to a set of states really close from one another. Those sets are called " bands ". The unavailable energy ranges separating two consecutive bands are called " forbidden bands ". In metals, the position of the chemical potential lies within a band, such that low energy excitations are possible and a charge current is likely to appear, contrary to insulators, where it lies within a forbidden band.

Within the context of band theory, only single electronic states are considered because the interaction between electrons is neglected[1]. This approach was very fruitful at the time since it allowed to describe the electronic properties of many materials. Nonetheless, some compounds presenting intriguing insulating behavior, when expected to be metals within the framework of band theory, were discovered. In order to interpret such physics, one needs to take into account correlations, or so to say, Coulomb interaction between electrons in this specific case.

A famous example of correlated system is the Mott insulator. In this section, we will present a short introduction to Mott Physics through the so-called Hubbard model. The calculations performed in the section are inspired by ref. [114].

Let us consider atoms sitting on an infinite periodic lattice with one electron per site and an inter-atomic distance a. For simplicity, all equations will be derived on a square lattice. The Hubbard model simply consists in considering both hopping to first neighbor and on-site Coulomb repulsion. The Hubbard Hamiltonian is the following :

$$H = H_{kin} + H_{int} = -\sum_{<i,j>,\sigma} (t_{ij} c^\dagger_{i,\sigma} c_{j,\sigma} + h.c.) + U \sum_i n_{i,\uparrow} n_{i,\downarrow}, \tag{4.1}$$

where $c^\dagger_\alpha$ is the electronic creation operator on the α site and c_β is the electronic annihilation operator on the β site. As fermionic operators, one has the anti-commutation relations $\{c^\dagger_\alpha, c^\dagger_\beta\} = \{c_\alpha, c_\beta\} = 0$ and $\{c^\dagger_\alpha, c_\beta\} = \delta_{\alpha\beta}$. The t_{ij} parameter is the hopping amplitude from site i to j. For simplicity, we will take t_{ij} constant and equal to t. U represents the on-site Coulomb repulsion, thus $U > 0$. The term $n_{\alpha,\sigma} = c^\dagger_{\alpha,\sigma} c_{\alpha,\sigma}$ is the number operator giving the number of electrons of spin σ on site α.

The first term is the kinetic part of the Hamiltonian. Supposing $U = 0$, it is possible to diagonalize H_{kin} in k-space. Then one can compute the following dispersion : $\varepsilon(\overrightarrow{k}) = -2t(\cos(k_x a) + \cos(k_y a))$. Because there is only one electron per site, the band is half-filled and the Hubbard Hamiltonian at $U = 0$ depicts a metallic behavior.

Now, we will turn on a finite Coulomb repulsion $U \neq 0$. An analytic solution of the Hubbard model on the square lattice is still not known such that one should get physical insight through simpler considerations. In the following, we will present one way of intuiting how the Hubbard model allows the opening of a gap when band theory predicts a metallic behavior.

For simplicity, let us first focus on the two-site Hubbard Hamiltonian (the sites are called respectively 1 and 2) :

$$H_{2\ sites} = -t(c^\dagger_{1\uparrow} c_{2\uparrow} + c^\dagger_{2\uparrow} c_{1\uparrow} + c^\dagger_{1\downarrow} c_{2\downarrow} + c^\dagger_{2\downarrow} c_{1\downarrow}) + U(n_{1\uparrow} n_{1\downarrow} + n_{2\uparrow} n_{2\downarrow}), \tag{4.2}$$

In the Foch basis $|n_{1\uparrow}, n_{1\downarrow}, n_{2\uparrow}, n_{2\downarrow}\rangle$, because both spin and number of particles are conserved, one can consider several state subspaces completely independent from each other. The first space corresponds to the case where both sites 1 and 2 are empty and is only formed by $|0,0,0,0\rangle$.

[1] The Fermi liquid theory justifies this approximation [113].

The energy of this state is equal to 0. The second subspace is composed of one particle states of spin up : $|1,0,0,0\rangle$ and $|0,0,1,0\rangle$. The expression of $H_{2\ sites}$ on the $(|1,0,0,0\rangle, |0,0,1,0\rangle)$ basis for this subspace is $\begin{pmatrix} 0 & -t \\ -t & 0 \end{pmatrix}$, such that the eigenvalues of the associated eigenstates are equal to $\pm t$, signifying that electrons can freely hop from one site to the other. The third subspace is composed of one particle states of spin down. Because of the symmetry of the model with respect to spin polarization, the associated eigenvalues are also equal to $\pm t$. The fourth (fifth) subspace includes two-particle states with spin up (down) electrons and is composed of $|1,0,1,0\rangle$ ($|0,1,0,1\rangle$). The eigenvalues associated to both fourth and fifth subspaces are equal to 0[2]. The sixth subspace contains two-particle states where both electrons have opposite spins. It includes $|1,1,0,0\rangle$, $|0,0,1,1\rangle$, $|1,0,0,1\rangle$, and $|0,1,1,0\rangle$. The expression of the two-site Hubbard Hamiltonian on the $(|1,1,0,0\rangle, |0,0,1,1\rangle, |1,0,0,1\rangle, |0,1,1,0\rangle)$ basis is $\begin{pmatrix} U & 0 & -t & -t \\ 0 & U & -t & -t \\ -t & -t & 0 & 0 \\ -t & -t & 0 & 0 \end{pmatrix}$. After calculation one finds the following four eigenvalues: 0, U and $\frac{U}{2} \pm \sqrt{4t^2 + \frac{U^2}{4}}$. The seventh (eighth) subspace touches the three-particle states $|1,1,1,0\rangle$ and $|1,0,1,1\rangle$ ($|1,1,0,1\rangle$ and $|0,1,1,1\rangle$). On the $(|1,1,1,0\rangle, |1,0,1,1\rangle)$ or the $(|1,1,0,1\rangle, |0,1,1,1\rangle)$ basis, the expression of $H_{2\ sites}$ is $\begin{pmatrix} U & -t \\ -t & U \end{pmatrix}$ such that the eigenenergies are equal to $U \pm t$ for both seventh and eighth subspaces. The ninth and final subspace is the four-particle state $|1,1,1,1\rangle$ when all sites are doubly occupied. The eigenvalue of this state is equal to $2U$.

Let us not forget that we were originally interested in a half-filled band for the full Hubbard model. In the two-site Hubbard model, a maximum of four electrons can occupy the available states. Thus, in order to be the closest to the physical situation of interest, we will only focus on fourth, fifth and sixth subspaces which are exclusively composed of two-particle states. We recall that the eigenvalues of this new subspace of dimension 6 can be equal to 0, U or $\frac{U}{2} \pm \sqrt{4t^2 + \frac{U^2}{4}}$. In the limit $U \gg t$, a set of four states at 0 energy is separated by U from an higher-energy set of two states[3]. One qualitatively understands that by going from the two-site system to the infinite lattice while staying in the large-U limit, the two sets of states will become two bands separated by a gap roughly equal to U. The lower-energy collection of states is called the "lower Hubbard band" (LHB) whereas the higher-energy collection of states is called the "upper Hubbard band" (UHB).

Let us imagine a lattice with one electron per site and antiferromagnetic ordering such that any electron with a given spin polarity is surrounded by nearest neighbor electrons with opposite spin polarity. If $U = 0$, then an electron can easily hop to its neighboring site, such that a charge current can flow : the system is metallic. Now, if U is turned on, it will be energetically unfavorable for an electron to jump to its nearby site unless its kinetic energy (represented by t) is sufficiently large to overcome Coulomb repulsion. If correlations are high enough, then the electrons are somehow bound to their sites, no electrical current is possible : the system becomes insulating. We can see that the ratio $\frac{U}{t}$ is at play in deciding the metallic or insulating nature of the materials. It will not be derived here but one can prove that the LHB of the two-site Hubbard model has exactly the same eigenspectrum as the two-site Heisenberg

[2]Because of Pauli's exclusion principle, no hopping is possible, and thus, the on-site Coulomb interaction does not contribute.

[3]It is important to keep in mind that those states are not single electronic states but many particles states. One cannot think in terms of single electron occupations of two out of the four lower energy states, and thus that two degenerate states are available. The excitations of the system are also many particles excitations and no longer single quasiparticle excitations.

Hamiltonian $H_{Heisenberg} = J\overrightarrow{S}_1 \cdot \overrightarrow{S}_2$ with an antiferromagnetic coupling $J = \frac{4t^2}{U}$ and $\overrightarrow{S}_i$ a 1/2 spin on site i (this is valid only when $U \gg t$ [29]). This suggests that a Mott insulator described by the Hubbard model possesses an antiferromagnetic order. Given this last statement one can now work out a hand-waving explanation of how insulating behavior arises in such materials.

It is possible to estimate a value of the ratio $\frac{U}{t}$ at which the metal-insulator transition (MIT) occurs by estimating the energy associated to the two ground states of the system in the two extremal limits $U = 0$ and $U \to +\infty$ of the model which are respectively the Fermi sea $|FS\rangle$[4] and the localized one-particle per atomic site state $|I\rangle = \prod_{i=1}^{N} c^{\dagger}_{i,\sigma_i} |0\rangle$, where N is the total number of sites and σ_i the spin of the electron on site i. The energy of the Fermi sea ground state is :

$$E_{FS} = \langle FS| H |FS\rangle = \langle FS| H_{kin} |FS\rangle + \langle FS| H_{int} |FS\rangle , \tag{4.3}$$

Considering a half-filled band of width $2W$, with the position of the Fermi level at 0 energy, one has the following expression for the kinetic part of the Fermi sea ground state energy :

$$\langle FS| H_{kin} |FS\rangle = \int_{-W}^{0} \rho(\varepsilon)\varepsilon d\varepsilon, \tag{4.4}$$

where ε is the energy and $\rho(\varepsilon)$ the density of states. The spin degeneracy is taken into account in $\rho(\varepsilon)$. If one now assumes a constant density of states $\rho = \frac{2N}{2W}$ one gets :

$$\frac{\langle FS| H_{kin} |FS\rangle}{N} = -\frac{W}{2}, \tag{4.5}$$

The interacting part of the Fermi sea ground state energy is :

$$\langle FS| H_{int} |FS\rangle = \langle FS| U \sum_i n_{i,\uparrow} n_{i,\downarrow} |FS\rangle = U \sum_i \langle FS| n_{i,\uparrow} n_{i,\downarrow} |FS\rangle , \tag{4.6}$$

$$\langle FS| H_{int} |FS\rangle = U \sum_i \langle FS| n_{i,\uparrow} |FS\rangle \langle FS| n_{i,\downarrow} |FS\rangle = U \sum_i \frac{1}{2} \times \frac{1}{2} = \frac{UN}{4}, \tag{4.7}$$

$$\frac{\langle FS| H_{int} |FS\rangle}{N} = \frac{U}{4}, \tag{4.8}$$

The total energy of the Fermi sea brought back to one site is :

$$\frac{E_{FS}}{N} = -\frac{W}{2} + \frac{U}{4}, \tag{4.9}$$

We can also compute the energy of the ground state for infinite U limit :

$$E_I = \langle I| H |I\rangle = \langle I| H_{kin} |I\rangle + \langle I| H_{int} |I\rangle , \tag{4.10}$$

Because in this case an electron is bounded to its atomic site, the kinetic part of E_I is equal to 0. This can easily be computed given the expression of H_{kin}. Moreover, by definition of $|I\rangle$, no double occupancy is possible such that $\langle I| H_{int} |I\rangle = 0$. In the end :

$$\frac{E_I}{N} = 0, \tag{4.11}$$

One can notice that if $U < 2W$ then the delocalized ground state $|FS\rangle$ is more favorable than $|I\rangle$. This observation is consistent with the fact that when the kinetic energy of the electrons is big enough, they tend to delocalize such that the system becomes metallic. The bandwidth $2W$ is indeed directly proportional to the transfer integral t. The approach which was just exposed

[4] In this picture, the electron are delocalized and labelled by crystalline momenta.

allows to highlight the existence of a critical value $U \simeq 2W$ (although very dependent on the band structure) of the on-site Coulomb repulsion above which one switches from metallic to an insulating state.

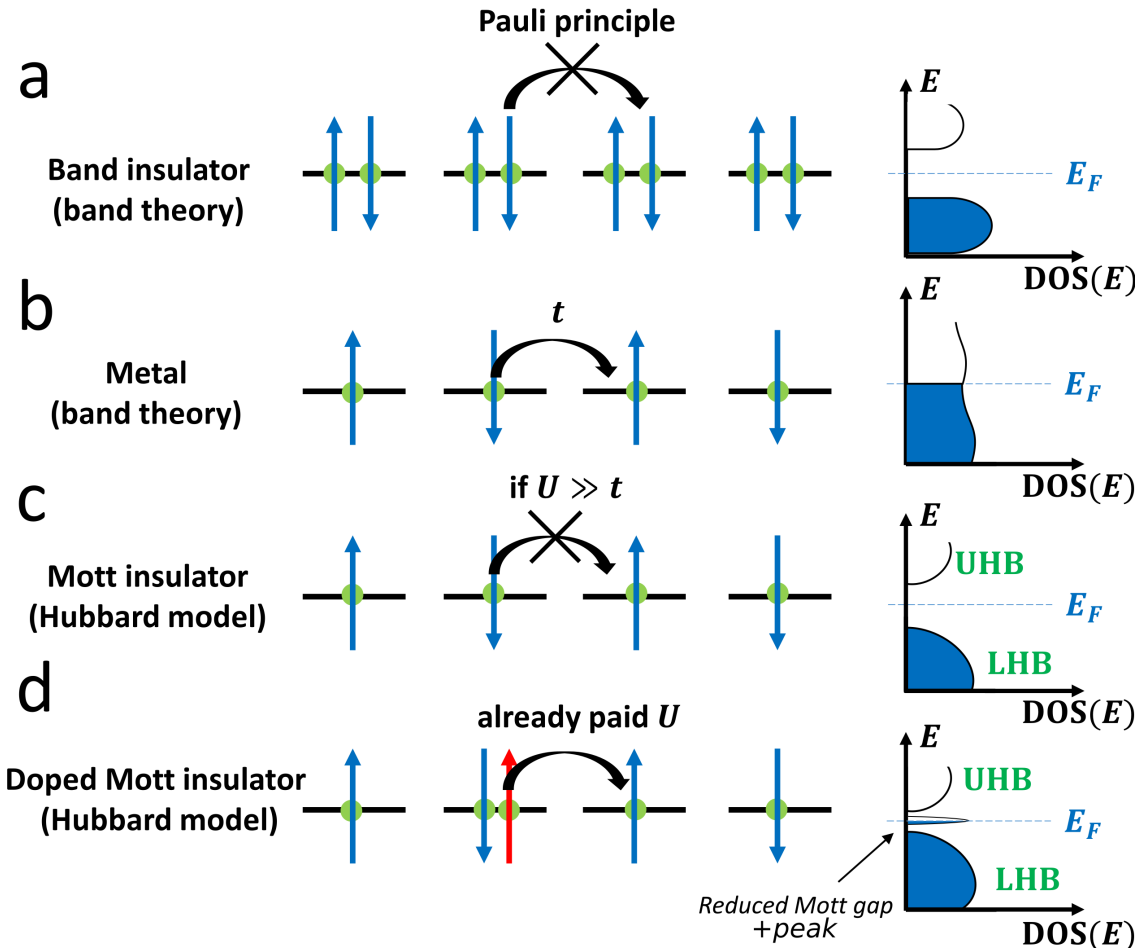

Figure 4.3: **a**. Cartoon of a band insulator. Every site is doubly occupied and no hopping is possible due to Pauli exclusion principle. **b**. Cartoon of a metal in band theory. Every site is singly occupied and electrons can hop from one site to the next potentially carrying current. **c**. Cartoon of a Mott insulator. Every site is singly occupied but the strong on-site Coulomb repulsion prevents hopping. **d**. Cartoon of a doped Mott insulator. Here It is electron doped. The Coulomb energy U has already been paid : a current can flow.

So far, we only discussed Mott Physics at half-filling. It may be interesting to look at what happens when the chemical potential lies above or under half-filling. Experimentally, a way of accessing such a situation is to dope either with electrons or hole a Mott insulator. If the undoped material is insulating, which implies $U > 2W$, then a ground state with one electron localized on each site is more likely to describe faithfully the system. If now the system is electron-doped, then a few sites will be doubly occupied, which means that some pairs of electrons will whatever happens be subject to Coulomb repulsion. For electrons sitting on a doubly occupied sites, hopping to singly-occupied nearest neighbor sites won't cost any additional energy such that delocalization becomes favorable. The reasoning is similar in the case of hole-doping where electrons can hop on many empty sites causing again delocalization. This way, electron or hole doping will reduce the size of the Mott gap, closing it for large enough dopant concentrations eventually turning the system into a metal. Moreover, a quasiparticle peak at Fermi level is expected to appear [115]. Through this very naive picture, one understands that introducing doping into a Mott insulator is a way of tuning the U/t ratio. For a given

Mott material, the values of both U and t can often be extracted by comparing the data with theory, however, the Hubbard model is most of the time insufficient for catching all the physics. In the next part, we will see the an example of compound in which the spin-orbit interaction has to be taken into account in order to explain the observed Mott features.

4.3 Spin-orbit induced Mott insulator Sr_2IrO_4

The Mott insulator behavior of 5d Transition Metal Oxide iridate compound Sr_2IrO_4 cannot be explained with the simple model presented previously. Contrary to localized 3d electrons which can lead to Mott physics [116], 5d electrons are more spatially extended such that the overlap of neighboring orbitals should increase, and thus, t also increases. Because of this last observation, iridium oxides were expected to be metallic, and yet, many were actually found to be insulating [117]. This last statement is illustated in figure 4.4 in which one can see the comparison between that the spatial extents of the radial part of the wave functions of 3d, 4d and 5d electrons.

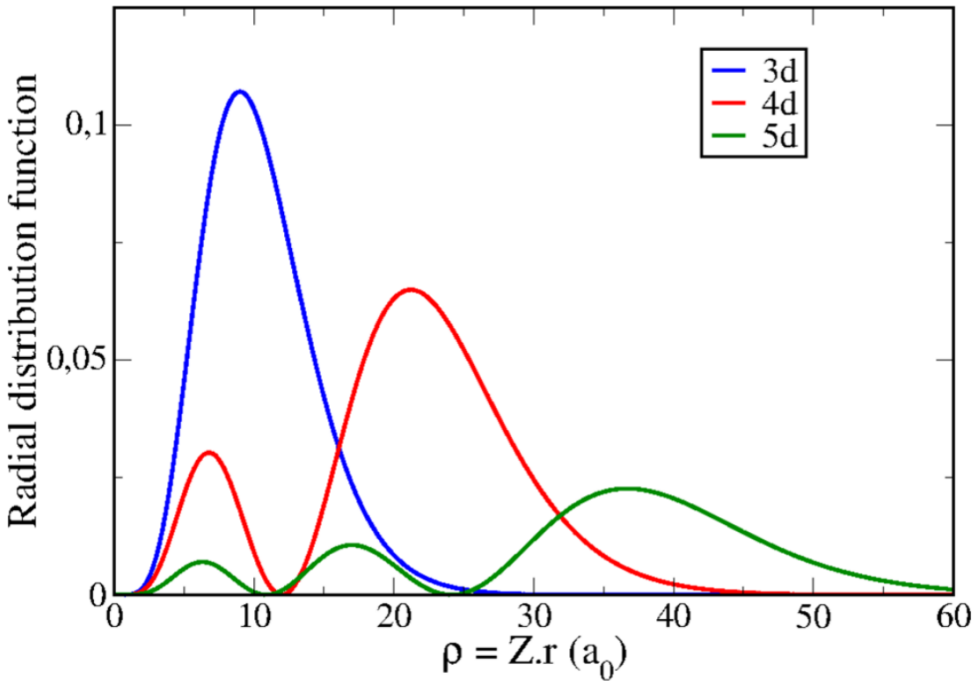

Figure 4.4: Comparison between the spatial extents of the radial part of the wave functions of 3d, 4d and 5d electrons. 5d are much more extended spatially which is not in favor of a Mott insulating behaviour (image taken from ref. [118]).

In order to understand the origin of the insulating properties of Sr_2IrO_4, one has to have a look at its crystal structure, represented on figure 4.1. It has a layered perovskite structure consisting in alternation of IrO_2 and SrO layers. Each Ir atom has a $5d^5$ electronic configuration and is located at the center of an octahedron (which 6 apexes are oxygen atoms), such that octahedral crystal field lifts the degeneracy of the 5d orbitals between t_{2g} and higher in energy e_g sets of states. In addition to this effect, Ir has a substantial atomic number (Z=77) which implies that the 5d electrons are subject to strong spin-orbit coupling. This spin-orbit coupling splits the t_{2g} states between a J_{eff}=3/2 completely filled band and a J_{eff}=1/2 half-filled band [29]. The correlations then suffice to split the J_{eff}=1/2 band into a lower Hubbard band (LHB) and an upper Hubbard band (UHB) separated by a gap, turning the system into a Mott insulator.

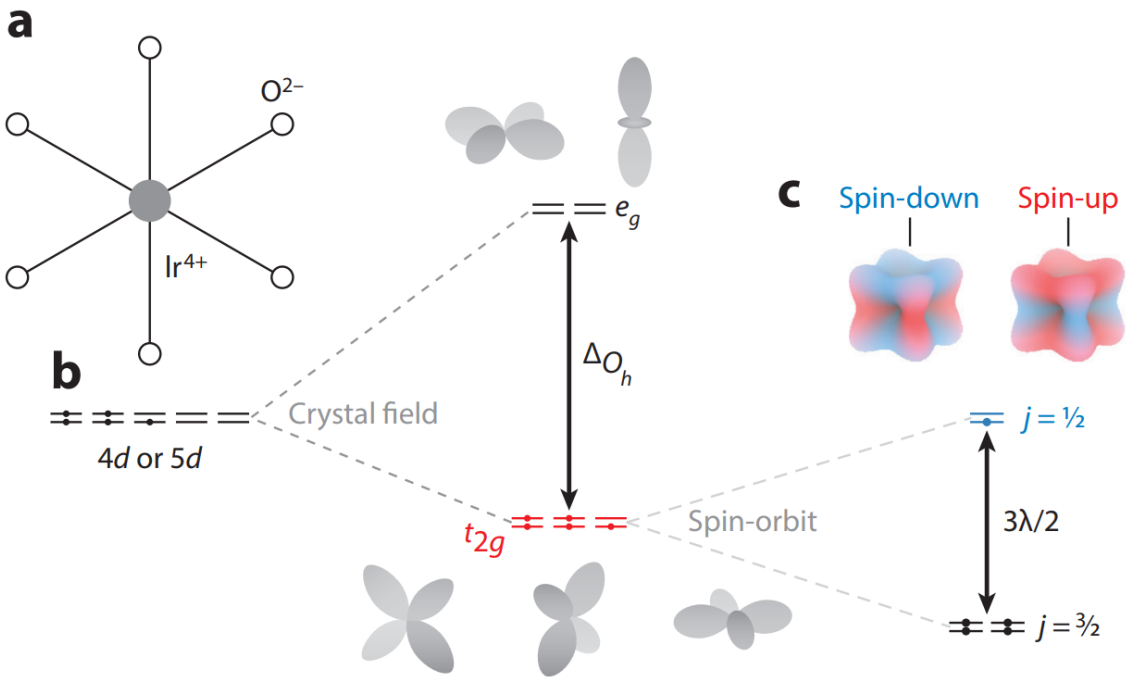

Figure 4.5: **a**. Ir atom at the center of an oxygen octahedron. **b**. Its electronic configuration is $5d^5$. The crystal field lifts the degeneracy between t_{2g} and e_g stets of states. **c**. The spin-orbit lifts the degeneracy within t_{2g} levels in a J_{eff}=3/2 completely filled band and a J_{eff}=1/2 half-filled band with reduced band width allowing the system to turn into a Mott insulating phase (image taken from ref. [29]).

4.4 Metal to insulator transition in $(Sr_{(1-x)}La_x)_2IrO_4$

Pure Sr_2IrO_4 has already been intensively studied by many methods such as angle-resolved photoemission spectroscopy (ARPES) [119, 120], optical conductivity [121, 122, 119], resonant inelastic X-ray scattering (RIXS) [123] and Scanning Tunnelling Microscopy/Spectroscopy (STM/STS) [124, 125].The measured values of the gap vary greatly from one experiment to the other but were partly reconciled by taking account tip-induced band bending effects in STM studies on lightly doped Sr_2IrO_4 samples [126].

The Metal-Insulator Transition (MIT) in doped Sr_2IrO_4 is actively investigated [127, 128, 129] but many questions remain unanswered. There are several ways to turn a Mott insulator into a metal such as applying pressure [130, 131], gating it by deposing another material on top of it [132, 133] or even doping the system[134, 135, 136]. In electron doped compound $(Sr_{(1-x)}La_x)_2IrO_4$, only few experiments were performed. The ARPES ones agree as to where in First Brillouin Zone the Mott gap should close for high enough dopants concentrations but not on the position of the LHB with respect to Fermi level for lightly doped samples [127, 128]. This last remark suggests to have a deeper look at the passage from pure Sr_2IrO_4 to lightly doped $(Sr_{(1-x)}La_x)_2IrO_4$. Because only occupied states can be observed in photoemission, the gap cannot be accessed which makes the interpretation of the results delicate. STS measurements allow to measure the local density of states (LDOS) both beneath and above Fermi level which makes it the perfect tool to probe the spatial distribution of the Mott gap in those materials. It was in this perspective that a recent STM/STS study was performed in $(Sr_{(1-x)}La_x)_2IrO_4$ [129], revealing a spatially inhomogeneous doping driven MIT as the Mott gap varies at nanometer scale. However, no STM/STS experiments as yet shown a full analysis of MIT with doping

including pure Sr_2IrO_4.

4.4.1 Topographic measurements

In this section, we present scanning tunnelling microscopy (STM) measurements which were carried out on pure Sr_2IrO_4 as well as on $(Sr_{(1-x)}La_x)_2IrO_4$ samples with varying La doping concentrations ($x = 1,5\%$, $x = 2,3\%$ and $x = 6\%$). The doping concentrations x were determined via EDX studies. Given the great variety of contradictory results in iridate compounds systems, it is also very important to emphasize that all the observed crystals were grown in the same conditions using the same self-flux method. The samples were cooled down to liquid nitrogen temperature and cleaved in ultrahigh vacuum under a pressure of approximatively $8 \cdot 10^{-11}$ mbar directly before being loaded into the STM head, also thermalized at 77 K. Cleaving samples at low enough temperature is mandatory in order to obtain clean surfaces. Samples cleaved at room temperature are indeed subject to unwanted surface reorganization of Sr and/or O atoms [137].

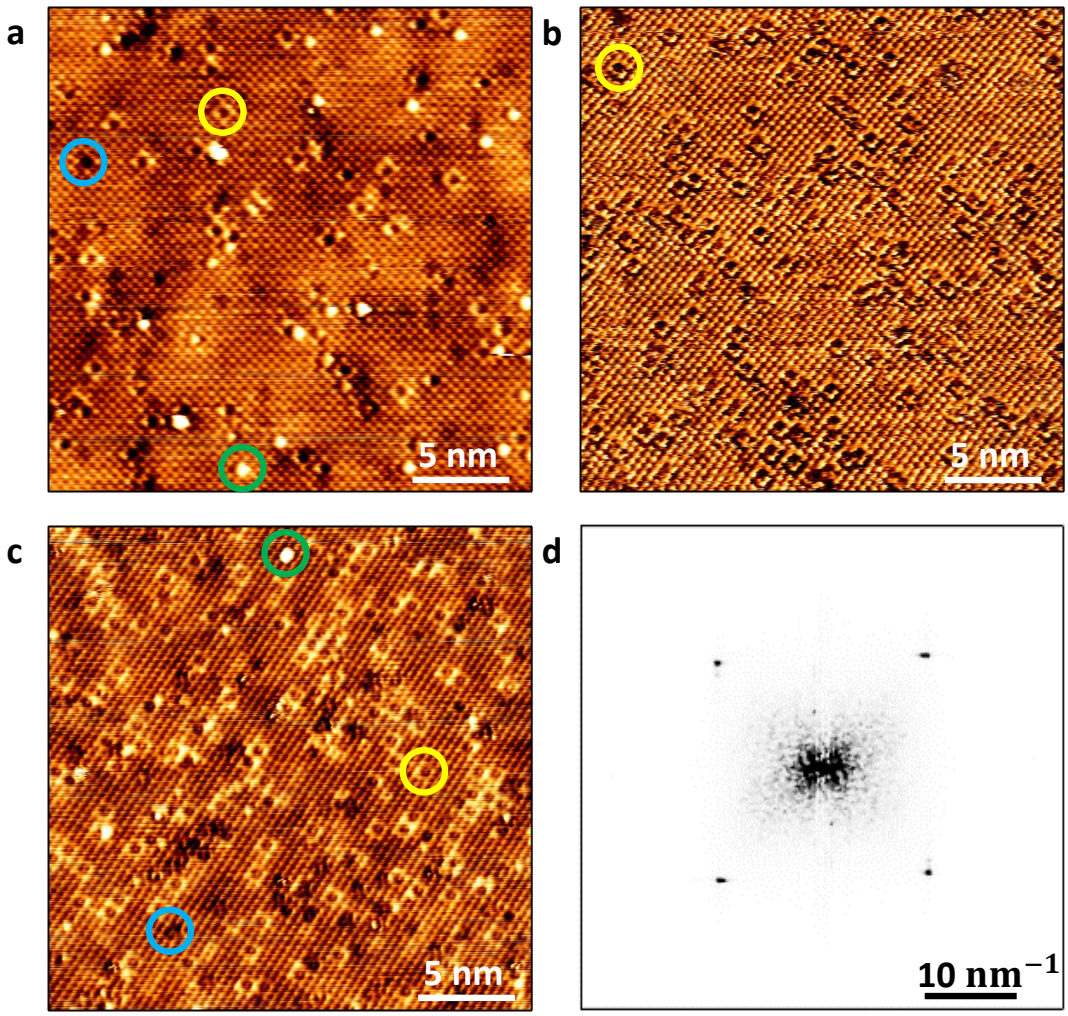

Figure 4.6: **a**. Topography map of the surface of $(Sr_{(1-x)}La_x)_2IrO_4$ with $x = 1,5\%$. **b**. Topography map of the surface of $(Sr_{(1-x)}La_x)_2IrO_4$ with $x = 2,3\%$. **c**. Topography map of the surface of $(Sr_{(1-x)}La_x)_2IrO_4$ with $x = 6\%$. **d**. Fourier transform of a topography image of $(Sr_{(1-x)}La_x)_2IrO_4$ with $x = 1,5\%$. The blue, yellow and red circles highlight vacancies, La dopants and adatoms, respectively.

The crystal structure of Sr_2IrO_4 is represented on figure 4.1. All iridium atoms are at the centers of oxygen octahedra. Those octahedra organize on a square lattice of lattice vectors **a** and **b** with $\| \mathbf{a} \| = \| \mathbf{b} \| = 3,9$ Å and $\mathbf{a} \perp \mathbf{b}$. Within an iridium plane, each oxygen atom is shared between two neighboring iridium. As a consequence, there are twice as much oxygen than iridium atoms in such a plane meaning it has a IrO_2 stoichiometry.

The IrO_2 planes are sandwiched between SrO bilayers. The Sr atoms of a given layer form also a square lattice of basis vectors **a** and **b** where each Sr is shifted of 1/2(**a**+**b**) with respect to its adjacent octahedra lattice nodes. The top most (or bottom most) oxygen atom of each octahedron indeed lies at the center of an on top (underlying) Sr square.

After cleaving, the sample terminates on a SrO layer [129, 125]. Figure 4.6 **a**, **b** and **c** represent the topography maps of $1,5\%$, $2,3\%$, and 6% samples, respectively. The topographic data show a square lattice of lattice parameter $a = 3,9$ Å. This value corresponds to the distance between two neighboring Sr atoms within a SrO layer. This can also be seen by looking at the Fourier transform of figure 4.6 **d** where a reciprocal square lattice is clearly distinguishable. It is important to emphasize that the oxygen atoms cannot be seen by STM such that the visible square lattice is composed out of Sr atoms [125].

Many defects cover the surfaces of our samples. It is possible to distinguish both vacancies and adatoms encircled respectively in blue and green on figure 4.6 **b** and **d**. Those are not due to improper growth processes of our crystals but rather to cleaving [137]. Some Sr/La atoms are indeed taken off either the newly obtained SrO layer or the thrown away one.

Adatoms and vacancies do not constitute the majority of defects. Most of them actually present a square-shaped modulation. Such kinds of defects are highlighted with yellow circles on $1,5\%$, $2,3\%$ and 6% maps. One can notice that all those square-defects sit at nodes of the Sr square lattice. This is no surprise since such features are commonly attributed to La dopants in substitution to Sr atoms [129]. Thus, by spotting the square-shaped defects on a given topography map, it is possible to access both the number of dopants (and by extension to compute the dopant concentration), and their spatial distribution. Such an approach was already performed in other studies [129]. The dopant concentrations were evaluated in this way for $1,5\%$, $2,3\%$ and 6% samples and are in good agreement with the measured EDX values.

The considered $1,5\%$ to 6% doping concentrations values are not arbitrary. It was indeed already observed that it is not possible to grow $(Sr_{(1-x)}La_x)_2IrO_4$ with x exceeding 6% because of the constraints induced by the substitutions of Sr atom by La dopants [129, 127]. Our study thus covers the full accessible La doping concentration range in doped Mott insulator $(Sr_{(1-x)}La_x)_2IrO_4$.

4.4.2 Inhomogeneous transition from insulating to pseudo metallic phase induced by La doping

The IrO_2 layers are the ones bearing the Mott physics of interest since the paradigmatic J_{eff}=1/2 ; 3/2 band picture is derived from the crystal field lifting of degeneracy of Ir atomic orbitals. It was already shown that there is a mixing between the Sr and IrO_2 [138] bands such that the observed LDOS on the SrO layer terminated surface should also present Mott physics features [125].

In order to access to the LDOS at different energies within a range [-1 eV,+1 eV], spectroscopic $I(V)$ maps were acquired, consisting in taking individual $I(V)$ spectra at many positions determined by a predefined spatial grid (see section 2.2). The differential conductance dI/dV maps (derived afterwards) at a given V can directly be related to the LDOS of the sample at the corresponding energy. Performing LDOS experiments at 77 K allowed us to exhibit spatial variations of both Mott gap and Fermi level position. The study was realized with an Omicron LT STM using Pt80%/Ir20% tips. Prior to each experiment, the DOS of the tip was verified on Pt and HOPG samples and checked to be featureless (see subsection 2.4.3). The topography

maps were taken in constant current mode and the spectra were taken at constant tip-sample distance for a given tunnelling set-point (mainly around $U = -1$ V, $I = 100$ pA).

The first part of this study focuses on describing the transition from a Mott insulating state to a (pseudo) metallic one as the doping concentration x goes up. The discussion is built on spatial representations referred to as " gap maps ". They simply represent the magnitude of the Mott gap as a function of space. The gaps are extracted from each spectrum/point of each spectroscopic map using a method illustrated on figure 4.7. In all $I(V)$ spectra, there is a whole energy range in which the current is equal to zero. This range is roughly equal to the insulating gap Δ. In order to extract Δ, we looked at the energy coordinates at which the crossing between the $I(V)$ spectrum and horizontal lines lying at $\pm 1\%$ of the set-point current $\|I_{setpoint}\|$ occur. Those two energies are called E_{min} and E_{max}, respectively. In the end : $\Delta = E_{max} - E_{min}$.

It is important to keep in mind that it is often delicate to extract the value of a gap. Here, we do not have any model which could give us an analytical expression of the expected differential conductance, and thus, allow us to efficiently fit our data. The method used here to extract gap is one out of many, and we do not pretend that such gap estimations are absolute. However, this process is good enough for what we intend to do, namely, looking at the spatial dependence of the gap in $(Sr_{(1-x)}La_x)_2IrO_4$ for several doping values.

On figure 4.8 is shown the evolution of the gap maps with doping concentrations $x = 1,5\%$, $x = 2,3\%$, $x = 6\%$. The selected areas have more or less the same size (typically 20nm×20nm). Those data are referred as large-scale experiments. All the gap maps share the same black and white color bar. The smaller the gaps the whiter they appear. The corresponding gap distributions are superimposed on figure 4.8 **d**, **e** and **f**.

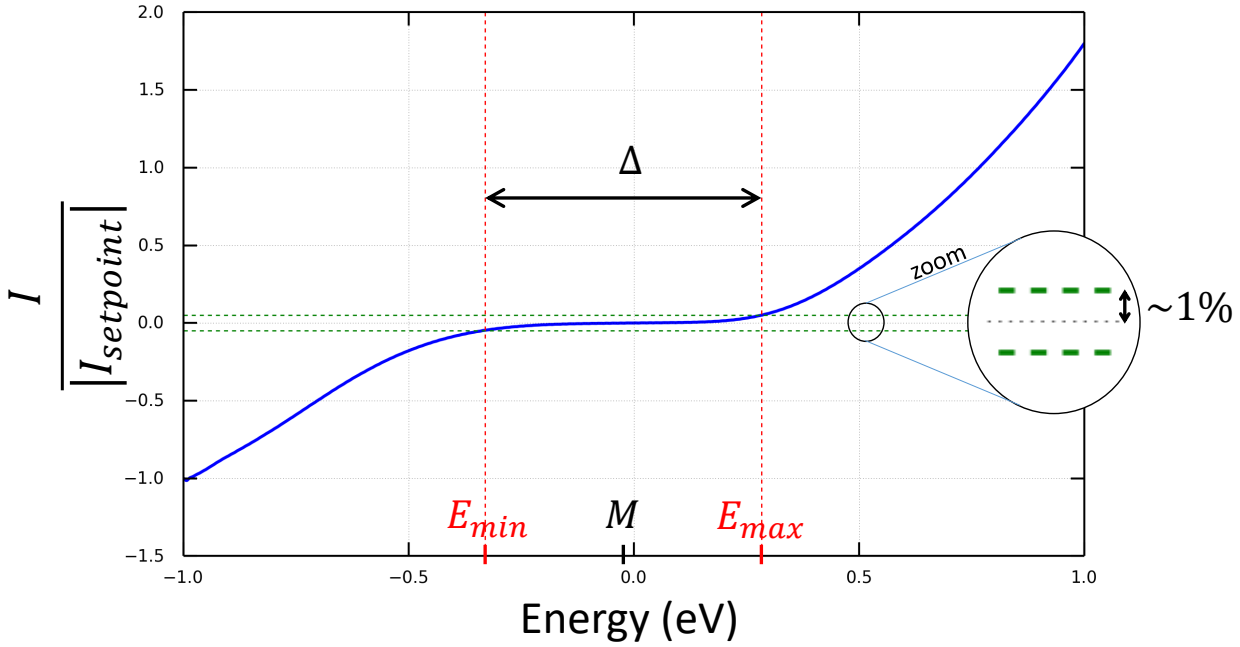

Figure 4.7: Illustration of the way the gaps were extracted from I(V) spectra. The blue curve is a typical I(V) spectrum and is normalized with respect to the set-point current. There is a whole range of biases voltages for which the spectrum is flat and for which the derivative and *a fortiori* the density of states will be equal to zero. The idea is to estimate this range which will be assimilated to the gap. In order to do so, we looked at the intersections between the spectrum and the horizontal lines $y = \pm 1\% \|I_{setpoint}\|$. The V coordinates at which those intersection occur are respectively called E_{max} (for $y = +1\% \|I_{setpoint}\|$) and E_{min} (for $y = -1\% \|I_{setpoint}\|$). The gap is finally defined as $\Delta = E_{max} - E_{min}$.

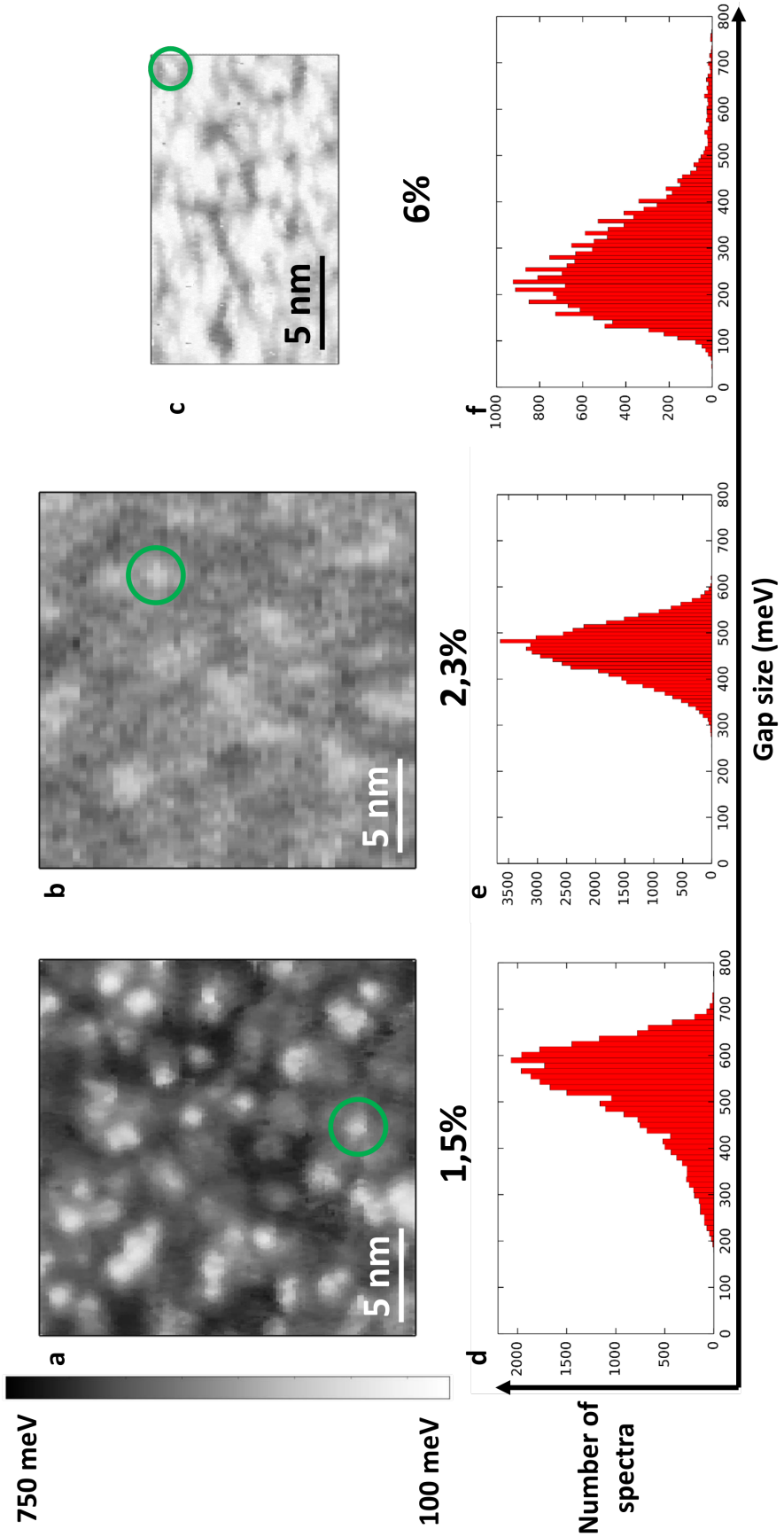

Figure 4.8: **a**. Gap map of the $x = 1,5\%$ sample. **b**. Gap map of the $x = 2,3\%$ sample. **c**. Gap map of the $x = 6\%$ sample. **d**. Gap distribution for the $x = 1,5\%$ sample. **e**. Gap distribution for the $x = 2,3\%$ sample. **f**. Gap distribution for the $x = 6\%$ sample.

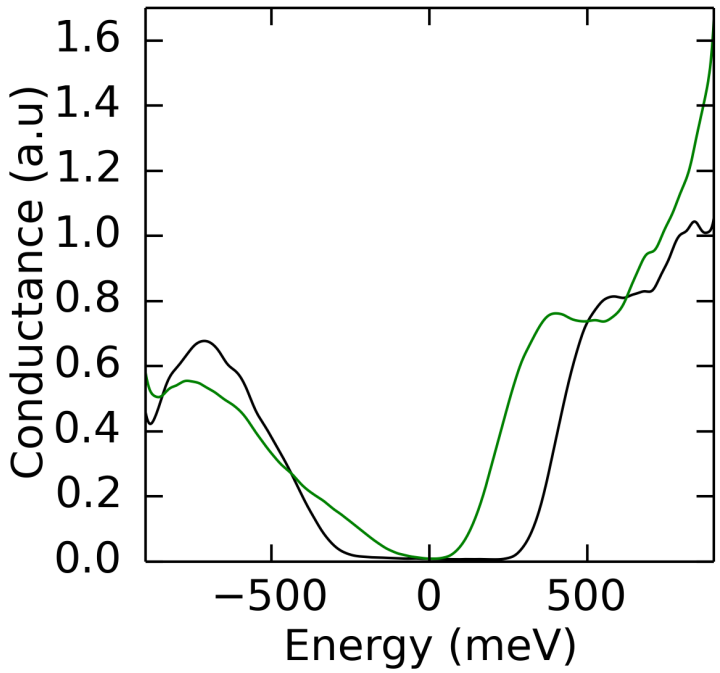

Figure 4.9: Two typical averaged dI/dV spectra taken in the $1,5\%$ sample on a bubble and on the background, respectively.

First of all, the spatial distribution of the gaps is very inhomogeneous, and this, for all doping concentrations. The magnitude of the gap evolves on energy ranges varying from one sample to another but typically going from 100 meV to 750 meV. This is also emphasized by the finite widths of the gap distributions. Those substantial gap variations occur at nanometer scale. The smaller-gap areas are disk-shaped such that we refer to them as " bubbles ". Such small-gap bubbles are highlighted with green circles on $1,5\%$, $2,3\%$, and 6% gap maps. The bubbles have a diameter approximatively equal to $2,5$ nm. Each gap map thus consists in many small-gap bubbles (white) distributed across a more insulating background (black). Two typical averaged dI/dV spectra taken in the $1,5\%$ gap map on a bubble and on the background respectively are represented in figure 4.9 and illustrate the gap inhomogeneities throughout the samples. Secondly, the gap maps are whiter and whiter as the doping concentration x increases implying that the samples become less and less insulating. This is consistent with a Mott insulator to metal transition driven by doping.

An inhomogeneous MIT in $(Sr_{(1-x)}La_x)_2IrO_4$ was also observed in the work of Battisti *et al.* [129] but their results/conclusions differ from ours. They report an abrupt transition from an homogeneous insulating phase for low doping concentrations ($2,1\%$ to $3,7\%$), to a mixed inhomogeneous phase where both pseudo metallic and insulating puddles cohabit for doping concentrations higher than $4,8\%$. It is important to point out that in our study the inhomogeneities start emerging even for lightly doped samples with x going as low as $1,5\%$. There are two possible explanations for such discrepancies between our study and the one of Battisti *et al.*. First, even though both our crystal growth methods are similar, they are not identical. Moreover, the used sources were also different. Maybe the physics of $(Sr_{(1-x)}La_x)_2IrO_4$ is very sensitive to the growth procedure, which would also explain the great variety of results reported in the literature. Second, in the last figure of ref. [129], spatial color plots representations equivalent to our gap maps (their way of extracting the gap is different) are compared for samples with different doping levels (namely $2,1\%$, $2,3\%$, $3,7\%$, $4,8\%$, $5,2\%$ and $5,5\%$). The color plots for $2,1\%$, $2,3\%$ and $3,7\%$ samples appear perfectly uniform, meaning that the images were somehow saturated and that spatial inhomogeneities were maybe killed.

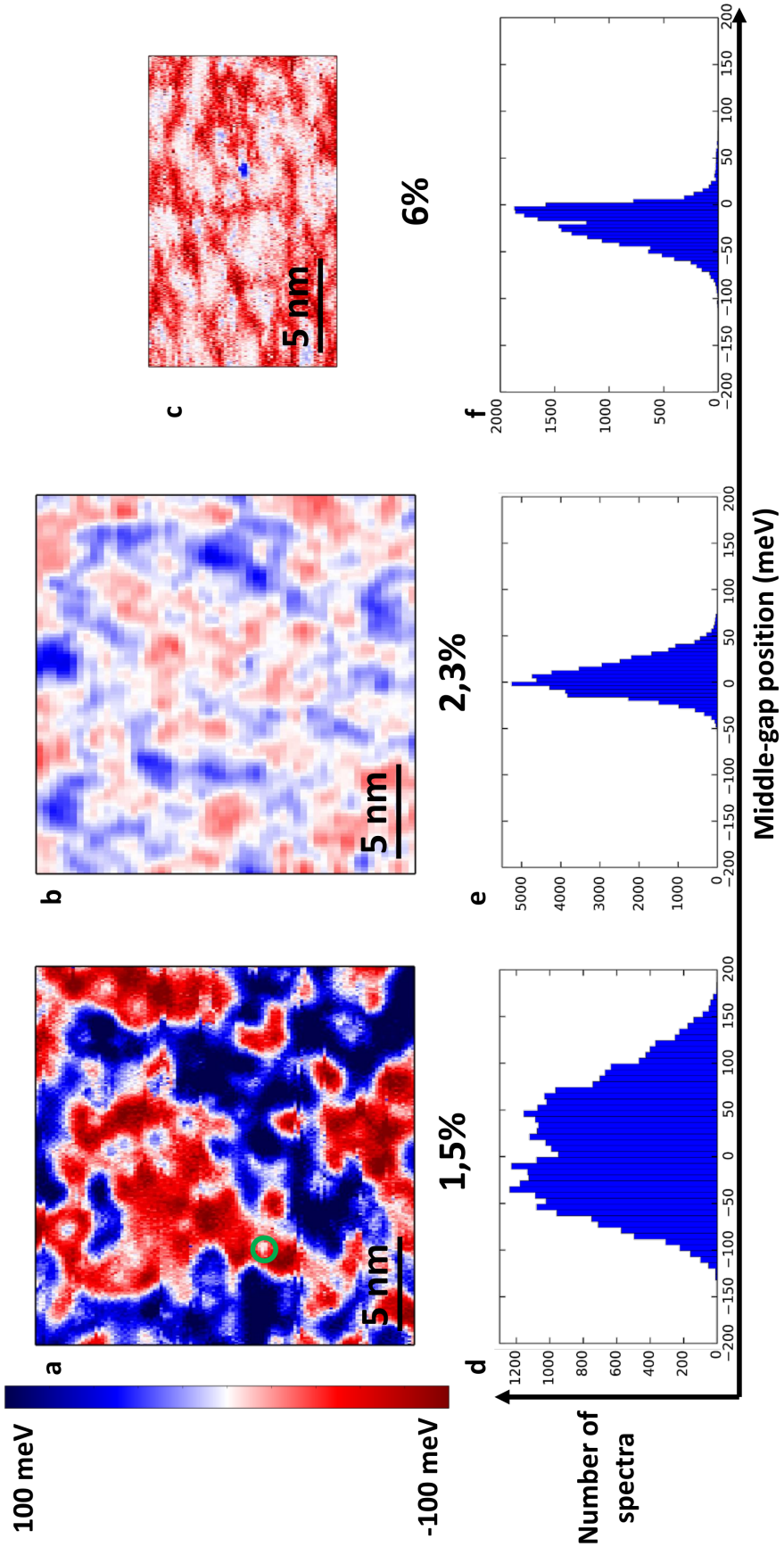

Figure 4.10: **a**. Middle-gap map of the $x = 1,5\%$ sample. **b**. Middle-gap of the $x = 2,3\%$ sample. **c**. Middle-gap of the $x = 6\%$ sample. **d**. Middle-gap distribution for the $x = 1,5\%$ sample. **e**. Middle-gap distribution for the $x = 2,3\%$ sample. **f**. Middle-gap distribution for the $x = 6\%$ sample.

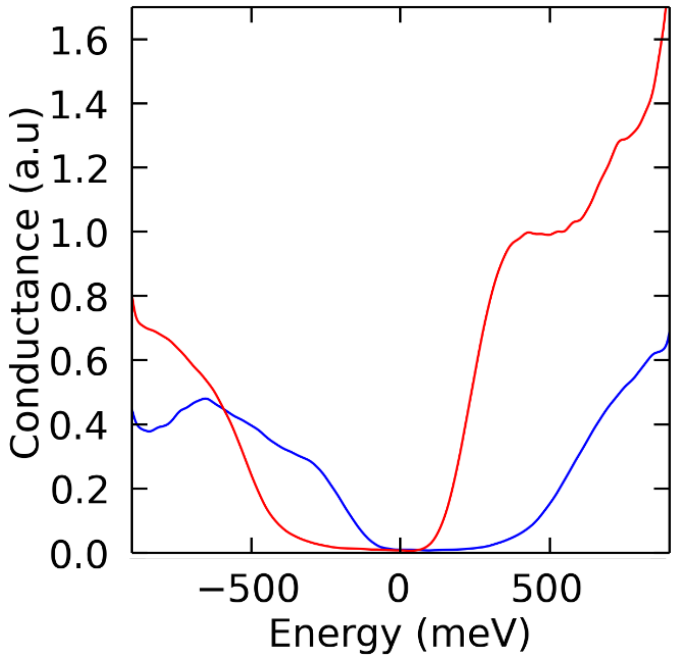

Figure 4.11: Two typical averaged dI/dV spectra taken respectively on a positive-valued middle-gap area and on a negative-valued middle-gap area in the $1,5\%$ sample.

In doped semiconductors, the presence of dopants leads to a chemical potential shift towards conduction or valence band depending to whether the semiconductor is n or d doped. In doped Mott insulators, dopants also induce displacements of the Fermi level towards LHB or UHB. However, contrary to semiconductors, a reduction of the gap (and a modification of the band structure) is likely to accompany this shift. In my work I tried to highlight such effects by building up different spatial representations referred to as " middle-gap maps ". Let $E_{min}(\mathbf{r})$ and $E_{max}(\mathbf{r})$ the energies of respectively the last occupied state and the first unoccupied state at a given position $\mathbf{r}$. A middle-gap map represents $M = (E_{max} + E_{min})/2$ as a function of space (the Mott gap is $\Delta = E_{max} - E_{min}$). It represents the position in energy of the "center" of the gap with respect to Fermi level. Only the combined information of both gap and middle-gap maps is likely to give without any ambiguity the shape of the LDOS as a function of space.

On figure 4.10 is shown the evolution of the middle-gap maps with doping concentrations $x = 1,5\%$, $x = 2,3\%$, $x = 6\%$. The selected areas are the same than in figure 4.8. All the middle-gap maps share the same red/white/blue color bar. The more negative (positive) the middle-gaps the redder (bluer) they appear. The corresponding middle-gap distributions are superimposed on figure 4.10 **d**, **e** and **f**.

Similarly to the Mott gap, the energy position of the middle of the gap is inhomogeneous in space as it can vary typically from -100 meV to 100 meV. For the $1,5\%$ sample, about half of the surface has negative middle-gaps values when the other half has positive middle-gaps values. Two typical averaged dI/dV spectra taken on a positive-valued middle-gap area and on a negative-valued middle-gap area, respectively, in the $1,5\%$ middle-gap map are represented in figure 4.11. The two spectra were especially picked up to show that some areas may present the same Mott gap while having different Fermi level positions.

Scattered white zones (gap center at Fermi level) can also be seen. Such a zone is encircled in green on figure 4.10 **a**. Most of the time, such areas correspond to small gap bubbles. This apparent correlation can be simply explained. In Mott physics, correlations between electrons around Fermi level open a gap. This implies that the Fermi level should lie within the gap. When the gap becomes smaller, as in a small-gap bubble, the middle of the gap can only vary within a limited energy range such that it is more likely to be close to 0.

As the doping concentration increases, the middle-gaps are more and more negative (red). The increasing asymmetry with respect to 0-energy of the middle-gap distributions in figure 4.10 **d**, **e** and **f**. comforts this last observation.

The short-range inhomogeneous character of both Mott gap and position of the middle of the gap can be further accentuated by investigating the variation of spectra at nanometer scale. In figure 4.12 are shown the different kinds of dI/dV spectra encountered in $x = 1,5\%$, $x = 2,3\%$ and $x = 6\%$ samples. Those are extracted from different spectroscopic grid measurements taken on zooms of the areas of figure 4.8/4.10. The color of a given spectrum corresponds to the magnitude of its gap. Each spectrum is obtained after averaging of a collection of similar spectra sharing the same general features enclosed in specific areas on the map. The number of spectra per unit of surface is higher than in the previous set of experiments (more than 50 times). This second set of spectroscopy measurements is more spatially resolved regarding the typical scale of both atomic variations and inhomogeneities such as La modulations. These measurements are referred to as small-scale experiments. In the insets of each collection of spectra are represented the corresponding gap maps. The presented collections of spectra are assumed to be representative of the samples.

Many of the remarks that were made on the large-scale experiments can also be made by analysing the spectra of figure 4.12.

First, all samples present spectra with significantly different magnitudes of the gap. The spectra with reduced gaps (red) are characteristic of the bubbles and the ones with higher gaps (blue) are characteristic of the insulating background. The inhomogeneity of the samples is thus again visible in small-scale experiments. The magnitude of the gap for the small-gap spectra reduces as doping concentration increases, which is consistent with previous observations. However, another piece of information arises from this second study. For the $1,5\%$ sample, there are no states at zero energy for the spectra taken on the bubbles. They thus have a well-defined gap and the bubbles remain insulating. On the contrary, for the 6% sample, the bubble-type spectra show some density of states at zero energy. This means that for high-enough doping concentrations the bubbles become pseudo-metallic. However, the magnitude of the gap of the insulating background-type spectra remains the same with doping (typically 650 ± 50 meV). The pseudo-metallic aspect of the Mott transited areas at high doping was also observed by Battisti *et al.* in their study. These last statements can all be summed up in the following way : doping the system induces the apparition of small gap/pseudo-metallic bubbles on top of an insulating background ; the insulating background gaps remains constant with doping while the magnitude of the bubble (pseudo-)gaps reduce as the number of dopants increases. In this system, the presence of dopants does not induce a smooth variation of the ratio U/t as additional electric charges are not delocalized throughout the sample but rather an inhomogeneous MIT.

Second, for low doping concentrations ($1,5\%$, $2,3\%$), the position of the middle of the gap greatly varies from negative values to positive values while for the 6% sample, it mainly stays negative. Moreover, the middle of the gap lies around 0-energy for small gap/pseudo-metallic spectra. Again, this is in agreement with large-scale experiments data.

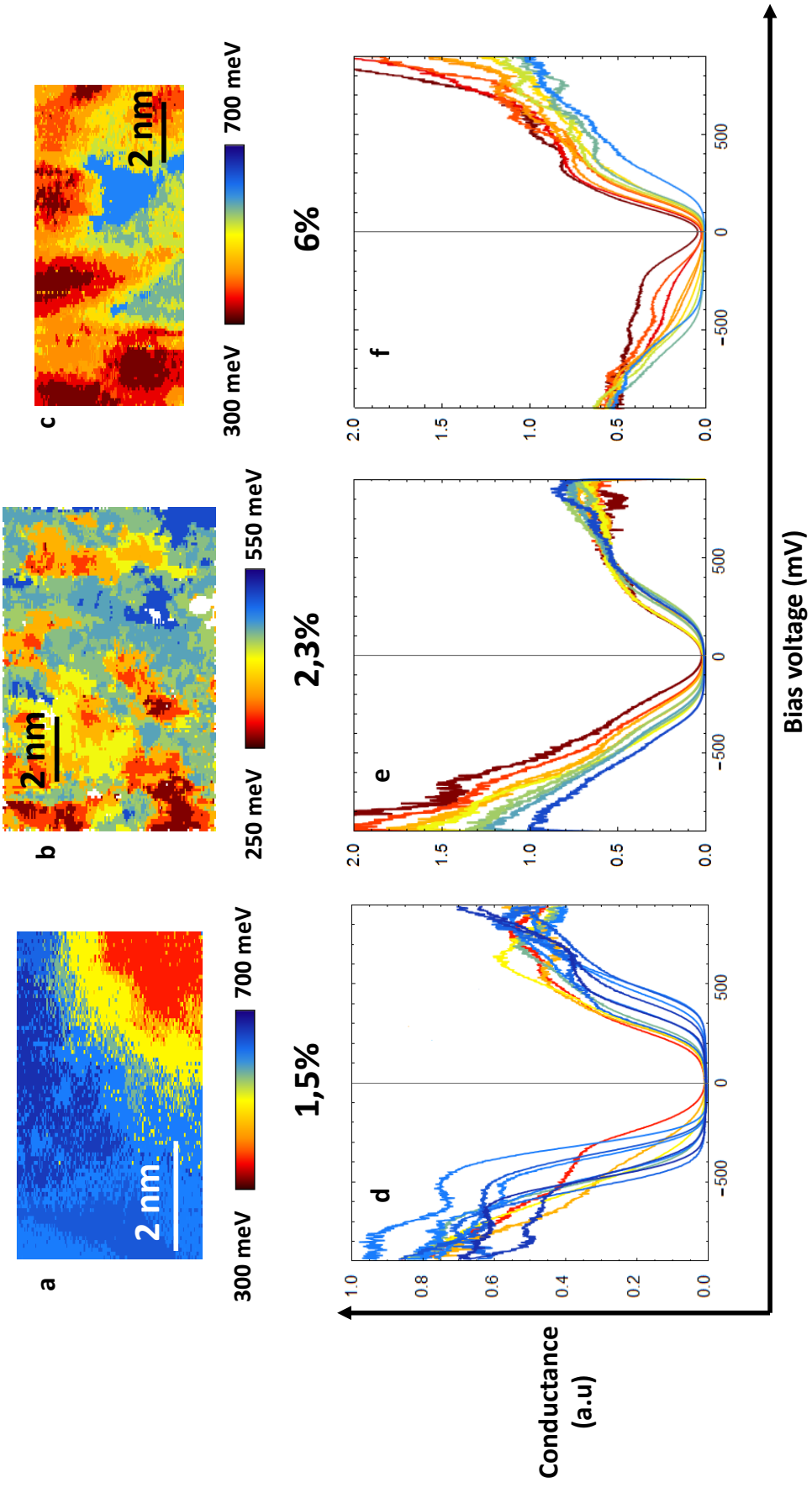

Figure 4.12: **a**. Small-scale gap map of the $x = 1,5\%$ sample. **b**. Small-scale gap map of the $x = 2,3\%$ sample. **c**. Small-scale gap map of the $x = 6\%$ sample. **d**. Typical spectra encountered in **a** area. **e**. Typical spectra encountered in **b** area. **f**. Typical spectra encountered in **c** area.

The question that immediately arises is whether there is or not a correlation between the positions of the dopants and the positions of the pseudo-metallic bubbles. In their article, Battisti *et al.* suggest that there is an equivalence between the locations of the La dopants and of the pseudo-metallic puddle areas. Our conclusion is partly in agreement with theirs. When doing the cross correlations between the gap maps and the position of the dopants maps, one finds a 33% matching for the $1,5\%$ sample and a bit less for higher doping samples. These values mean there exist a certain degree of correlations between the locations of La atoms and the positions of metallic bubbles since by generating a random spatial distribution with an equal number of dopants one rarely reaches values above 10%. A rough estimation by the eye would indeed suggest correlations because for large-scale images a great number of dopants are localized in the pseudo metallic areas. Yet, it is also very common for dopants to lie within the insulating background. Figure 4.13 displays on the left a dopants concentration map of the same $1,5\%$ large-scale area than in figure 4.8 **a** (displayed on the right). In order to obtain the dopants concentration map, the positions of the dopants were targeted, after what a map was created with signal peaked at those positions. A Gaussian filter was applied to this map to give a spatial extension to the dopants. The width of the Gaussian in the filtering process was fixed to maximize the cross-correlations between the gap map and the dopants concentration map. For $1,5\%$ large-scale images, one can clearly see dopants sitting in the very middle of large-gap areas as suggested by pink circles in figure 4.13. The fact that one does not observe a one to one correspondence can naively be understood in the following way: in STM, only the SrO layer is visible, nevertheless, Mott physics emanates from the electrons of IrO_2 layers. The presence of La atoms substituting the Sr atoms in the neighboring layers modifies the physical properties of the system such that potentially half of what causes the MIT is invisible to our probe. With this last statement in mind, it would then be odd to find perfect matching between the positions of the dopants at the surface and of the pseudo-metallic bubbles. An additional way of interpreting this mismatch will be discussed in section 4.5.

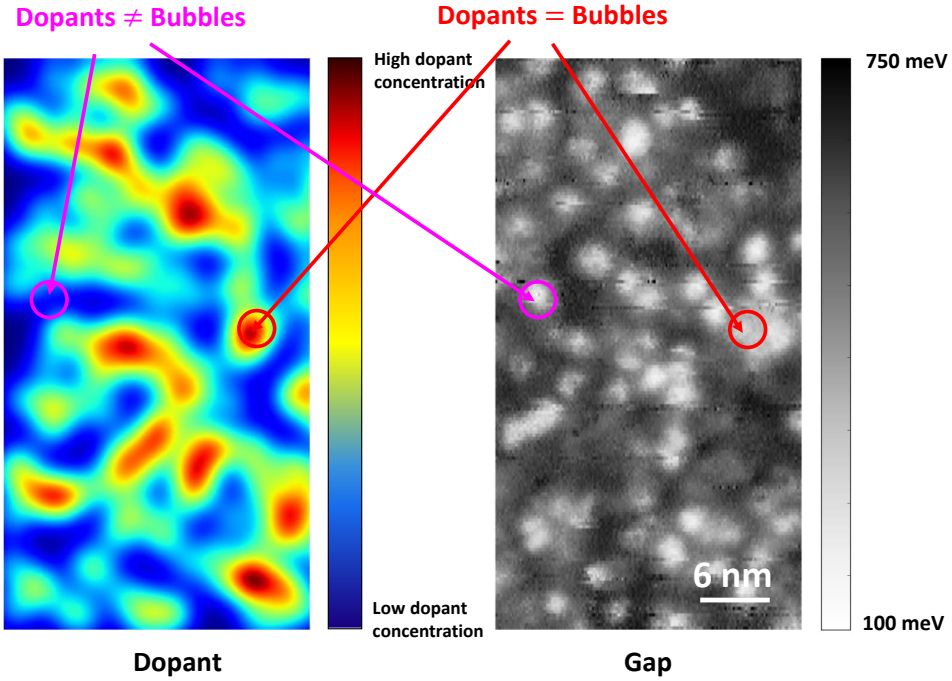

Figure 4.13: On the left is displayed a dopants concentration map. The hotter the color, the more dopants are present. On the right is represented a gap map of the same area. These data correspond to the $1,5\%$ case.

It also looks like there is a correlation between the locations of pseudo-metallic bubbles and the 0-valued middle gap areas (in white). In Mott physics, a gap opens because of correlations between electrons at Fermi level, which implies that the Fermi level should lie within the gap. When the gap becomes smaller, as in a pseudo-metallic bubble, the middle of the gap can only vary within a limited energy range such that it is more likely to be close to 0. Given the discussion of the previous paragraph, this suggests a correspondence between the locations of La atoms and the negative valued middle-gap areas. One can thus conjecture the following statement : the introduction of dopants locally shifts the chemical potential towards lower energies because new electric charges are brought in the material ; as more and more dopants are present, the chemical potential starts to homogenize across the sample and the Fermi level position locks right beneath the UHB. Here, our observations are partly in agreement with the Battisti *et al.* study. They indeed do not see any spatial chemical potential shifts in lightly doped samples $(2, 2\%)$. Yet, in the case of highly doped samples $(5, 5\%)$, they also observe a locking of the Fermi level position close to the UHB, which is in agreement with electron doping (seen also in La-doped bilayer iridate $Sr_3Ir_2O_7$ [139] and which is the opposite of what is observed in hole-doped cuprates [140]).

4.5 Orientational emergent order in $(Sr_{(1-x)}La_x)_2IrO_4$

Up to now, no comment was made on the distribution and number of pseudo-metallic bubbles and their evolution with doping concentration x. A good way of accessing these information is to compute the autocorrelation maps of gap maps. The autocorrelation of a given map is the 2D-autoconvolution of that map. It roughly consists in sliding a map on top of itself for many displacement vectors and see for which the obtained translated maps coincide in the best way with the original one. Our convention is that the center of the autocorrelation map corresponds to no displacement at all such that both original and translated maps match perfectly. Autocorrelation functions are a powerful tool for exhibiting order and periodicity in a system.

In figure 4.14, are represented the autocorrelation maps of the large-scale gap maps of figure 4.8. By construction, at the center of every autocorrelation map, the value is equal to 1. The directions of the Sr atomic square lattice were drawn as black dotted arrows on top of each autocorrelation map.

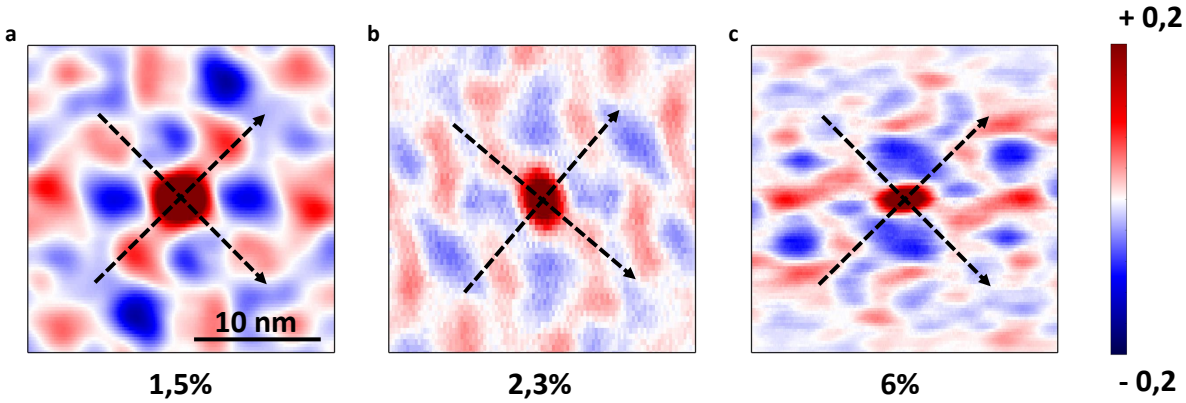

Figure 4.14: **a**. Autocorrelation map of the gap map of figure 4.8 **a**. **b**. Autocorrelation map of the gap map of figure 4.8 **b**. **c**. Autocorrelation map of the gap map of figure 4.8 **c**. The black arrows represent the atomic directions of the Sr lattice.

The first noticeable result one gets by looking at the autocorrelation maps is that the widths

of the central spots are more or less constant with doping. The width of a central spot can directly be related to the typical size of the smallest objects in a gap map, namely the pseudo-metallic bubbles. At 20% the height of the central autocorrelation peaks, one can then evaluate the diameter of a bubble: $D_{bubble} = 2,5 \pm 0,5$ nm, which is consistent with both large-scale and small-scale experiments. The second observation one can make is that the autocorrelation patterns seem to organize along the atomic directions. It is visible for all doping concentrations but is particularly remarkable in the $1,5\%$ case where one can even distinguish the development of a rectangular lattice fading as one goes away from the center.

In the $1,5\%$ case, the first neighboring spot to the center lies at $L = 5 \pm 1$ nm from the central peak. This last piece of information suggests that, for this level of doping, the pseudo-metallic bubbles do not distribute in a glassy way, but rather tend to organize along the surface atomic directions forming a square-like lattice of lattice parameter L. Thus, the locations of pseudo-metallic bubbles do not reflect the random distribution of dopants, which consolidates what was already told in the previous part. Further studies would need to be performed to see whether the formation of a lattice is typical of the lightly doped regime.

Our study highlights what we interpret as being the emergence of a short-range orientational order in the gap spatial distribution. If the appearance of a lattice is not necessarily obvious for all doping, one can however claim that the pseudo-metallic bubbles preferentially arrange along the Sr lattice atomic directions.

A similar order, manifesting as pseudo-gap stripes, was also observed in the study of Battisti *et al.* [129] and in lightly hole-doped cuprate parent compounds [141, 142, 143, 144, 140]. It would seem that the appearance of such orders is representative of the inhomogeneous insulator to metal transition in lightly doped Mott insulators.

4.6 Pure sample case

As it was already mentioned, the different studies that were carried out so far on pure Sr_2IrO_4 are not in agreement regarding the value of the Mott gap. Gaps as low as $0,1$ eV have been reported in transport [145] and optical conductivity [119] measurements. In angle-resolved photoemission spectroscopy experiments, the maximum of the valence band was measured around $-0,2$ eV, implying a Mott gap at least equal to $0,2$ eV [119, 120, 127, 128]. In the first STM/STS study performed on pure Sr_2IrO_4, the value of the gap was evaluated to be equal to $\sim 0,15$ eV [124]. However, even down to $4,2$ K, the spectra did not exhibit a hard gap but rather a strong depletion of the density of states around Fermi level. Two other STM/STS studies were published one year later. In the first study, again, no hard gap was observed, which the authors interpreted as gap filling due to inelastic magnons features [146]. In the second study, J. Dai *et al.* reported a substantial Mott gap of 620 meV [125]. Nevertheless, the measured samples presented many defects and local spectroscopy measurements performed on top of these defects exhibited drastic changes of the local density of states. In their study on Mott insulator to metal transition in $(Sr_{(1-x)}La_x)_2IrO_4$, Battisti *et al.* did not pursue any measurements on pure Sr_2IrO_4 [129]. According to their complementary article (see ref. [126]), the reason was that the quality of the samples was such that the tip would crash during the approach, consequently preventing any STM experiment.

One of the strong points of the STM/STS work presented in this chapter is the additional experiments performed on **pure** Sr_2IrO_4 samples. The chemical composition of the observed Sr_2IrO_4 samples was checked beforehand by mean of EDX. No trace of any of the usual elements used in the doping process was found (namely La and Rh). Besides, the measured stoichiometric ratio corresponds to the one of pristine Sr_2IrO_4. The experiments were carried out in the exact same conditions as for the $(Sr_{(1-x)}La_x)_2IrO_4$ samples.

Figure 4.15 **a** represents a typical topography map of pure Sr_2IrO_4. One can clearly see the Sr square lattice of lattice parameter $3,9$ Å. The absence of the square-shaped defects

associated to La atoms further supports the pureness of the samples. Nonetheless, similarly to all previous STM studies performed on pure Sr_2IrO_4, some defects are visible on the surface. In our case, they appear as "dark spots" on the topography map. The nature of these last defects is not known for, most of the time, no Sr atom is missing. Dark patches with similar appearance and interpreted as oxygen-related defects were reported in ref. [125]. On top of such dark patches, J. Dai *et al.* saw a significant reduction of the Mott gap. Such a behaviour was not observed in the case of our "dark spots" defects and their nature is still unclear, their origin potentially lying deeper within the structure.

In addition to those defects, one can also see bright density of states puddles encircled in blue on figure 4.15 **a**. Their nature is also unknown. An averaged dI/dV spectrum taken on such a bright area is represented in blue in 4.15 **b**. The local Mott gap was determined using the same method as the one of ref. [125], namely linearly extrapolating both LHB and UHB as illustrated by the blue dotted lines in 4.15 **b**. By doing so, one finds a value for the Mott gap equal to approximatively 260 meV. Even if the method to extract the gap was different, we recall that in $(Sr_{(1-x)}La_x)_2IrO_4$, insulating areas could display Mott gaps bigger than 500 meV.

For now, we only commented on spectroscopic features on top of defects. By performing spectroscopy far from such "dark or bright spots" one should recover the density of state of pristine Sr_2IrO_4. Such an averaged dI/dV spectrum was taken in an free-of-defects area like the one encircled in green on figure 4.15 **a** and is represented in green in figure 4.15 **b**.

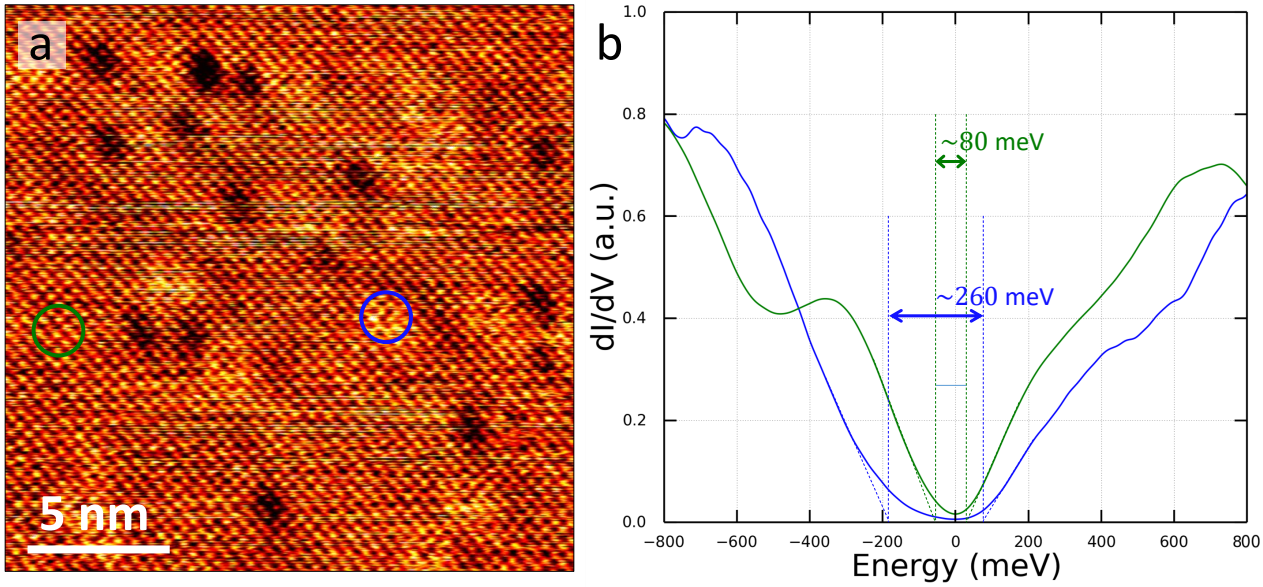

Figure 4.15: **a**. Typical topographic map of the surface of pure Sr_2IrO_4. **b**. dI/dV spectra taken on top of a "bright" density of states puddle (blue curve) and away from any apparent defect (green curve), respectively.

Surprisingly, by applying the same gap-determining method as for the blue curve, one finds a Mott gap of pure Sr_2IrO_4 approximatively equal to 80 meV, or so to say much smaller than the one of any insulating area of $(Sr_{(1-x)}La_x)_2IrO_4$. This value is actually much closer to the one reported in transport [145] and optical conductivity [119] than the ones reported in both ARPES and STS.

Our study of $(Sr_{(1-x)}La_x)_2IrO_4$ teaches us that increasing the electron doping level drives a transition from a Mott insulating phase to a pseudo-metallic phase. However, this last statement seems to be true only when the system is already electron-doped. By going from $x = 0\%$ to $x = 1,5\%$ the system indeed at first becomes more insulating than it was. It is only when the doping level further increases that the Mott insulator to metal transition seems to pursue in

the expected direction.

We will now propose possible reconciliation between our data and the literature. In ARPES measurements, the position of the maximum of the valence band with respect to Fermi level can potentially be explained by the fact that photoemission is an integrative method, which by definition will average all the different contributions found in the sample. Our extrapolated Mott gap on top of bright areas, is actually large enough for this interpretation to be plausible. Moreover, the differential conductance spectra that were observed in STM/STS studies of refs. [124, 146] are also compatible with ours. Also, it remains purely speculative but, from our study, it looks like introducing disorder tends to first increase the value of the Mott gap[5]. The large gaps observed in ref. [125] could possibly be explained by the presence of many superficial defects.

4.7 Conclusion

In this chapter, we have observed by mean of grid spectroscopy a spatially inhomogeneous Mott insulator to pseudo-metallic phase transition driven by electron doping in $(Sr_{(1-x)}La_x)_2IrO_4$ (with x the La concentration). This result further justifies the use of a local probe and that integrative methods like ARPES are not sufficient to study the Mott physics in this material. Contrary to previous work reported in the literature, our study exhibits the inhomogeneous character of the transition down to the lightly doped regime. We also observed the appearance of a short-range orientational order in the pseudo-metallic puddles distribution, in qualitative agreement with similar orders observed in lightly hole-doped cuprates parent compounds. Moreover, our study is the first one which includes STM/STS measurements on pure Sr_2IrO_4. The smallness of the Mott gap exhibited in our pristine compound allowed us to propose a reconciliation between the great variety of results reported in the literature. More particularly, our study suggests a significant dependence of the physical properties of $(Sr_{(1-x)}La_x)_2IrO_4$ on the crystal growth processes and/or on disorder. Finally, signatures of superconductivity were observed in a recent experimental study in which potassium was deposited at the surface of pristine Sr_2IrO_4 (which would be an alternative way to electron-dope the system). We plan on carrying out similar studies since, according to literature, electron or hole doped Sr_2IrO_4 could host topological superconductivity.

[5]The origin of this behaviour still as to be determined.

Conclusion

First have shown that superconducting misfit transition metal dichalcogenide compound $(LaSe)_{1,14}(NbSe_2)_2$ possesses a band structure similar to the one of $0,3$ eV electron-doped monolayer $NbSe_2$. Moreover, we highlighted the unconventional nature of the superconducting order parameter in this misfit compound.

In view of our study, one can imagine to use bulk misfit heterostructures such as $(LaSe)_{1,14}(NbSe_2)_2$ in order to investigate the physics of monolayer transition metal dichalcogenides. The generic formula of misfit heterostructures of the same family is $([MX]_{1+\delta})_m(TX_2)_n$, where M is either Sn, Pb, Bi, Sb or any lanthanide element, T is a group 4 (such as Ti) or a group 5 (such as Nb) transition metal and X is a either S or Se chalcogen element. m and n represent the number of rock-salt and transition metal dichalcogenide layers, respectively. Finally, δ represents the degree of structural mismatch between MX and TX_2 layers.

There would be several ways on tuning the doping level in such heterostructures. For simplicity, we will base our discussion on comparison with our compound. Let us imagine that we change the LaSe layers for PbSe layers. The main difference resides in the fact that the PbSe layer neither gives or accepts any electrons (the same can be said of SnX layers). In this configuration, we can thus imagine that the newly obtained compound should behave as regular undoped monolayer $NbSe_2$ (it has been shown in ref. [9] that this compound is superconducting under $3,64$ K). Such a behaviour was actually observed in $(SnS)_{1,17}(NbS_2)$, where ARPES measurements exhibited monolayer NbS_2-dominated Fermi level spectroscopic features [147]. One could also imagine to substitute a fraction of the La atoms with Pb atoms. Depending on the degree of substitution, the whole [0 eV, $+0,3$ eV] electron doping interval of monolayer $NbSe_2$ could theoretically be explored, and one could potentially perform a study of the evolution of both charge density wave order and superconductivity with continuous doping values. Also, reducing n (which is equal to 2 in our compound) down to 1 should theoretically double the number of additional carriers brought to each $NbSe_2$ layer. In this way, even higher doping value could in principle be reached. The transition metal dichalcogenide monolayer of interest could also be for MoS_2 or NbS_2 just as an example (in ref. [147], similar conclusions were made in a misfit compound based on NbS_2 instead of $NbSe_2$). As it was already mentioned in the main text, one possible route towards topological superconductivity consists in inducing superconductivity in topological insulators [64][7]; It has been shown very recently that single-layer 1T'-WSe_2 is a topological insulator exhibiting topological edge states [148]. By replacing $NbSe_2$ by 1T'-WSe_2, it might be that the electron doping is such that 1T'-WSe_2 layers become superconducting, hence potentially turning the whole system into a topological superconductor. Moreover, even though we exhibited signatures of unconventional superconductivity in $(LaSe)_{1,14}(NbSe_2)_2$, it does not mean that it is automatically topologically non trivial. One could think of replacing non magnetic La by magnetic lanthanide elements such as Eu or Dy. Then, it is possible that the underlying magnetic lattice acts as an external magnetic field potentially turning the system into a topologically non trivial regime.

Second, we have exhibited the spatially inhomogeneous character of the Mott insulator to pseudo-metallic phase transition in electron doped Sr_2IrO_4. In view of our study, it appears that integrative methods such as ARPES, although very powerful, are not sufficient to entirely

address the Mott physics in iridium oxyde compounds and that the use of a local probe such as the STM is of the atmost importance. Moreover, the discrepancies between our study and previous STM/STS works reported in the literature suggests that the physical properties of interest are highly sensitive to the crystal growth processes and also, potentially to disorder. Those questions have to be further investigated. For example, it would be interesting to study the effect of disorder on the physics of the system by introducing defects in a controlled way using electron irradiation. Also, as it was already mentioned, it would also be interesting to deposit potassium at the surface of pristine Sr_2IrO_4 to see whether it is possible or not to turn the system into a superconducting (topological) phase. Performing the same kind of study on other iridium oxide compounds of the same family such as $Sr_3Ir_2O_7$ [139] would also be a good idea.

Appendices

.1 Computation of the tunneling conductance.

This part can be inserted in part 1.4.1 where a reference to this appendix was made.

For simplicity reasons and because the intensity of the tunneling current is low, we will consider that the number of electrons in both systems 1 and 2 remains conserved such that $[\hat{H}_\alpha, \hat{N}_\beta] = 0$ with $\alpha, \beta = 1, 2$.

$$\frac{d\hat{N}_1}{dt} = i[\hat{H}, \hat{N}_1](t) = ie^{i\hat{H}t}[\hat{H}, \hat{N}_1]e^{-i\hat{H}t},$$

$$\frac{d\hat{N}_1}{dt} = ie^{i\hat{H}t}(\underbrace{[\hat{H}_1, \hat{N}_1]}_{=0} + \underbrace{[\hat{H}_2, \hat{N}_1]}_{=0} + [\hat{H}_T, \hat{N}_1])e^{-i\hat{H}t},$$

$$[\hat{H}_T, \hat{N}_1] = \sum_{kk',\sigma} \sum_{k'',\sigma'} T_{kk'} \underbrace{[c^\dagger_{1k\sigma} c_{2k'\sigma}, c^\dagger_{1k''\sigma'} c_{1k''\sigma'}]}_{-\delta_{kk'}\delta_{\sigma\sigma'} c^\dagger_{1k''\sigma'} c_{2k'\sigma}} + \sum_{kk',\sigma} \sum_{k'',\sigma'} T^*_{kk'} \underbrace{c^\dagger_{2k'\sigma} c_{1k\sigma}, c^\dagger_{1k''\sigma'} c_{1k''\sigma'}]}_{\delta_{kk'}\delta_{\sigma\sigma'} c^\dagger_{2k'\sigma} c_{1k''\sigma'}},$$

$$[\hat{H}_T, \hat{N}_1] = T^\dagger(0) - T(0),$$

Thus one gets equation 12:

$$\hat{I}_p = i(T(t) - T^\dagger(t)). \tag{12}$$

Let us derive the induced current using linear response theory. Indeed, one can treat H_T perturbatively because the probability of tunneling exponentially decreases with the distance between the two conducting materials (see 1.1).

Reminder (Kubo formula): Let us consider a system described by the Hamiltonian $\hat{H}$, and $\hat{A}$ an observable. We now add a perturbation $\hat{V}(t)$ in the system so that the Hamiltonian of the system is $\hat{H} + \hat{V}(t)$. $\hat{V}(t)$ can be written as $\hat{V}(t) = \sum_\alpha B_\alpha f_\alpha(t)$, where $f_\alpha(t)$ is a field and B_α the conjugate variable of the field. If we are in linear response theory, then one can derive the Kubo Formula:

$$\langle \hat{A}(t) \rangle - \langle \hat{A} \rangle_0 = \sum_\alpha \int_{-\infty}^{+\infty} dt' \chi^R_{AB_\alpha}(t - t') f_\alpha(t') + o(f^2), \tag{13}$$

$$\chi^R_{AB_\alpha}(t - t') = -i\Theta(t - t')\langle [\hat{A}(t), \hat{B_\alpha}(t')] \rangle_0, \tag{14}$$

Where $\chi^R_{AB_\alpha}$ is the susceptibility and $\langle ... \rangle_0$ is the mean value taken on the unperturbed system.

In our case, $\hat{V}(t) = \underbrace{\hat{H}_T(t)}_{B} \underbrace{\Theta(t)}_{f}$ and $\langle \hat{I}_p \rangle_0 = 0$. All this leads to equation 15:

$$\langle \hat{I}_p(t)\rangle - = \int_{-\infty}^{+\infty} dt' \chi^R(t-t')\Theta(t'), \tag{15}$$

$$\chi^R(t-t') = -i\Theta(t-t')\langle [\hat{I}_p(t), \hat{H}_T(t')]\rangle_0, \tag{16}$$

Let us compute $\chi^R(t-t')$:

$$\chi^R(t-t') = \Theta(t-t')\langle [(T-T^\dagger)(t), (T+T^\dagger)(t')]\rangle_0,$$

But $\langle [T(t), T(t')]\rangle_0 = \langle [T^\dagger(t), T^\dagger(t')]\rangle_0 = 0$ because of Wick's theorem (the mean value is taken for the unperturbed system).

Indeed, because of Wick's theorem, only terms like $\langle c_\alpha c_\alpha\rangle_0$ or $\langle c_\alpha^\dagger c_\alpha^\dagger\rangle_0$, which give 0, intervene in the computation.

$$\chi^R(t-t') = \Theta(t-t')\langle [T(t), T^\dagger(t')] \underbrace{-[T^\dagger(t), T(t')]}_{[T(t),T^\dagger(t')]^\dagger}\rangle_0,$$

$$\chi^R(t-t') = 2\Re[\Theta(t-t')\langle [T(t), T^\dagger(t')]],$$

$$\chi^R(t-t') = 2\Re[\Theta(t-t')\sum_{kk',\sigma}\sum_{k''k''',\sigma'} T_{kk'}T^*_{k''k'''}(\langle c^\dagger_{1k,\sigma}(t)c_{2k',\sigma}(t)c^\dagger_{2k''',\sigma'}(t')c_{1k'',\sigma'}(t')\rangle_0 - \langle c^\dagger_{2k''',\sigma'}(t')c_{1k'',\sigma'}(t')c^\dagger_{1k,\sigma}(t)c_{2k',\sigma}(t)\rangle_0)],$$

Here again, also because of Wick's theorem:

$$\begin{cases} \langle c^\dagger_{1k,\sigma}(t)c_{2k',\sigma}(t)c^\dagger_{2k''',\sigma'}(t')c_{1k'',\sigma'}(t')\rangle_0 = \langle c^\dagger_{1k,\sigma}(t)c_{1k'',\sigma'}(t')\rangle_0\langle c_{2k',\sigma}(t)c^\dagger_{2k''',\sigma'}(t')\rangle_0. \\ \langle c^\dagger_{2k''',\sigma'}(t')c_{1k'',\sigma'}(t')c^\dagger_{1k,\sigma}(t)c_{2k',\sigma}(t)\rangle_0 = \langle c^\dagger_{2k''',\sigma'}(t')c_{2k',\sigma}(t)\rangle_0\langle c_{1k'',\sigma'}(t')c^\dagger_{1k,\sigma}(t)\rangle_0. \end{cases}$$

The greater and lesser Greens functions are defined as follows:

$$\begin{cases} G^>_{ab}(t,t') = -i\langle c_a(t)c_b^\dagger(t')\rangle_0, \\ G^<_{ab}(t,t') = i\langle c_b^\dagger(t')c_a(t)\rangle_0, \end{cases} \tag{17}$$

Moreover, one has the following relations:

$$\begin{cases} G^>_{ab}(\omega) = -2i\pi(1-n_F(\omega-\mu))A_{ab}(\omega-\mu), \\ G^<_{ab}(\omega) = 2i\pi n_F(\omega-\mu)A_{ab}(\omega-\mu), \end{cases} \tag{18}$$

Where n_F is the Fermi-Dirac distribution and A_{ab} the spectral function.

In our case, assuming the lesser and greater Green's functions are diagonal in k, one gets:

$$\langle \hat{I}_p\rangle = \int_{-\infty}^0 2\Re[\sum_{kk',\sigma\sigma'} |T_{kk'}|^2(G^<_{1k,\sigma}(t')G^>_{2k',\sigma'}(-t') - G^>_{1k,\sigma}(t')G^<_{2k',\sigma'}(-t'))],$$

$$\langle \hat{I}_p\rangle = \int_{-\infty}^0 2\Re[\sum_{kk',\sigma\sigma'} |T_{kk'}|^2\frac{1}{(2\pi)^2}\int d\omega d\omega' e^{-i(\omega-\omega')t'}(G^<_{1k,\sigma}(\omega)G^>_{2k',\sigma'}(\omega') - G^>_{1k,\sigma}(\omega)G^<_{2k',\sigma'}(\omega'))],$$

$$\langle \hat{I}_p\rangle = \int_{-\infty}^0 2\Re[\sum_{kk',\sigma\sigma'} |T_{kk'}|^2\frac{1}{(2\pi)^2}\int d\omega d\omega' e^{-i(\omega-\omega')t'}(G^<_{1k,\sigma}(\omega)G^>_{2k',\sigma'}(\omega') - G^>_{1k,\sigma}(\omega)G^<_{2k',\sigma'}(\omega'))],$$

Because $\int_{-\infty}^{+\infty} dt e^{i\alpha t} = \int_{-\infty}^{0} dt 2\Re e^{i\alpha t}$ and because $\int_{-\infty}^{+\infty} \frac{dt}{2\pi} e^{-i(\omega-\omega')t} = \delta(\omega-\omega')$ one gets:

$$\langle \hat{I}_p \rangle = \frac{1}{(2\pi)^2} \int_{-\infty}^{+\infty} d\omega \sum_{kk',\sigma\sigma'} |T_{kk'}|^2 (G^{<}_{1k,\sigma}(\omega) G^{>}_{2k',\sigma'}(\omega) - G^{>}_{1k,\sigma}(\omega) G^{<}_{2k',\sigma'}(\omega)),$$

Using relation 18:

$$\langle \hat{I}_p \rangle = 2\pi \sum_{kk',\sigma\sigma'} |T_{kk'}|^2 \int_{-\infty}^{+\infty} d\omega A_{1k,\sigma}(\omega-(\mu+eV_1) A_{2k',\sigma'}(\omega-(\mu+eV_2)[n_F(\omega-(\mu+eV_1))-n_F(\omega-(\mu+eV_2))],$$

$$\langle \hat{I}_p \rangle = 2\pi \sum_{kk',\sigma\sigma'} |T_{kk'}|^2 \int_{-\infty}^{+\infty} d\omega A_{1k,\sigma}(\omega) A_{2k',\sigma'}(\omega+eV)[n_F(\omega) - n_F(\omega+eV)],$$

One finally gets equation 19:

$$\hat{I} = -e2\pi \sum_{kk',\sigma\sigma'} |T_{kk'}|^2 \int_{-\infty}^{+\infty} d\omega A_{1k,\sigma}(\omega) A_{2k',\sigma'}(\omega+eV)[n_F(\omega) - n_F(\omega+eV)], \tag{19}$$

Now, if we assume $|T_{kk'}|$ to be constant equal to $|T|$ (which is often the case if the fermi surface is not too anisotropic), then we get:

$$\hat{I} = -e2\pi|T|^2 \int_{-\infty}^{+\infty} d\omega n_1(\omega) n_2(\omega+eV)[n_F(\omega) - n_F(\omega+eV)]. \tag{20}$$

Where $n_i = \sum_{k,\sigma} A_{ik,\sigma}$ is the density of states of conductor $i = 1$ or 2.

Let us now suppose that conductor 2 is a normal metal. Therefore, its density of states can be considered as constant and equal to n_0 because only electrons close to Fermi level participate to the dynamics of the whole system. The conductance of the system is then:

$$\frac{d\hat{I}}{dV} = e^2 2\pi |T|^2 n_0 \int_{-\infty}^{+\infty} d\omega n_1(\omega) \frac{dn_F}{d\omega}(\omega+eV). \tag{21}$$

Bibliography

[1] V. Mourik. Signatures of Majorana fermions in hybrids superconductor-semiconductor nanowire devices. *Science*, **336**(6084), 2012.

[2] S. Nadj-Perge. Observation of Majorana fermions in ferromagnetic atomic chains on a superconductor. *Science*, **346**(6029), 2014.

[3] G. C. Ménard. Two-dimensional topological superconductivity in $Pb/Co/Si(111)$. *Nature Communications*, **8**(2040), 2017.

[4] G. C. Ménard. Isolated pairs of Majorana zero modes in a disordered superconducting lead monolayer. *arXiv*, 2018.

[5] D. Longo. *Engineering topological states in arrays of magnetic molecules in interaction with a 2D superconductor*. PhD thesis, Sorbonne Université, Paris, 2019.

[6] J. Xu. Experimental detection of a Majorana mode in the core of a magnetic vortex inside a topological insulator-superconductor $Bi_2Te_3/NbSe_2$ heterostructure. *Physical Review Letters*, **114**(017001), 2015.

[7] D. Wang. Evidence for Majorana bound states in an iron-based superconductor. *Science*, **362**(333-335), 2018.

[8] D. Shaffer. Crystalline nodal topological superconductivity in monolayer $NbSe_2$. *arXiv*, 2019.

[9] P. Monceau. Anisotropy of the superconducting properties of misfit layer compounds $(MX)_n(NbX_2)_m$. *Physica B*, **194-196**(2361-2362), 1994.

[10] M. Zare. Mixed-pairing superconductivity in 5d Mott insulators with antisymmetric exchange: application to Sr_2IrO_4. *Physical Review B*, **96**(205156), 2017.

[11] F. London and H. London. The electromagnetic equations of the supraconductor. *Proceedings of the Royal Society of London A*, **149**(71-88), 1935.

[12] V.L. Ginzburg and L.D. Landau. Contribution to the theory of superconductivity. *Zh. Eksp. Teor. Fiz.*, **20**(1064-1082), 1950.

[13] J. Bardeen. Theory of superconductivity. *Physical Review Journals archive*, **108**(1175-1204), 1957.

[14] Leon N. Cooper. Bound electron pairs in a degenerate Fermi gas. *Physical Review Journals archive*, **104**(1189), 1956.

[15] N.N. Bogoliubov. A new method in the theory of superconductivity I. *JETP*, **7**(41), 1958.

[16] N.N. Bogoliubov. A new method in the theory of superconductivity III. *JETP*, **7**(51), 1958.

[17] P.W. Anderson. Random phase approximation in the theory of superconductivity. *JETP*, **112**(1900), 1958.

[18] M. Combescot. *Excitons and Cooper pairs*. OXFORD University Press, New York, 2016.

[19] Michael Tinkham. *Introduction to superconductivity*. DOVER PUBLICATIONS, INC, Mineola, New York, 2004.

[20] A. Rahman. A review on cuprate based superconducting materials including characteristics and applications. *American Journal of Physics and Applications*, **3**(2), 2015.

[21] P.W. Anderson. Localized magnetic states in metals. *Physical Review Journals archive*, **124**(41), 1961.

[22] D. Jérome. Superconductivity in a synthetic organic conductor $(TMTSF)_2PF_6$. *J. Physique Lett.*, **41**(4), 1980.

[23] I.J. Lee. Unconventional superconductivity in a quasi-one-dimensional system $(TMTSF)_2X$. *Journal of the Physical Society of Japan*, **75**(5), 2006.

[24] D. Aoki. Review of U-based ferromagnetic superconductors: Comparison between UGe_2, $URhGe$, and $UCoGe$. *Journal of the Physical Society of Japan*, **88**(022001), 2019.

[25] S. Saxena. Superconductivity on the border of itinerant-electron ferromagnetism in UGe_2. *Nature*, **406**(587-592), 2000.

[26] F. Laube. Spin-triplet superconductivity in Sr_2RuO_4 probed by Andreev reflection. *Physical Review Letters*, **84**(7), 2000.

[27] M. Nishiyama. Spin triplet superconducting state due to broken inversion symmetry in Li_2Pt_3B. *Physical Review Letters*, **98**(047002), 2007.

[28] V. B. Berestetskii. *Quantum electrodynamics, second edition*. Pergamon Press, 1982.

[29] J. G. Rau. Spin-orbit physics giving rise to novel phases in correlated systems : iridates and related materials. *Annual Review of Condensed Matter Physics*, **7**(195-221), 2016.

[30] V.M. Edel'shtein. Characteristics of the Cooper pairing in two-dimensional noncentrosymmetric electron systems. *Zh. Eksp. Teor. Fiz.*, **95**(2151-2162), 1989.

[31] Lev P. Gor'kov and Emmanuel. I. Rashba. Superconducting 2D system with lifted spin degeneracy: mixed singlet-triplet state. *Physical Review Letters*, **87**(3), 2001.

[32] H. Wang. High-quality monolayer superconductor $NbSe_2$ grown by chemical vapour deposition. *Nature Communications*, **8**(394), 2017.

[33] Xiaoxiang Xi. Ising pairing in superconducting $NbSe_2$ atomic layers. *Nature Physics*, **12**(139-143), 2016.

[34] Sergio C. de la Barrera. Tuning Ising superconductivity with layer and spin-orbit coupling in two-dimensional transition metal dichalcogenides. *Nature Communications*, **9**(1427), 2018.

[35] T. Dvir. Spectroscopy of bulk and few-layer superconducting $NbSe_2$ with van der Waals tunnel junctions. *Nature Communications*, **9**(598), 2018.

[36] J.M. Lu. Evidence for two-dimensional Ising superconductivity in gated MoS_2. *Science*, **350**(6266), 2015.

[37] B. Andrei Bernevig, Taylor L. Frank Hugues, and Alexander Samarin. *Topological insulators and topological superconductors.* Princeton University Press, Princeton and Oxford, 2013.

[38] D. A. Ivanov. Non-abelian statistics of half-quantum vortices in p-wave superconductors. *Physical Review Letters*, **86**(2), 2001.

[39] Li-Wei Yu. More about the doubling degeneracy operators associated with Majorana fermions and Yang-Baxter equation. *Scientific Reports*, **5**(8102), 2015.

[40] S. Das Sarma. Majorana zero modes and topological quantum computation. *npj Quantum Information*, **1**(15001), 2015.

[41] T.E. O'Brien. Majorana-based fermionic quantum computation. *Physical Review Letters*, **120**(220504), 2018.

[42] M. McGinley. Robustness of Majorana edge modes and topological order: Exact results for the symmetric interacting Kitaev chain with disorder. *Physical Review B*, **96**(241113(R)), 2017.

[43] A Yu Kitaev. Unpaired Majorana fermions in quantum wires. *Physics-Uspekhi*, **44**, 2001.

[44] A. Das. Zero-bias peaks and splitting in an $Al-InAs$ nanowire topological superconductor as a signature of Majorana fermions. *Nature Physics*, **8**(887–895), 2012.

[45] S.M. Albrecht. Exponential protection of zero modes in Majorana islands. *Nature*, **531**(206-209), 2016.

[46] M.T. Deng. Majorana bound state in a coupled quantum-dot hybrid nanowire system. *Science*, **354**(6319), 2016.

[47] C. Reeg. Zero-energy Andreev bound states from quantum dots in proximitized Rashba nanowires. *Physical Review B*, **98**(245407), 2018.

[48] T.P. Choy. Finite-size effects in a nanowire strongly coupled to a thin superconducting shell. *Physical Review B*, **96**(125426), 2017.

[49] C. Reeg. Metallization of a Rashba wire by a superconducting layer in the strong-proximity regime. *Physical Review B*, **97**(165425), 2018.

[50] S. Vaitiekenas. Flux-induced Majorana modes in full-shell nanowires. *arXiv*, 2018.

[51] T.P. Choy. Majorana fermions emerging from magnetic nanoparticles on a superconductor without spin-orbit coupling. *Physical Review B*, **84**(195442), 2011.

[52] S. Nadj-Perge. Proposal for realizing Majorana fermions in chains of magnetic atoms on a superconductor. *Physical Review B*, **88**(020407(R)), 2013.

[53] B. Braunecker. Interplay between classical magnetic moments and superconductivity in quantum one-dimensional conductors : toward a self-sustained topological Majorana phase. *Physical Review Letters*, **111**(147202), 2013.

[54] J. Klinovaja. Topological superconductivity and Majorana fermions in RKKY systems. *Physical Review Letters*, **111**(186805), 2013.

[55] M.M. Vazifeh. Self-organized topological state with Majorana fermions. **111**(206802), 2013.

[56] B.E. Feldman. High-resolution studies of the Majorana atomic chain platform. *Nature Physics*, **13**(286-291), 2017.

[57] S. Jeon. Distinguishing a Majorana zero mode using spin-resolver measurements. *Science*, **358**(6364), 2017.

[58] M. Ruby. End states and subgap structure in proximity-coupled chains of magnetic adatoms. *Physical Review Letters*, **115**(197204), 2015.

[59] H. Kim. Toward tailoring Majorana bound states in artificially constructed magnetic atom chains on elemental superconductors. *ScienceAdvances*, **4**(5), 2018.

[60] J. Li. Two-dimensional chiral topological superconductivity in Shiba lattices. *Nature Communications*, **7**(12297), 2016.

[61] A. Palacio-Morales. Atomic-scale interface engineering of Majorana edge modes in a 2d magnet-superconductor hybrid system. *arXiv*, 2018.

[62] B. Lian. Topological quantum computation based on chiral Majorana fermions. *PNAS*, **115**(43), 2018.

[63] G. E. Volovik. Fermion zero modes on vortices in chiral superconductors. *JETP letters*, **70**(9), 1999.

[64] L. Fu. Superconducting proximity effect and Majorana fermions at the surface of a topological insulator. *Physical Review Letters*, **100**(096407), 2008.

[65] G. Xu. Topological superconductivity on the surface of Fe-based superconductors. *Physical Review Letters*, **117**(047001), 2016.

[66] P. Zhang. Observation of topological superconductivity on the surface of an iron-based superconductor. *Science*, **360**(182-186), 2018.

[67] Q. Liu. Robust and clean Majorana zero mode in the vortex core of high-temperature superconductor $(Li_{0.84}Fe_{0.16})OHFeSe$. *Physical Review X*, **8**(041056), 2018.

[68] G. Binnig and H. Rohrer. Scanning tunneling microscopy. *IBM journal of research and development*, **30**(355–369), 1986.

[69] J. Tersoff. Theory and application for the scanning tunneling microscope. *Physical Review Letters*, **50**(25), 1983.

[70] J. A. Silva-Guillen. Tunneling and electronic structure of the two-gap superconductor MgB_2. *Physical Review B*, **92**(064514), 2015.

[71] M. Iavarone. Two-band superconductivity in MgB_2. *Physical Review Letters*, **89**(187002), 2002.

[72] A. Savitzky and J.E. Golay. Smoothing and differentiation of data by simplified least squares procedures. *Analytical Chemistry*, **36**(8), 1964.

[73] J.E. Hoffman. *A Search for Alternative Electronic Order in the High Temperature Superconductor $Bi_2Sr_2CaCu_2O_{8+\delta}$ by Scanning Tunneling Microscopy.* PhD thesis, University of California, Berkeley, 2003.

[74] M.F. Crommie. Imaging standing waves in a two-dimensional electron gas. *Nature*, **363**(524-527), 1993.

[75] Y. Kohsaka. Spin-orbit scattering visualized in quasiparticle interference. *Physical Review B*, **95**(115307), 2017.

[76] P. Leicht. Rashba splitting of graphene-covered $Au(111)$ revealed by quasiparticle interference mapping. *Physical Review B*, **90**(241406(R)), 2014.

[77] Y. Noat. Quasiparticle spectra of $2H - NbSe_2$: two-band superconductivity and the role of tunneling selectivity. *Physical Review B*, **92**(134510), 2015.

[78] C. J. Arguello. Visualizing the charge density wave transition in $2H - NbSe_2$ in real space. *Physical Review B*, **89**(235115), 2014.

[79] K. Rossnagel. Fermi surface of $2H - NbSe_2$ and its implications on the charge-density-wave mechanism. *Physical Review B*, **64**(235119), 2001.

[80] X. Zhu. Classification of charge density waves based on their nature. *PNAS*, **112**(8), 2015.

[81] I. Guillamon. Intrinsic atomic-scale modulations of the superconducting gap of $2H - NbSe_2$. *Physical Review B*, **77**(134505), 2008.

[82] J.G. Rodrigo. STM study of multiband superconductivity in $NbSe_2$ using a superconducting tip. *Physical C*, **404**(306), 2004.

[83] S. Gao. Atomic-scale strain manipulation of a charge density wave. *PNAS*, **115**(27), 2018.

[84] A. Wieteska. Uniaxial strain tuning of superconductivity in $2H - NbSe_2$. *arXiv*, 2019.

[85] K. Cho. Using controlled disorder to probe the interplay between charge order and superconductivity in $NbSe_2$. *Nature Communications*, **9**(2796), 2018.

[86] Huixia Luo. S-shaped suppression of the superconducting transition temperature in Cu-intercalated $NbSe_2$. *Chemistry of Materials*, **29**(3704-3712), 2017.

[87] Xiaoxiang Xi. Gate tuning of electronic phase transitions in two-dimensional $NbSe_2$. *Physical Review Letters*, **117**(106801), 2016.

[88] Xiaoxiang Xi. Strongly enhanced charge-density-wave order in monolayer $NbSe_2$. *Nature Nanotechnology*, **10**(765-769), 2015.

[89] R. Roeski. Structure and electronic transport properties of the misfit layer compound $(LaSe)_{1,14}(NbSe_2)$, "$LaNb_2Se_5$)". *Zeitschrift für Anorganische und Allgemeine Chemie*, **619**(117-122), 1993.

[90] U. Chaterjee. Emergence of coherence in the charge-density wave state of $2H - NbSe_2$. *Nature Communications*, **6**(6313), 2015.

[91] C.J. Arguello. Quasiparticle interference, quasiparticle interactions, and the origin of the charge density wave in $2H - NbSe_2$. *Physical Review Letters*, **114**(037001), 2015.

[92] Masaru Onoda. Disorder-induced delocalization in an incommensurate potential. *Physical Review B*, **74**(121101(R)), 2006.

[93] G. Reményi. Incommensurate systems as model compounds for disorder revealing low-temperature glasslike behavior. *Physical Review Letters*, **114**(195502), 2015.

[94] Miguel M. Ugeda. Characterization of collective ground states in single-layer $NbSe_2$. *Nature Physics*, **12**(92-97), 2016.

[95] Maxime Leroux. Strong anharmonicity induces quantum melting of charge density wave in $2H - NbSe_2$ under pressure. *Physical Review B*, **92**(140303(R)), 2015.

[96] A. Kormanyos. Monolayer MoS_2 : Trigonal warping, the valley, and spin-orbit coupling effects. *Physical Review B*, **88**(045416), 2013.

[97] Wen-Yu He. Magnetic field driven nodal topological superconductivity in monolayer transition metal dichalcogenides. *Communications Physics*, **1**(40), 2018.

[98] Yi-Ting Hsu. Topological superconductivity in monolayer transition metal dichalcogenides. *Nature Communications*, **8**(14985), 2017.

[99] E.S. Kadantsev. Topological superconductivity in monolayer transition metal dichalcogenides. *Solid State Communications*, **152**(10), 2012.

[100] P. Fulde. Superconductivity in a strong spin-exchange field. *Physical Review Journal Archive*, **135**(A550), 1964.

[101] H. Suderow. Imaging superconducting vortex cores and lattices with a scanning tunneling microscope. *Superconductor Science and Technology*, **27**(6), 2014.

[102] A. Kohen. Superconducting vortex profile from fixed point measurements the "lazy fisherman" tunneling microscopy method. *Applied Physics Letters*, **86**(212503), 2005.

[103] B. B. Zhou. Visualizing nodal heavy fermion superconductivity in $CeCoIn_5$. *Nature Physics*, **9**(474-479), 2013.

[104] G. C. Ménard. Coherent long-range magnetic bound states in a superconductor. *Nature Physics*, **11**(1013-1016), 2015.

[105] G. C. Ménard. Yu-Shiba-Rusinov bound states versus topological edge states in $Pb/Si(111)$. *The European Physical Journal SPecial Topics*, **227**(15-16), 2019.

[106] J. Kim. Universal quenching of the superconducting state of two-dimensional nanosize *Pb*-island structures. *Physical Review B*, **84**(014517), 2011.

[107] Y. Noat. Signatures of multigap superconductivity in tunneling spectroscopy. *Physical Review B*, **82**(014531), 2010.

[108] H. Watanabe. Monte Carlo study of an unconventional superconducting phase in iridium oxide $J_{eff} = 1/2$ Mott insulators induced by carrier doping. *Physical Review Letters*, **110**(027002), 2013.

[109] F. Wang. Twisted Hubbard model for Sr_2IrO_4 : magnetism and possible high temperature superconductivity. *Physical Review Letters*, **106**(136402), 2011.

[110] Q. Wang. Neutron powder diffraction study of the crystal structures of Sr_2RuO_4 and Sr_2IrO_4 at room temperature and at 10 K. *Journal of Solid State Chemistry*, **112**(2), 1994.

[111] Y. Yang. Superconductivity in doped Sr_2IrO_4: a functional renormalization group study. *Physical Review B*, **89**(094518), 2014.

[112] Y.J. Yan. Electron-doped Sr_2IrO_4: an analogue of hole-doped cuprate superconductors demonstrated by scanning tunneling microscopy. *Physical Review X*, **5**(041018), 2015.

[113] P. Phillips. *Advanced solid state physics*. Cambridge University Press, 2012.

[114] A. De La Torre. *Spectroscopic studies of layered iridium oxides.* PhD thesis, Université de Genève, 2015.

[115] A. Georges. Hubbard model in infinite dimensions. *Physical Review B*, **45**(12), 1992.

[116] I. Masatoshi. Metal-insulator transitions. *Reviews of Modern Physics*, **70**(1039), 1998.

[117] D. Mandrus. Continuous metal-insulator transition in the pyrochlore $Cd_2Os_2o_7$. *Physical Review B*, **63**(195104), 2001.

[118] C. Martins. Coulomb correlations in 4d and 5d oxides from first principles or how spin-orbit materials choose their effective orbital degeneracies. *Journal of Physics : Condensed Matter*, **29**(263001), 2017.

[119] B. J. Kim. Novel $J_{eff} = 1/2$ Mott state induced by relativistic spin-orbit coupling in Sr_2IrO_4. *Physical Review Letters*, **101**(076402), 2008.

[120] Q. Kim. Dimensionality-controlled Mott transition and correlation effect in single-layer and bilayer perovskite iridates. *Physical Review B*, **87**(245109), 2013.

[121] S. J. Moon. Temperature dependence of the electronic structure of the $J_{eff} = 1/2$ Mott insulator Sr_2IrO_4 studied by optical spectroscopy. *Physical Review B*, **80**(195110), 2009.

[122] B. H. Kim. Magnetic couplings, optical spectra, and spin-orbit exciton in 5d electron Mott insulator Sr_2IrO_4. *Physical Review Letters*, **109**(167205), 2012.

[123] J. Kim. Magnetic excitation spectra of Sr_2IrO_4 probed by resonant inelastic X-ray scattering: establishing links to cuprate superconductors. *Physical Review Letters*, **108**(177003), 2012.

[124] Q. Li. Atomically resolved spectroscopic study of Sr_2IrO_4 : experiment and theory. *Scientific Reports*, **3**(3073), 2013.

[125] J. Dai. Local density of states study of a spin-orbit-coupling induced Mott insulator Sr_2IrO_4. *Physical Review B*, **90**(041102(R)), 2014.

[126] I. Battisti. Poor electronic screening in lightly doped Mott insulators observed with scanning tunneling microscopy. *Physical Review B*, **95**(235141), 2017.

[127] V. Brouet. Transfer of spectral weight across the gap of Sr_2IrO_4 induced by La doping. *Physical Review B*, **92**(081117(R)), 2015.

[128] A. De la Torre. Collapse of the Mott gap and emergence of a nodal liquid in lightly doped Sr_2IrO_4. *Physical Review Letters*, **115**(176402), 2015.

[129] I. Battisti. Universality of pseudogap and emergent order in lightly doped Mott insulators. *Nature Physics*, **13**(21-25), 2017.

[130] L. Li. Tuning the $J_{eff} = 1/2$ insulating state via electron doping and pressure in the double-layered iridate $Sr_3Ir_2O_7$. *Physical Review B*, **87**(235127), 2013.

[131] D. A. Zocco. Persistent non-metallic behavior in Sr_2IrO_4 and $Sr_3Ir_2O_7$ at high pressures. *Journal of Physics : Condensed Matter*, **26**(25), 2014.

[132] Y. K. Kim. Fermi arcs in a doped pseudospin-1/2 Heisenberg antiferromagnet. *Science*, **345**(187-190), 2014.

[133] Y. K. Kim. Observation of a d-wave gap in electron-doped Sr_2IrO_4. *Nature Physics*, **12**(37-41), 2016.

[134] A. De la Torre. Coherent quasiparticles cith a small Fermi surface in lightly doped $Sr_3Ir_2O_7$. *Physical Review Letters*, **113**(256402), 2014.

[135] X. Chen. Influence of electron doping on the ground state of $(Sr_{(1-x)}la_x)_2IrO_4$. *Physical Review B*, **92**(075125), 2015.

[136] A. Louat. Formation of an incoherent metallic state in Rh-doped Sr_2IrO_4. *Physical Review B*, **97**(161109(R)), 2018.

[137] Y. Okada. Imaging the evolution of metallic states in a correlated iridate. *Nature Materials*, **12**(707-713), 2013.

[138] Q. Wang. Dimensionality-controlled Mott transition and correlation effects in single-layer and bilayer perovskite iridates. *Physical Review B*, **87**(245109), 2013.

[139] T. Hogan. First-order melting of a weak spin-orbit Mott insulator into a correlated metal. *Physical Review Letters*, **114**(257203), 2015.

[140] P. Cai. Visualizing the evolution from the Mott insulator to a charge-ordered insulator in lightly doped cuprates. *Nature Physics*, **12**(1047-1051), 2016.

[141] C. V. Parker. Fluctuating stripes at the onset of the pseudogap in the high-tc superconductor $Bi_2Sr2CaCu_2O_{8+x}$. *Nature*, **468**(677), 2010.

[142] Y. Kohsaka. Visualization of the emergence of the pseudogap state and the evolution to superconductivity in a lightly hole-doped Mott insulator. *Nature Physics*, **8**(534-538), 2012.

[143] Y. Kohsaka. Imaging nanoscale electronic inhomogeneity in the lightly doped Mott insulator $Ca_{(2-x)}Na_xCuO_2Cl_2$. *Physical Review Letters*, **93**(9), 2004.

[144] A. R. Schmidt. Electronic structure of the cuprate superconducting and pseugap phases from spectroscopic imaging STM. *New Journal of Physics*, **13**(06514), 2011.

[145] M. Ge. Lattice-driven magnetoresistivity and metal-insulator transition in single-layered iridates. *Physical Review B*, **84**(100402(R)), 2011.

[146] J. Nichols. Tunneling into the mott insulator Sr_2IrO_4. *Physical Review B*, **89**(085125), 2014.

[147] W. Bai. Monolayer behavior of NbS_2 in natural van der Waals heterostructures. *Journal of Physical Chemistry Letters*, **9**(6421-6425), 2018.

[148] M. M. Ugeda. Observation of topologically protected states at crystalline phase boundaries in single-layer WSe_2. *Nature Communications*, **9**(3401), 2018.